The Fate of Airborne Nanoparticles Released from a Leak in a Nanoparticle Production Process into a Simulated Workplace Environment

A DISSERTATION
SUBMITTED TO THE FACULTY OF THE GRADUATE SCHOOL
OF THE UNIVERSITY OF MINNESOTA
BY

NICHOLAS JAMES STANLEY

IN PARTIAL FULFILLMENT OF THE REQUIREMENTS
FOR THE DEGREE OF
DOCTOR OF PHILOSOPHY

ADVISOR

THOMAS H. KUEHN

August 2010

Acknowledgements

This thesis is the result of years of research, experimentation, analysis, presentations, coursework, and writing, which could not have been accomplished without the guidance and assistance provided by many within and outside of the University of Minnesota. First and foremost, I would like to acknowledge my advisors Professors Thomas Kuehn and David Y.H. Pui for their helpful guidance, insightful comments, encouragement, and financial support throughout the duration of my studies. I would also like to especially thank Professors Sean Garrick, Peter Raynor, and David Kittelson for their contributions while serving on my PhD examining committee.

Several more Mechanical Engineering faculty helped me through this experience. Professors Thomas Chase and Eph Sparrow supported my decision to attend graduate school by writing letters of recommendation. Professor James Ramsey provided encouragement as well as continued financial support as I served as a teaching assistant for him and Professor Thomas Kuehn in ME 4131. Finally I would like to acknowledge Professors Virgil Marple, Peter McMurry, and Chris Hogan for their research and suggestions in support of my project.

I would also like to acknowledge my collaborators in Germany for their continued support throughout this project. Dr. Christof Asbach, in particular, has done an incredible amount in support of my efforts. His astute suggestions, writing critique, and direction were very helpful. I am hopeful that our collaboration will continue in the future. Dr. Heinz Fissan and Dr. Thomas Kuhlbusch also deserve recognition for their support.

Thank you to the contributors within the Center for Filtration Research including: 3M, Boeing, Cummins, Donaldson, Entegris, W.L. Gore, Samsung, Shigematsu, TSI, and NIOSH for the interesting discussions, helpful suggestions, technical and financial support and hospitality during presentation visits. The post-docs contributing to this research include Seong Chan Kim, Chaolong Qi, Jing Wang, and Kyoungtae Kim.

Many students within the department also deserve acknowledgement for their helpful discussions and critique of my research. These students include Anil Bika, Rebecca Anthony, Julia Haltiwanger, Josh Quinnell, Josh Rocklage, Jake Swanson, Tsz Yan Ling, Adam Boies, Luke Franklin, Thomas Shepard, Weihua Tang, Nikhil Ramesh, and Jake Scheckman. Several more provided indirect support through discussions not directly related to the thesis, such as Ben Adams and members of GENS. The personal, moral, and intellectual support provided by all these students was invaluable and much appreciated.

Former students Jim Farnsworth, Liming Lo and Sho Takagaki, deserve thanks for their initial guidance. I would also like to acknowledge the support during my Master's Thesis by Senthil Anantharaman, M.A. Ramakrishnan, Seung Won Kim, and Professors Thomas Kuehn, Peter Raynor, and Sagar Goyal.

Supporting staff within the Mechanical Engineering Department also deserve acknowledgement for their assistance, especially Jennifer Dahal, Bob Nelson, and John Gardner. I appreciate the assistance given by Ozan Urgulu in the Characterization Facility, and would like to acknowledge the Doctoral Dissertation Fellowship for the financial support during the final year of my program. I would also like to acknowledge the financial support provided through the NSF G2006-STAR-F2 Grant.

Last, but not least, I would like to acknowledge my family and friends. Being born and raised in Minnesota I had the advantage of a great base of support. The pursuit of my degree would have been much more difficult without this support and encouragement.

Dedication

In loving memory of my grandfather, Emory Castle Stanley.

Abstract

A leak in nanoparticle production equipment can cause large quantities of nanoparticles to be emitted into a workplace environment. Toxicity studies have shown hazards of inhaling nanoparticles; however these studies may not be using the proper particles. Physical and chemical changes may occur as these nanoparticles travel from the production site through ambient air, causing worker exposure. With the correct size and concentration known at distances from the leak, realistic worker exposure can be determined and appropriate worker protection and occupational monitoring schemes can be developed.

Different nanoparticle materials were produced with a diffusion burner and injected through an experimentally simulated leak into a wind tunnel (simulated workplace environment). The wind tunnel background face velocity was 0.25 m/s. Soot distributions (d_g = 59 and d_g = 113 nm) and TiO_2 (d_g = 21 nm) were used as the test aerosols. A smaller distribution of particles (d_g < 8 nm) was also noticed at the injection site for soot and TiO_2. Lung deposited surface area concentration was measured using a NSAM and the number size distribution was measured with a SMPS at distances of 0.9 m, 1.8 m, and 3.4 m (times of 3.6 s, 7.2 s, and 13.6 s, respectively) from the injection point. TEM images were gathered at the injection point and 3.4 m downstream.

The soot (d_g = 113 nm) and TiO_2 (d_g = 21 nm) distributions produced loose, chain-type agglomerates at the injection point with primary particle sizes of d_{pp} = 30 nm and d_{pp} = 4.5 nm, respectively. These distributions experienced an increase in geometric mean particle size between the injection point and 0.9 m downstream. Surface area per particle (NSAM/SMPS ratio) also increased between the injection point and 0.9 m

downstream. There was no additional particle change after 0.9 m. Primary particle size also increased after the injection point within the wind tunnel. Therefore the agglomerate size change may have been caused by the primary particle size change, as coagulation is an unlikely cause of particle growth in this situation. The soot (d_g = 59 nm) aerosol was not relevant for this analysis.

The soot (dg = 59 nm) distribution was created using a Rich fuel/air mixture (φ = 2.05), which produced unburned fuel in the exhaust. When the simulated leak size was changed from 27 mm to 10 mm, the Richardson number of the leak changed from 197 to 0.42, and a bi-modal distribution formed at 0.9 m downstream (1^{st} mode: d_g = 16 nm, 2^{nd} mode: d_g = 70 nm). The first mode particle formation was likely caused by turbulent mixing of the leaked exhaust gases with background air, causing local supersaturation and new particle formation.

Table of Contents

List of Tables

List of Figures

List of Nomenclature

A_2	Cross-Sectional Area of Orifice (m^2)
A_s	Cross-sectional area of Nanometer Aerosol Sampler (NAS) at grid location (cm^2)
C	Orifice flow coefficient (dimensionless)
C_c	Cunningham's slip correction (dimensionless)
C_c	Contraction coefficient for vena contracta (dimensionless)
C_i	Number concentration (#/cm^3)
C_{sa}	Concentration of sub-primary particles sampled by NAS, by volume (#/cm^3)
C_{sp}	Concentration of sub-primary particles within wind tunnel (#/cm^3)
$C_{sp,corr}$	C_{sp} corrected for penetration, dilution, and capture efficiency (#/cm^3)
C_m	Number concentration of particle with mobility diameter, d_m (#/cm^3)
c*	Dimensionless drag force on an agglomerate (dimensionless)
D	Diffusion coefficient of particles (m^2/s)
D_f	Fractal dimension (dimensionless)
D_r	Dilution Ratio of sampling equipment (dimensionless)
D_H	Hydraulic diameter of wind tunnel (D_H = 61 cm)
d	Diameter of simulated leak (mm)
d.f.	Degrees of freedom (dimensionless)
d_i	Particle diameter (nm)
d_g	Geometric mean particle mobility diameter (nm)
d_m	Particle mobility diameter (nm)
d_p	Particle diameter (nm or m)
d_{pp}	Primary particle diameter (nm)
d_{sp}	Sub-primary particle diameter (nm)
g	Gravitational acceleration (9.8 m/s^2)
K	Scaling factor (dimensionless)
k	Boltzmann's constant (1.38 x 10^{-23} kg-m^2/K-s^2)
k	Specific heat ratio, used in Equation 3.5.5 only (dimensionless)
L	Length of sampling line (m)
M	Molar mass of gas (kg/kmole)
mfr	Mass flow rate (kg/s)
N	Sample size (#)
N_i	Sample size for ith data set (#)
N_{pp}	Number of primary particles per agglomerate (#)
n_{in}	Particle concentration upstream of sampling tube (cm^{-3})
n_{out}	Particle concentration downstream of sampling tube (cm^{-3})
P	Particulate penetration through sampling tube (dimensionless)
P_1	Pressure upstream of orifice (N/m^2)
P_2	Pressure downstream of orifice (N/m^2)
Q	Volumetric flow rate (m^3/s)
Q_s	Sample flow rate of NAS (l/min)
R	Universal gas constant (N-m/kmole-K)
R_g	Radius of gyration (nm) (assumption: $2R_g = d_m$)
SE	Standard Error (dimensionless)

s_i	Sample variance for data set i
T	Time between injection point and final sampling location (s)
T	Temperature (K)
T_1	Temperature upstream of orifice (K)
T_{amb}	Temperature within wind tunnel (K)
T_{jet}	Temperature of exhaust (jet) gases (K)
T_s	Sample time with NAS (min)
t	Time between injection point and sampling location
$t_{\alpha/2,N-1}$	t-statistic from Student's t-distribution with $\alpha = 0.05$ and d.f. = N-1
U	Velocity (m/s)
$V_{agg,m}$	Volume concentration of agglomerates with mobility diameter, d_m ($\mu m^3/cm^3$)
V_i	Volumetric concentration of particle diameter, d_i ($\mu m^3/cm^3$)
V_{jet}	Velocity of jet (m/s)
V_{sp}	Volumetric concentration of sub-primary particles ($\mu m^3/cm^3$)
V_T	Total volume concentration of particles within a distribution ($\mu m^3/cm^3$)
x_i	Data point i within data set
$\bar{x}_i$	Sample mean for data set i
z	Distance between injection point and sampling location (cm or m)
Z	Gas compressibility factor at P_1 and T_1 (dimensionless)

α	Alpha level ($\alpha = 0.05$ indicates 95% confidence)
β	Thermal expansion coefficient (1/K).
σ_g	Geometric standard deviation of particle number distribution
σ	Geometric mean standard deviation
λ	Gas mean free path (nm)
μ	Dynamic viscosity (kg/m-s)
μ	Diffusion deposition parameter (dimensionless)
ν	Kinematic viscosity (m^2/s)
φ	Equivalency ratio (dimensionless)
ρ	Density (kg/m^3)
$\%\eta$	Sub-primary particle collection efficiency for TEM grid (NAS Manual)

95% CI	95% Confidence Interval
LDSA	Lung Deposited Surface Area ($\mu m^2/cm^3$)
Re	Reynolds number ($Re = Ud/\nu$)
Gr	Grashof number ($Gr = g\beta(T_{amb} - T_{jet})d^3/\nu^2$)
Ri	Bulk Richardson number ($Ri = Gr/Re^2$)

Section 1
Introduction

Section 1.1: Motivation and Objectives

The toxicity of nanoparticles has received increased attention in recent years. The total airborne nanoparticle surface area has been proposed by toxicologists as the most health relevant measure in order to assess worker exposure with respect to inhalation and deposition in different compartments of the lung. Currently number and mass based measurements are used as standards for airborne particle exposure limits by regulatory agencies such as NIOSH and the EPA. However nanoparticles have a large amount of surface area for their mass, making mass measurements inappropriate for such small particles (although mass measurements are appropriate when measuring particles larger than 0.3 μm). Number based measurements are inadequate for nanoparticles because the sensors used in these measurements can easily become overloaded when sampling high particle concentrations.

If there is a leak in nanoparticle production equipment, nanoparticles can be emitted at very high concentrations. However, as the aerosol travels between the leak and

the point of human exposure, the nanoparticles may undergo physical or chemical reactions that can change the nanoparticle properties. Number and surface area concentration, morphology, or chemical composition may change as the NPs traverse from the leak through ambient air. In this project the fate of nanoparticles will be determined, after being emitted through a leak in a nanoparticle production process into a simulated work place environment. Overall we hope to provide a link between production and adverse health effects of industrially produced nanoparticles by showing the potential worker exposure during a worst case leak scenario.

Section 1.2: Methods

An ASHRAE 52.2-2007 Classified wind tunnel was used to simulate the ambient air of a work place environment. Particles were injected into this enclosed wind tunnel through an injection probe as outlined in Figure 1.2.1. The injection probe is designed to mimic a leak in nanoparticle production equipment as well as accommodate a variety of leak parameters, including velocity, diameter, and flow rate of the leak.

This wind tunnel was chosen because the nanoparticles remain isolated from the laboratory personnel and the conditions inside the wind tunnel can be precisely controlled. The wind tunnel is also very versatile and can be reconfigured since it is made up of several sections. It has a 600 mm x 600 mm (24” x 24”) cross section and an active length of approximately 9.50 m with a 180° bend (610 mm radius) along the way. The bend may not have an impact on the NP distribution in the wind tunnel due to the low inertia of nanoparticles, however this must be verified. There are several possible sampling locations along the wind tunnel, where particle properties can be measured.

The wind tunnel includes environmental monitoring sensors for temperature, relative humidity, flow rate, and pressure and was originally operated in a closed loop configuration in order to eliminate the risk of exposure to any test aerosols. During the current study, the wind tunnel was opened to allow for the placement of an injection probe and venting of combustion gases. Measurements were taken at locations throughout the wind tunnel during the initial dispersion testing with a Scanning Mobility Particle Sizer (SMPS), Nanoparticle Surface Area Monitor (NSAM), and Condensation Particle Counter (CPC), specified in Figure 1.2.1.

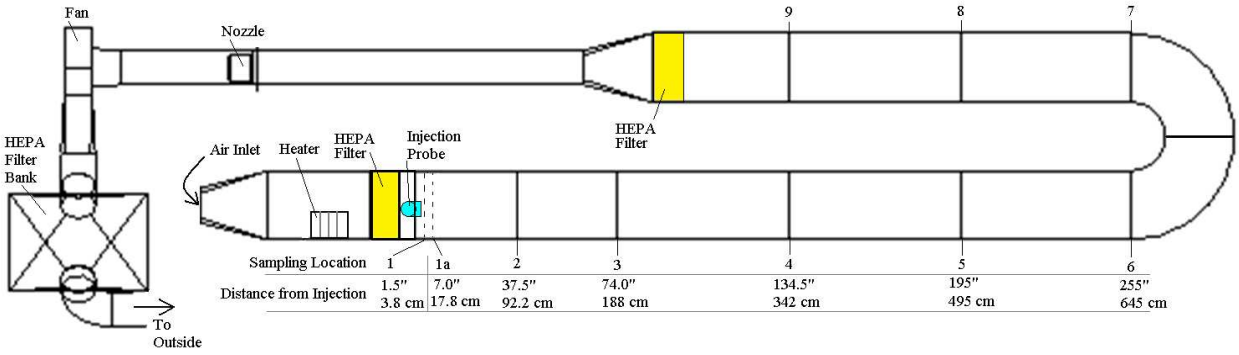

Figure 1.2.1: ASHRAE 52.2-2007 Classified wind tunnel showing possible measurement locations.

Section 1.3: Instrumentation

A SMPS was used to determine the number size distribution of the sampled aerosol. This distribution can then be converted into surface area size distribution, and then into the total lung deposited surface area using ICRP (publication 66, 1994) lung deposition curve models (Figure 3.1.1). The total lung deposited surface area can also be determined in real time using the NSAM. The NSAM is a diffusion charger which can determine the total lung deposited surface area in various regions of the human lung. The

feasibility study outlined in Section 3.1 (along with other published literature) shows agreement between the total lung deposited surface area determined with the SMPS and NSAM. A CPC was used to measure the total number concentration in real time, and much less time consuming than using the SMPS. Particle morphology was determined during the initial burner classification with passive sampling and TEM analysis. Passive sampling onto a TEM grid was accomplished using the Nanometer Aerosol Sampler (NAS, Model 3089, TSI, Shoreview, MN). The feasibility study, dispersion tests, velocity profiles and burner particle characterization are discussed in Section 3.

The possible test aerosols to be produced for this study include carbon black (soot), TiO_2, and SiO_2, which will be produced at very high concentrations by the diffusion burner. Various air-to-fuel ratios can be used to adjust the concentration of soot particles emitted from the burner. The diffusion burner is pictured in Figure 1.3.1. This burner was constructed according to designs by Dr. Seong Chan Kim.

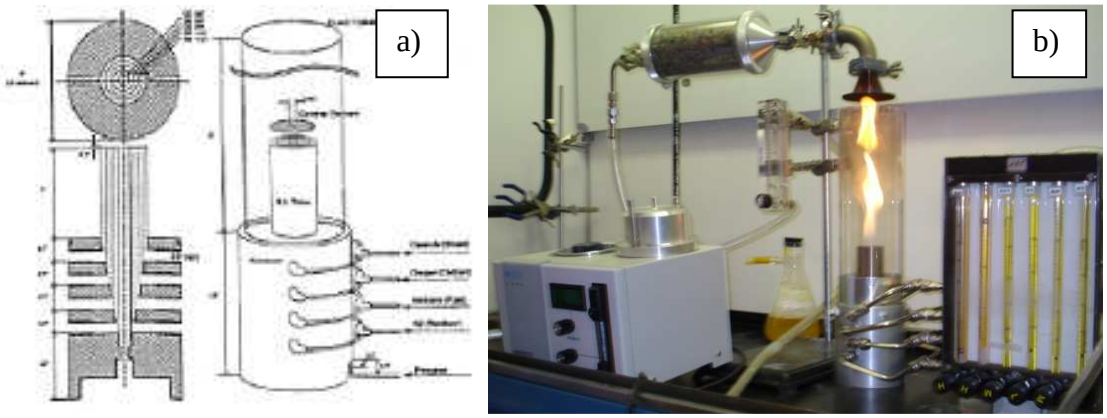

Figure 1.3.1: Diffusion burner a) design and b) pictured sampling onto TEM grid.

A dilution set (which dilutes the sampled air) was developed, tested and verified. This dilutor is required to stop particle dynamics from continuing after sampling the

aerosol from within the wind tunnel. This dilution set is further described in Section 3.5. A similar method was used by Maricq (2007a) in a soot production and sampling study. In the Maricq (2007a) study, a dilution set was used to remove soot from a flame reactor before pumping it into a room temperature chamber to allow for coagulation without competing temperature and aerosol processes (Maricq, 2007a). The dilution set was used to stop this coagulation and measure characteristics of the aerosol as it approached the self-preserving size distribution (Maricq, 2007a).

There will be competing processes in the current study including: evaporation, coagulation, and thermal, electrostatic and diffusion kinetics. The clean, dry dilution air should cause any condensed liquid to evaporate out of the sampled aerosol stream. The thermal, electrostatic, and diffusion losses can be accounted for. Therefore as long as the dilution stops coagulation, the sampled aerosol should represent the aerosol in the wind tunnel.

It was necessary to construct new equipment for this study, including: a sampling section, dilutor, exhaust port, burner housing, injection probe, and injection section. The wind tunnel in Figure 1.2.1 will serve to house the aerosol as it traverses downstream from the injection probe. The wind tunnel required several adjustments in order to obtain uniform flow throughout the wind tunnel cross section. Uniform flow is necessary for modeling, because it would be almost impossible to accurately model non-uniform flow. These adjustments are discussed further in Section 3. The exhaust port and upstream HEPA filter section will not be discussed in detail as they are fairly simple and self explanatory. The dilutor is reviewed in Section 3.5.

The sampling section is shown in Figure 1.3.2. This sampling section can be placed anywhere there is a break in the wind tunnel, since the wind tunnel is made up of many sections. It is light-weight, so moving it is not too difficult or time consuming. The sampling section allows for precise placement of the sampling probe within the wind tunnel cross section, which is important in determining the extent of particle diffusion. There is a tight seal around all wind tunnel openings, which protects lab workers as well as ensures only burner produced particles are present within the wind tunnel. The orifice sampling nozzle on the end of the sampling probe allows for a real-time flow rate measurement to ensure the proper dilution ratio during sampling. The pressure drop across the orifice nozzle can be measured in real-time with a liquid manometer. Using a calibration curve (Figure 3.5.1.4), this pressure drop is converted into flow rate. The development of this orifice nozzle is examined in Section 3.5.

Figure 1.3.2: Pictures of sampling section.

A high pressure drop across the injection probe was not desired and the primary focus of the design of the probe. The injection probe was also designed to allow for laminar flow at flow rates up to approximately 45 l/min. Flow rates of 12 and 10.5 l/min were used during the burner particle injection study to ensure laminar flow within the injection probe. Different orifice diameters can be used to simulate different leak sizes. The orifice insert and injection probe are shown in Figure 1.3.3 along with the injection section. The injection section consists of the injection probe and a honeycomb mesh to limit flow non-uniformities within the wind tunnel. The flow profiles are reviewed in Section 3.3, and the original designs for the injection section are located in Appendix A.

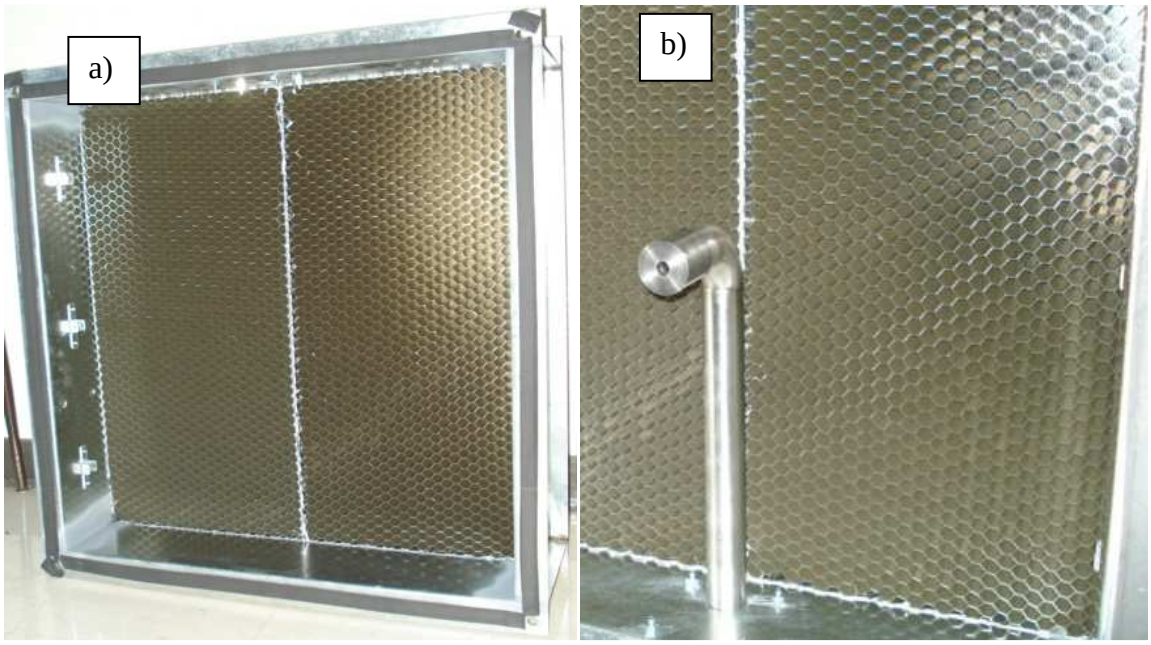

Figure 1.3.3: Picture of a) injection section and b) injection probe with orifice insert installed in injection section.

The burner particles cannot be allowed to enter the lab space. Even a small leak could accumulate to a hazardous level for laboratory personnel due to the high concentration of particles and potential for chronic exposure. The wind tunnel was designed to be leak free, but the injection system and particle generator (burner) must also enclose the produced particles. Therefore a housing was designed and built to contain the burner particles between production and injection. This housing was adapted to fit the burner and injection probe snuggly, with an O-ring at each opening to ensure a tight seal. The temperature profile measured on the outside of the housing reached a maximum temperature of 161°C after 30 minutes of operation. The housing, along with the burner, is pictured in Figure 1.3.4.

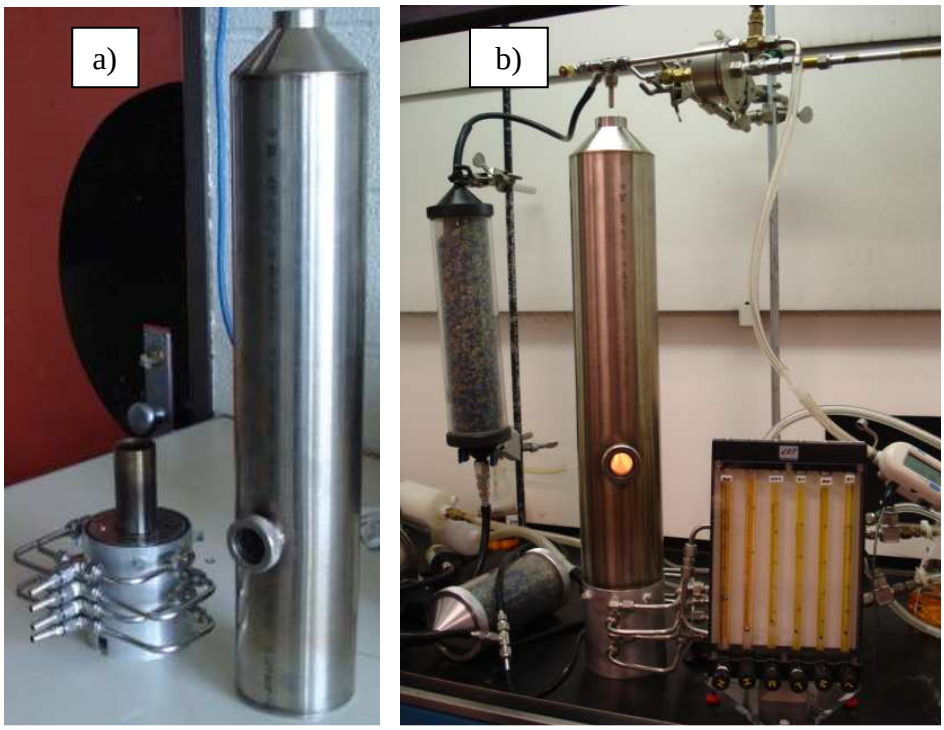

Figure 1.3.4: Burner housing: a) not in use and b) in use during burner particle characterization tests.

The housing was originally designed to be made out of a crystalline material or Pyrex glass due to the high temperatures of the burner and desire to see the flame. These materials are very fragile and expensive, so steel was used instead. There may also be an overpressure experienced by the burner housing and glass or crystal could shatter under such pressure, which would be an extremely dangerous event. The flame can be viewed through the small port hole on the front of the housing, which is a crystalline material, sealed with an O-ring.

Section 2: Literature Review

Section 2.1: Burner Particle Production

There is a significant amount of literature available on production of several different types of particles using a burner under various configurations. The most abundantly produced nanoparticles in industry are soot, titania (TiO_2), and silica (SiO_2). These can be produced in several ways, but are commonly produced in diffusion flame burners. In diffusion flame burners these particles can be produced safely in mass quantities with a high degree of control. The particle size, degree of agglomeration, and particle size distribution are just three particle characteristics that can be controlled by adjusting various burner parameters. The specific gases used in the production of these particles also play a role in the final properties of the burner produced particles. Particles can be produced in the presence of an electric field to yield more control over various particle properties as well.

Section 2.1.1: Carbon Black (Soot) Background

In 1983, 4748 Megatons of carbon black were reportedly produced (mainly by furnace black process) (Balthasar et al., 2002). Today, carbon black is acknowledged as

the largest burner produced commodity (Oberdorster et al., 2005). Carbon black, or soot, is used for improving material structure as well as a black pigment (Balthasar, et al., 2002). However, soot formation is also a major pollutant. Soot, as well as other fine particles, is generally acknowledged as a significant health hazard to the public, not just workers in the carbon black industry (Kim et al., 2008). The formation of soot in flames has been the focus of several studies (Balthasar and Frenklach, 2005; Balthasar et al., 2002; Kim et al., 2008; Kim et al., 2006; Maricq, 2006; Pandey et al., 2007), but there is a lack of understanding of flame produced soot phenomena. This is makes it difficult to develop a robust computational combustion method to predict emitted soot properties and estimate the radiation properties of soot generating flames (Kim et al., 2008).

Soot synthesis modeling was attempted by Balthasar and Frenklach (2005) who examined the effect of initial conditions on soot aggregate growth and coalescence. This revealed a relationship between particle nucleation, surface growth, and coagulation. However accurate measurements of soot particle temperature are needed before detailed soot modeling can be carried out to determine: gas phase mechanisms, particle inception, coagulation, soot formation, and oxidation (Kim et al., 2008).

Soot formation has been studied experimentally as soot particles are formed through incomplete combustion of methane and air in a laminar flow, diffusion burner (similar to the process described in Section 3.4). Several processes occur simultaneously in the burner as the combustion process occurs (D'Anna and Kent, 2008; Frenklach, 2002; Kaplan and Kailsanath, 2001). Soot nuclei begin the process by condensing from small aromatics, free reactive molecules, and radicals. Sub-primary soot particles form as these nuclei collide and coalesce. These particles grow into primary soot particles as

small aromatics, free reactive molecules and radicals chemically condense on soot nuclei. Soot particles may shrink as desorption occurs and large Polycyclic Aromatic Hydrocarbons (PAHs) leave the soot particle surface. Internal restructuring, sintering, and graphitization of soot particles may occur, while the primary particle size is solidified. These primary particles collide to form chain-like agglomerates. This entire process, from nuclei condensation to the formation of agglomerates and oxidation can occur in the same area of the burner/flame (Dobbins et al., 1998). For carbon particles formed in flames, particle formation is relatively independent of fuel type, the phase of the fuel, and the conditions in which it is burnt (Palmer and Cullis, 1965). The final carbon structures are sensitive to temperature (Fugaciu et al., 1999; Hermann et al., 2001).

Graphitization can occur during the particle formation process, which causes the particles to become more dense (Siegmann et al., 2002). Graphite is the most thermodynamically stable carbon modification (Donnet et al., 1993). This graphitization process only occurs during heating. Therefore a higher flame temperature will result in a more thermodynamically stable particle. Soot particle density also increases as the particles cool off (Ossler et al., 2009).

A higher flame temperature can be achieved by increasing fuel oxidation. As soot particles oxidize, the particle size decreases and the soot particle concentration reduces to zero for complete combustion (Siegmann et al., 2002). When the particles do not completely oxidize they can exist in very high concentrations, collide, and form long, chain-type aggregates/agglomerates. These soot agglomerates are composed of randomly

arranged spherical primary particles, which overlap (Balthasar and Frenklach, 2005). The differences between aggregates and agglomerates are defined in Section 4.1.1.

In a diffusion flame burner, higher temperatures lead to faster coagulation, but particle sizes are influenced by the intensity of gas mixing within the flame (Balthasar et al., 2002). Height above the burner also plays a role in soot (and other burner produced particle) formation. A bimodal distribution was measured by Maricq (2006), but as the height above the burner increased, surface growth and coagulation occurred, causing an increase in the mean diameter of the soot particles. Basically, the mean number of primary particles per aggregate increases as the particles move further from the burner (Kim et al., 2008).

Other studies have indicated soot formation occurs in various stages. Kim et al. (2006) reported 4 distinct growth stages of soot in laminar diffusion flames. Primary particles first coagulate under three-dimensional diffusion limited cluster aggregation (DLCA) forming stage 1 aggregates (Balthasar and Frenklach, 2005; Kim et al., 2006; Pandey et al., 2007). After this, environmental restructuring occurs with further coagulation to form stage 2 super-aggregates, then a stage 3 super-super-aggregate (~10 μm) is formed through 2d DLCA, and then a 2d gel network is formed through more restructuring (~100 μm) (Kim et al., 2006). There is not sufficient evidence to suggest that these aggregates can break apart due to mechanical disruption (Maynard, 2002). Partial sintering of particles within primary agglomerates may also occur (Maynard, 2002).

Different hydrocarbon fuels produce different flames and are used in different industrial applications. Higher sooting fuels than methane, such as ethylene and butane,

contain higher concentrations of benzene and acetylene following pyrolysis (D'Anna and Kent, 2008). Although the amount of soot produced may change, the overall structure of soot aggregates is very similar across different fuels, even with different measurement methods (Gwaze et al., 2006). Koylu et al. (1995) discovered fuel type and flaming conditions only partially influence soot primary particles and agglomerate parameters after testing four different fuel types (acetylene, propylene, ethylene, and propane) with TEM analysis. Soot particle nucleation rate is thought to increase as hydrogen atom concentration increases within the flame (Kim et al., 2008). Hydrogen gas addition to the flame can affect soot formation by changing the flame temperature, changing the amount of carbon per unit mass of fuel gas mixture (dilution effect), or by direct chemical action (Pandey et al., 2007).

Sources of soot exist in everyday situations, and these have been studied by several authors (Afshari et al., 2005; Fan and Zhang, 2001; Gehin et al., 2008; Lee et al., 2001; Wasson et al., 2002). Laser printers, burning incense, burning candles, and smoking cigarettes are soot producing activities (Afshari et al., 2005; Gehin et al., 2008; Wasson et al., 2002). Burning candles emits soot in high concentrations (Wasson et al., 2002). Afshari et al. (2005) found candles and cigarettes emitted the highest concentrations of ultrafine particles of 2.41×10^5 and 2.13×10^5 cm^{-3}, respectively, among common sources of household soot production. If the candle wick contains lead, then lead can be emitted when the candle is burned (Wasson et al., 2002). Burning plain candles, perfumed candles, and incense produced mode diameters of 170 nm, 6 nm, and 100-180 nm, respectively (Gehin et al., 2008). Laser printers can emit nanoparticles with

a mode diameter of 21 nm when the particles do not adhere to the drum within the printer (Lee et al., 2001).

Section 2.1.2: TiO_2 Background

2 – 4 million tons of titania are reportedly produced annually (Pratsinis et al., 1996; Ullmann, 2005). This makes titanium dioxide particles the second largest aerosol-made commodity in the world (Tsantilis and Pratsinis, 2004). TiO_2 or titania, is used in cosmetics, sunscreens, electronics, filters (for air and water purification), and solar cells (Akurati et al., 2006; Oberdorster et al., 2005). It is used extensively as a white pigment as well as in photo catalysis, nitrogen fixation, catalyst supports, synthesis of inorganic membranes, and photocatalytic splitting of water (Akurati et al., 2006). Titania white pigment has been applied to paints, papers, plastics, inks, and even food or toothpaste (Heine and Pratsinis, 2007). More recently, titania has been used as a coating on self-cleaning windows (Parkin and Palgrave, 2005). Titania, as well as other oxide nanoparticles can be produced safely with a diffusion flame burner on a commercial scale (Akurati et al., 2006). This also allows flexible production of different particle sizes and phase compositions for various applications (Akurati et al., 2006). Composite nanoparticles have been produced through diffusion flame synthesis as well, such as SnO_2/TiO_2 (Akurati et al., 2005).

The most common way to produce TiO_2 in a diffusion flame is through the combustion/oxidation of a Titanium based precursor known as Vapor-fed Aerosol Flame Synthesis (VAFS). Some of the reactors used in titanium oxide (and other metal oxide) nanoparticle production resemble rockets of space shuttles (Strobel et al., 2006). The two

most common precursors are Titanium Tetrachloride ($TiCl_4$) and Titanium Isopropoxide (TTIP) (Nakaso et al., 2003). About half of the industrially produced TiO_2 is produced through the chloride process by oxidizing $TiCl_4$ (Grass et al., 2006).

The formation of titania nanoparticles is affected by several parameters of the diffusion flame. Flame temperature, height above the flame, residence time in the flame, and burner configuration affect the final particle produced (Arabi-Katbi et al., 2002; Grass et al., 2006; McCormick et al., 2004; Nakaso et al., 2003; Tsantilis et al., 2002; Tsantilis and Pratsinis, 2004). McCormick et al. (2004) found the process temperature to have the greatest effect on particle size, morphology, and phase/composition. With increasing height in the flame, the flame temperature decreases and the average primary particle size increases (Arabi-Katbi et al., 2002). Particle growth predominantly occurs through coagulation and sintering (Nakaso et al., 2003); however fully coalesced single particles occur when tiny primary particles coagulate and sinter while passing through the highest temperature region of the flame (Arabi-Katbi et al., 2001). Usually the initial particle evolution steps are interrupted by coagulation (Tsantilis et al., 2002). Particle collision, resulting in agglomerates occurs later in the flame. These particles traverse a temperature profile which affects the structure of the final particle (Grass et al., 2006).

Rutile and anatase are the two most common crystalline compositions/structures of titania nanoparticles (Yeh et al., 2004). Changing the oxidizer composition from O_2/N_2 = 20/80 to 50/50 leads to a higher oxygen concentration during particle formation, which will significantly increase the anatase content (Yeh et al., 2004). Annealing (post burner heating) can increase primary particle size and rutile mass fraction (McCormick et al., 2004). The shape of the rutile will also change to a thermodynamically favored shape

under annealing (McCormick et al., 2004). Under different reactor configurations, the average primary particle size can change dramatically, even when maintaining reactant composition (Pratsinis et al., 1996). A clean reactor yields similar particles as a reactor with particle laden walls for higher reaction temperatures (Nakaso et al., 2003).

The precursor also seems to affect particle growth rates. TTIP exhibited faster oxidation kinetics than $TiCl_4$, which enhances surface growth allowing larger particles to be formed with narrower size distributions (Tsantilis and Pratsinis, 2004). TTIP oxidation has better potential to produce titania particles with a low degree of polydispersity, however increasing process temperature, pressure, or initial precursor molar fraction has the same effect (Tsantilis and Pratsinis, 2004).

Electric fields have been used to precisely control the specific surface area of burner produced metal oxide nanoparticles (Kammler and Pratsinis, 2000). Close to the burner, the primary particle diameter is not affected by an electric field (Kammler et al., 2003). However the flame is cooled faster in the presence of an electric field, which slows particle growth (Kammler et al., 2003). Therefore the primary particle size of titania is reduced in the presence of an electric field (Yeh et al., 2004).

Section 2.1.3: SiO_2 Background

Silica and titania are produced with similar techniques, though silica is produced at a smaller worldwide volume. Silica has many uses including: thickening, thixotropy, and reinforcement control, suspension stabilization, and as an agent in chemical mechanical polishing during integrated circuit fabrication (Kammler et al., 2001). Silica can be combined with carbon black to create a more effective rubber reinforcement in the

manufacture of “green tires” (Kammler et al., 2001). Silica is also used in the fabrication of optical fibers, as an electrical insulator, and in cosmetics (Zhu and Pratsinis, 1997). Just like titania, it can be safely manufactured in a flame reactor (Briesen et al., 1998). There are many different precursors which can be used to produce silica in a flame reactor, the most common being $SiCl_4$ (Briesen et al., 1998). More precursors have been used successfully by other researchers (Mueller et al., 2004; Strobel et al., 2006). Different flame temperatures, particle residence times, and electric field strengths can be used to affect the growth of silica particles (Vemury and Pratsinis, 1996; Zhu and Pratsinis, 1997).

The sintering rate of silica is enhanced at higher flame temperatures, which results in larger particles (Kammler et al., 2001; Zhu and Pratsinis, 1997). The size and morphology are strongly affected by the residence time of the particles at high temperatures (Mueller et al., 2004). When the residence time at high temperatures is larger than the characteristic time for sintering, the gas-to-particle conversion can be completed resulting in non-agglomerated particle formation (Mueller et al., 2004). A silica primary particle size of 15 nm occurs in about 1 ms (Briesen et al., 1998). although this formation occurs quickly, the primary particle size of the oxide metal can also be controlled by changing the amount of oxygen in the oxidant, or by changing the reactant mixing configuration (Zhu and Pratsinis, 1997). More oxygen means higher flame temperature (so more sintering), but also a shorter residence time and smaller flame height (less time for particle growth resulting in smaller particles) (Briesen et al., 1998).

An electric field can be used to affect particle size and morphology of flame produced silica (Vemury and Pratsinis, 1996). When no electric field is present, the

agglomerate length and primary particle size are larger than they would be with an electric field across the flame (Vemury and Pratsinis, 1996). The polarity of the electric field does not seem to matter. The specific surface area of silica particles increases with increasing potential across the flame regardless of the polarity of the electric field (Vemury and Pratsinis, 1996).

The chloride process is used in most large scale production of fumed or fused (flame produced) silica (Briesen et al., 1998). This process uses $SiCl_4$ as the precursor, which means harmful and corrosive byproducts are produced including HCl and Cl_2. These chemicals contribute to equipment wear-out and expensive cleaning requirements (Briesen et al., 1998). Another precursor has been used successfully. HMDSO or Hexamethyl-disiloxane ($C_6H_{18}OSi_2$) has been used in flame synthesis of silica (Briesen et al., 1998; Mueller et al., 2004; Strobel et al., 2006). Briesen et al. (1998) used HMDSO and OMCTS or octamethylcyclotetrasiloxane as organic precursor materials. These organic precursors contain additional fuel, which causes an increase in flame temperature (Briesen et al., 1998). This higher flame temperature can then affect the final particle size, morphology, and distribution.

Section 2.1.4: Commercial Production of Other Nanoparticles

Other nanoparticles produced on a commercial scale include silver, Al_2O_3, and SnO_2 (Akurati et al., 2006; Mitrakos et al., 2008; Nagamine et al., 2007; Zhu and Pratsinis, 1997). Silver can be produced in a tube furnace reactor, where silver powder is evaporated in the furnace and the vapor is carried to a cooling region (Mitrakos et al., 2008). As the vapor cools, particles grow by homogeneous nucleation. Al_2O_3 and SnO_2

are oxide metals like titania and silica and can be produced in a diffusion flame reactor (Zhu and Pratsinis, 1997). The oxide metal particles grow by chemical reaction and Brownian coagulation, before shear-induced coagulation dominates particle growth (Xiong and Pratsinis, 1991). TiO_2 nanoparticles can be produced without the use of a flame reactor.

Titania can be produced through a catalyst free, low temperature synthesis (Chuang and Chen, 2008), spray pyrolysis (Wang et al., 2005), and by spraying water droplets into a solution of TTIP (Nagamine et al., 2007). Chuang and Chen (2008) developed a method of producing anatase TiO_2 nanoparticles through a chemical process by mixing tetra-n-butyl (TnBT) with ethylene glycol and water. The process created nanoparticles with a mean diameter of 4.97 nm (Chuang and Chen, 2008). Nagamine et al. (2007) produced hollow TiO_2 particles by spraying water droplets into a TTIP solution. The ratio of the diffusion rate to reaction rate of TTIP, as well as TTIP concentration, governed the particle formation process (Nagamine et al., 2007). Wang et al. (2005) used three different organic precursors (TTIP was one of them) to produce nanoparticles with a nominal size of 10 nm through spray pyrolysis. The nanoparticles may form through droplet breakup, fast crystal growth, and fragmentation of dried particles (Wang et al., 2005).

Section 2.2: Nanoparticle and Ultrafine Particle (UFP) Toxicity

There is a potential for worker exposure to ultrafine particles at relatively high concentrations in industrial workplaces where nanoparticles are manufactured (Kim and Jaques, 2004). Several studies have been conducted involving the toxicity of ultrafine

particles at ambient concentrations, but adverse health effects may not be caused by exposure to ultrafine particles at these low ambient concentrations (Kim and Jaques, 2005). Health effects do not entirely depend on particulate exposure, they depend on the dose. Dose is derived from a measured particle concentration (the exposure), the breathing flow rate, and the breathing frequency of the individual (Asbach et al., 2008). Factors such as sex, age, and activity level may affect the dose of ultrafine particles. Occupational exposure, TiO_2 toxicity, soot toxicity, and various other particulate toxicity studies are reviewed here to explain the dangers of ultrafine particle exposure.

Section 2.2.1: Positive and Negative Health Effects of Nanoparticles

Nanotechnology will benefit human health through advances in medicine, science, and industry through imaging and diagnosis, drug delivery, anticancer therapy, and gene therapy (Balbus et al., 2007; Gwinn and Vallyathan, 2006; Yin Win and Feng, 2005), with a necessity for large scale production (Donaldson et al., 2004). Yin Win et al. (2005) showed biodegradable spherical nanoparticles (200 – 300 nm) can be used to help deliver anti-cancer drugs into the bloodstream via the oral route due to their adhesion to and interaction with biological cells. The downside of nanoparticles includes cardiovascular disease, pulmonary effects, and translocation to other organs (Gwinn and Vallyathan, 2006). Even rather benign particles at high concentrations can cause serious adverse health effects, especially when inhaled chronically (Oberdorster, 1995). Respirable crystalline silica, crocidolite asbestos fibers, and some hardwood dusts have been identified and classified as human carcinogens, although soot and TiO_2 have been identified as potential carcinogens as well (Knappen et al., 2004). TiO_2 also causes

genotoxic effects, which include DNA strand breakage and damage to DNA bases (Knappen et al., 2004).

Engineered nanoparticles can disrupt the intracellular communications of the immune system with severe consequences (Balbus et al., 2007). Also, with lung macrophages busy clearing particles, it opens up the potential for lung biocontamination (Becker et al., 2003). Even at low concentrations, nanoparticles are biologically more reactive than larger sized particles (Donaldson et al., 2004; Frampton, 2001; Warheit et al., 2006). Carbon black nanoparticles are more potent when generating harmful oxidants than fine particles (Wilson et al., 2002). Grassian et al. (2007) found smaller TiO_2 nanoparticles (6 nm) are more toxic than larger TiO_2 nanoparticles (16 nm) inhaled by mice. Nanosized particles can deposit inside the lung due to turbulent and Brownian diffusion (Bemer et al., 2002). Systemic health effects may be caused when inhaled nanoparticles evade phagocytosis, cross cell membranes, and redistribute to other parts of the body besides the lungs (Gwinn and Vallyathan, 2006). Nanoparticles have a large and active surface, which are responsible for several acute and chronic biological endpoints, including neoplastic lesions (Oberdorster, 2001).

These deposited nanoparticles may not stay in the lung. There is evidence that after nanoparticles are deposited in the lungs they are not efficiently removed by alveolar macrophages (Avakian et al., 2002). Translocation may also occur to the liver and other organs (Avakian et al., 2002). The olfactory nerve can serve as a route of nanoparticle translocation from the upper respiratory tract to the central nervous system (Oberdorster et al., 2004). In general, these translocation routes remain largely unknown; although probably very low, they are likely to change in a person with a compromised immune

system or diseased state (Oberdorster et al., 2005). Wiebert et al. (2006) found no translocation difference of 35 nm carbonaceous nanoparticles between healthy and asthmatic subjects, but noted there may be differences between healthy and asthmatic lungs significant for health effects.

Inhalation is not the only route of nanoparticle deposition and translocation. When dermal contact occurs (contact with the skin) there is evidence of translocation by the lymphatic system to regional lymph nodes after the nanoparticles penetrate the skin (Oberdorster et al., 2005). Upon ingestion, the lymphatic system can uptake the nanoparticle into the organism, although most would be excreted as feces (Oberdorster et al., 2005). If the nanoparticles are in the blood, they are free to distribute throughout many parts of the body, being taken up by the liver, spleen, heart, bone marrow, and other organs (Oberdorster et al., 2005). Further work in understanding the composition, sources, and health impacts of course, fine, and nano-sized (ultrafine) particles is necessary to fully understand the potential impact of these particles (Avakian et al., 2002).

Section 2.2.2: Nanoparticles as Occupational and Combustion Aerosols

Holman et al. (2007) estimated $147 billion worth of products including nanotechnology sold in 2007. In 2003, most sectors of nanotechnology were developing without regulation, using the Material Safety Data Sheet (MSDS) of bulk material for the nanoparticles (Colvin, 2003). Most information on nanoparticles in consumer products is protected from public exposure by trade secrets (Colvin, 2003). There must be more

disclosure on particle size and quantity in consumer products in order for nanotechnology to be developed safely and with public confidence (Schulte et al., 2009).

The resulting toxicity of particles is affected by the mixture of gas phase and semivolitile species in which the aerosol is suspended (Holder et al., 2008). Flame generated particles, as well as diesel generated particulate matter are typically suspended in such a mixture (Holder et al., 2008). Most individuals are exposed to some combustion generated aerosols in home and/or occupational settings (Avakian et al., 2002). Hauser et al. (2001) linked the particulate matter exposure of boilermakers to loss of lung function. This suggests that adverse health effects on lung function is associated with working at gas, oil, and coal fired plants. Inhaled carbon (soot) nanoparticles are translocated to the central nervous system to a significant extent (Oberdorster et al., 2004). Occupational exposure to nanoparticles can be assessed using data from rodent studies (Kuempel et al., 2006). Rodents, mice, and humans are all mammals, and all mammalian lungs are similar in structure, so rodent toxicity studies can be used to assess toxicity for humans (Gradon et al., 1996). Epidemiological studies show inadequate evidence for the carcinogenicity of soot, TiO_2, and talc (Baan et al., 2006). These substances are listed as possibly carcinogenic because of animal studies. At certain exposures, these substances have caused cancer in rats, mice, and/or hamsters (Baan et al., 2006).

Several animal studies have provided valuable information regarding health outcomes from exposure to certain toxins for risk assessment purposes (Knaapen et al., 2004). Rats, mice, and other mammalian species have been used to determine the toxicity of certain cosmetic products, as well nanoparticles including TiO_2 (Gradon et al., 1996; Fabian et al., 2008) and soot (Gradon et al., 1996). Fabian et al. (2008) intravenously

administered TiO_2 nanoparticles of 20 – 30 nm in rats to achieve a 100% bioavailability, or a worst case scenario. The dose was 5 mg/kg-body weight as this is believed to be a threshold dose for adverse health effects. The TiO_2 did not cause toxic effects in the experimental animals within the 28 day observation time. However the TiO_2 did accumulate in the liver and spleen, without being cleared during the observation time (Fabian et al., 2008). Another recent inhalation study of TiO_2 nanoparticles showed strong agglomeration and settling of the nanomaterial, with very little remaining suspended in the atmosphere (Ma-Hock et al., 2007). Several long-term diesel exhaust exposure studies have shown accumulation of carbonaceous particles (soot) in the lungs of the exposed rats (Gradon et al., 1996). So these studies indicate accumulation of nanoparticles, but no toxic effects due to this accumulation. Toxic effects have been reported at higher dose levels, as mentioned earlier (Avakian et al., 2002; Gwinn and Vallyathan, 2006; Knappen et al., 2004; Oberdorster et al., 2005; Oberdorster et al., 2004; Oberdorster, 2001).

Fibers are a notorious occupational hazard (asbestos), and the potential risk still exists for fiber-related diseases for workers in the man-made vitreous fiber (MMVF) material industry (Su and Cheng, 2006). Workers are likely to be affected by dispersed or aggregated nanoparticles during the synthesis or recovery phase of the nanoparticle production process through inhalation (Aitken et al., 2004). Risk assessment for nanomaterial exposure is made more difficult when adequate exposure data is unavailable (Han et al., 2008). Maynard et al. (2004) and Han et al. (2008) carried out monitoring studies to determine potential occupational exposure risk for workers in the carbon nanotube (CNT) industry. Low lung solubility and the extreme aspect ratio of individual

nanotubes may lead to similar toxic effects observed with other fibrous particles (Maynard et al., 2004).

Maynard et al. (2004) monitored a CNT production facility, and found the greatest risk to be in the handling of unrefined material, although the airborne concentration of CNTs was low (approximately 53 $\mu g/m^3$). These results were associated with a lot of uncertainty due to the mass-based sampling method (Maynard et al., 2004). Baron et al. (2003) observed millimeter sized nanotube material on equipment surfaces within a CNT production facility, and noted the nanometer sized material can remain airborne for some time. The release of larger particles into the workplace is usually caused by the process the worker is attending and the worker's actions (Liden and Harper, 2006). Han et al. (2008) monitored a CNT research facility, and found low concentrations (172 to 193 cm^{-3}). Another study focusing on the nanoparticle exposure of welding workers showed 30,000 cm^{-3}, but this dropped by 3-fold when a rotary-type oil vacuum pump was in operation for ventilation purposes (Brouwer et al., 2004).

Handling and packaging of the manufactured nanoparticles has been recognized by several authors as the most likely activity which can lead to exposure to airborne nanoparticles in a nanoparticle production facility (Berges et al., 2007; Boffetta et al., 2004; Kuhlbusch et al., 2004; Maynard et al., 2004). Kuhlbusch et al. (2004) measured the particle size distribution in a carbon black production facility to be elevated during work periods in the material handling area. The most common primary particle size within the reactor was between 10 and 100 nm, but particle size in the material handling area started at approximately 400 nm with mode diameters at 1 μm and > 8 μm (Kuhlbusch et al., 2004). Berges et al. (2007) reported elevated nanoparticle

concentrations in the material handling area of a TiO_2 production facility. Liao et al. (2009) reported packers and surface treatment workers in a TiO_2 nanoparticle production facility have significant risk of cytotoxicity response at relatively high concentrations of airborne anatase TiO_2 nanoparticles in the size range 10-30 nm. Higher ventilation rates for more dilution could be used to improve worker protection in the event of an aerosol release (Whicker et al., 2002).

Epidemiology studies have been conducted to see if workers in the particle production industry are at a greater risk of illness than the general public both in the United States (Fryzek et al., 2003) and Europe (Boffetta et al., 2004). The examined TiO_2 producing facilities in the US did not show exposure associated with an increase of death from cancer or other diseases (Fryzek et al., 2003). The TiO_2 plants examined in Europe also showed no carcinogenic effect of the TiO_2 dust on the human lung (Boffetta et al., 2004). There are no published studies of engineered nanoparticle exposure risks as there is insufficient evidence to support it (Schulte et al., 2009).

Overall the occupation health risks of man-made nanomaterials are not very well understood, which is mostly due to the lack of exposure data (Han et al., 2008). The exposure assessment is further complicated by not knowing whether the aerosol form is nonaggregated/nonagglomerated or aggregated/agglomerated (Han et al., 2008). The aerosol chemical composition changes due to interaction with background particles (Seipenbusch et al., 2008), and should be investigated further. Ambient aerosol exposure and risk assessment has been carried out by several authors using different methods of exposure assessment (Chen et al., 2007; Ntziachristos et al., 2007; Peters et al., 1997; Qi

et al., 2008a; Qi et al., 2008b; Wichmann and Peters, 2000). The differences between aggregates and agglomerates are defined in Section 4.1.1.

Section 2.2.3: Nanoparticles as Ambient Aerosols

Ambient aerosol concentrations can reach hazardous levels in the ultrafine particle size range. Urban ambient aerosol ultrafine particulate fractions are more likely to cause adverse health effects by lung function decrement than fine particles (Peters et al., 1997; Wichmann and Peters, 2000). Some studies have shown the risk of lung cancer increases with ambient air particulate matter exposure, because inflammatory responses within lung airways are induced by particulate matter, which may mediate adverse health effects (Chen et al., 2007).

There has been some disagreement on which measurement metric is best suited to reflect adverse health effects; mass, surface area, or number particle concentration. Mass measurements are used by the Occupational Safety and Health Administration (OSHA) to examine workplace exposure; however nanoparticles with a large number concentration have a very small mass concentration. Also, there is a growing amount of scientific evidence suggesting surface area is the best metric (Ntziachristos et al., 2007).

Ultrafine and nano-sized particles are deposited in the lung by diffusion due to their high diffusivity and constitute a large part of the particulate number and surface area concentrations, while contributing very little to the mass concentration (Kim and Jaques, 2005). There is some evidence between morbidity and nanoparticle number concentration, but it is not definitive (Penttinen et al., 2001). Number concentration has been suggested as the best indicator of adverse health effects of particulate matter under

certain environmental conditions (Kim and Jaques, 2005). It has also been proposed that the relatively high surface area of nanoparticles and their potential for crossing the airway epithelial membrane may be important in the toxicity assessment of the ambient particle fraction (Frampton, 2001).

Number concentration of nanoparticles and adverse health effects has been correlated in several epidemiological studies (Utell and Frampton, 2000; Wichmann et al., 2000). Other toxocologic and epidemiology research suggests that nanoparticles are more harmful per unit mass than larger particles (Oberdorster, 1996; Peters et al., 1997; Seaton et al., 1995). However there are also surface area studies, showing that upon transition from the fine to ultrafine (nanoparticle) size range, surface area is the most important factor affecting lung inflammatory response (Brown et al., 2000; Oberdorster, 1996; Renwick et al., 2004; Tran et al., 2000). Oberdorster (2002) also showed inflammatory response correlates well with retained particle surface area for fine to ultrafine (nano-sized) particles. Others have reported the nanoparticle surface characteristics and phase of nano-TiO_2 to be the determining factor for cell damage, and not surface area (Borm, 2002; Sayes et al., 2006). Exposure potential may also differ due to large differences in dustiness between phases of TiO_2 (Schneider and Jensen, 2008).

Surface area is beginning to gain significance in the literature as more researchers begin to recognize the potential importance of this metric. Ntziachristos et al. (2007) monitored number and surface area concentrations at urban and road side sites. Qi et al. (2008a) performed on-road testing of cabin air filters against ambient air concentrations. Surface area and number concentrations were monitored during this filtration study, which concluded surface area is the more accurate measurement metric for ultrafine

(nano-sized) particles (Qi et al., 2008a). This change may be due to the development of diffusion chargers for surface area measurement.

Diffusion chargers have been refined to a state where lung deposited surface area can be specifically measured in real-time (Fissan et al., 2007). The Nanoparticle Surface Area Monitor (TSI Model 3550 NSAM) provides an easy way to measure lung deposited surface area for nanoparticles (Shin et al., 2007). The calibration factor used within the NSAM may be affected by particle morphology, change in particle size, and particle material (Shin et al., 2007). Other studies have shown very good agreement of the NSAM with number based measurements coupled with conversion to lung deposited surface area using the ICRP model for lung deposition (Asbach et al., 2008; Stanley et al., 2010). Particle loss in diffusion chargers has been estimated to be below ~15%, attributable to flow and electrostatic loss (Park et al., 2007). The effect of agglomerates on the response of the NSAM requires further investigation (Asbach et al., 2008).

Nanoparticles (primary particle size of ~70 nm) form agglomerates after being taken into cells (Wottrich et al., 2004). Limbach et al. (2005) reported that in biological fluids, untreated oxide suspensions can agglomerate rapidly. In fact, aggregates and agglomerates are the main form of carbon black particle exposure (Baan et al., 2006). TiO_2 particles form aggregates as well (Grassian et al., 2007). Loose TiO_2 aggregates can be created through hydrothermal reactions (Sayes et al., 2006). Handy and Shaw (2007) even suggest the convention of strictly defining nanoparticles as particles between 1 and 100 nm should be changed to include larger aggregates made up of nanometer sized primary particles. These heterogeneous particles are used in commercially relevant materials, which should be of interest to regulators (Balbus et al., 2007). Liao et al.

(2009) suggests this TiO_2 agglomeration is good because it limits transport through settling and drives crystal growth, which decreases nanoparticle solubility in human cells.

Section 2.2.4: Nanoparticle Exposure and Dose

Ultrafine particulate matter in the lungs of elderly subjects has been compared to data from younger adults (Kim and Jaques, 2005). The younger subjects experienced a higher dose than the elderly subjects under the same exposure conditions (Kim and Jaques, 2005). This can be explained by tidal volume and breathing rate differences between the subject groups. Aerosol exposure, tidal volume, and breathing rate explain the dose administered to anyone exposed to (and breathing) an aerosol (Asbach et al., 2008). Tidal volume is the amount of inhaled air per breath. Breathing rate is the number of breaths taken per unit of time. A lower dose for the elderly subjects, under the same exposure as the younger group, implies a lower breathing rate or smaller tidal volume for elderly subjects. People exercising or working tend to breathe faster and deeper than when at rest, which means a higher breathing rate and tidal volume, respectively, and therefore a higher dose under the same exposure. People with asthma are more sensitive to nanoparticles then people who do not suffer from asthma, which is most likely due to the higher dose of retained particles experienced by asthma sufferers (Chalupa et al., 2004).

Daigle et al. (2003) compared particle deposition during rest and while exercising using experimental measurements and a theoretical model. The model predicted very little increase in deposition fraction with exercise, whereas the experimental data showed an increase (Daigle et al., 2003). Exercise increased intake of particles, total particles

deposited, and amount of particles reaching the alveolar region of the lung, which may increase the likelihood of adverse health effects (Nemmar et al., 2001).

Section 2.2.5: Environmental Impact of Ultrafine Particulate Matter

Ultrafine and nano-sized particles do not only affect people, but they have environmental impacts as well. Some studies have shown the physiology of various aquatic species can be affected by fullerenes, carbon nanotubes (CNT), and metal oxide nanoparticles (Behra and Krug, 2008). TiO_2 has been used as a coating on the top layer of a side walk, which is activated by sunlight to convert ambient nitrogen dioxide gas into less toxic nitrates and act as a "smog busting" agent (Fabian et al., 2008). This layer of TiO_2 particles may become separated from the sidewalk and enter the environment as either an aerosol or within water. Natural waters and drinking water supplies do not currently contain engineered nanoparticles (that can be detected) (Handy and Shaw, 2007). It will remain very difficult to extrapolate lab data to the larger ecosystem until the environmental concentration of engineered nanoparticles is known, as well as where they end up (Behra and Krug, 2008).

Section 3
Initial Experimentation for Wind Tunnel Setup

The ASHRAE 52.2-2007 Classified wind tunnel served as the containment volume for the burner produced aerosols in the current study. However there is no standard method of using the wind tunnel in this fashion. The wind tunnel was originally designed to induce turbulent mixing for testing filter efficiency with a uniformly distributed aerosol. Therefore the wind tunnel required some alterations in order to fit the requirements of the current study. All other equipment was tested under the same scrutiny to ensure accurate and repeatable data are gathered for analysis. The measurement instruments and techniques also required testing for accuracy and consistency.

Section 3.1: NSAM/SMPS Feasibility study

A feasibility study has been conducted to test the feasibility of using the SMPS and NSAM simultaneously. It is desired to use each instrument to measure the number and surface area concentrations of the test aerosols. Several examples are present in the

literature of the NSAM being used successfully in field trials, however not many have shown a successful, precise match between the SMPS and NSAM data. Discrepancies have been reported (Ntziachristos et al., 2007). This comparison can most easily be made when sampling high particle concentrations within the size range limits for both instruments. This is important because field trials have suggested the difference in size range for each instrument may be the cause for the discrepancy between SMPS and NSAM measurements (Ntziachristos et al., 2007).

The objective of this feasibility study was to evaluate the two measurement instruments in order to find the total Lung Deposited Surface Area (LDSA) concentration in various regions of the lung. LDSA represents the dose of the aerosol and has been identified as an important metric for determining the toxicity and health relevance of an aerosol (Asbach et al., 2008; Frampton, 2001; Stoeger et al., 2006). When a filter is used to remove nanoparticles from the air to reduce human exposure, it is important to rate the filter based on surface area, or LDSA, to obtain a more health relevant filter efficiency value. The NSAM was developed to measure LDSA in real-time. In this feasibility study, a NSAM and SMPS were used to sample upstream and downstream of a test filter. The lung deposition curves developed by the American Conference of Governmental Industrial Hygienists (1994) for a reference worker were used to find the lung deposited surface area from the measured surface area distribution (SMPS measurement). These curves show the deposition efficiencies for each particle size within the human respiratory system for a reference worker (see Figure 3.1.1). The LDSA (i.e. in alveolar and tracheobronchial region), determined with each instrument, was then plotted for

comparison. If the SMPS and NSAM produce similar LDSA concentrations in this feasibility study, then it is feasible to use them simultaneously in future studies.

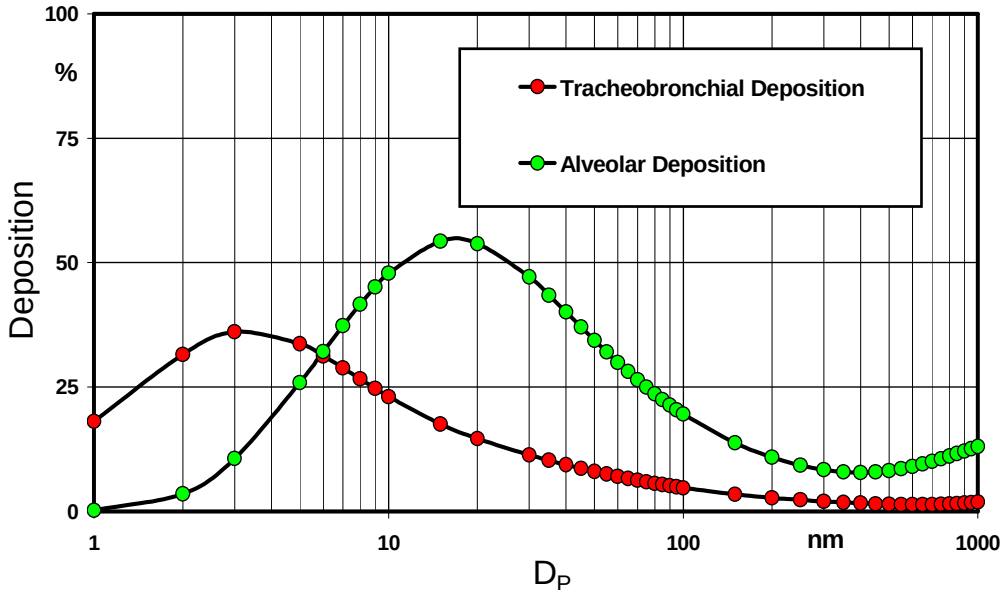

Figure 3.1.1: Particle deposition curves as a function of size according to ACGIH model for a reference worker, breathing through nose; deposition in alveolar and tracheobronchial regions are currently measured with NSAM.

The SMPS (Model 3080, TSI, Shoreview, MN) consisted of a Condensation Particle Counter (CPC) (Model 3025A, TSI, Shoreview, MN) and a long Differential Mobility Analyzer (DMA) (TSI, Shoreview, MN). The NSAM (Model 3550, TSI, Shoreview, MN) sampled at 2.5 lpm, and the SMPS was set to a sample flow rate of 1.5 lpm and a sheath flow rate of 10 lpm, giving a size range of 7.37 – 289 nm. This SMPS size range was selected because it covered the majority of the sample particles; but was partially imposed due to the CPC model and desired sample flow rates. The size range of the NSAM is 10 – 1000 nm as set with a cutoff cyclone. However the response of the NSAM is only accurate between approximately 20 nm and 400 nm (personal

communication with Dr. Fissan), which is why an aerosol mainly distributed within this size range is desired. At sizes above 400 nm the material of the particle is important because the response functions of the instrument deviate from the lung deposition curves. In reality, most particles of interest for inhalation studies are below 400 nm. Furthermore the contribution of particles below 20 nm to the measured surface area is usually so small that it can be neglected.

The NSAM output is directly correlated with the LDSA in various regions of the lung in real-time by utilizing diffusion charging. In diffusion charging, the surfaces of the sampled particles become positively charged according to the amount of surface area. Therefore the NSAM may not be shape dependant as agglomerates may be measured accurately along with spherical particles (more work is needed in this area).

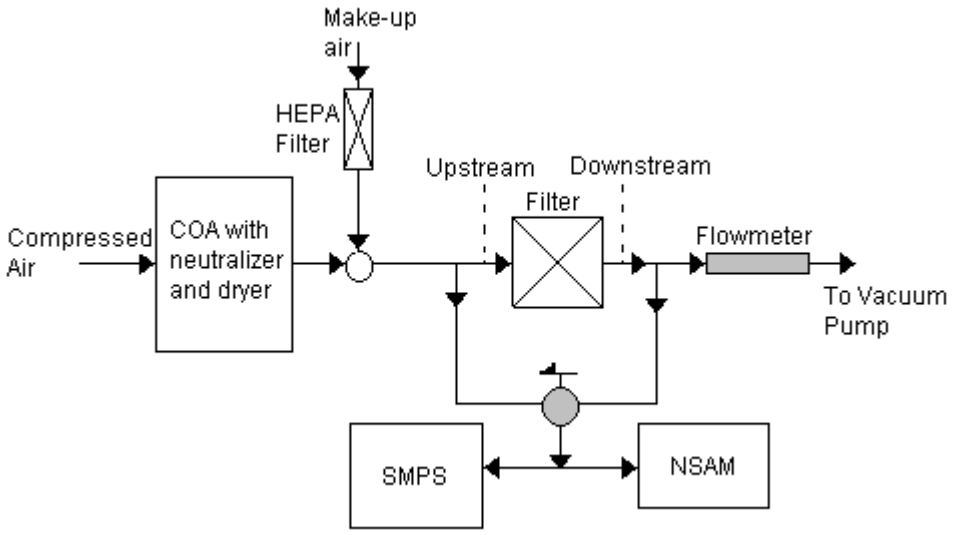

Figure 3.1.2: Filtration efficiency test schematic using NSAM and SMPS.

Dioctyl sebacate (DOS) particles were generated with a Colison atomizer (COA) (Model 3076, TSI, Shoreview, MN) to test filtration efficiency based on number and LDSA (Figure 3.1.2). The lab setup allowed for high particle concentrations and no

background interference of the COA generated aerosol. DOS usually forms spherical particles and is thus very suitable for the comparison of these instruments (since the SMPS assumes spherical particles for the surface area distribution calculation).

The generated particle size distributions shown in Figures 3.1.4 and 3.1.5 contributed to the lung deposited surface area shown in Figure 3.1.3. These figures show a very close correlation between the overall lung deposited surface area measured by the NSAM and calculated from the SMPS data. The SMPS values fall a little short of the corresponding NSAM values, but this is due to the difference in size range available to the SMPS. The NSAM had the ability to measure all particles of size 10 – 1000 nm, whereas the SMPS was only measuring particles of size 7.37 – 289 nm. The SMPS size range was adequate for the majority of the particles in the distribution; however it did miss some of the larger particles, particularly for the measurements with 10 ppm DOS. Due to the d_p^2 dependency, even a low number of these larger particles can contribute noticeably to the total surface area and could be the reason for the small discrepancy between the two instruments.

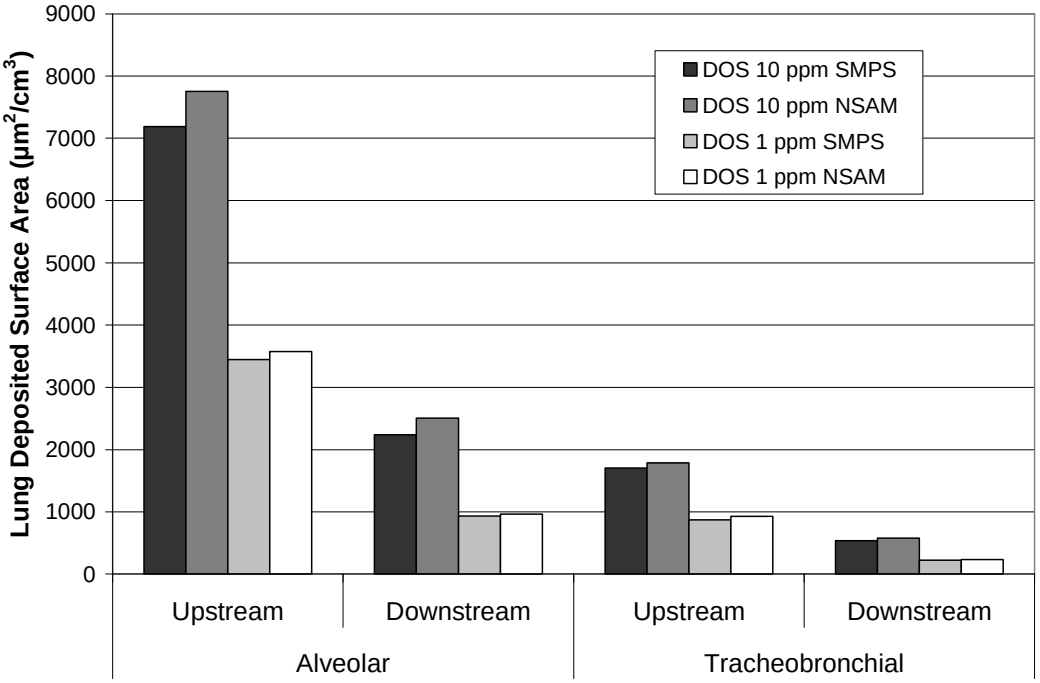

Figure 3.1.3: Total lung deposited surface area measured with SMPS and NSAM.

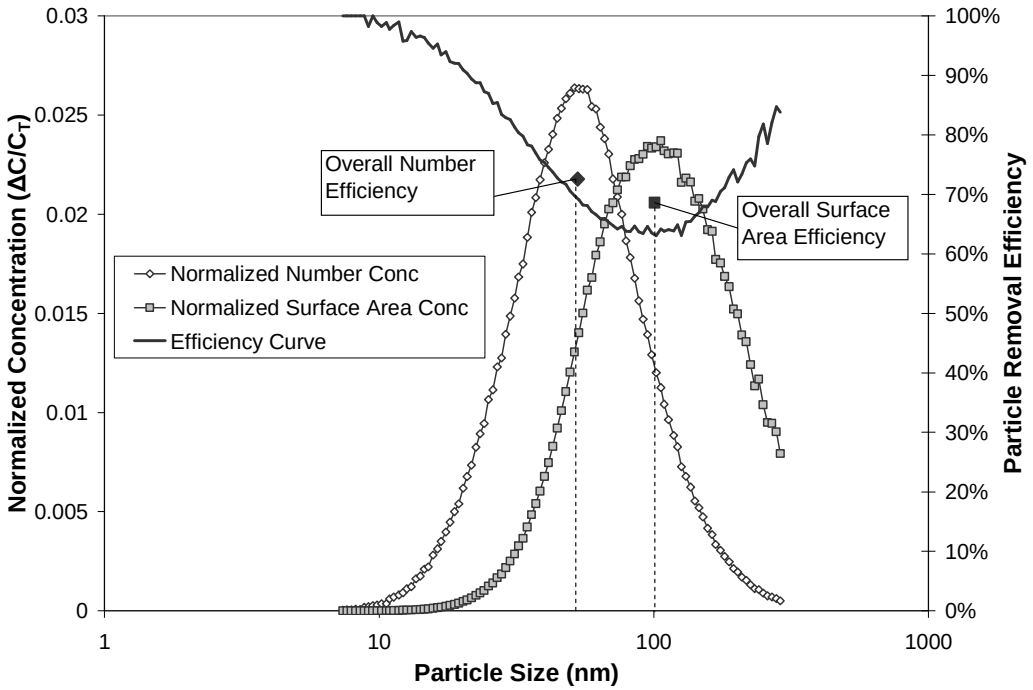

Figure 3.1.4: 10 ppm DOS aerosol solution filter efficiency curve with upstream and downstream concentrations.

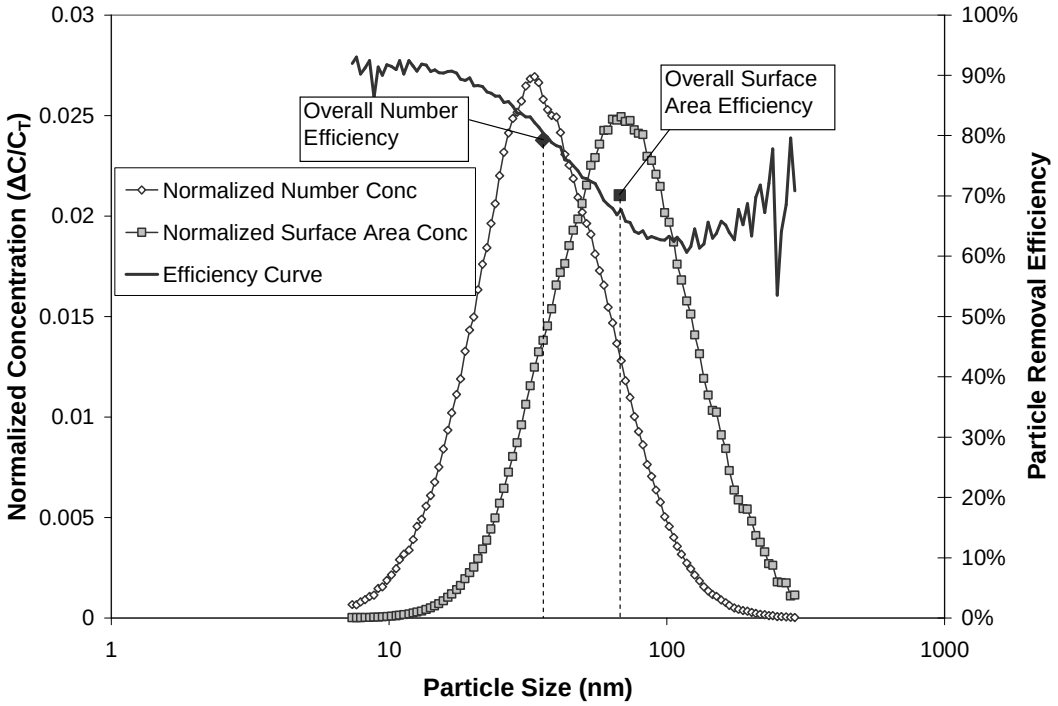

Figure 3.1.5: 1 ppm DOS aerosol solution filter efficiency curve with upstream and downstream concentrations.

For nanoparticles, which mainly distribute less than 300 nm, the LDSA concentration measured with the NSAM is very consistent with the calculated concentration from the lung deposition curves and the particle size distribution measured by the SMPS. The LDSA based filter efficiency obtained from NSAM and SMPS data agree very well with each other (with a difference of only 0.3 – 1.8%) for the test filter. Since filters typically have a most penetrating particle size (MPPS) of 100-300 nm, the geometric mean size of nanoparticles based on surface area is closer to the MPPS than that based on number. Hence, the LDSA based filter efficiency is closer to the minimum efficiency of the filter than the number based efficiency. Similar observations were also obtained in on-site and on-road filter tests with atmospheric aerosols (Qi et al., 2008a). Due to the high surface area to mass ratio of nanoparticles and the concerns raised by

toxicologists regarding surface area toxicity, this LDSA filter efficiency measurement represents not only a more health relevant filter evaluation but also a better characterization of the filter when concerned with an aerosol mainly composed of nanoparticles.

In regards to the objectives of the feasibility study, the differences between the SMPS and NSAM results were within a few percent. This proves that the NSAM calibration is correct for spherical particles. Therefore these instruments can be used to measure the particle concentrations simultaneously.

The NSAM was used simultaneously with a CPC (Model 3025A, TSI, Shoreview, MN) to compare the instruments under a typical filter test. The test was conducted using atmospheric air as the filter challenge aerosol. This study shows an application of the NSAM in an area dominated by the CPC. The results, discussion, and concluding remarks are located in Appendix B.

Section 3.2: Particle Dispersion Studies Using Non-Burner Aerosol

A 6-jet atomizer (TSI Model 9306A, Shoreview, MN) was used to aerosolize a 0.1% solution of KCl in DI water. This aerosol is a good surrogate for the burner produced aerosols to be produced later because they fall in the same size range. However an atomizer cannot produce the high concentrations of a diffusion burner. The total flow rate was ~12 l/min (from Atomizer User's Manual) injected through the 10 mm orifice located at the outlet of the injection probe. The aerosol was injected at the centerline of the wind tunnel a short distance downstream from a HEPA filter, which removed any background particles. The wind tunnel was operated at flow rates of 200 and 500 ft^3/min

(average face velocities of 0.25 and 0.64 m/s, respectively). Measurements were taken at wind tunnel Locations 1 – 6, outlined in Figure 1.2.1. The flow was sampled simultaneously by an NSAM (TSI, AeroTrak 9000) and an SMPS (TSI, Model 3034). These atomizer tests will help determine appropriate sampling locations throughout the wind tunnel, test the performance of the injection probe, investigate if a well-defined jet of aerosol is maintained, and provide a basis for comparison when conducting the burner tests.

Several samples were taken throughout the cross-section of the wind tunnel at each measurement location (for the initial dispersion tests). A sample was taken at the centerline, as well as up, down, left, and right of the centerline measurement at each location downstream from the particle injection point. Three samples were gathered at each point to ensure repeatability. Figures 3.2.1 and 3.2.2 show the average centerline measurement results at Locations 1 – 6 as specified in Figure 1.2.1 (no measurement was taken at Location 5).

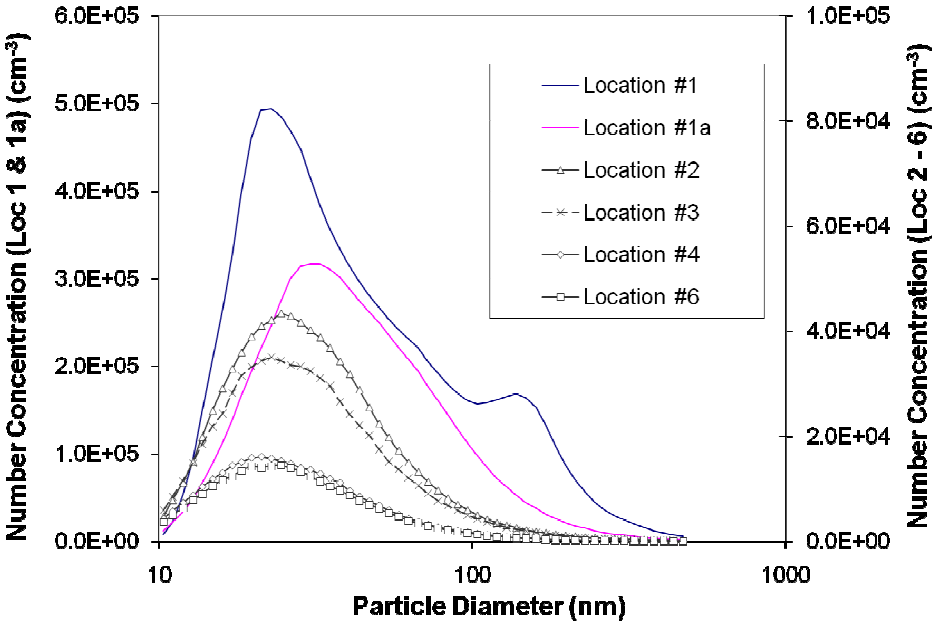

Figure 3.2.1: Centerline (0,0) particle number concentration distributions at each measurement location for an average free stream velocity of 0.64 m/s.

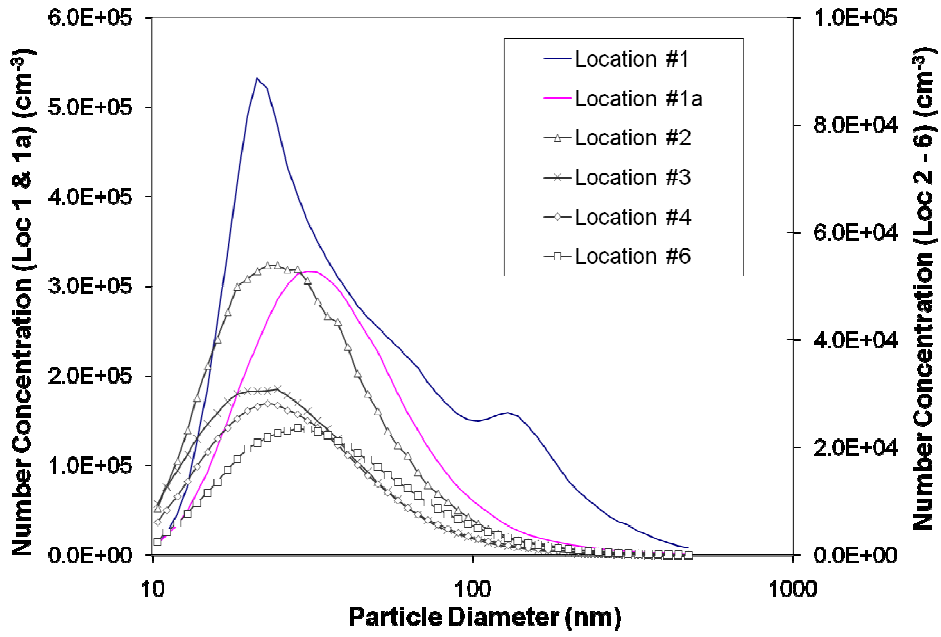

Figure 3.2.2: Centerline (0,0) particle number concentration distributions at each measurement location for an average free stream velocity of 0.25 m/s.

A dryer was not used during these experiments, which may account for the bi-modal distribution at Location 1 and the large shift in particle size between Locations 1 and 1a. The two peaks may be larger particles that have not yet dried, and smaller particles which have dried. The smaller peak could also be small drops of water, which have not dried. Once the larger particles dried out between Locations 1 and 1a, the true distribution became apparent. However this does not explain why the average particle size increases between Locations 1 and 1a and then decreases between Locations 1a and 2. The particles may be undergoing two phenomena simultaneously, evaporation and coagulation. Evaporation would cause the particle size to decrease and coagulation would cause the particle size to increase. It appears that evaporation and coagulation both occur between Locations 1 and 1a, and then evaporation is the dominant phenomenon between Locations 1a and 2. Therefore proper drying is essential to ensure evaporation is not disguising potential coagulation. After Location 3 the jet begins to disperse and diffusion becomes the dominant phenomenon for both flow rates. This diffusion is more apparent in Figures 3.2.2.1 and 3.2.2.2, as the aerosol becomes uniformly dispersed throughout the wind tunnel after Location 3. Figures C.1 – C.10 in Appendix C show concentration data for each location downstream of the injection probe for each measurement point.

Figure 3.2.3 shows the NSAM vs. SMPS comparison data for each measurement location (Locations 2, 3, 4, and 6 only). The SMPS data was converted into lung deposited surface area in the plot. The instruments show a linear correlation, but the slope of the fit curve is not equal to one. This could be due to the assumption that the particles

are spheres, where they are most likely cubical shaped. TEM analysis was not performed, therefore particle morphology is unknown and only assumed in this case.

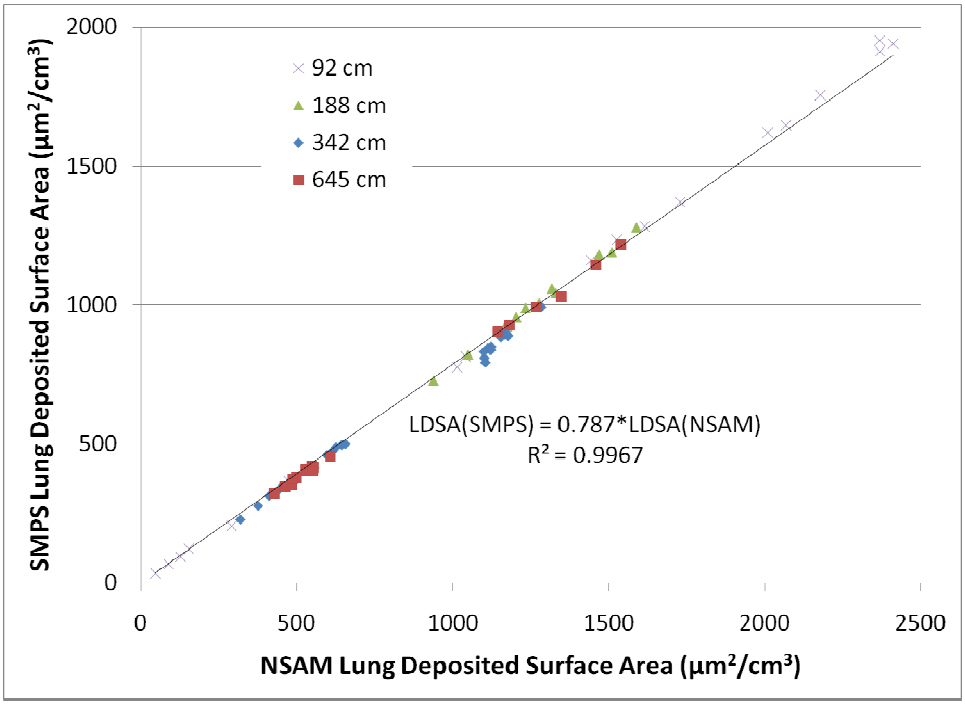

Figure 3.2.3: NSAM vs. SMPS lung deposited surface area for Locations 2, 3, 4, and 6 (distance from injection point is listed).

Section 3.2.1: Additional Aerosol Dispersion Tests (Using CPC only)

The dispersion of the aerosol jet can be better shown as the total particle number concentration plotted over the cross section of the wind tunnel. A setup similar to the initial dispersion tests was used to conduct these tests. The 6-jet atomizer (TSI Model 9306A, Shoreview, MN) was used to aerosolize a 0.1% solution of KCl, and a diffusion dryer was used to ensure only dry KCl particles were injected. A CPC was used to measure the total particle concentration at various locations within the wind tunnel (instead of the SMPS), because dispersion throughout the wind tunnel is the only concern in this case. A CPC also has a much faster response time than a SMPS, requiring less

time for each sample. Horizontal sampling traverses were conducted with the sampling probe positioned in the center of the wind tunnel (Center (y = 0 cm)) as well as at two other locations: up (Up 15 cm (y = 15 cm)) and down (Down 15 cm (y = -15 cm)). These traverse locations are outlined in Figure 3.2.1.1 and the wind tunnel schematic (the first 4 measurement locations) is Figure 3.2.1.2.

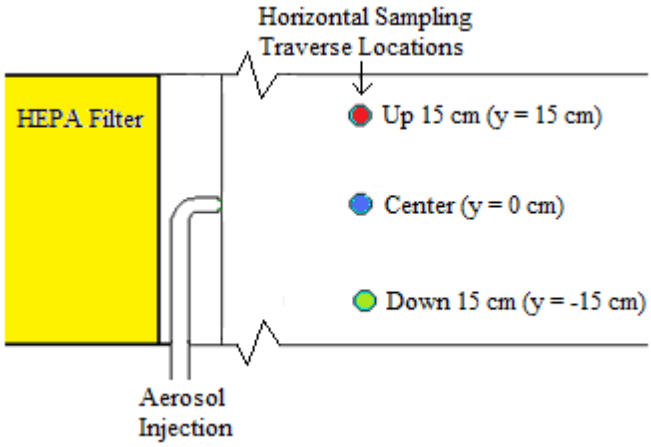

Figure 3.2.1.1: Locations for horizontal sampling traverses (values in parentheses indicate distances from bottom of the tunnel).

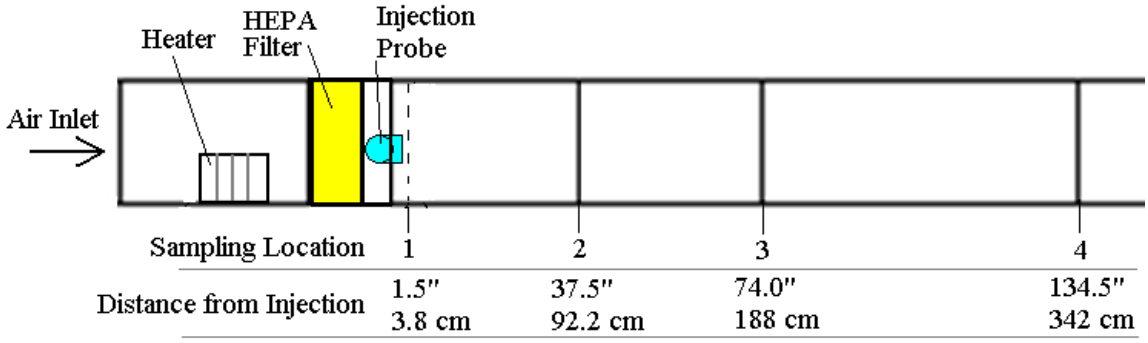

Figure 3.2.1.2: Schematic of wind tunnel, first 4 measurement locations for particle dispersion tests.

During the initial dispersion tests the aerosol became uniformly dispersed near Location 4, and was not well dispersed at Locations 1 or 1a. Therefore, only Locations 2, 3, and 4 were sampled during these additional (CPC only) dispersion tests. The results of

these tests are shown in Figures 3.2.1.3 – 3.2.1.5 and Figure 3.2.2.1. Figures 3.2.2.3 – 3.2.2.5 show the dispersion throughout the wind tunnel at sampling Locations 2 – 4, respectively. These figures indicate full dispersion throughout the cross section by Location 4, 342 cm downstream from the injection point.

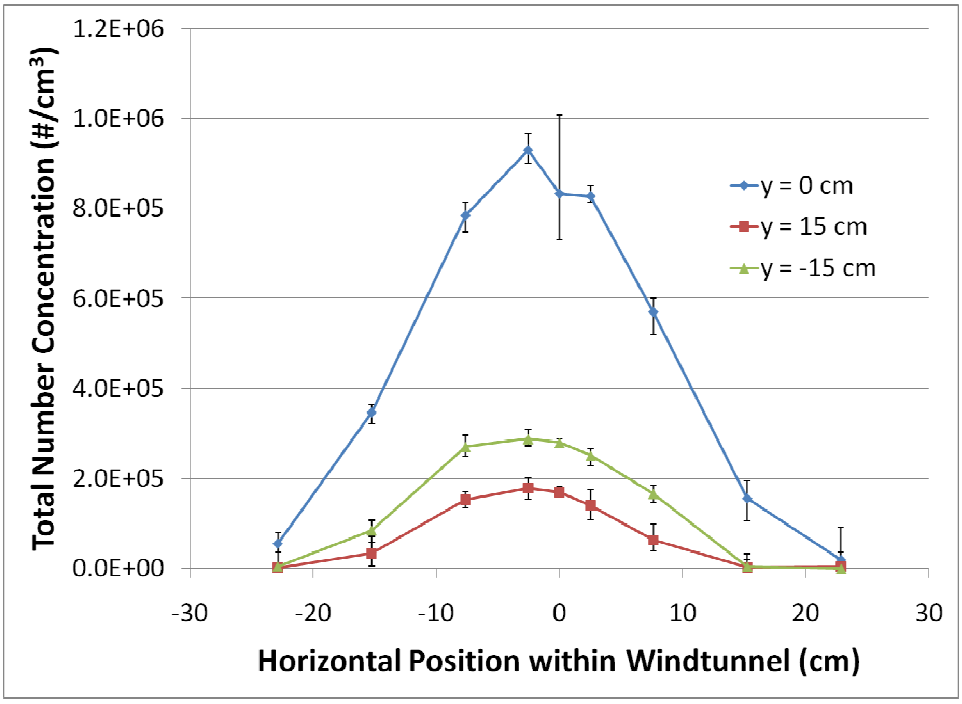

Figure 3.2.1.3: Aerosol dispersion test results at sampling Location 2, 92.2 cm downstream from injection, average air velocity 0.25 m/s.

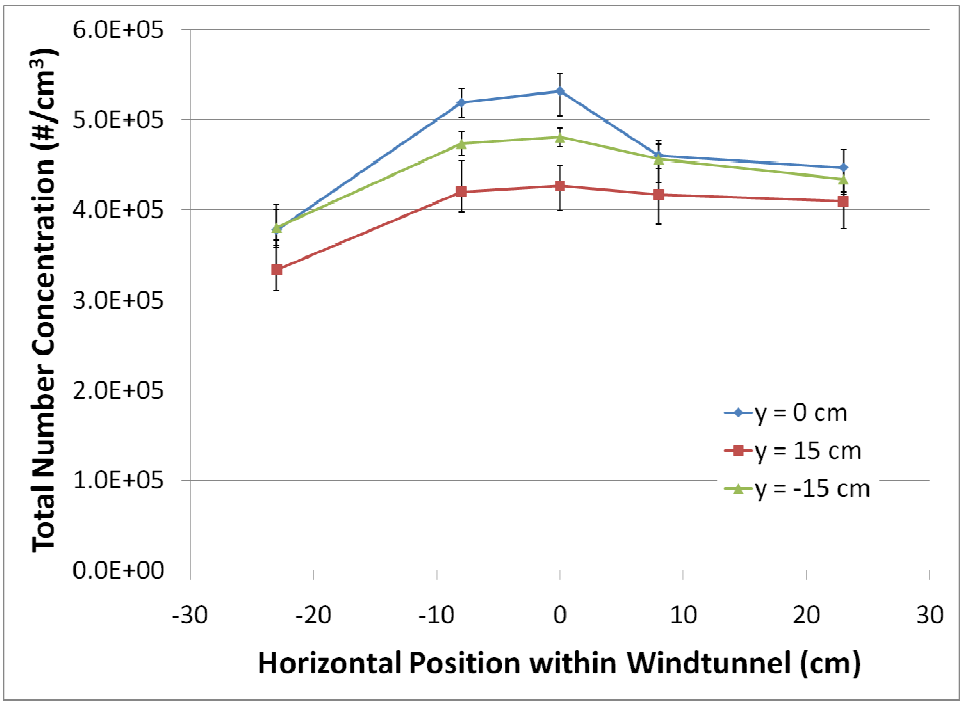

Figure 3.2.1.4: Aerosol dispersion test results at sampling Location 3, 188 cm downstream from injection, average air velocity 0.25 m/s.

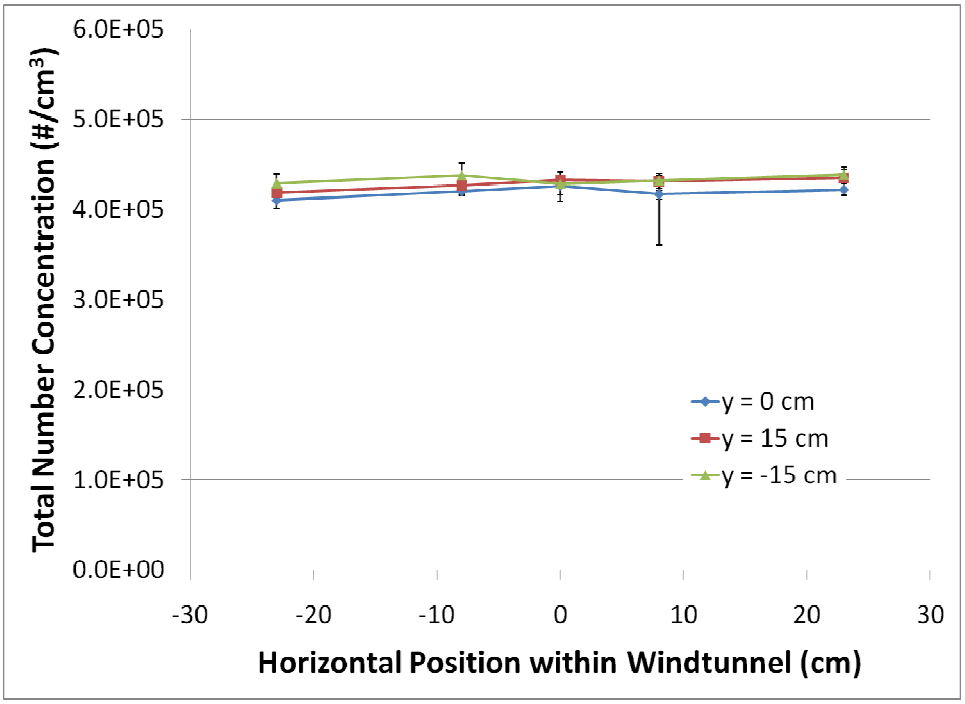

Figure 3.2.1.5: Aerosol dispersion test results at sampling Location 4, 342 cm downstream from injection, average air velocity 0.25 m/s.

Section 3.2.2: Comparison of Aerosol Dispersion Results (SMPS vs. CPC)

Figure 3.2.2.1 shows the aerosol number concentration results from horizontal traverses for each sampling location using a CPC, which can be compared to the initial dispersion test results (which utilized a SMPS) shown in Figure 3.2.2.2. During both dispersion tests there appears to be a well defined plume at Location 2. By the time the flow reaches Location 3 the aerosol is very close to being uniformly dispersed. There is still a noticeable plume, but it is not nearly as well defined as it was at Location 2. At Location 4, the dispersion throughout the wind tunnel is uniform for both cases. Air turbulence introduced by the HEPA filter at the inlet of the wind tunnel may affect the particle dispersion. Velocity profiles must be measured to determine if the air flow within the wind tunnel affects the particle dispersion.

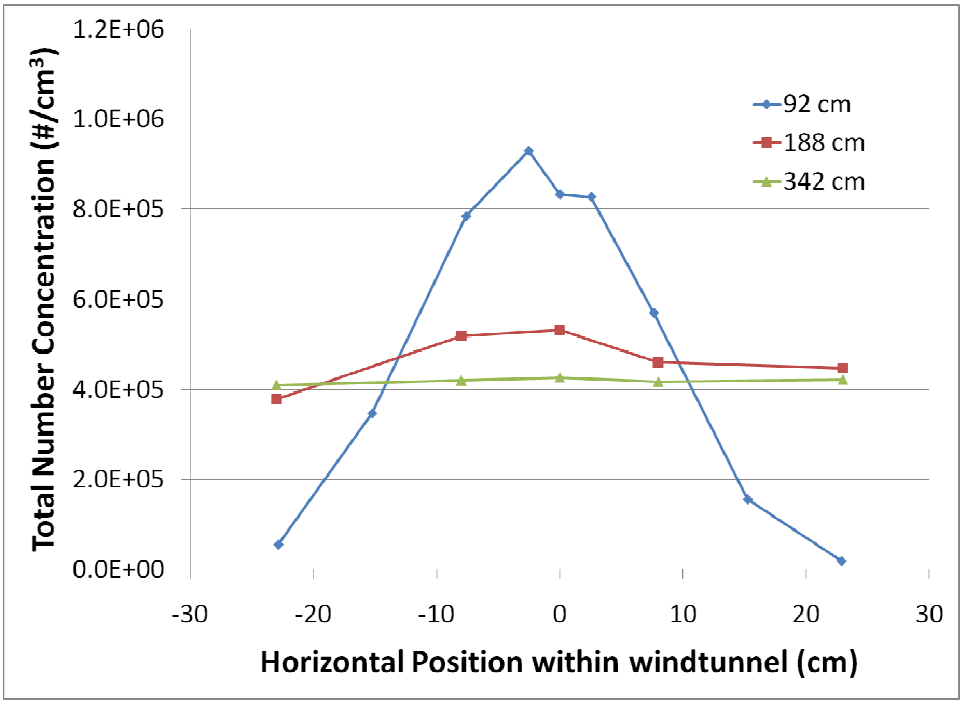

Figure 3.2.2.1: CPC only dispersion test results at center (y = 0 cm) location, 0.25 m/s.

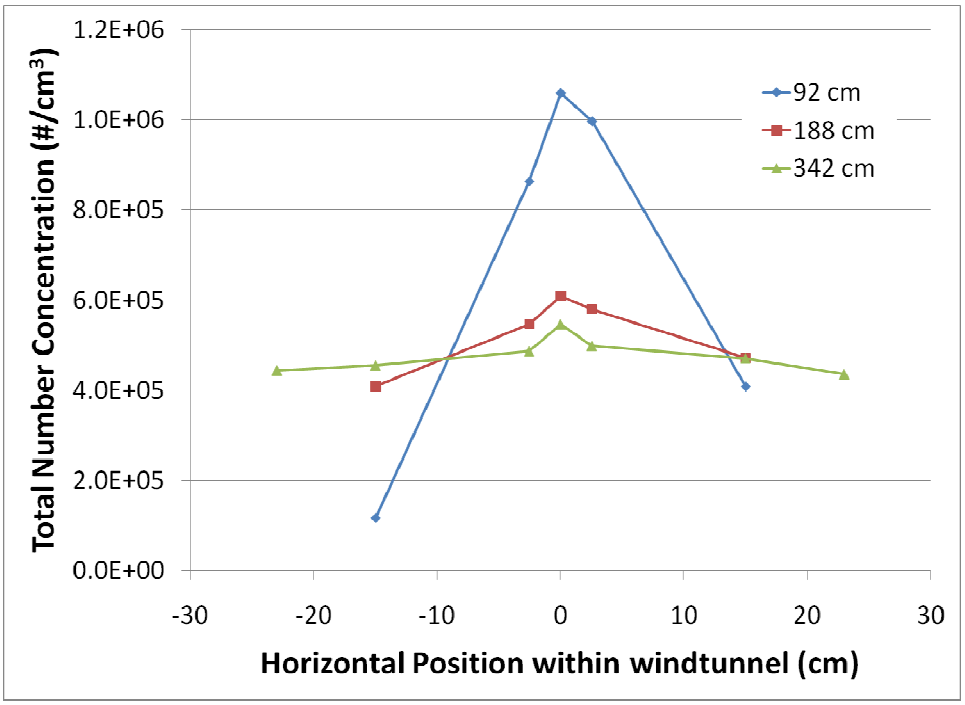

Figure 3.2.2.2: SMPS initial dispersion test results at center (y = 0 cm) location, 0.25 m/s.

Section 3.3: Wind Tunnel Velocity Profiles

The wind tunnel was originally constructed as a filter testing facility, where a test aerosol is thoroughly mixed after being injected. This mixing allows for a uniformly distributed aerosol throughout the cross-section of the duct, which is important when testing filters. The flow profile within the duct does not need to be uniform or laminar for filter testing, but it is necessary to have uniform flow to simulate a workplace environment, ensure repeatable trials, and allow confident comparisons to future work. Several flow profiles were measured throughout the cross-section of the wind tunnel to determine if the flow is uniform and/or laminar at various points downstream of the injection point.

The initial flow profile measurement locations were based on the log-chebychev distribution. The log-chebychev distribution allows a fair estimate of the flow profile

when initially characterizing the flow distribution within an air handling unit. This consisted of 25 measurement locations throughout the cross section of the duct. The results are shown in the contour plot in Figure 3.3.1. Numerically simulated velocity profiles are located in Appendix D. These simulations show the potential for future work through numerical analysis.

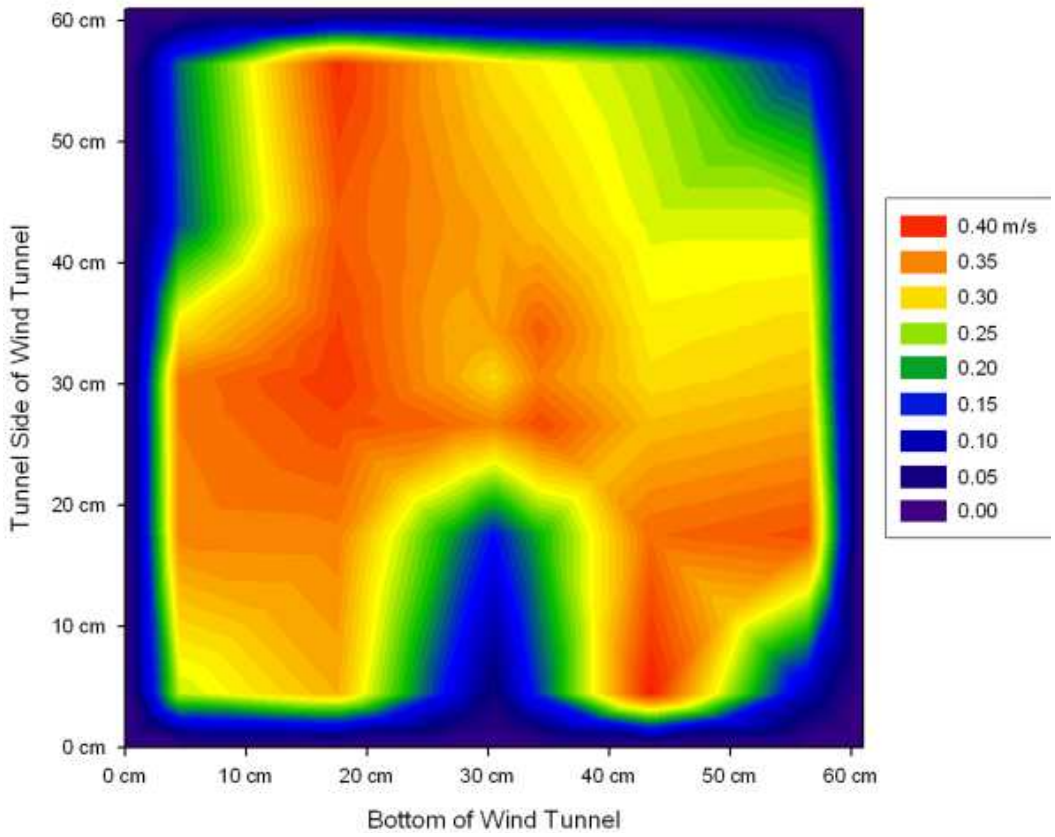

Figure 3.3.1: Experimentally determined velocity profile of wind tunnel cross section at 20 cm downstream.

A better way of determining the flow profile was to concentrate the measurement positions around the injection probe. This is the area of most interest and where most of the non-uniformities should occur. Figure 3.3.2 shows the results of this measurement, which shows a more specific effect of the injection probe (compared to Figure 3.3.1).

Therefore the log-chebychev measurement grid should be substituted with a more refined grid during future velocity measurements. Therefore, the grid from the Additional Particle Dispersion tests (CPC only), outlined in Section 3.2.1 and shown in Figure 3.2.1.1, was used during future velocity profile measurements.

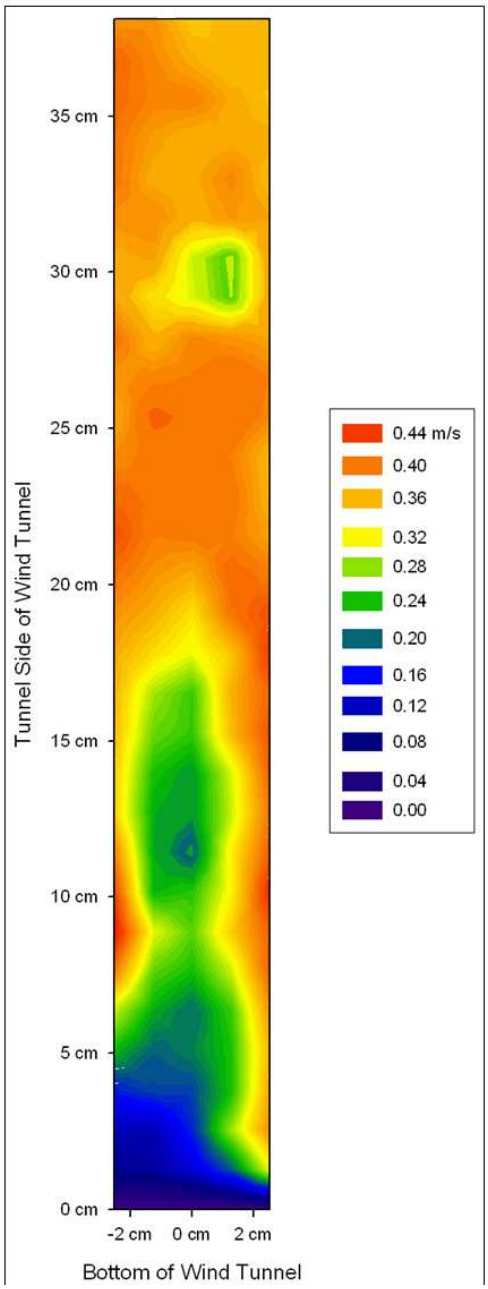

Figure 3.3.2: Velocity profile of injection probe area at 20 cm downstream.

New velocity profiles were taken at various locations throughout the wind tunnel corresponding to positions in Figure 1.2.1. Figures 3.3.3 and 3.3.4 show the velocity profiles at Locations 2 and 4 in the wind tunnel. These new velocity profiles clearly show non-uniformity in the flow; which is apparent by the velocity differences horizontally and vertically throughout the cross section of the wind tunnel. These differences increase with distance from the injection probe, as the flow splits.

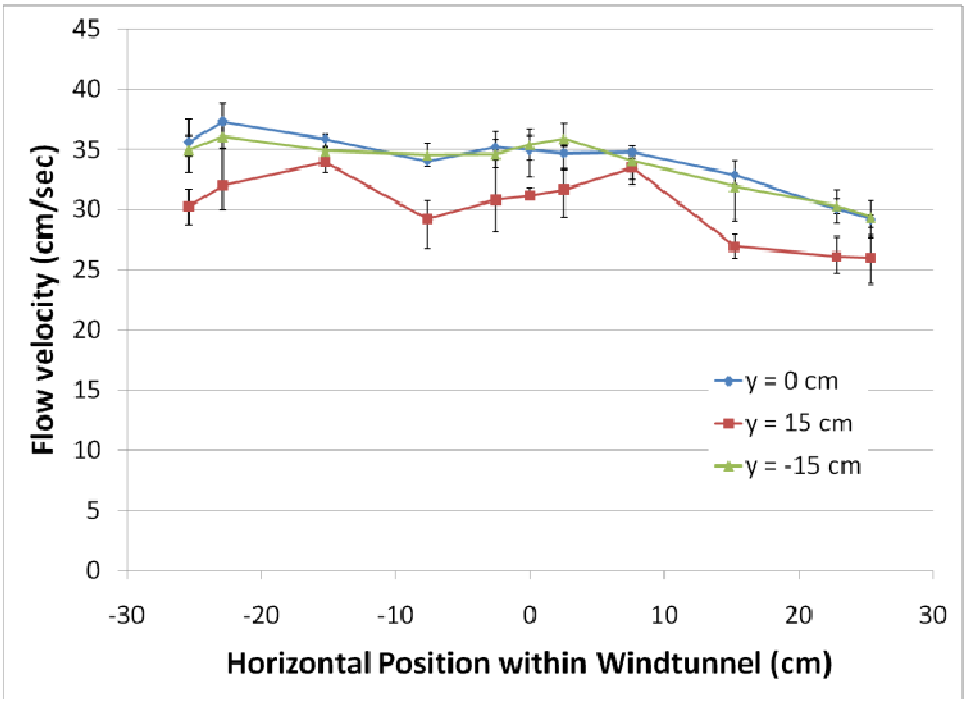

Figure 3.3.3: Velocity profile at 0.9 m downstream (Location 2).

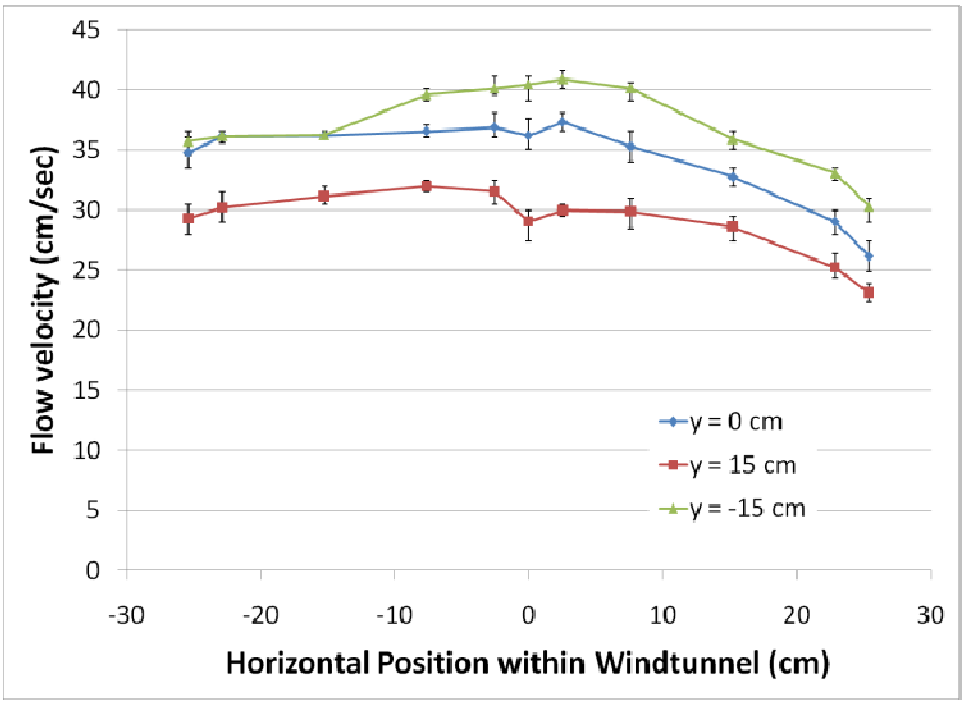

Figure 3.3.4: Velocity profile at 3.4 m downstream (Location 4).

A different wind tunnel configuration was tested to determine if the 180° bend could be causing some of the non-uniformities noticed at Locations 2 and 4 in Figures 3.3.3 and 3.3.4. The new wind tunnel setup is shown in Figure 3.3.5. This is a straight duct, which does not include the 180° bend depicted in the ASHRAE 52.2-2007 Classified wind tunnel schematic (Figure 1.2.1).

Figure 3.3.5: Picture of air handling unit without 180° bend.

The tunnel segments were positioned exactly as they had been prior to removing the bend. The real-time flow meter needed to be removed, meaning the wind tunnel flow rate could not be monitored. However, the voltage supplied to the fan was set to the value used during the first velocity profiles to obtain a similar flow rate. The velocity profiles were gathered at Locations 2, 3, and 4 and are shown in Figures 3.3.6 – 3.3.8. Velocity profiles for Locations 1 and 1a are shown in Appendix D.

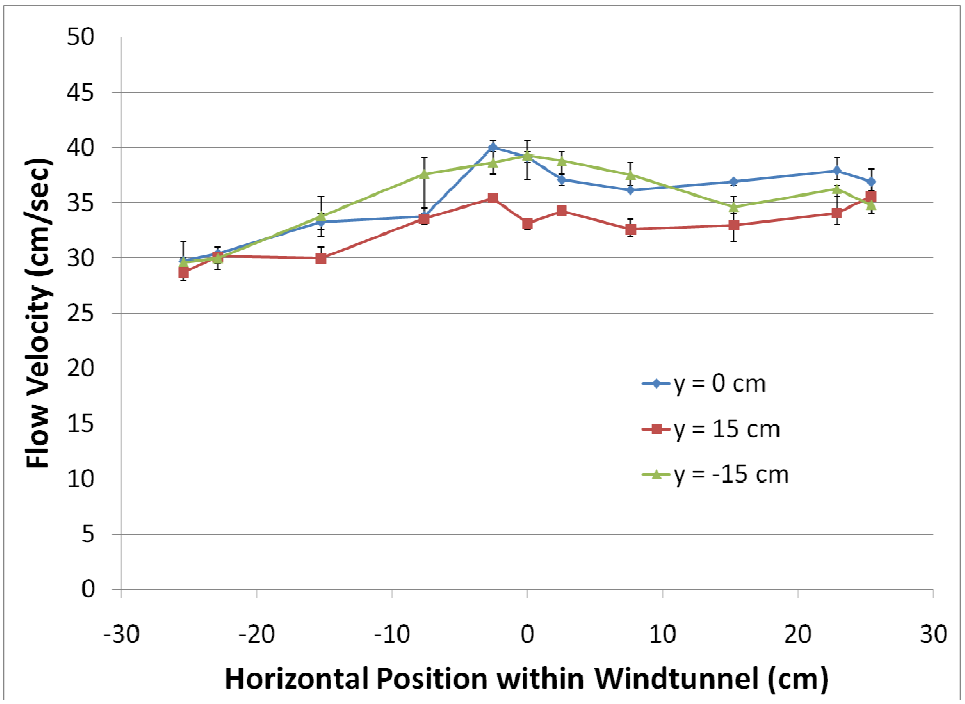

Figure 3.3.6: Velocity profile at 0.9 m downstream (Location 2) with straight duct.

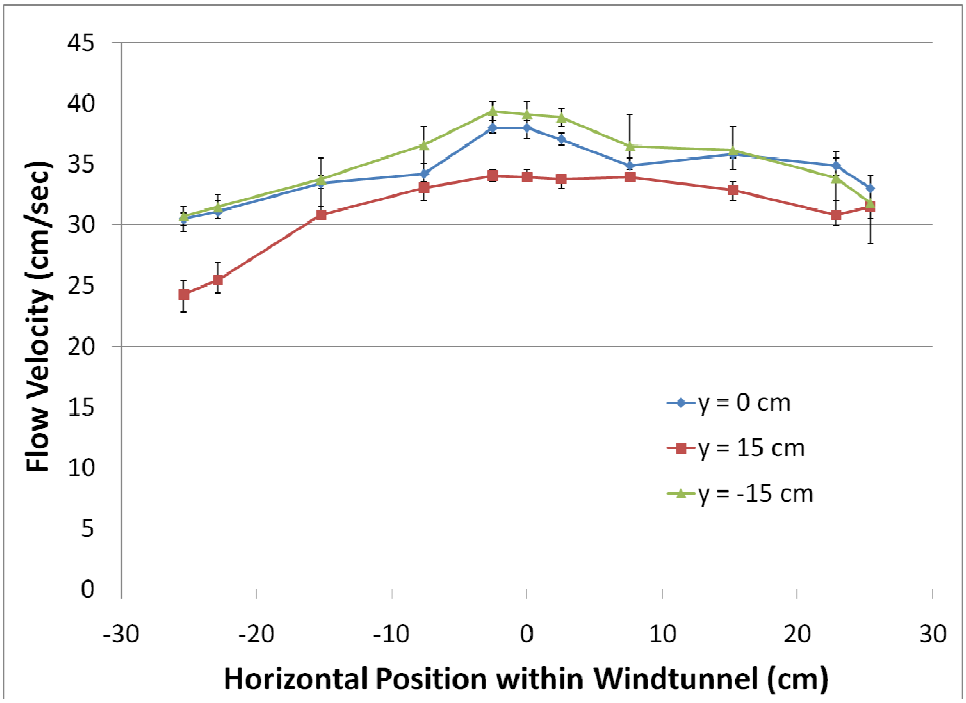

Figure 3.3.7: Velocity profile at 1.8 m downstream (Location 3) with straight duct.

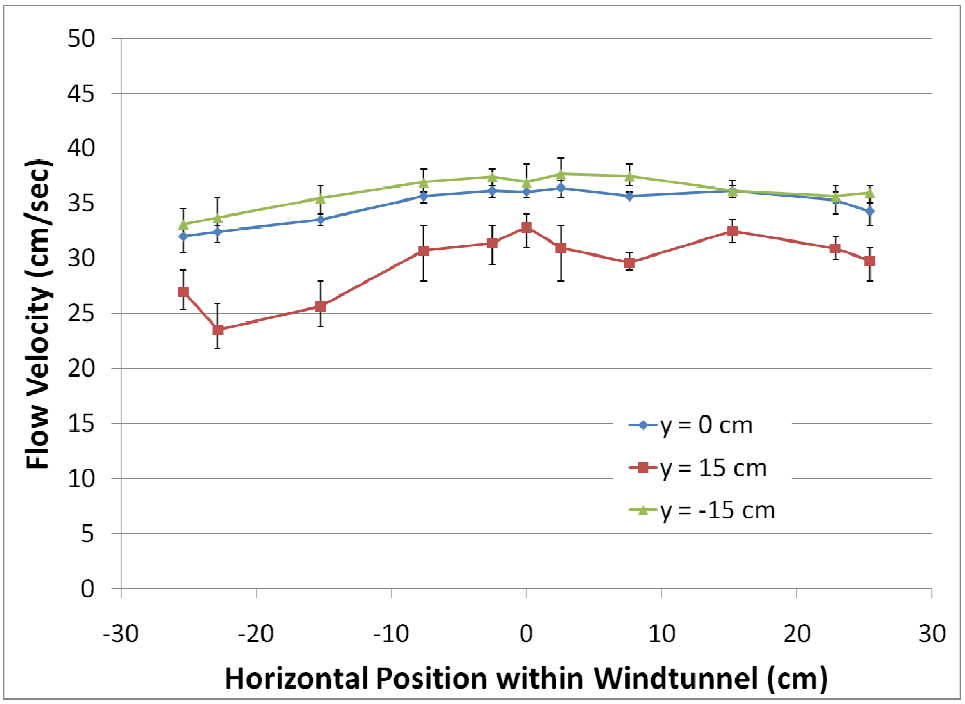

Figure 3.3.8: Velocity profile at 3.4 m downstream (Location 4) with straight duct.

Figures 3.3.6 - 3.3.8 are slightly closer to uniformity, but still not quite there. This may be as close as we can get to a uniform flow profile under the circumstances of the current study. A more complete velocity traverse (i.e. gathering velocity data for both horizontal and vertical flow directions in order to obtain turbulence intensity) would be better for determining specific areas of concern. This capability was not available.

Flow straighteners were inserted into the wind tunnel in a final attempt to obtain a uniform velocity profile throughout the cross section of the duct. The flow straighteners were part of a volumetric flow rate measurement system (Model STRA-R24x24) sold by Dwyer. After removing the tubes from inside of the system and covering the pressure taps on the outside, a hole was drilled for the injection probe. The injection probe was removed from the HEPA filter section, and the HEPA filter section was moved to the end of the wind tunnel as shown in the new experimental schematic (Figure 3.3.9). This

experimental setup was utilized for future burner aerosol experiments. The time after injection and distance from injection are both reported in Figure 3.3.9. The distance from the leak is the most convenient, accurate, and versatile parameter for analysis. A number of dimensionless parameters can be determined from the distance after injection (as shown in Section 4.2). The time after injection is based on the background flow, because the relaxation time for the injected particles is very small (~0.1 μs for 100 nm particle in air). However due to the nature of the jet at the injection point, the time after injection cannot be accurately (and confidently) determined.

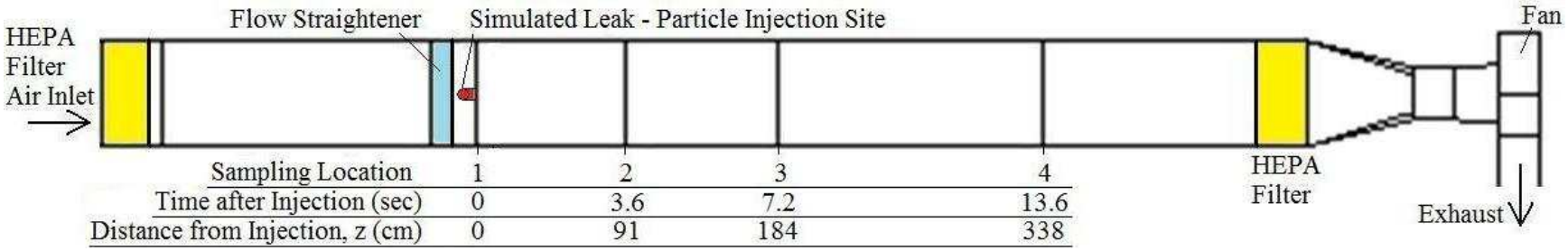

Figure 3.3.9: Reconfigured wind tunnel allowing for near uniform flow within the wind tunnel.

The new velocity profiles are shown in Figures 3.3.10 – 3.3.12. Locations 1 and 1a are shown in Appendix D. These are very uniform throughout the duration of the duct. The initial flow profile is completely uniform throughout the entire cross section (besides at the centerline, where the injection probe initially interfered). The upper portion of the duct also shows this effect (at the centerline). This is because the flow straighteners are not one continuous grid; but instead two grids are glued to a metal plate (splitting the two honeycomb grids down the middle). This metal plate is thick enough to cause flow non-uniformity. Even with this non-uniformity, the flow is much more uniform than it was without the use of the flow straighteners. Therefore this experimental schematic was used for the remainder of the current study. The new injection section with the flow straighteners can be seen in the introduction section as Figure 1.3.3.

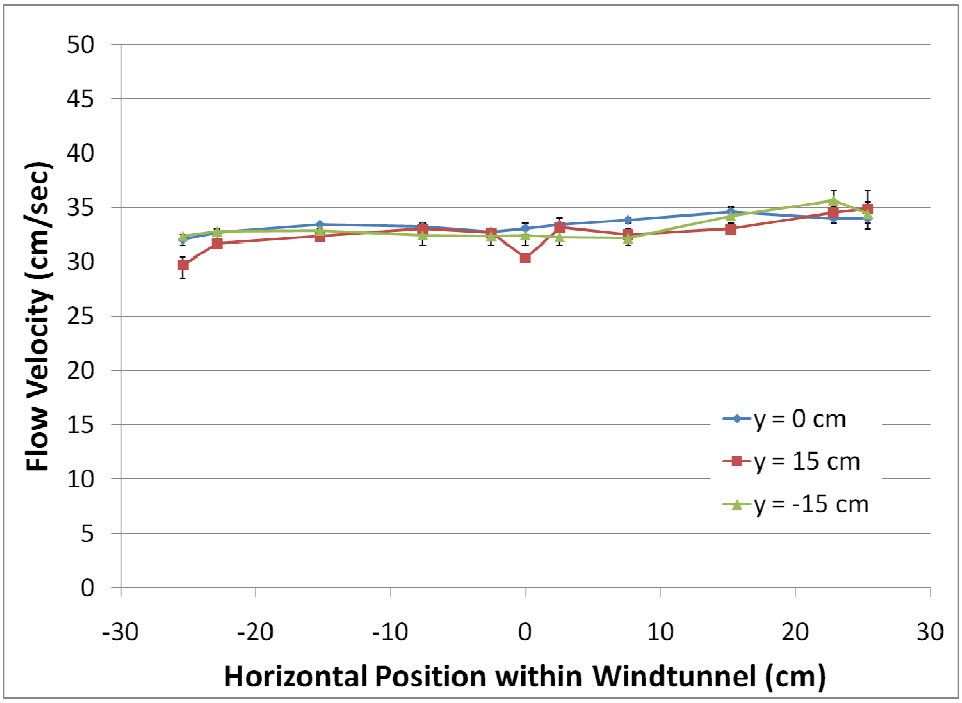

Figure 3.3.10: Velocity profile at 0.9 m downstream (3.6 seconds) with flow straightener.

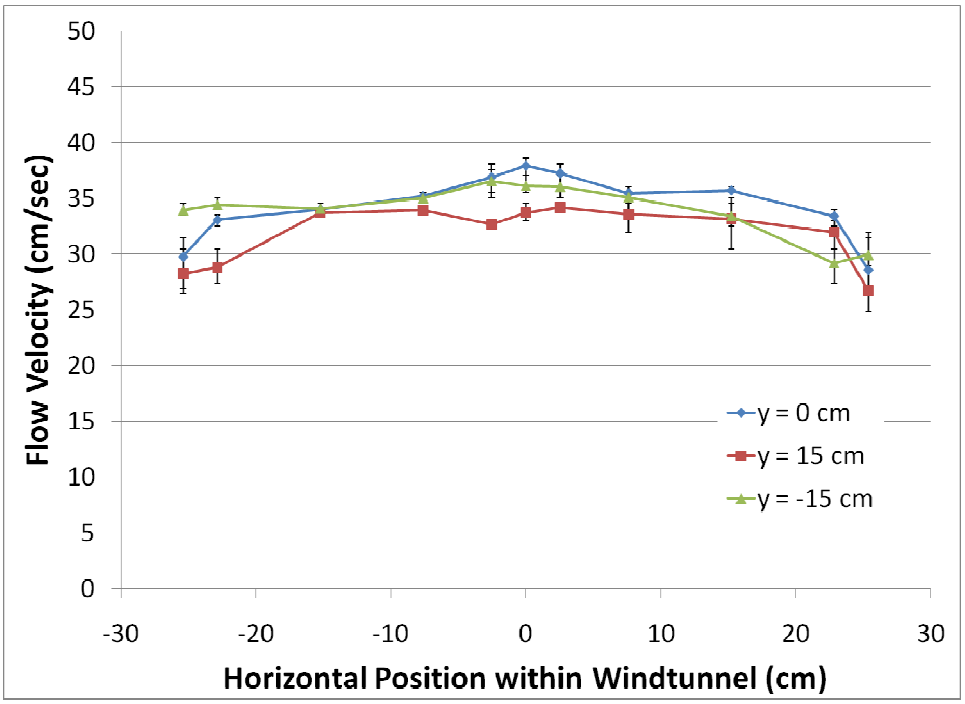

Figure 3.3.11: Velocity profile at 1.8 m downstream (7.2 seconds) with flow straightener.

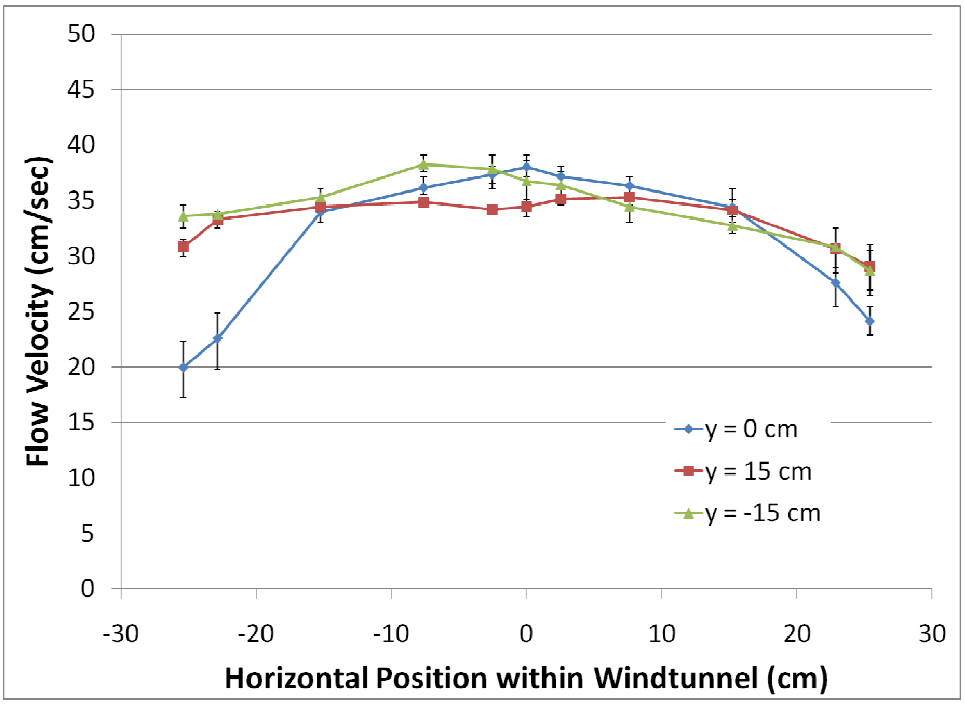

Figure 3.3.12: Velocity profile at 3.4 m downstream (13.6 seconds) with flow straightener.

Section 3.4: Burner Particle Characterization Within Fume Hood

A diffusion burner will be used to produce test aerosols for the current study, which includes carbon black (soot), TiO_2, and SiO_2. Before the burner can be used in the wind tunnel it is necessary to define the burner operating parameters to produce a known particle size distribution and morphology. The burner is pictured in Figure 3.4.1. Simulations to be carried out at IUTA require this information (initial particle size distribution, concentration, and morphology). A starting point should be known for the experimental side as well. Therefore the burner particles must be characterized before wind tunnel tests are carried out with the burner. However, the burner produces particles at a very high concentration, too high for a CPC (TSI Model 3025A) to count, even when these particles are characterized by a SMPS (TSI Model 3080) and long DMA (TSI Model 3081).

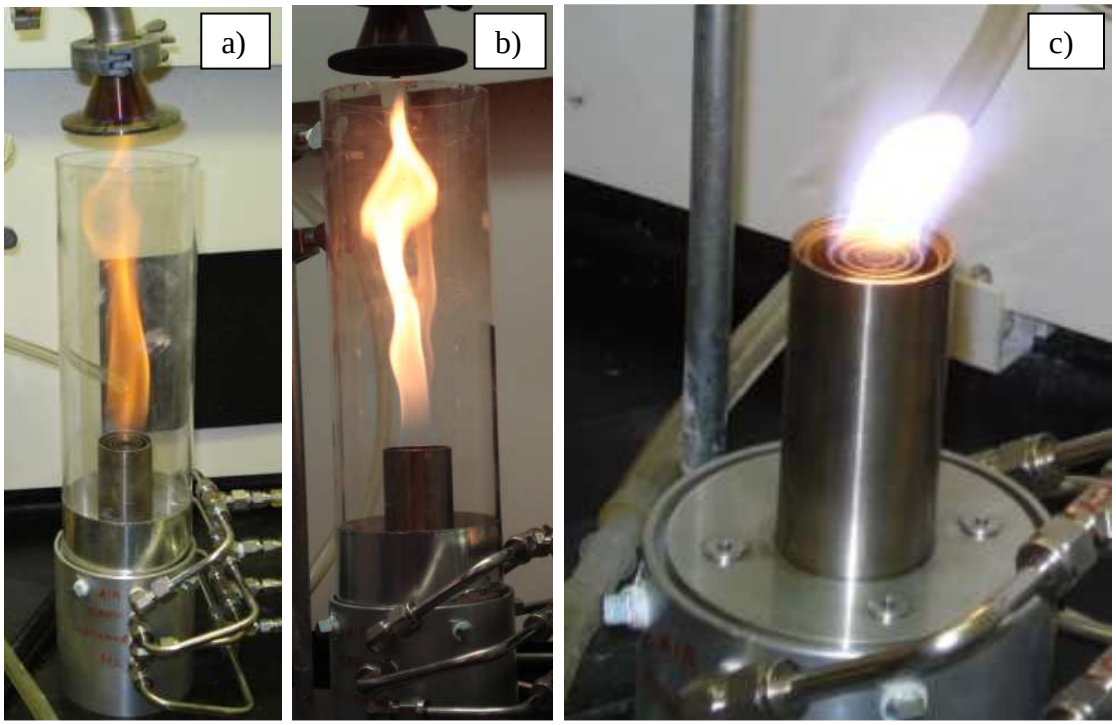

Figure 3.4.1: The diffusion burner operating in a fume hood: a) and b) are fuel/air flames only, c) is a fuel/air/oxygen flame, which did not produce much soot.

The dilutor allows for accurate sampling of burner produced aerosols with the SMPS. The dilution set development is outlined in Section 3.5. Particle morphology can be determined by depositing the particles on a TEM grid and viewing with a Transmission Electron Microscope (TEM). Figure 3.4.2 shows TEM images of the sampled soot particles under various magnifications. These particles are highly agglomerated (mostly as chains), but appear to have a primary particle size of 20 – 50 nm (this was not measured). Therefore burner gas flow rate parameters have been identified, which allow particles in the desired size range to be produced.

SMPS measured particle concentrations are shown in Figure 3.4.3. The burner settings were 0.6 l/min of methane (CH_4) and 15 l/min of air. This is a lean mixture with 143% excess air being supplied to the burner. Higher concentrations were measured when using less excess air (62% and 8%), but the sampling line clogged up quicker when using these burner settings. When using the burner in the wind tunnel, mixtures will be able to be richer without the risk of clogging the sampling line due to dilution within the wind tunnel.

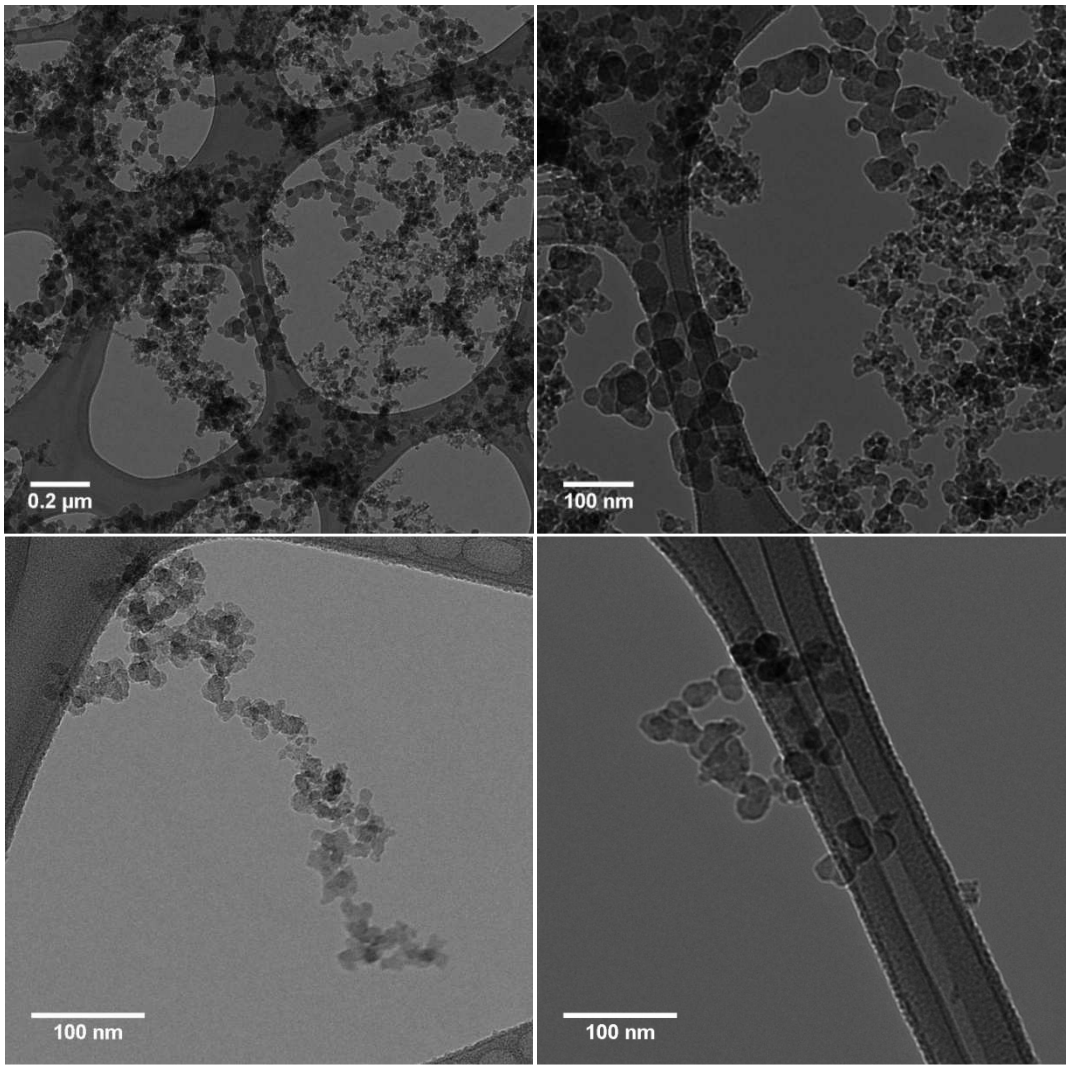

Figure 3.4.2: TEM images of soot particles from burner in fume hood.

The TEM images in Figure 3.4.2 are from the first burner particle characterization. A second characterization was conducted with the actual burner housing and injection probe to be used in the wind tunnel. The second characterization trials utilized the burner gas parameter settings from the initial characterization. Measurements were taken (with 100:1 dilution) at various distances from the injection point. Distances of 0, 1, 3, and 5 cm from the injection point were measured due to limited space and

unknown flow patterns in the fume hood. Due to the unknown flow patterns within the fume hood, the time between the injection and sampling points was not determined.

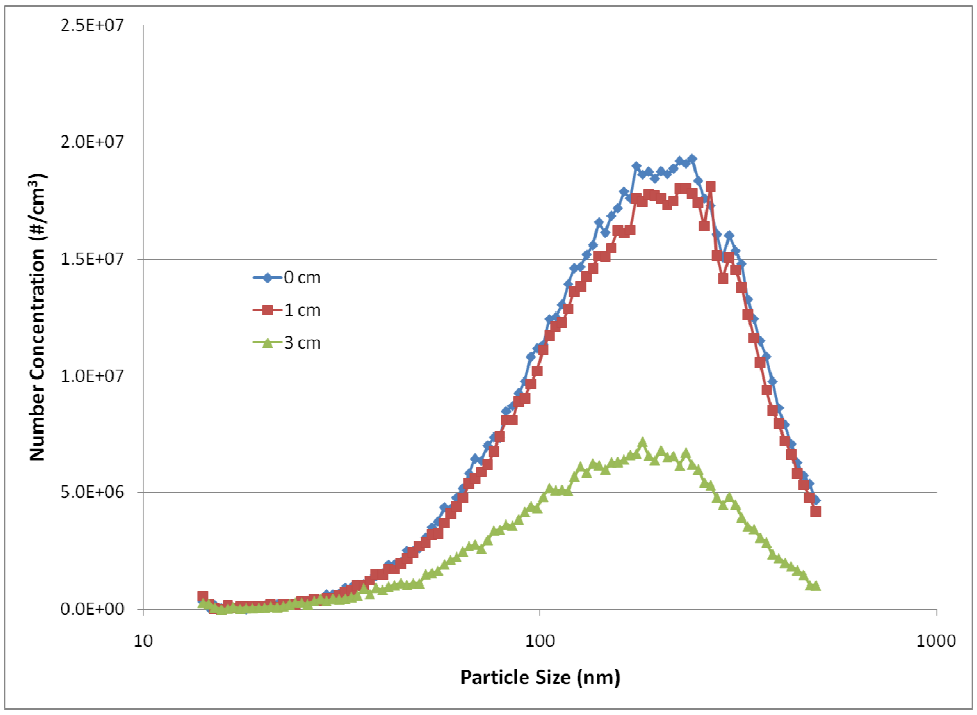

Figure 3.4.3: Burner particle concentration at various distances from injection point.

The concentrations measured at 5 cm from the outlet were insignificant, most likely due to advection effects of the fume hood on the burner plume. Therefore the plume center was not being sampled even though the sampling probe was in line with the injection point. Soot, TiO_2, and SiO_2 particle concentrations were classified at the injection point during wind tunnel testing, which are outlined in later sections of this thesis.

Section 3.5: Dilution Set Development and Calibration

Dilution is necessary in order to measure the aerosol concentrations produced by the burner in the current study. Clean, dry lab air is mixed with the sampled aerosol, causing the aerosol concentration to decrease, in order to create this dilution. This decreased level is too low for significant coagulation to occur and can be measured accurately by the measurement instruments. The dilution air also provides a drying effect, which limits the evaporation effect further downstream. This effect was observed in the initial dispersion studies as a decrease in mean particle size at locations downstream of the particle injection point, outlined in Section 3.2.

A dilution set was constructed and calibrated to a 100:1 dilution ratio (100 parts clean, dry lab air to 1 part sample aerosol). This dilution set is pictured below in Figure 3.5.1. The appropriate amount of dilution is difficult to obtain since such a small amount of sample aerosol is required for a 100:1 dilution ratio.

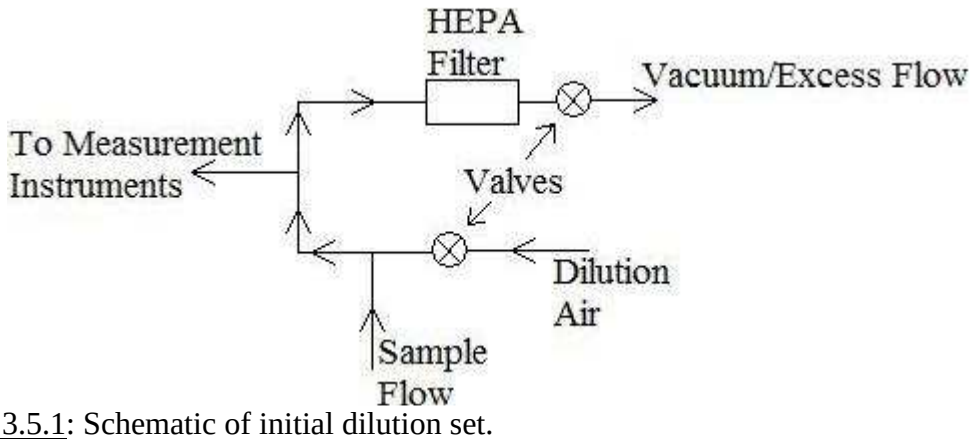

Figure 3.5.1: Schematic of initial dilution set.

A KCl 0.1% solution was used in the Constant Output Atomizer (COA) to create the test aerosol for the initial calibration of the dilution set. A Scanning Mobility Particle Sizer was used to measure the concentration and distribution of the aerosol. The

concentration was low enough for the instrument to make an accurate measurement without dilution air. The dilution air was carefully set by volumetric measurements to 10:1, 20:1, and 100:1. Each trial was conducted 3 times. In between each dilution ratio trial a reference measurement was taken to ensure a consistent aerosol was being produced by the COA. The dilution ratio was calculated for each particle size based on these SMPS measurements. The theoretical volumetric dilution ratio, the total dilution ratio (based on total particle concentration), and the specific dilution ratio for each particle size are plotted in Figures 3.5.2 – 3.5.5 for no dilution and dilution ratios of 10:1, 20:1, and 100:1, respectively.

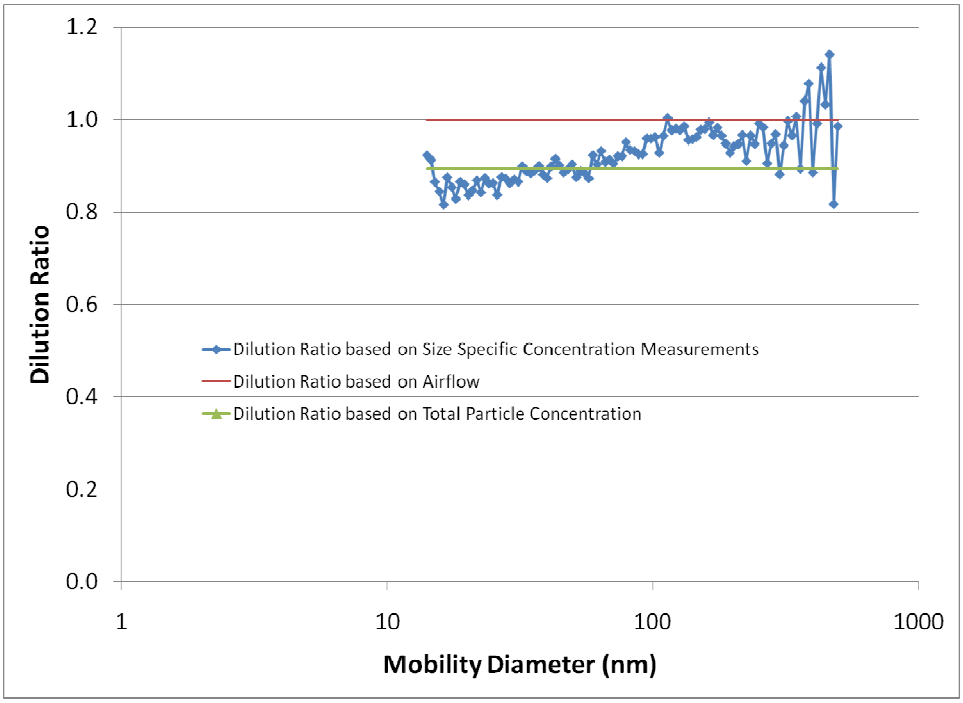

Figure 3.5.2: Initial dilution set with no dilution air.

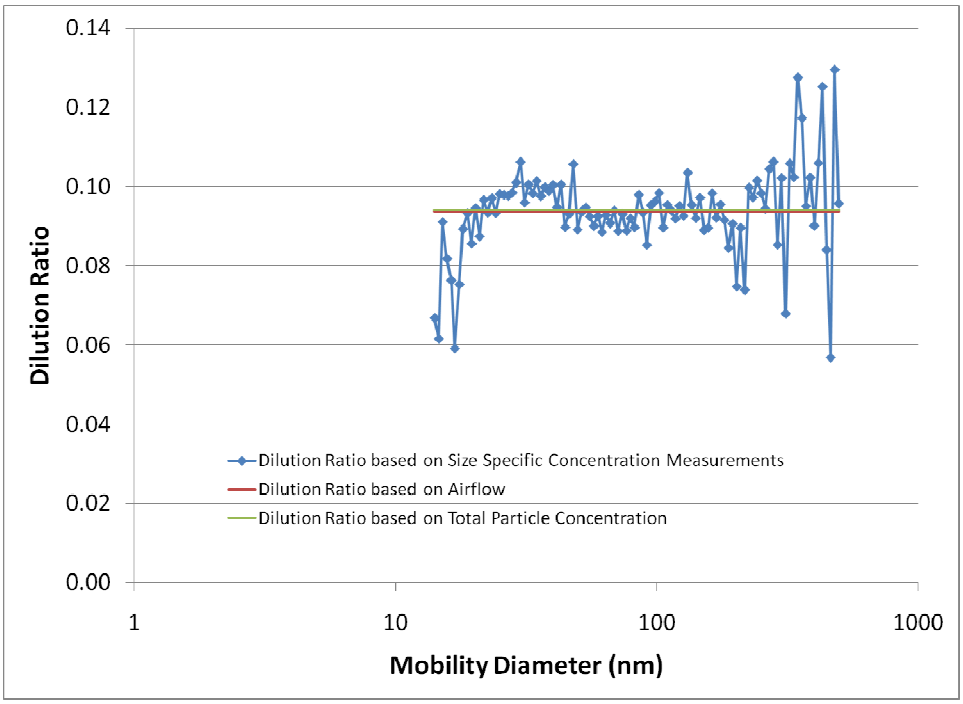

Figure 3.5.3: Initial dilution set with 10:1 dilution ratio.

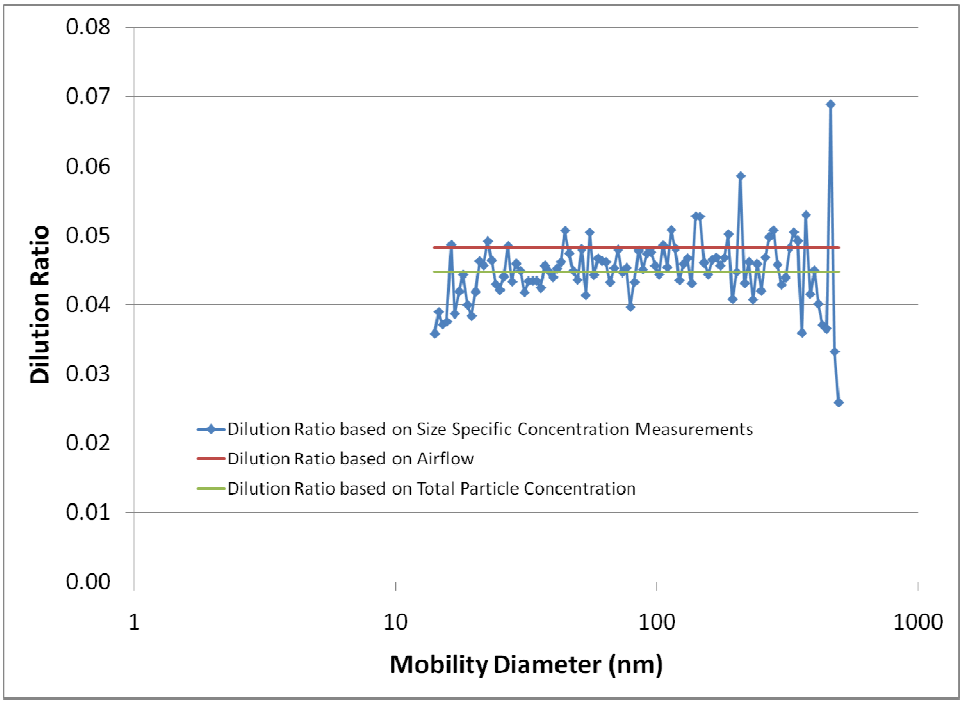

Figure 3.5.4: Initial dilution set with 20:1 dilution ratio.

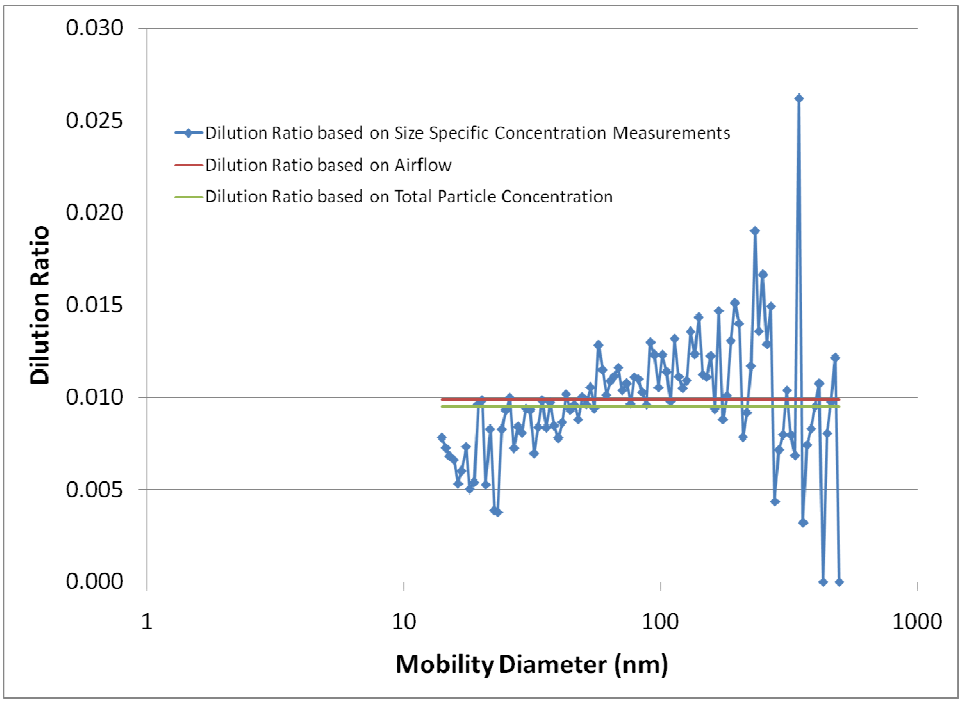

Figure 3.5.5: Initial dilution set with 100:1 dilution ratio.

These figures were corrected for diffusion losses in the sampling line using Equations 3.5.1 – 3.5.4 (Hinds, 1999). This dilution ratio is plotted vs. particle size along with the total particle dilution and the theoretical volumetric dilution. The total particle dilution ratio represents the total particle concentration measured with dilution air divided by the total particle concentration. The theoretical volumetric dilution ratio represents the sample volumetric flow rate divided by the total volumetric flow rate. These volumetric flow rates were measured with 4100 series Flow Meters (TSI, Shoreview, MN) and set prior to the experiment. Accounting for losses shows the dilution ratio is not constant for all particle sizes.

Equation 3.5.1: $$D = \frac{kTC_c}{3\pi\mu d_p}$$

D = Diffusion coefficient of particles (m^2/s)
k = Boltzmann's constant (1.38×10^{-23} kg-m^2/K-s^2)
T = Temperature (K)
C_c = Cunningham's slip correction (dimensionless)
μ = Dynamic viscosity (1.8134×10^{-5} Pa-s for air at NTP)
d_p = Particle diameter (m)

Equation 3.5.2: $$C_c = 1 + \frac{\lambda}{d_p}\left[2.34 + 1.05exp^{-0.39\frac{d_p}{\lambda}}\right]$$

λ = Gas mean free path (0.066 μm for air at NTP)

Equation 3.5.3: $$\mu = \frac{DL}{Q}$$

μ = Diffusion deposition parameter (dimensionless)
L = Length of sampling line (m)
Q = Volumetric flow rate (m^3/s)

Equation 3.5.4a: $P = \frac{n_{out}}{n_{in}} = 1 - 5.50\mu^{2/3} + 3.77\mu$ for $\mu < 0.009$

Equation 3.5.4b: $P = 0.819exp^{-11.5\mu} + 0.0975exp^{-70.1\mu}$ for $\mu \geq 0.009$

P = Penetration through sampling tube (ratio)
n_{out} = Particle concentration downstream of sampling tube (cm^{-3})
n_{in} = Particle concentration upstream of sampling tube (cm^{-3})

This initial dilution set seemed to work well enough and it was used during the initial burner characterization studies, conducted in the fume hood. However in order to obtain a representative sample within the wind tunnel, there must be dilution at the point of sampling. This initial dilution set could provide this type of dilution for the initial characterization of the dilution set and the burner characterization studies, but not in the wind tunnel. The initial dilution system cannot provide dilution at the point of sampling within the wind tunnel unless the entire dilution set is placed within the tunnel. Without

dilution at the point of sampling, the aerosol has over 18 seconds of travel through narrow sampling lines, which could cause the particle properties to change significantly. Therefore another system of dilution was developed.

Introducing dilution air at the point of sampling provides a quenching affect which freezes the aerosol/particle properties as they were at the sampling location. This allows a representative sample to be obtained within the wind tunnel. The dilution air can be introduced at the point of sampling as shown in Figure 3.5.6, although experimentation showed the dilution ratio cannot be controlled accurately in this manner.

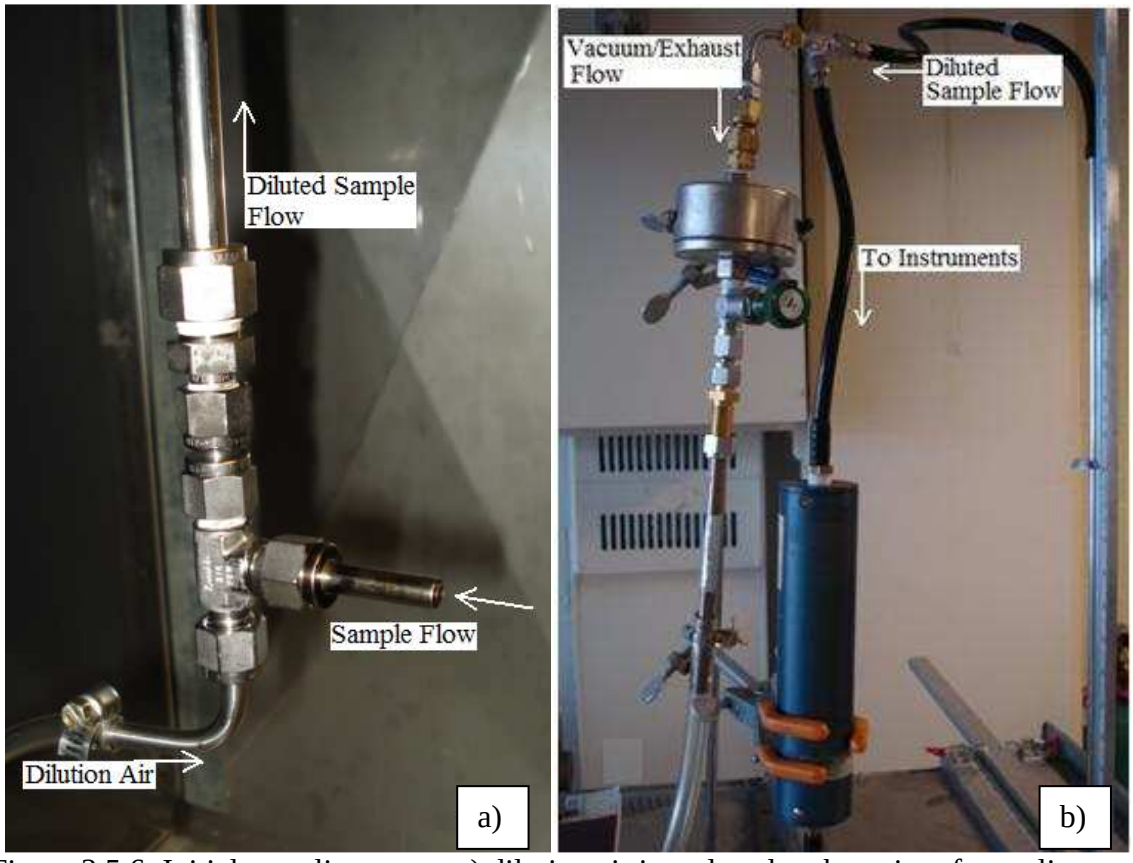

Figure 3.5.6: Initial sampling setup: a) dilution air introduced at the point of sampling and b) the split sample flow to instruments and exhaust.

The flow meters are not sensitive enough to distinguish between 100:1 dilution compared to 130:1 or 70:1. Using smoke as a tracer gas it is possible to determine if the sampling nozzle is at least drawing air under different flow rates. These air flow visualization results are shown as Figure 3.5.7; however when the dilution ratio was set to the 100:1 (based on carefully calibrated flow meter volumetric flow rates) the nozzle did not draw in the smoke. Different dilution and sampling flow rates drew the smoke into the sampling nozzle and blew the smoke away from the sampling nozzle; however the setup was not sensitive enough to get a true 100:1 dilution ratio. The system was checked for leaks throughout this experiment by smearing soapy water on all connections. Few leaks were detected. All leaks were fixed following detection.

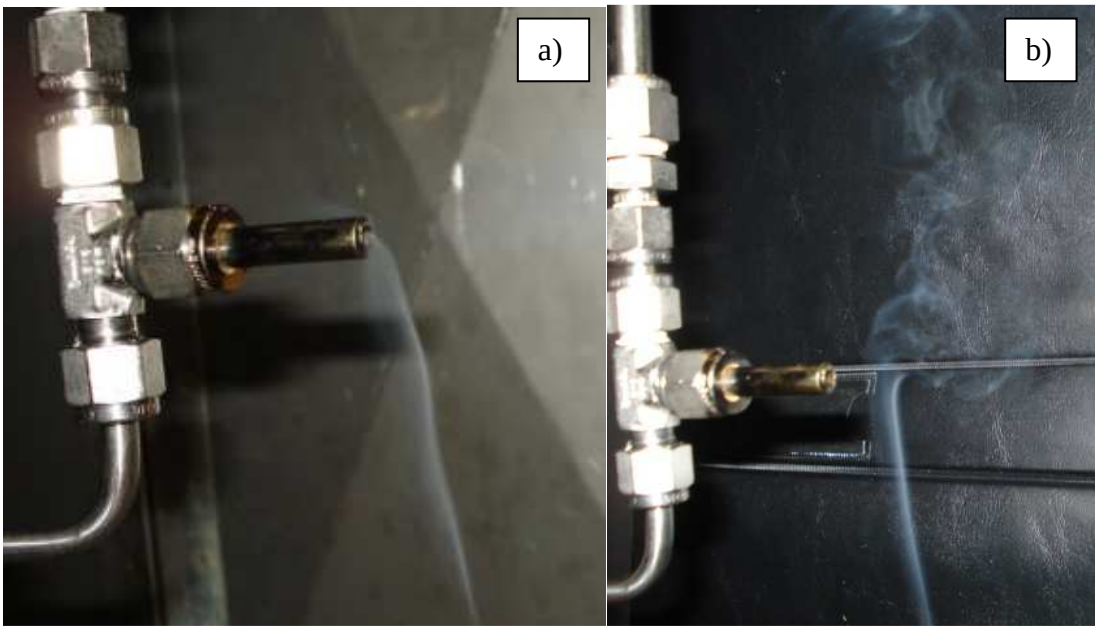

Figure 3.5.7: Smoke tracer gas experiments showing the smoke: a) drawn into and b) blown away from the sampling nozzle.

A more accurate way of setting the dilution ratio involves using an orifice as the sampling nozzle. The pressure drop across this orifice can be used to determine a set flow

rate with good accuracy. A derivation of Bernoulli's Equation (Equation 3.5.5) was used to calculate the theoretical pressure drop required for 100:1 dilution. A Dwyer liquid manometer was used to measure the pressure drop across the orifice. The orifice was calibrated before use. The completed orifice is examined in Section 3.5.1.

Equation 3.5.5: $$mfr = CA_2P_1\sqrt{\left(\frac{2M}{ZRT_1}\right)\left(\frac{k}{k-1}\right)\left[\left(P_2/P_1\right)^{2/k} - \left(P_2/P_1\right)^{(k+1)/k}\right]}$$

mfr = Mass flow rate (kg/s)
C = Orifice flow coefficient (dimensionless)
A_2 = Cross-Sectional Area of Orifice (m^2)
P_1 = Pressure upstream of orifice (N/m^2)
P_2 = Pressure downstream of orifice (N/m^2)
T_1 = Temperature upstream of orifice (K)
M = Molar mass of gas (kg/kmole)
Z = Gas compressibility factor at P_1 and T_1 (dimensionless)
R = Universal gas constant (N-m/kmole-K)
k = Specific heat ratio (dimensionless)

Equation 3.5.5 describes the theoretical operation of the sampling orifice. Using an upstream pressure of 1 atm, and a volumetric flow rate (Q) of 0.18 lpm in Equation 3.5.5 produces Figure 3.5.8. The upstream temperature and orifice size are varied to show the sensitivity of the pressure drop. Due to minor pressure fluctuations, the pressure drop across the orifice will vary slightly throughout the course of the experiment. With an orifice size of 0.5 mm, if the pressure drop changes 20%, then the flow rate will change 10%. Therefore the pressure drop can alter and it should not have a large impact on the flow rate.

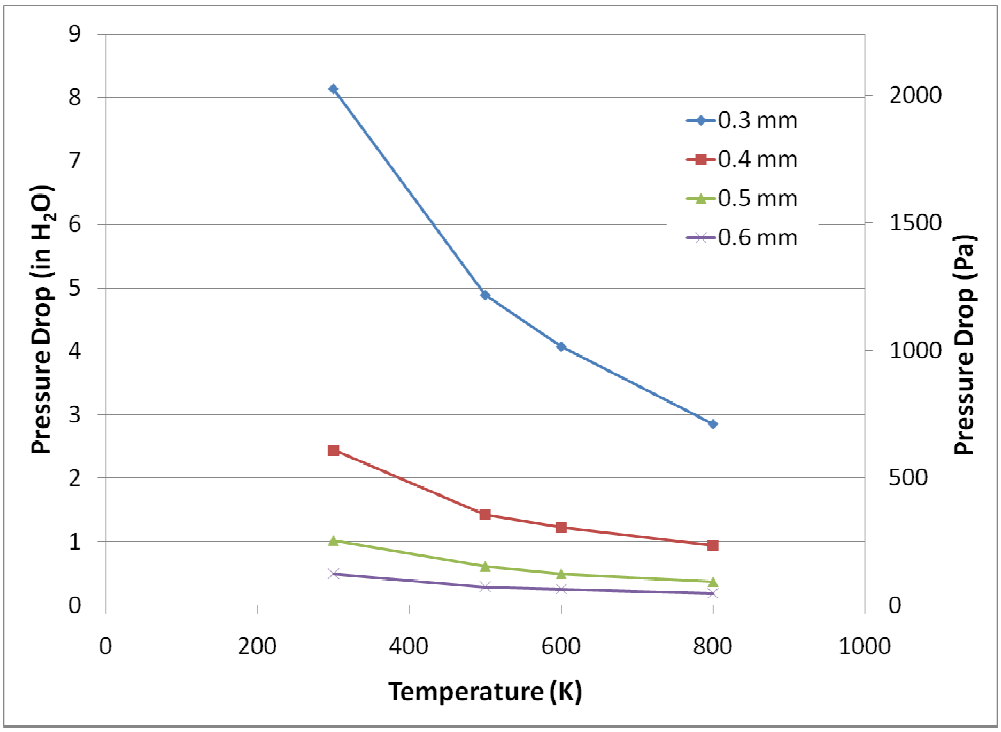

Figure 3.5.8: Theoretical Orifice Pressure Drop with P_1 = 1 atm and Q = 0.18 lpm.

Section 3.5.1: Orifice Calibration

The completed orifice is shown in Figure 3.5.1.1. One major problem was attaching a tube to the front of the nozzle in order to attach a flow meter for calibration. A pipe clamp did not work because there was not enough room upstream of the pressure tap. The pressure tap needed to be in that exact spot as well, to ensure a proper measurement across the orifice. The tube was cut so a pipe clamp could be applied behind the pressure tap, but this could not be sealed tight enough and several leak checks showed the system was leaking. A tube needed to be cut, wrapped around the pressure tap, glued to the orifice, and clamped in place in order to eliminate all leaks out of and into the sampling orifice (as shown in Figure 3.5.1.2).

Figure 3.5.1.1: Orifice sampling nozzle installed in sampling section. Thermocouple installed for gas temperature measurement to ensure proper flow calculation.

Figure 3.5.1.2 shows the leak check. Once the glue dried the entire assembly was submersed in a bucket of water to check for bubbles. Leaks were not detected prior to,

during, or after each calibration experiment when the submerged dilution system was placed under positive pressure. Figure 3.5.1.3 shows the inclined manometer (Dwyer Instruments, Inc., Michigan City, IN, 46360) and flow meters (Model 4143, TSI, Shoreview, MN) used during the calibration process. The inclined manometer and flow meter #3 will remain attached to the sampling section to monitor the flow rate of the sampled aerosol (and dilution air) during the burner experiments. Both flow meters were calibrated against a Gilibrator II (Gilian Instrument Corp.) prior to being installed on sampling orifice. The calibration curves for the flow meters are shown in Appendix E.

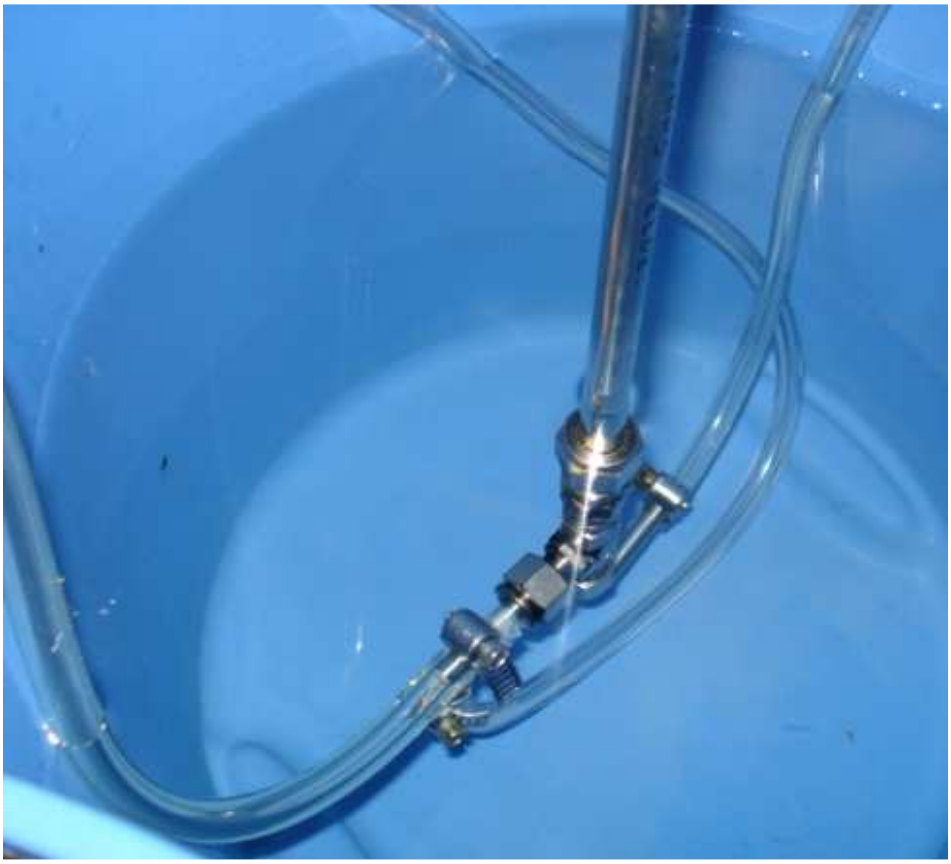

Figure 3.5.1.2: Orifice leak check before, during, and after each calibration experiment.

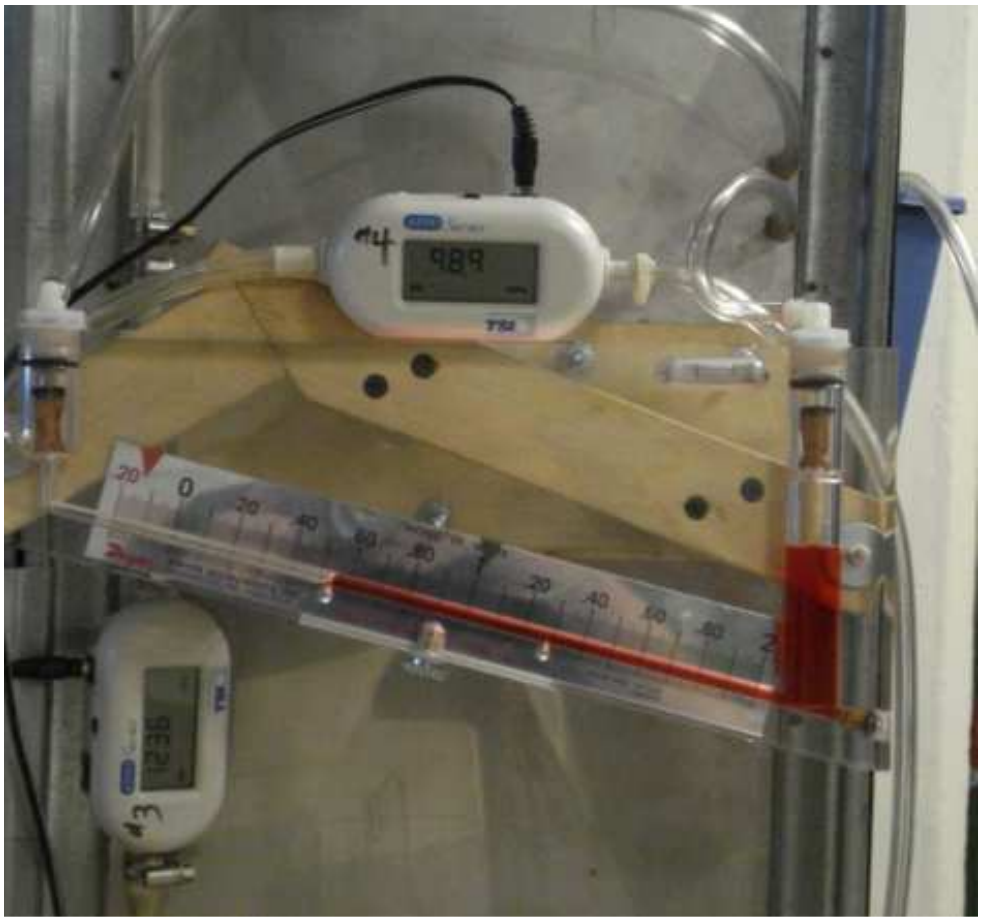

Figure 3.5.1.3: Measurement instruments for sampling orifice calibration.

Once the leaks were fixed (as shown in Figure 3.5.1.2) the calibration curves were fairly consistent. Four calibration trials were completed with no leaks. These calibration curves are in Appendix E. The data from each calibration curve is plotted in a single figure (Figure 3.5.1.4). This represents the overall calibration curve for the sampling setup. The theoretical orifice nozzle diameter that most closely resembles the experimental data is 0.52 mm, which is close to the design orifice diameter (the design diameter was 0.5 mm).

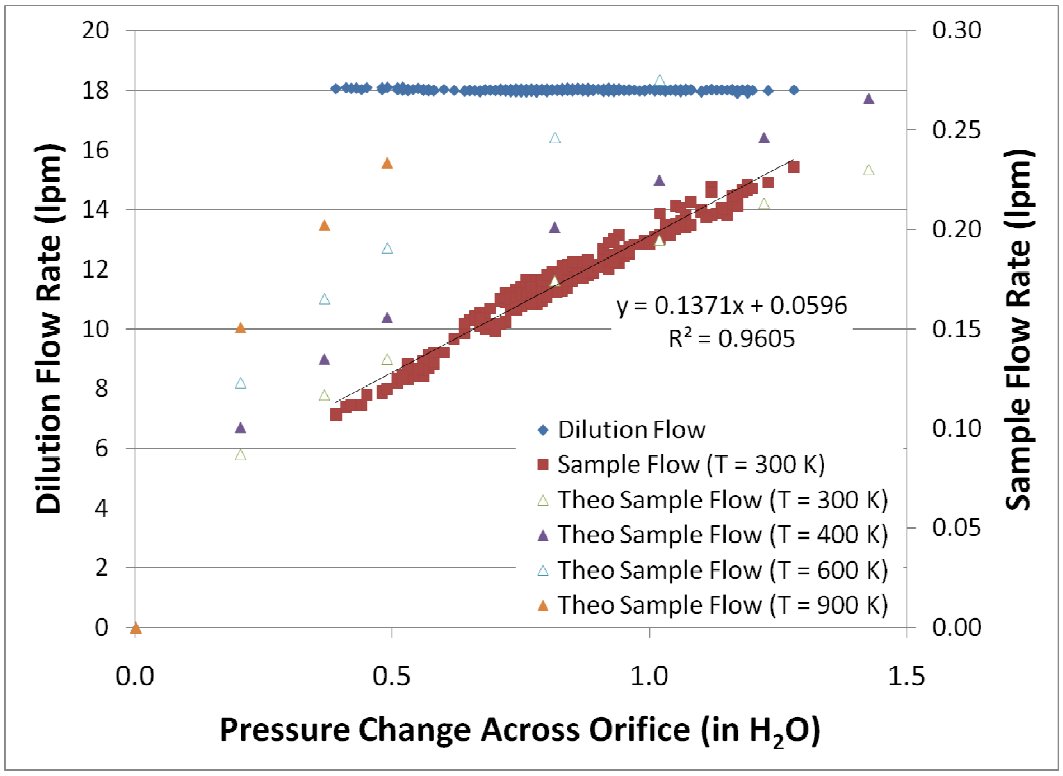

Figure 3.5.1.4: Overall calibration curve for the sampling orifice.

Higher temperatures may be present in the wind tunnel (in the presence of hot combustion gases). Therefore theoretical curves must be fit to account for potential high gas temperatures. These curves are also shown in Figure 3.5.1.4, however a spreadsheet is a better way of determining the required pressure drop for various temperatures, in real-time. In order to correct for higher temperatures there must be a method of measuring the temperature of the sampled aerosol and carrier gas. Therefore, a type-T thermocouple was attached to the end of the sampling orifice. The final orifice setup (with thermocouple attached) is shown as Figure 3.5.1.5.

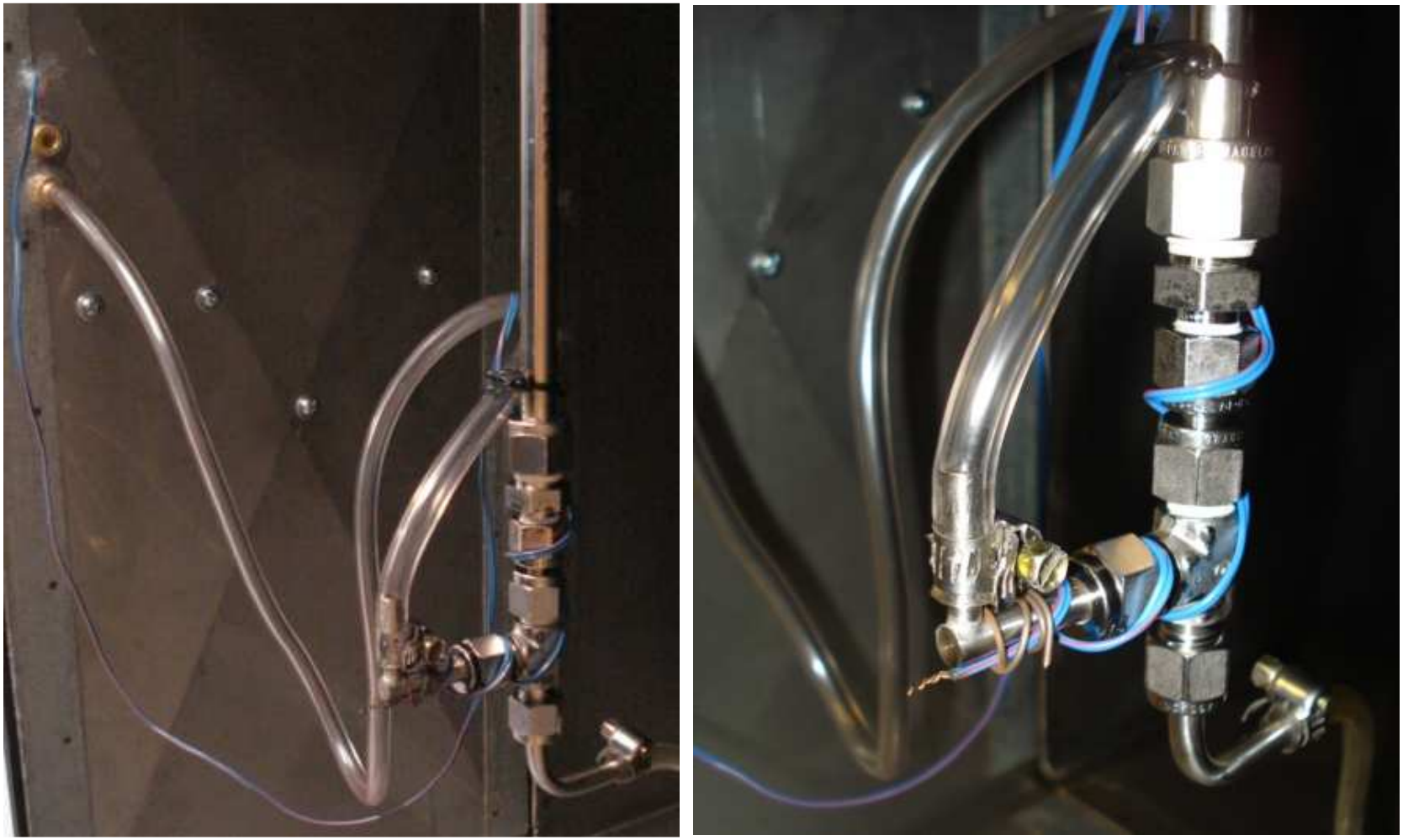

Figure 3.5.1.5: Final orifice setup with thermocouple.

Section 4

Soot Transport and Particle Change through a Simulated Workplace Environment

Section 4.1: Introduction

In the current study, soot nanoparticles are injected into a modified ASHRAE 52.2-2007 Classified wind tunnel (Figure 3.3.9) in order to determine their fate. This injection is a simulation of a leak in a nanoparticle production process, causing airborne nanoparticles to spill into a workplace environment (the wind tunnel). This represents a worst-case exposure scenario. If such a leak went undetected, workers may be exposed to dangerous levels of hazardous nanoparticles. The particles may remain mobile, airborne, and highly concentrated, or they may coagulate to larger sizes and settle out of the airstream. Proper detection and protection measures must be implemented to ensure worker safety in the event of such a leak. The current discussion focuses on the soot experiments. TiO_2 and SiO_2 nanoparticles are examined in Section 5.

Section 4.1.1: Soot Primary Particle and Agglomerate Formation

Small nuclei particles (which coalesce to form primary particles) are held together by fresh condensed matter, which acts like glue as primary particles form (Mitchell et al., 2009). As the particles grow, other small nuclei particles are able to fill easily and cover uniformly into a consistent size and spherical shape (Frenklach, 2002). The shape of most soot primary particles is due to this rapid surface growth by nucleation, as well as internal restructuring for a final spherical particle (Kim et al., 2006; Mitchell and Frenklach, 1998).

Soot agglomerates are composed of randomly arranged, overlapping spherical primary particles (Balthasar and Frenklach, 2005). These agglomerates are fairly consistent in both physical structure and chemical composition (Dobbins and Megaridis, 1987). Agglomerates are held together by weaker adhesion forces, such as van der Waals forces whereas aggregates are held together by strong chemical bonds or sintering. Long, chain-type aggregates/agglomerates form when primary particles collide while at very high concentrations, such as during incomplete hydrocarbon combustion. These can have a wide number of primary particles per agglomerate (Xu et al., 1998). When agglomerates form within the high temperature region of the flame, the primary particles become partially sintered and somewhat melt together (this is known as necking). Increasing height above the burner results in reduced soot primary particle growth rates (Xu et al., 1998), and agglomeration becomes the dominant particle dynamic mechanism (necking will no longer occur). When the particles are released into the environment, diffusion limited cluster aggregation (DLCA) can occur, resulting in aggregate

restructuring (Kim et al., 2006). The primary particle and agglomerate change are examined in the current study by the methods described below.

Section 4.2: Methods

The soot particles were created using a diffusion burner described in the instrumentation section. Methane (Airgas North Central, >93%) was used as the fuel and clean, dry lab air was the oxidizer. The gas flow rates were controlled with Rotameters (Cole Palmer), specifically assigned to each type of gas. The combustion process was contained within the burner housing described in the Section 1.3. The burner housing connected to the injection probe (also described in the Section 1.3). This probe served as the simulated leak into the simulated workplace environment, and was placed at the centerline of the wind tunnel during experimental trials (removed periodically for cleaning). The reconfigured ASHRAE 52.2-2007 Classified wind tunnel (Section 1.3) served as the simulated workplace environment as shown in Figure 4.2.1.

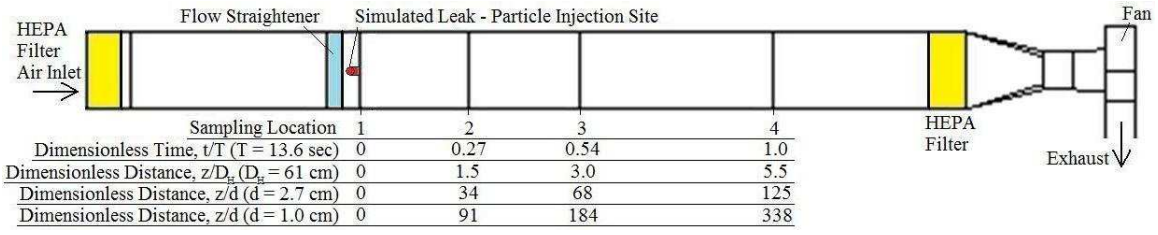

Sampling Location	1	2	3	4
Dimensionless Time, t/T (T = 13.6 sec)	0	0.27	0.54	1.0
Dimensionless Distance, z/D_s (D_s = 61 cm)	0	1.5	3.0	5.5
Dimensionless Distance, z/d (d = 2.7 cm)	0	34	68	125
Dimensionless Distance, z/d (d = 1.0 cm)	0	91	184	338

Figure 4.2.1: Reconfigured ASHRAE 52.2-2007 Classified wind tunnel.

Figure 3.3.9 depicts sampling locations relative to time (t) and distance (z) from the leak. The particle change is characterized by distance from the leak throughout the current study (although both time and distance from a leak are relevant in an industrial

setting). The dimensionless distances and times (shown in Figure 4.2.1) were calculated by several methods. The dimensionless time represents the time between the simulated leak and the sampling location divided by the time between the simulated leak and final sampling point (T = 13.6 seconds). This is assuming a constant background face velocity of 0.25 m/s. The dimensionless distances are defined relative to the leak diameters. These dimensionless values are represented in Figure 4.2.1. These non-dimensional terms are intended to simplify the analysis; however in the current study, not much is gained by analyzing the data in this manner. Therefore, this non-dimensional terminology may be more convenient during comparisons to future research.

Two background flow rates were used during initial experimentation: 200 ft^3/min (0.25 m/s face velocity) and 500 ft^3/min (0.64 m/s face velocity). The background flow rate showed no effect on particle distributions during these initial experiments. Therefore the background flow rate was maintained at a constant 200 ft^3/min (0.25 m/s) for the remainder of the current study. All analysis was conducted using data from the 0.25 m/s background face velocity.

Two different burner fuel/air flow rates and two different leak sizes were tested. The fuel-to-air ratio was set to either a Lean fuel/air mixture (195% theoretical air, φ = 0.51) or a Rich fuel/air mixture (49% theoretical air, φ = 2.05) for each trial. The equivalency ratio (φ) is the actual fuel-air ratio to the fuel-air ratio for complete combustion with the theoretical amount of air (Moran and Shapiro, 2004). The Lean fuel/air mixture consisted of 0.5 l/min of methane and 10 l/min of air. The Rich fuel/air mixture consisted of 2.0 l/min of methane and 10 l/min of air. These different fuel-to-air ratios produced two different particle distributions and different adiabatic flame

temperatures. The balanced combustion equations are listed below for the Rich and Lean fuel/air mixtures in terms of moles/hr. These equations do not take into account the formation of semi-volatile species, NO_x, or CO, which may be formed during this combustion process.

Rich: $5.36CH_4 + 5.22O_2 + 19.63N_2 \rightarrow 2.61CO_2 + 5.22H_2O + 2.75CH_4 + 19.63N_2$

Lean: $1.34CH_4 + 5.22O_2 + 19.63N_2 \rightarrow 1.34CO_2 + 2.68H_2O + 2.54O_2 + 19.63N_2$

The leak size was set to either 27 mm or 10 mm. The 27 mm leak size is the diameter of the injection probe. The 10 mm leak size is a 10 mm orifice installed on the outlet of the injection probe. This allowed the same injection probe to be used throughout the current study. However, the jet properties at the injection point changed when the orifice was used (the flow rate was constant for each leak size). The change in the jet must be taken into account when analyzing the difference in leak sizes. Dimensionless numbers (such as Re, Gr, Ri, and velocity ratio) were used to better characterize the leak.

Density and viscosities for air at normal conditions (NTP, T = 293 K and P = 101.3 kPa), exhaust gas conditions, and adiabatic flame temperature conditions, are shown in Table 4.2.1 (Moran and Shapiro, 2004; ET website). However changing between the 27 and 10 mm leak size caused a change in: the pressure within the combustion chamber, the leak velocity, and the Reynolds number (as well as the other previously mentioned dimensionless parameters). Tables 4.2.2, 4.2.3, and 4.2.4 outline the pressures, velocities, and Reynolds numbers for NTP, exhaust gas, and adiabatic flame temperatures. The adiabatic flame temperatures are shown in Table 4.2.1, as well

as the air properties used in the calculations. All parameters in Tables 4.2.2 - 4.2.4 were calculated using air due to the unknown composition of the exhaust gas.

Table 4.2.1: Measured exhaust gas temperatures at injection point and calculated adiabatic flame temperatures for Lean and Rich flames. Density and viscosity of air at NTP, exhaust, and adiabatic flame temperatures (P = 101.3 kPa).

		Temperature (K)	ρ (kg/m^3)	μ (kg/m-s)	ν (m^2/s)
	NTP	293	1.2	1.81E-05	1.51E-05
Exhaust	Rich	329	1.09	2.04E-05	1.86E-05
	Lean	317	1.16	2.01E-05	1.74E-05
Adiabatic Flame	Rich	2022	0.21	5.98E-05	2.91E-04
	Lean	1365	0.32	4.44E-05	1.39E-04

Table 4.2.2: Leak pressure drop, Reynolds number, and velocity for air at NTP.

		ΔP (atm)	ΔP (Pa)	Re	V (m/s)
Injection Probe	Rich	1.60E-06	0.16	625	0.35
	Lean	1.40E-06	0.14	547	0.31
Orifice	Rich	3.81E-08	3.86E-03	1688	2.55
	Lean	2.91E-08	2.95E-03	1477	2.23

Table 4.2.3: Leak pressure drop, Reynolds number, and velocity for air at exhaust temperatures (P = 101.3 kPa).

		ΔP (atm)	ΔP (Pa)	Re	V (m/s)
Injection Probe	Rich	1.80E-06	0.18	556	0.38
	Lean	1.56E-06	0.16	492	0.32
Orifice	Rich	3.47E-08	3.51E-03	1501	2.80
	Lean	2.81E-08	2.85E-03	1328	2.31

Table 4.2.4: Leak pressure drop, Reynolds number, and velocity for air at adiabatic flame temperatures (P = 101.3 kPa).

		ΔP (atm)	ΔP (Pa)	Re	V (m/s)
Injection Probe	Rich	5.28E-06	0.54	189	2.04
	Lean	3.43E-06	0.35	223	1.15
Orifice	Rich	6.52E-09	6.60E-04	511	14.87
	Lean	7.76E-09	7.86E-04	602	8.37

Tables 4.2.2 - 4.2.4 show the range of possible leak conditions in the current study. The highest Reynolds number occurs at NTP conditions. The lowest occurs at

adiabatic flame temperatures (listed in Table 4.2.1). However the exhaust conditions are of most interest, because these are the most likely conditions for the injection site. Further analysis will be conducted using values at exhaust conditions (Table 4.2.5). Since the specific products of combustion are unknown, all values were calculated for air.

Table 4.2.5: Air properties at exhaust temperatures for the Rich and Lean fuel/air mixtures.

	Rich	Lean
T (°C)	56	44
T (K)	329	317
ν (m^2/s)	1.86E-05	1.74E-05
μ (kg/m-s)	2.04E-05	2.01E-05
ρ (kg/m^3)	1.09	1.16
C_p (J/kg-K)	1008	1006
k (J/m-s-K)	0.0282	0.0274
β (1/K)	3.04	3.16
Pr	0.73	0.74

The Scanning Mobility Particle Sizer (SMPS Model 3034, TSI, Shoreview, MN) and the Nanoparticle Surface Area Monitor (NSAM Model Aerotrak 9000, TSI, Shoreview, MN) were used to measure particle number size distribution and lung deposited surface area (LDSA) concentration of the sampled aerosol, respectively. The Nanometer Aerosol Sizer (NAS Model 3089, TSI Shoreview, MN) was used to capture particles onto Lacey grids for analysis using a Transmission Electron Microscope (TEM, FEI Tecnai T12). The SMPS and NSAM were operated simultaneously. The NAS was used simultaneously with the NSAM, but only during few selected trials due to the time-intensive sampling and analysis procedures required when using the TEM. Primary particle sizes were measured using TEM images. Several primary particles were sized, an average size was determined for each condition sampled, and a 95% confidence interval

for each average primary particle size was calculated using the student's t-distribution. Sample calculations for this statistical analysis are located in Appendix K.

The injected aerosol could not be measured without diluting the sample flow by 100:1 with clean, dry lab air. This dilution lowered the particle concentration to within the measureable range for the SMPS. Diluting the flow also minimized additional particle dynamics (coagulation, diffusion losses, growth by condensation). Without this freezing affect, the particles would likely change within the sampling lines and not represent a true sample from within the wind tunnel. The dilution set is described in Section 3.5. This dilution was not typically required at locations downstream of the injection point since the wind tunnel flow provided an adequate amount of dilution air. A 10:1 dilution ratio was required for the highest particle concentrations at sampling locations downstream from the injection point. Again, this dilution air was supplied to the sampling line at the point of sampling to prevent any additional particle change within the sampling line. The measurement locations within the wind tunnel cross section are represented by the x- and y-axes as shown in Figure 4.2.2. The point of highest concentration was typically (0,23).

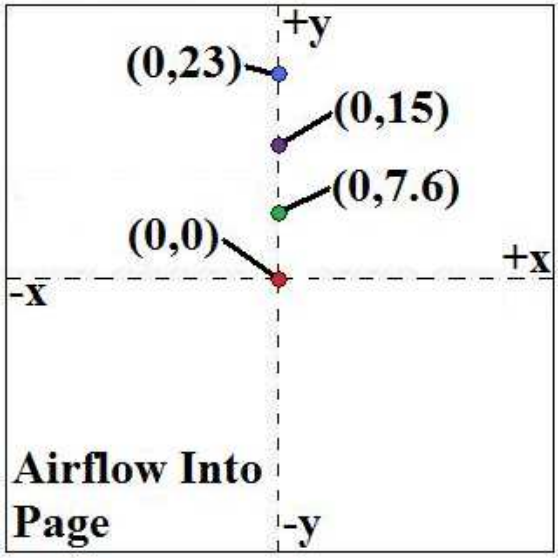

Figure 4.2.2: Sampling Locations within the cross-section of the wind tunnel. Centerline is y-axis. Injection probe outlet is located at position (0,0). All units are in cm.

Section 4.3: Results and Discussion

Section 4.3.1: Initial Soot Aerosol Properties

While monitoring particle size and concentration in bag filling areas of a carbon black production facility, Kuhlbusch et al. (2004) noted primary particle sizes ranging between 1 and 500 nm. The particles were commonly between 10 and 100 nm, rapidly aggregating due to high concentrations in the closed reaction area of the flame (Kuhlbusch et al., 2004). Holder et al. (2008) used a geometric mean particle size of 80 nm from an aerosol flame and 122 nm from diesel exhaust for combustion aerosol toxicity studies. The soot particles in the current study must be within range of the soot particle sizes reported in the literature.

The initial soot aerosol distributions are shown in Figure 4.3.1.1 for the Lean and Rich fuel/air mixtures. As shown in Figure 4.3.1.1, the different mixtures produced

different particle distributions, and different particle morphology. Figures 4.3.1.2 and 4.3.1.3 show TEM images for each fuel/air mixture at the injection point. The 100:1 dilution ratio was used to sample these particles using the NAS. A higher concentration could have been used to sample for a shorter duration; however using the 100:1 dilution ratio helps ensure the particles imaged with the TEM are the same as the particles sampled by the NSAM and SMPS.

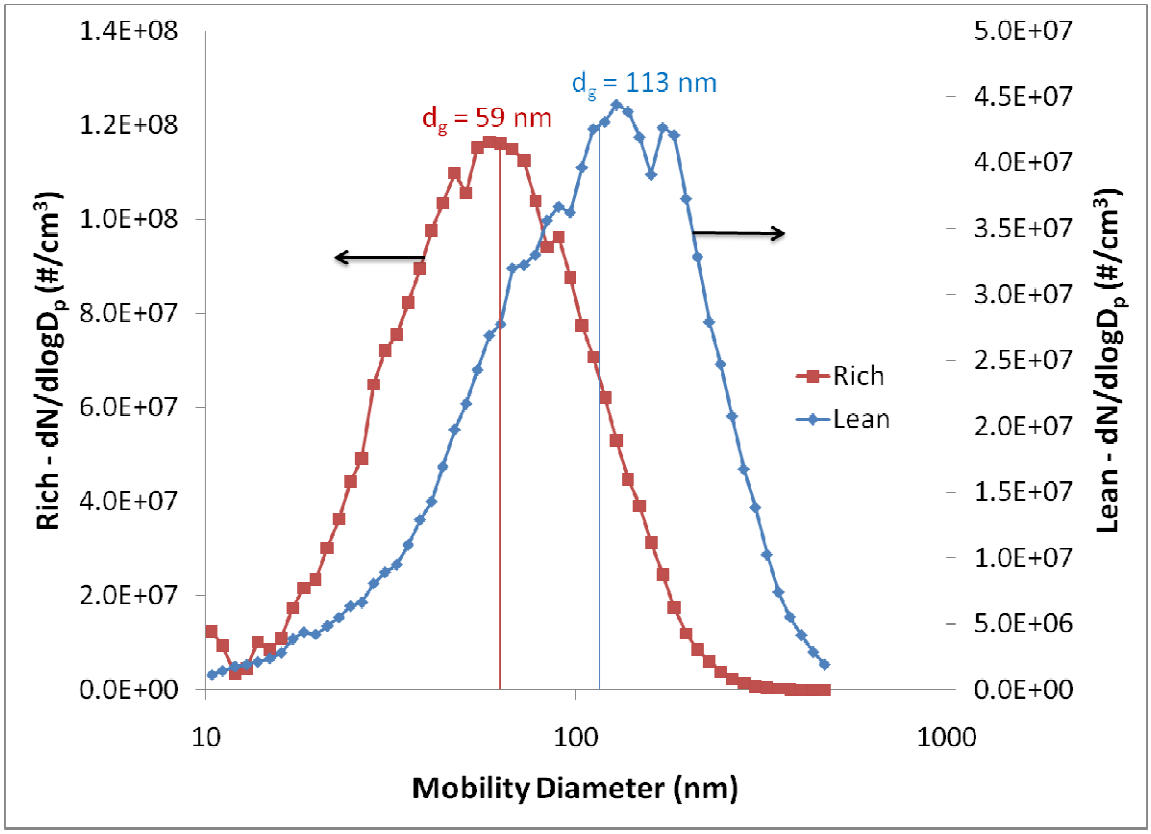

Figure 4.3.1.1: Injected soot aerosol distributions for Rich and Lean fuel/air mixtures.

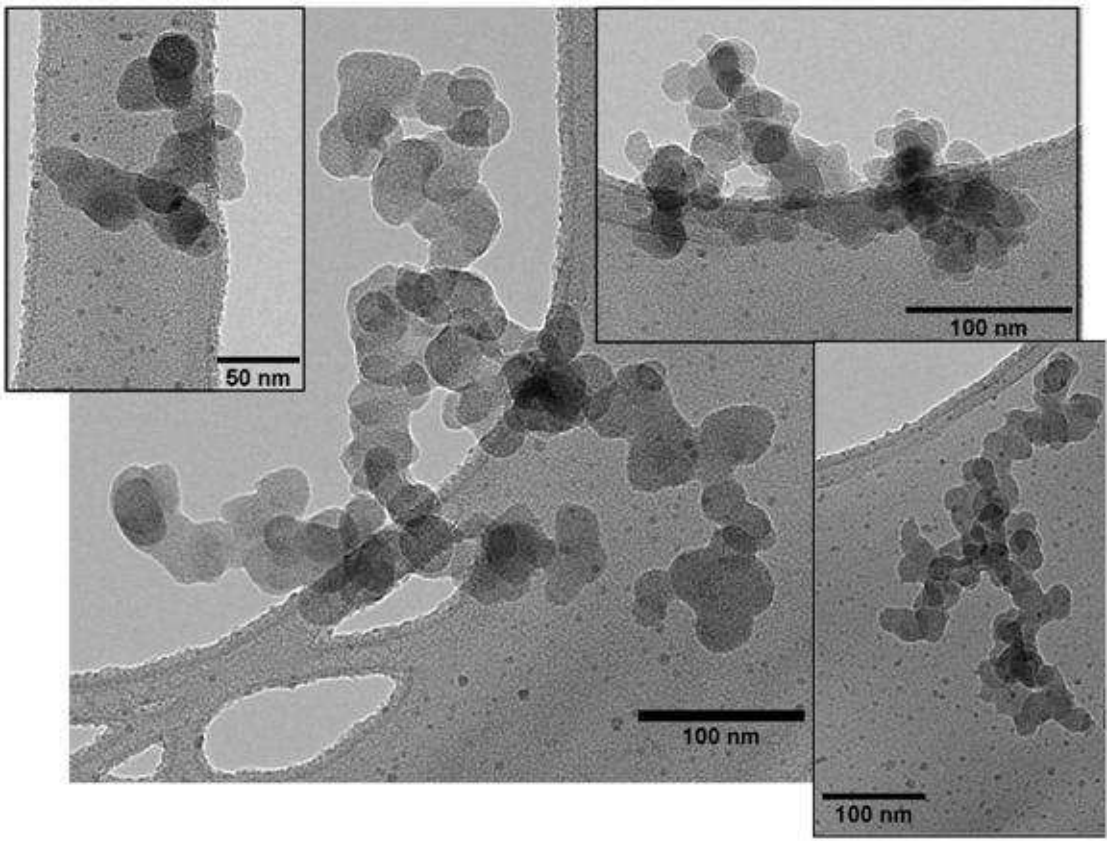

Figure 4.3.1.2: Injected soot aerosol morphology for the Lean fuel/air mixture.

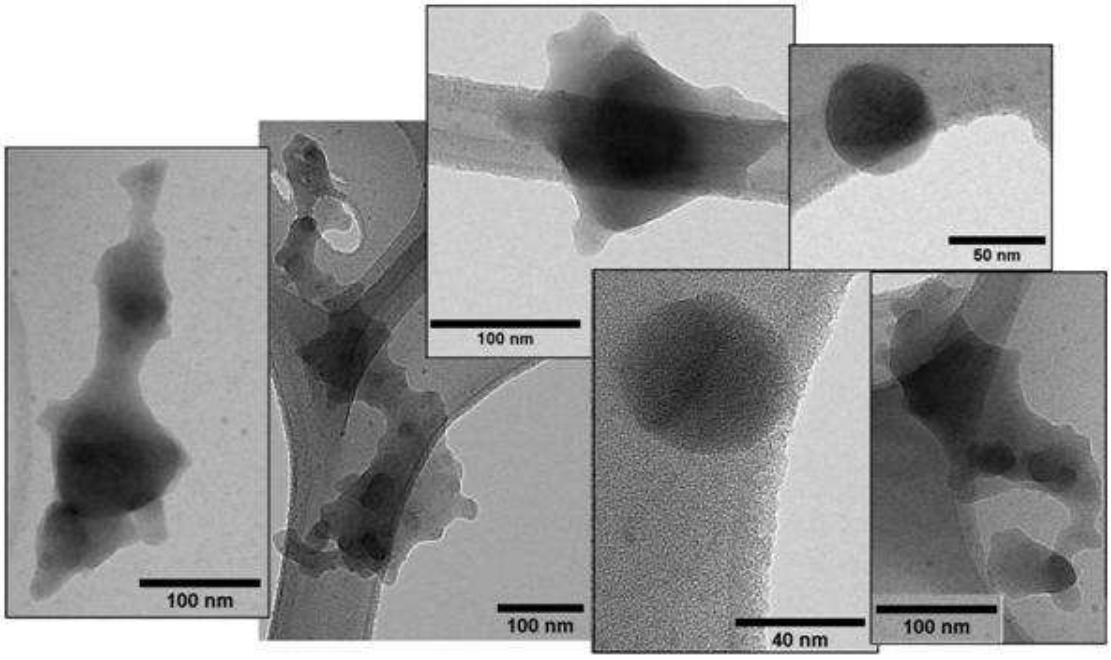

Figure 4.3.1.3: Injected soot aerosol morphology for the Rich fuel/air mixture.

The Soot (Lean fuel/air mixture) formed long, chain-type agglomerates, indicating the many small particles initially produced by the burner had agglomerated prior to the injection point. Chained and branched agglomerates with fractal-like morphology are typically the type of soot particle produced through combustion processes (Holder et al., 2008). The Soot (Rich fuel/air mixture) produced mostly singular spherical primary particles, with few agglomerates observed (more agglomerates are shown in Figure 4.3.1.3 than single primary particles to illustrate the variation in morphology). The agglomerates were also not chain-type, but sintered. This is nothing out of the ordinary, as rich flames and high load operating conditions for diesel engines have been found to produce different particles than their lean flame and low load diesel engine counterparts (DeFilippo and Maricq, 2008; Meyer and Ristovski, 2007). The basic soot particle formation process is described briefly below, and in more detail in Section 2.1.1.

Primary particle size was determined after gathering several TEM images of soot particles and measuring the primary particle size using computer software (ImageJ). Figure 4.3.1.4 shows examples of how this computer software was used by manually drawing circles around each reasonably identified primary particle. The height and width of each drawn circle were output by computer software. These were averaged for each labeled particle to obtain the diameter measurement. The primary particle size could have been qualitatively estimated from Figures 4.3.1.2 and 4.3.1.3 using the scale bar. However if a primary particle could be reasonably identified within the agglomerate, then it can be measured with much greater precision using the computer software.

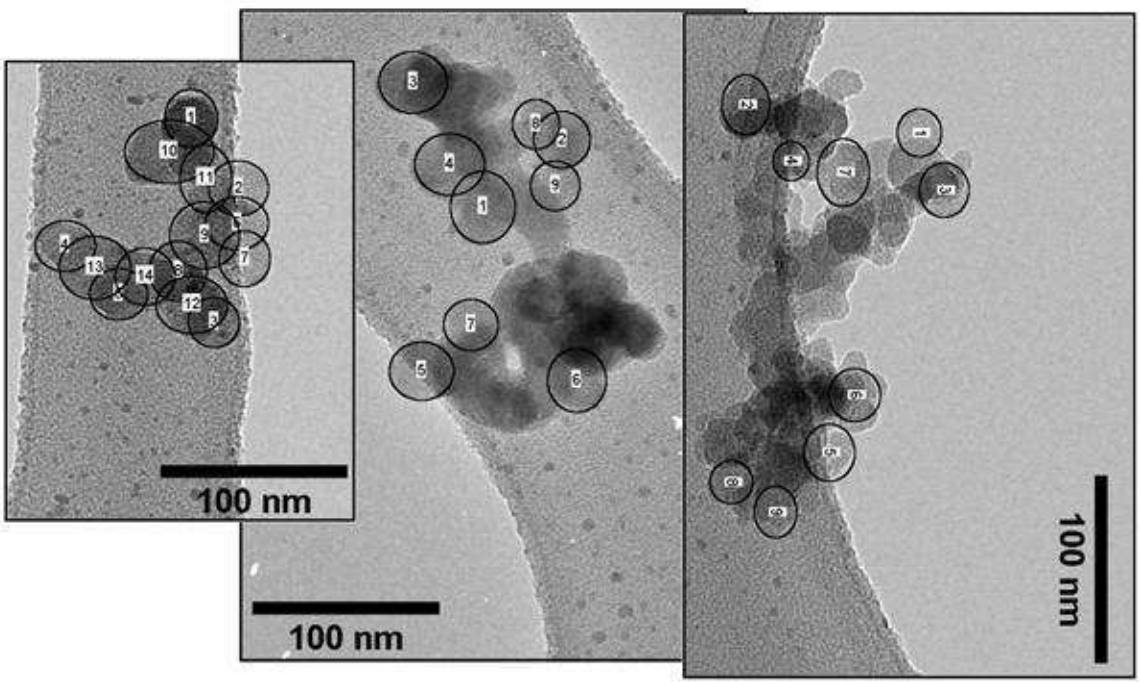

Figure 4.3.1.4: Soot primary particles identified within agglomerates using ImageJ.

Unfortunately the agglomerates produced using the Rich fuel/air mixture were much too sintered to reasonably identify any primary particles, so the primary particle sizes in the Rich fuel/air mixture were determined using single primary particles. The Lean fuel/air mixture produced primary particles of $d_{pp} = 30 \pm 2.0$ nm and the Rich fuel/air mixture produced primary particles of $d_{pp} = 56 \pm 4.9$ nm. So although the geometric mean particle size (determined by the SMPS) is larger for the Lean fuel/air mixture, the Rich fuel/air mixture produced a larger soot primary particle size.

The different fuel/air mixtures each produced a similar mode of particles, which only appears in the TEM images (these particles are below the SMPS size range used in the current study). The size of these smaller particles was determined to be $d_{sp} = 6.0 \pm 0.5$ nm for the Lean fuel/air mixture and $d_{sp} = 6.9 \pm 0.4$ nm for the Rich fuel/air mixture (from TEM images). These particle sizes are not significantly different, and these TEM-

determined sizes are likely an overestimate of particle size, because the smallest of these particles could not be reasonably identified and measured. The TEM image resolution decreases for smaller particles, hence the largest of the small particles composed the majority of particles measured in this TEM analysis.

These smaller particles have been characterized by other researchers (di Stasio, 2001; Maricq, 2006). Prior to the formation of agglomerates, soot size distributions typically consist of a mixture of two main particle sizes, resulting in a bimodal particle distribution (Maricq, 2006). di Stasio (2001) showed evidence of three distinct size scales for nanoparticles including primary particles (20-50 nm), sub-primary particles (6-9 nm), and graphitic nuclei (0.5-2 nm) surrounded by transparent amorphous carbon shells (4 nm). These sub-primary particles make up primary particles, following rapid coagulation and held together by condensed matter (Mitchell et al., 2009). Maricq (2006) observed these sub-primary particles at various heights above the burner using a Nano-DMA setup.

Section 4.3.2: Mapping Experiments

Experiments were conducted to map the path of the injected aerosol throughout the wind tunnel cross-section. The total aerosol concentration was measured at 16 different locations within the wind tunnel cross section at 0.9 m, 1.8 m, and 3.4 m downstream of the injection site for two test conditions: Lean fuel/air mixture, 27 mm leak (Lean/27) and Rich fuel/air mixture, 10 mm leak (Rich/10). The buoyancy of the plume and turbulence within the wind tunnel caused the location of the highest particle concentration change throughout the wind tunnel cross-section. Even though this highest particle concentration position was not always at (0,23), the measurement at position

(0,23) is a good representation of the highest particle concentration. The (0,23) measurement position always had the same geometric mean particle size, the same geometric standard deviation, and in most cases, a similar concentration (never off by more than a factor of 3) as the highest particle concentration measurement. These mapping experiments are outlined in Appendix F.

Section 4.3.3: Soot Aerosol Properties at Locations Downstream of Leak

The initial soot particle concentration was measured at the centerline of the wind tunnel, directly in front of the injection probe. However the highest particle concentrations downstream of the injection probe were not at the centerline of the wind tunnel. The combustion aerosol was much hotter than the background air, causing the plume of particles to rise due to buoyancy forces. Mapping experiments were carried out to determine how the particles dispersed throughout the wind tunnel, discussed in Appendix F.

Measurements were taken along the centerline of the wind tunnel as depicted in Figure 4.2.2 to determine how the particle properties change downstream of the leak. The results at each measurement location (0.9 m, 1.8 m, and 3.4 m downstream) for each experimental trial condition: leak size (27 or 10 mm) and fuel/air mixture (Lean or Rich) are shown in Appendix F. These figures for each measurement location in Figure 4.2.1 show the average soot distribution for each sampling location depicted in Figure 4.2.2, and reiterate the results of the mapping experiments. For each experimental trial, the sampling probe was set at each measurement location for three successive samples. These measurements were repeated at least once during an experimental trial. Each

experimental trial was repeated (at least once) at a later date, to ensure consistency. At first, the experimental trials were conducted more than 3 times downstream of the leak. However the consistency of the results indicated such measures were not necessary and the number of trials was decreased. If a repeated experimental trial was not consistent with the first trial, then the condition was tested a third time. Consistency was determined by comparing average geometric mean diameters and geometric standard deviations between trials.

The distribution with the highest particle concentration is the best representation of the particles within the plume. Therefore this distribution was used for statistical analysis and comparisons between conditions (leak sizes and fuel/air mixtures). This representative distribution is an average of the measurements throughout the experimental trials at the point of highest concentration, which was measured up to 24 times for each condition over the course of two experimental trials (trials randomly conducted on separate days). Normalized distributions (normalized representative distributions) for each leak size and fuel/air mixture are shown as Figures 4.3.3.1 – 4.3.3.4. The raw data for each figure is located in Appendix F.

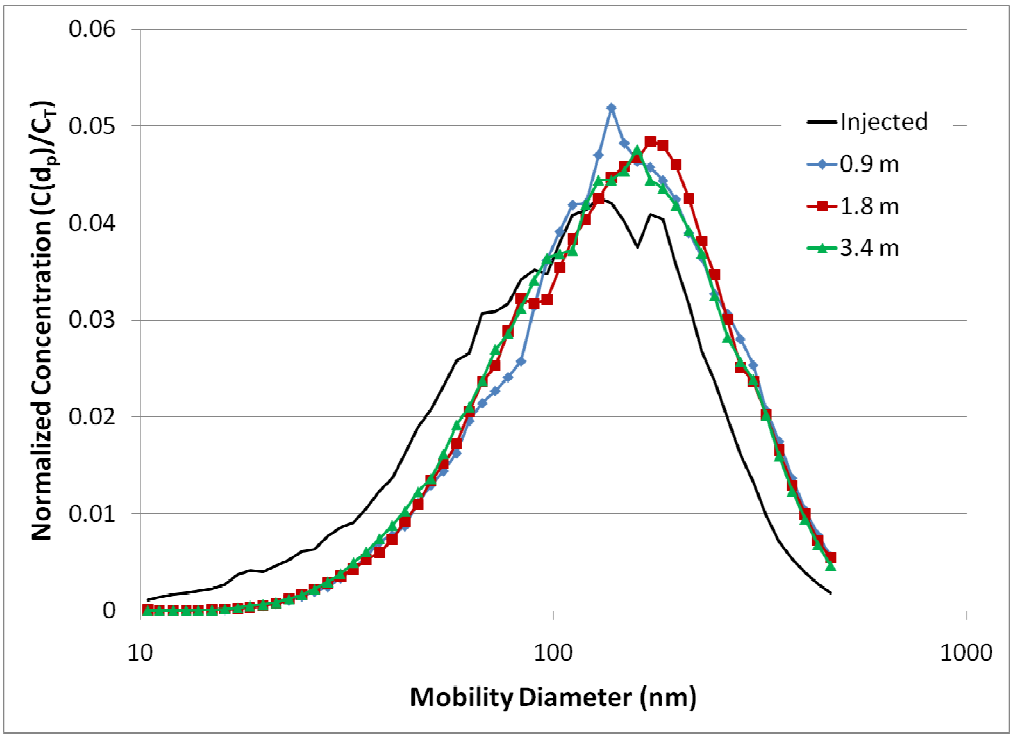

Figure 4.3.3.1: Lean fuel/air mixture and 27 mm leak normalized particle distributions for each measurement location.

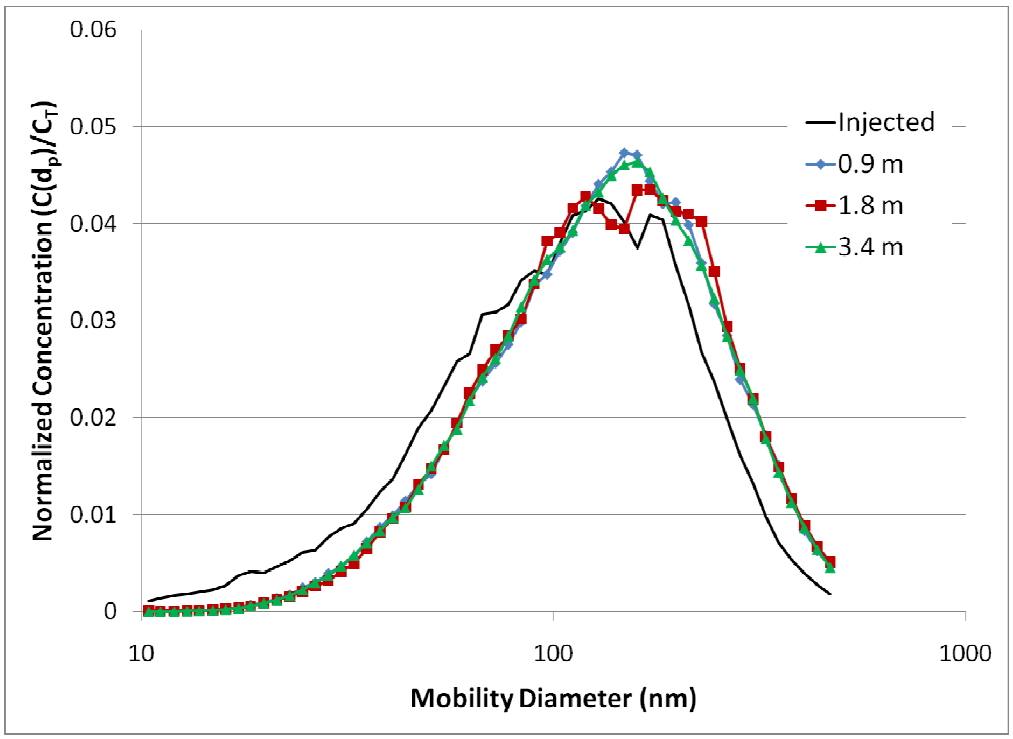

Figure 4.3.3.2: Lean fuel/air mixture and 10 mm leak normalized particle distributions for each measurement location.

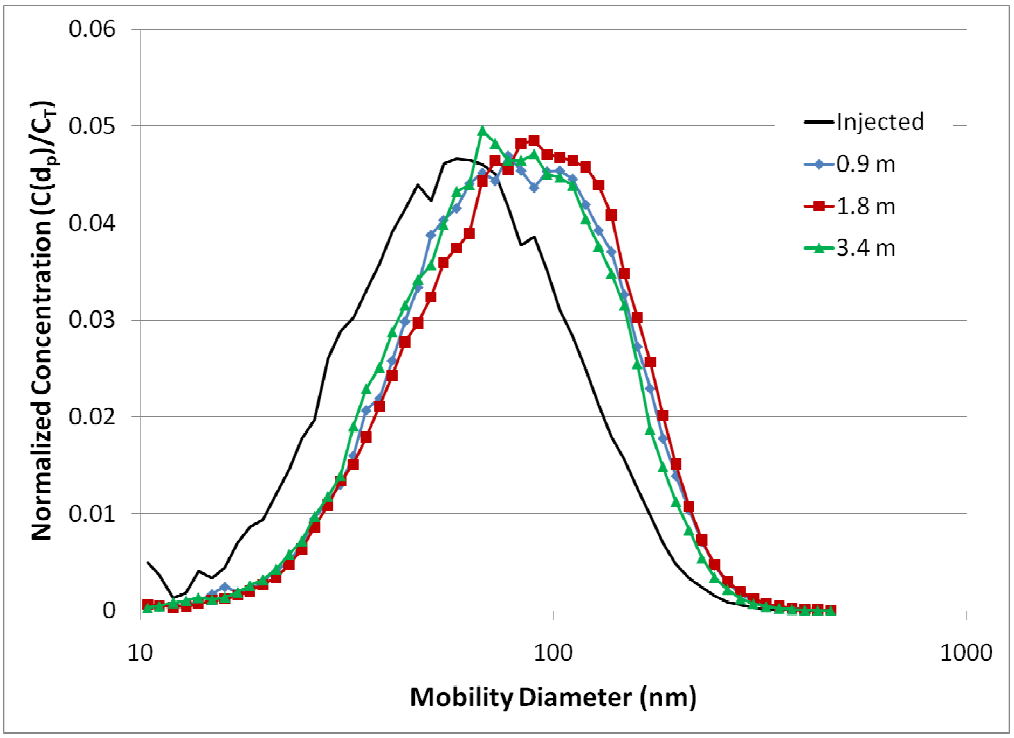

Figure 4.3.3.3: Rich fuel/air mixture and 27 mm leak normalized particle distributions for each measurement location.

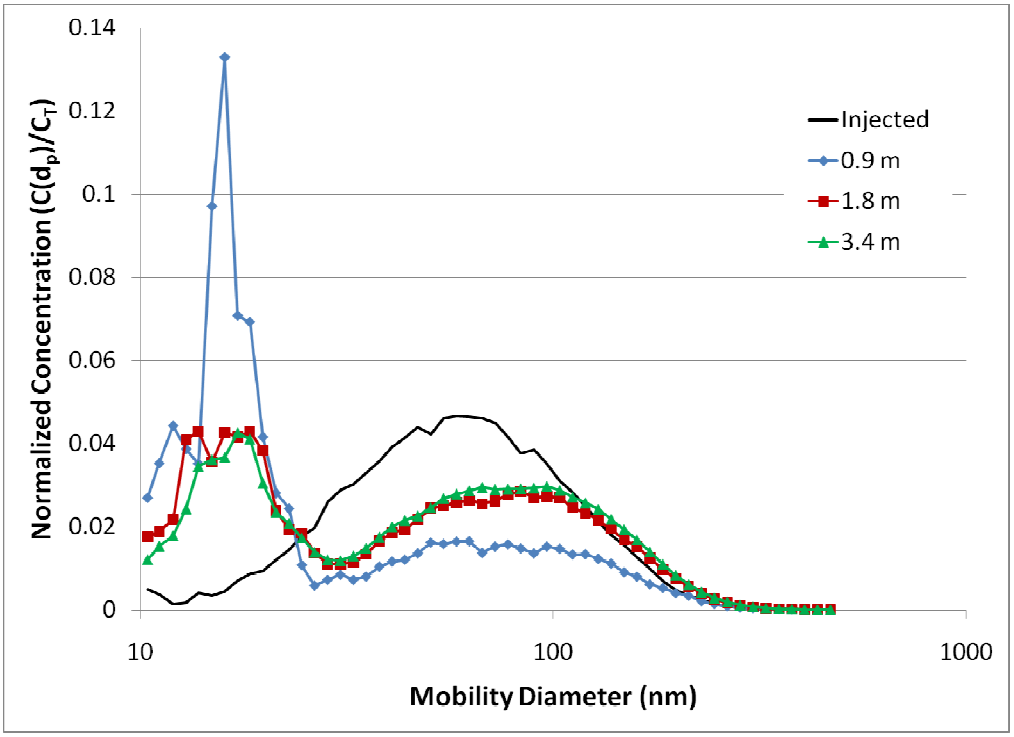

Figure 4.3.3.4: Rich fuel/air mixture and 10 mm leak normalized particle distributions for each measurement location.

Normalized distributions account for inconsistencies in particle concentration, potentially caused by turbulent mixing within the wind tunnel. Figures 4.3.3.1 and 4.3.3.2 show the aerosol properties of the Soot (Lean fuel/air mixture) with a 27 mm and 10 mm leak, respectively. Each figure shows no significant difference between normalized particle distributions at 0.9 m, 1.8 m, and 3.4 m downstream. Therefore when using the Lean fuel/air mixture and either leak size, the particle distribution does not change after 0.9 m downstream from the leak. This will be further examined later in this section to determine if this change is statistically significant.

Figures 4.3.3.3 and 4.3.3.4 show the aerosol properties of the Soot (Rich fuel/air mixture) with a 27 mm and 10 mm leak, respectively. Figure 4.3.3.4 shows much different results than anything previously examined and will be discussed later in this section. Figure 4.3.3.3 indicates little difference between the particle distributions at 0.9 m, 1.8 m, and 3.4 m downstream. Therefore, when using the Rich fuel/air mixture and 27 mm leak size, the particle distribution does not change after 0.9 m downstream from the leak.

The particle concentration changes as the particles travel downstream, but the concentrations are not always decreasing (Table 4.3.3.1). At first, particle concentration should decrease due to diffusion (and possibly coagulation). This concentration decrease only occurred between the injection point and 0.9 m downstream. After 0.9 m downstream, the total particle concentration should decrease steadily throughout the wind tunnel due to particle deposition on the walls of the tunnel. Particle deposition on the walls does occur (noticed during visual inspection of the wind tunnel interior), however for each condition, the particle concentration increased between 0.9 m and 3.4 m

downstream. The burner output was not monitored at the injection point during each trial (the fuel/air mixture fed to the burner was set and monitored). Therefore slight day-to-day variations in burner particle output could have affected the downstream concentrations; however turbulent mixing is the more likely cause of this apparent increase. The effects of turbulent mixing are described in Appendix F.

Table 4.3.3.1: Total particle concentrations of representative distribution for each fuel/air mixture and leak size at each measurement Location.

	Lean		Rich	
	27 mm	10 mm	27 mm	10 mm
0 m downstream	3.3E+07		7.8E+07	
0.9 m downstream	1.2E+05	1.7E+05	3.3E+05	5.5E+05
1.8 m downstream	2.7E+05	1.4E+05	6.1E+05	5.2E+05
3.4 m downstream	3.0E+05	2.5E+05	5.2E+05	6.4E+05

Table 4.3.3.2 shows the geometric mean particle size, of the representative distribution, for each leak size and fuel/air mixture. Since several trials were conducted, a statistical analysis may be conducted to determine if the geometric mean particle sizes are statistically different at measurement locations downstream of the leak. The differences in geometric mean particle sizes were analyzed using a t-test of unequal variances with degrees of freedom calculated using Welch's method. A statistically significant difference was determined between the injection point and each downstream location at a confidence level of 95% for each condition. For all fuel/air mixture and leak size combinations, there is not a statistically significant difference between the geometric mean particle size at 0.9 m, 1.8 m, and 3.4 m downstream. Therefore, after 0.9 m downstream, there is not a statistically significant change in geometric mean particle size

for any condition. The specific details of this statistical analysis can be found in Appendix K.

Table 4.3.3.2: Geometric mean particle size for each fuel/air mixture and leak size at each measurement Location.

	Lean		Rich	
	27 mm	10 mm	27 mm	10 mm
0 m downstream	113		59	
0.9 m downstream	137	129	77	29
1.8 m downstream	136	130	80	43
3.4 m downstream	132	129	75	45

Figure 4.3.3.4 shows the aerosol properties of the Soot (Rich fuel/air mixture) with a 10 mm leak. A bi-modal particle distribution formed downstream of the leak, which does not appear under any other previously examined condition. Each mode of the distribution was maintained throughout the duration of the wind tunnel, although there is a slight change between 0.9 m and 1.8 m downstream. There is no change between 1.8 m and 3.4 m downstream. Therefore the aerosol properties continue to change after 0.9 m downstream from the leak (for the Rich fuel/air mixture and 10 mm leak size condition only), but do not continue to change after 1.8 m downstream of the leak.

Figure 4.3.3.5 and 4.3.3.6 show the normalized distributions for each mode normalized separately. With a multi-modal distribution, the modes must be treated as separate distributions. The modes were split by particle size; all data below 26 nm was counted as the first mode with data above 26 nm counted as the second mode. Total particle concentration was determined for each mode and the concentration for each particle size was normalized according the corresponding total particle concentration.

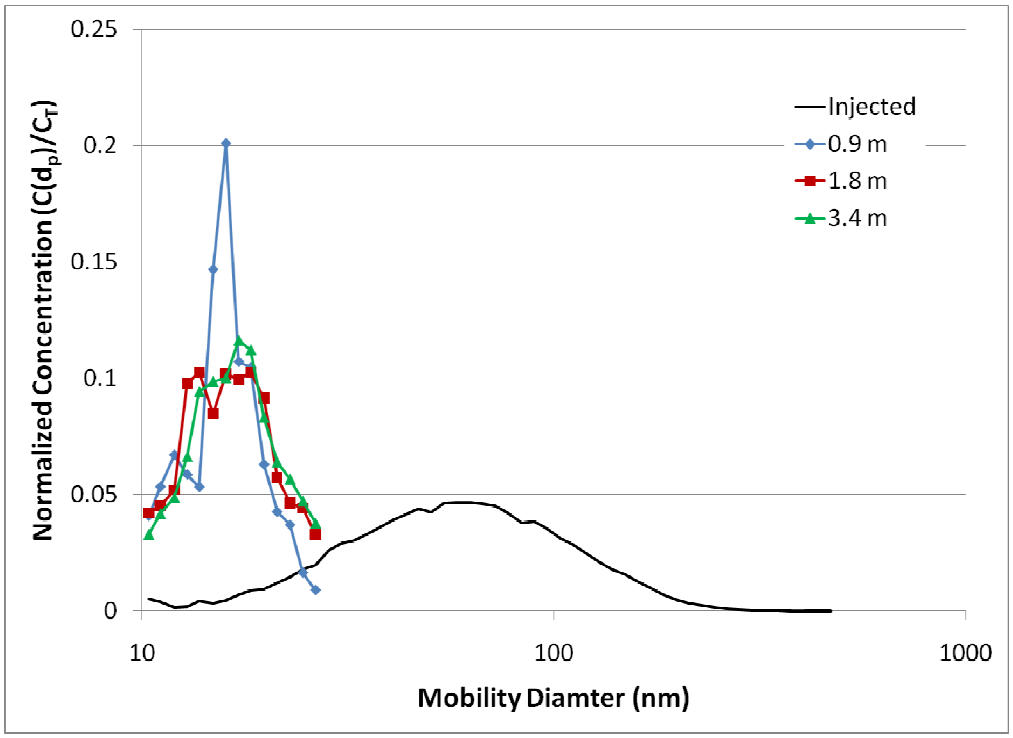

Figure 4.3.3.5: Rich fuel/air mixture and 10 mm leak with 1st mode separately normalized for each measurement location.

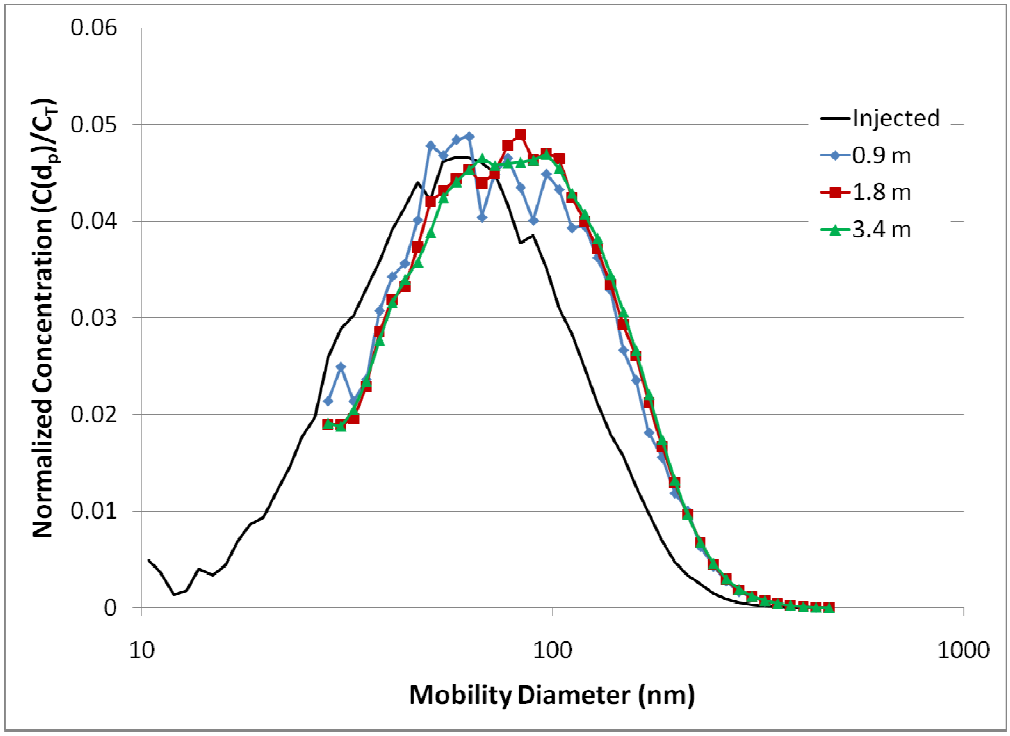

Figure 4.3.3.6: Rich fuel/air mixture and 10 mm leak with 2nd mode separately normalized for each measurement location.

From this new figure (Figure 4.3.3.6), the larger particle mode does not change after 0.9 m downstream. Figure F.19 located in the appendix, shows this second mode normalized distributions match the normalized distributions from Figure 4.3.3.3. Therefore changing the leak size does not affect the larger particles, and these larger particles do not change after 0.9 m downstream from the leak. The first mode of particles does change after 0.9 m downstream of the leak, which explains why the overall aerosol properties change.

A bi-modal distribution was noticed at the injection point (in TEM imaging); however the first mode was too small to be measured by the SMPS. A SMPS-measured bi-modal distribution occurred when using the Rich fuel/air mixture and 10 mm leak size. Therefore this combination of fuel/air mixture and leak size caused a reaction the other fuel/air mixture and leak size combinations could not. Two comparisons are immediately available to determine the cause of this occurrence: 10 mm leak size - Lean versus Rich fuel/air mixture and Rich fuel/air mixture - 27 mm versus 10 mm leak size.

The difference between the Lean and Rich fuel/air mixture is simple, amount of fuel. In the Rich fuel/air flame there is more fuel and more combustion, which leads to more combustion vapors. There should also be some left over, non-combusted vaporized fuel (methane). Therefore there is a higher concentration of combustion (and fuel) vapor in the Rich fuel/air combustion exhaust, compared to the Lean fuel/air flame, which burned with excess air. Unburned fuel and high hydrocarbon vapor content can lead to semi-volatile particle formation (Meyer and Ristovski, 2007; Ristimaki et al., 2007; Ronkko et al., 2007). This phenomenon has been noticed in diesel exhaust studies.

Diesel exhaust has been studied thoroughly over the past several years as emission standards become stricter. The standard for sampling diesel exhaust outlines the use of a wind tunnel with background dilution flow (~20:1) (Maricq, 2007b). The diesel engine exhaust is vented into this wind tunnel and sampled at more than 10 tunnel diameters downstream of the exhaust entrance (Maricq, 2007b). A bimodal distribution is typically noticed during diesel exhaust measurement, consisting of nucleation and accumulation modes (DeFilippo and Maricq, 2008; Kittelson et al., 2006; Ronkko et al., 2007). The nucleation mode particles consist of volatile material condensed onto a solid, non-volatile core particle (Meyer and Ristovski, 2007; Ronkko et al., 2007). The first mode particles of the Rich fuel/air mixture and 10 mm leak size of the current study are likely similar.

The leak size must also play a role in creating this SMPS-measured first mode of particles. Changing the leak size changes the jet properties and a number of descriptive variables (Re, Ri, Gr, and velocity ratio), listed in Table 4.3.3.3. Additionally, since the orifice has a sharp edge (90°), the vena contracta must be taken into account when changing from the 27 mm leak to the 10 mm leak. Typical values for the contraction coefficient (C_c = Area at vena contracta/Area of orifice) range from 0.62 to 1.0 for single-phase flow through a sharp-edged orifice (Shannak et al., 1999). Values for the high and low end of C_c are presented in Table 4.3.3.3.

Table 4.3.3.3: Dimensionless numbers (Re, Ri, Gr, velocity ratio) and pressure drops for Rich and Lean flames accounting for vena contracta. Values calculated for air at Rich and Lean exhaust gas temperatures.

	Injection Probe		Orifice (C_c = 1.0)		Orifice (C_c = 0.62)	
	Rich	Lean	Rich	Lean	Rich	Lean
ΔP (atm)	1.80E-06	1.56E-06	3.47E-08	2.81E-08	9.12E-08	7.39E-08
ΔP (Pa)	0.18	0.16	3.51E-03	2.85E-03	9.24E-03	7.49E-03
Re	556	492	1501	1328	1906	1686
V_{jet} (m/s)	0.38	0.32	2.80	2.31	3.55	2.94
Gr	6.08E+07	4.83E+07	3.09E+06	2.45E+06	1.51E+06	1.20E+06
Ri	197	200	1.37	1.39	0.42	0.42
V_{bulk}/V_{jet}	0.65	0.79	0.09	0.11	0.07	0.09

The Reynolds number (Re), Grashof number (Gr), and Richardson number (Ri) are each dependent upon diameter and there are minor differences between the maximum and minimum contraction coefficient values for the orifice. The Re, Gr, and velocity ratio do not significantly change between the injection probe and orifice conditions; however the change in Richardson number is significant. The Richardson number represents the ratio of buoyancy to inertia. In the current study, it was determined by: $Ri = Gr/Re^2$, which is equivalent to Ri = Buoyant/Inertial Forces. This change in Richardson number is responsible for formation of the bi-modal particle distribution when using the Rich fuel/air mixture and 10 mm leak size.

Wehner et al. (2010) characterized the formation of new ultrafine particles in the atmosphere at sub-critical Ri values (Ri < 0.25). This phenomenon was made possible by the presence of precursor gases (pollution), caused by hydrocarbon combustion (Wehner et al., 2010). Precursor gases in the presence of turbulent mixing causes local supersaturation and the formation of new ultrafine particles (Wehner et al., 2010). Other

authors studying Beijing (Wu et al., 2007) and Mexico City (Dunn et al., 2004) have noticed new ultrafine particle formation in these areas of high pollution as well.

Under the assumptions of the current study, the Richardson number never decreases below the critical value of 0.25 (defined by Wehner et al., 2010), though critical Richardson numbers (Ri_c) between 0.2 and 1.0 have been suggested (AMS glossary). In the current study, there is a high concentration of precursor gases within the exhaust of the Rich fuel/air mixture due to unburned fuel. When using the 27 mm leak and Rich fuel/air mixture (Ri = 197), dilution occurs before the exhaust vapor cools into a supersaturated vapor. When using the 10 mm leak and Rich flame (Ri = 0.42), the cooling takes place before dilution can occur, and a supersaturated vapor is formed, leading to the formation of new ultrafine particles. This is all able to happen very quickly, and therefore the growth of these ultrafine particles cannot be observed under the current experimental setup. New particle formation is possible; however particle growth seems more likely due to the high concentration of "sub-primary" particles at the injection point.

Figure 4.3.1.3 shows plenty of sub-primary particles with a mean particle size of $d_{sp} = 6.89 \pm 0.41$ nm for the Rich mixture. These particles are observed in abundance in Figure 4.3.1.3 and would provide an excellent start for heterogeneous nucleation. Supersaturated combustion gases can condense on the surface of these particles causing growth as the smaller mode particles are formed. However these newly formed particles are not noticed under TEM imaging, as shown in Figure 4.3.3.7, because only "solid" particles can be observed under TEM (non-Cryo TEM). When combustion vapors nucleate, "semi-volatile" particles are formed (DeFilippo and Maricq, 2008; Onasch et al., 2009). In diesel engines, combustion vapors include sulfates, organic components,

and unburned fuel or lubricating oil (Meyer and Ristovski, 2007; Onasch et al., 2009; Ristimaki et al., 2007), although hydrocarbon compounds from unburned fuel comprise most of the particle mass (Tobias et al., 2001). Dilution conditions (dilution ratio and residence time), temperature, and humidity can strongly affect semi-volatile particle formation (Meyer and Ristovski, 2007). High saturation ratios (high concentrations of vapor) cause an increase in small particle growth (Ristimaki et al., 2007; Ronkko et al., 2007); however these particles are not very stable (Meyer and Ristovski, 2007) and evaporate under low pressure or high temperature conditions.

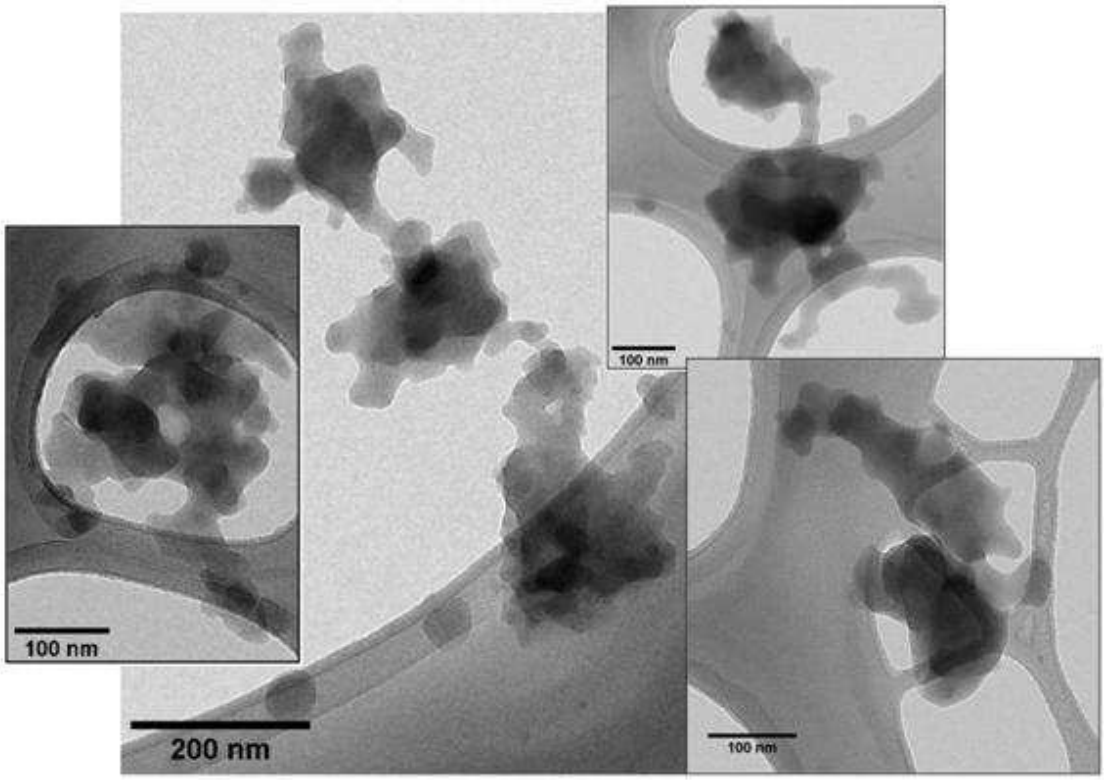

Figure 4.3.3.7: TEM images at 3.4 m downstream for Rich flame, 27 mm leak.

The TEM is held at a very low pressure and the electron beam within the TEM is high energy (high temperature). Such an environment would cause semi-volatile particles to evaporate (Meyer and Ristovski, 2007), which is why these particles were detected by

the SMPS, yet not apparent under TEM analysis. Further experiments would need to be conducted in order to remove the first mode of the bi-modal distribution (10 mm leak and Rich fuel/air mixture); hence proving these particles are truly semi-volatile. Ronkko et al. (2007) conducted experiments to remove the volatile components of the semi-volatile particles using a thermodenuder while sampling the exhaust of a heavy-duty diesel vehicle. Once the volatile material was removed, a bi-modal distribution was still apparent with $d_g < 9$ nm for the first mode and $d_g = 37\text{-}47$ nm for the second mode (Ronkko et al., 2007).

Semi-volatile particles formed from combustion vapors have health relevance other than being small enough to penetrate into the deep regions of the lung and deposit with a high efficiency. Holder et al. (2008) noted gas phase and semi-volatile species as a mixture with combustion particles during toxicity studies. They concluded the overall toxicity may be affected, as these semi-volatile species can be present as both a gas and absorbed to the particle (Holder et al., 2008). Oxidative stress in living cells can be caused by the volatile fraction of diesel particulate matter (Koike and Kobayashi, 2005). Soot composition should be known in order to accurately evaluate potential adverse health effects (Ristimaki et al., 2007) as solid and semi-volatile particles have different implications for sampling, atmospheric fate, and health effects (Maricq, 2007b).

Section 4.3.4: TEM Image Analysis Downstream of Leak

The Lean fuel/air flame produced a high concentration of agglomerates and sub-primary particles (at the injection point). There were no single primary particles injected when using the Lean fuel/air mixture. The Rich fuel/air mixture produced mostly single

primary particles (at the injection point); along with an abundance of sub-primary particles and few highly sintered agglomerates. The SMPS-measured distributions for the Lean and Rich fuel/air mixtures increased in geometric mean particle size after being injected into the wind tunnel, although this was not clear through TEM analysis. TEM images from 3.4 m downstream are compared to the injection point to determine how the particles have changed after the injection point. TEM images for the Lean and Rich fuel/air mixture particles at 3.4 m downstream are shown in Figures 4.3.3.6 and 4.3.4.1.

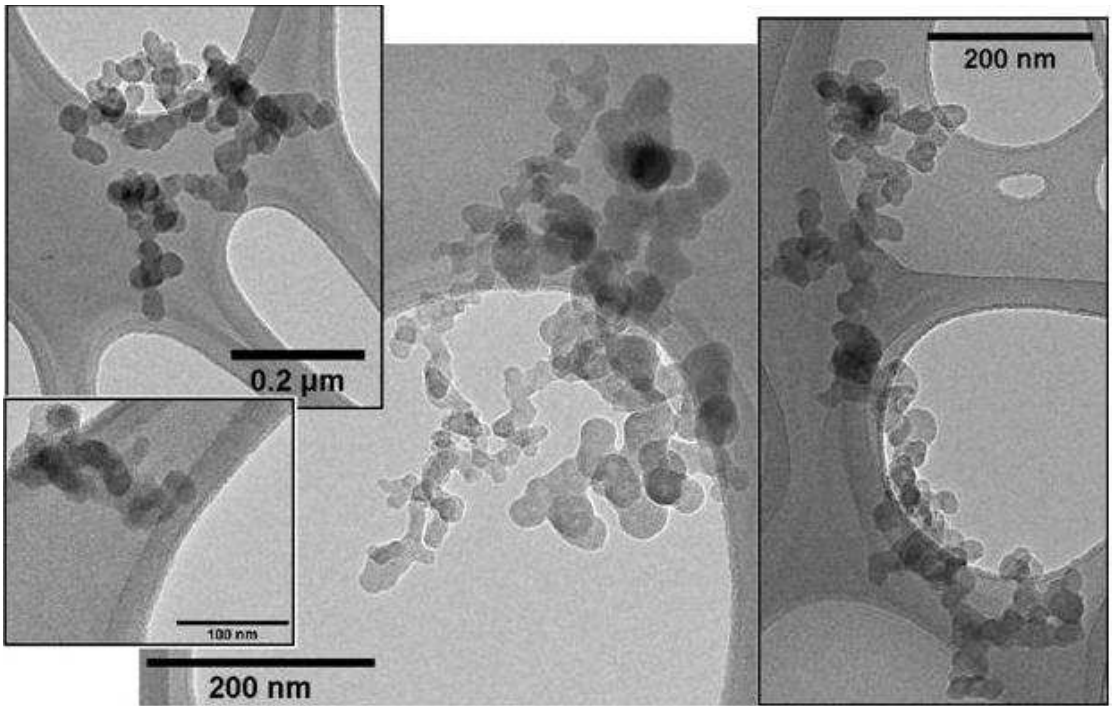

Figure 4.3.4.1: TEM images at 3.4 m downstream for Lean flame, 27 mm leak.

The sub-primary particles noticed in TEM images at the injection point are no longer apparent as single, non-agglomerated particles at 3.4 m downstream. In some instances, sub-primary particles seem to appear within agglomerates downstream of the injection point, but the image resolution is not high enough to draw a confident

conclusion. Sub-primary particle attachment to the agglomerates could have caused the SMPS-measured geometric mean particle size to increase between the injection point and downstream measurement locations. The nucleation of combustion vapors may have also influenced the final particle size. Particle cooling and internal particle restructuring could have potentially affected the size of the primary particles within the agglomerate as well. The agglomerates may have coagulated together, causing the size distribution shift, but this is unlikely due to the low particle concentrations throughout the wind tunnel.

The primary particle size at 3.4 m downstream was determined to be $d_{pp} = 34 \pm 1.4$ nm (compared to $d_{pp} = 30 \pm 2.0$ nm at the injection point) for the Lean fuel/air mixture. Therefore there is a statistically significant difference between the primary particle size at the injection point and 3.4 m downstream for the Lean fuel/air mixture. This indicates the agglomerates within the air flow were not coagulating together to form larger particles, but instead the primary particles within the agglomerates were growing. This primary particle growth may have resulted in the larger particles of the downstream SMPS-measured particle distributions.

The primary particle size at 3.4 m downstream was determined to be $d_{pp} = 47 \pm 9.2$ nm for the Rich fuel/air mixture. Therefore there is not a statistically significant difference between the primary particle size of the Soot (Rich fuel/air mixture) at the injection point and 3.4 m downstream. However, the Rich fuel/air flame particles altered morphology between the injection point and 3.4 m downstream. Agglomerates of the injected particles were observed downstream of the Rich fuel/air flame. These were much more apparent (as opposed to the Lean flame) because the Rich fuel/air flame formed mostly single primary particles at the injection point. This agglomeration may have

caused the increase in the SMPS-measured geometric mean particle size; however this is strictly a qualitative observation. Combustion vapor nucleation, particle cooling, and internal restructuring are also potential causes of the shift. Theories of particle growth by coagulation and nucleation are examined in Section 6.

Section 4.3.5: NSAM/SMPS Ratio for Soot

The NSAM was operated simultaneously with the SMPS, measuring the Alveolar Lung Deposited Surface Area (LDSA) concentration (concentration of particulate surface area deposited in the Alveolar region of the lung for an average worker based on a model from ICRP publication 66). The NSAM results may be used to determine a ratio of surface area per particle. This ratio can be used to determine if the particles are growing through any method of adding surface area (coagulation or nucleation). The NSAM measured lung deposited surface area was plotted against the corresponding SMPS measurement of total particle number concentration for each trial. These plots revealed linear correlations, determined by fitting a regression curve to the plotted data. A 95% confidence interval was also calculated for each regression fit and is plotted as error bars (which include instrumentation bias determined in the feasibility study) in Figure 4.3.5.1. Figure 4.3.5.1 shows this surface area per particle value for each condition at each measurement location. The plots for each location are located in Appendix F.

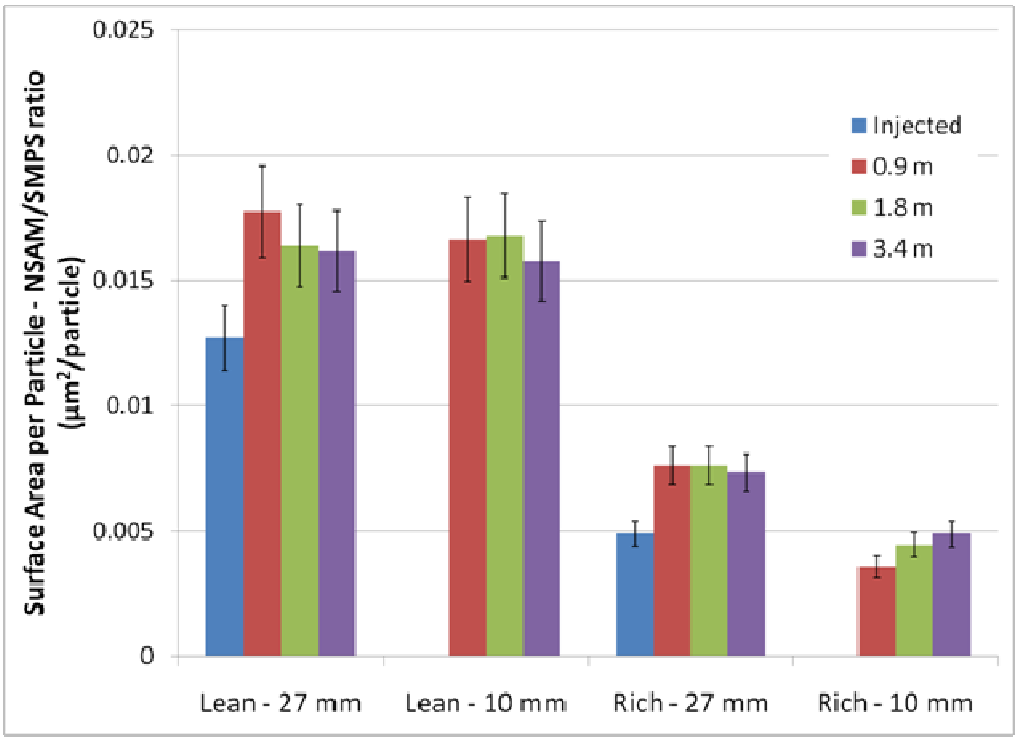

Figure 4.3.5.1: NSAM/SMPS ratio (µm^2/particle) for each Location and each condition. Error bars obtained through regression analysis with 95% confidence interval.

The Lean and Rich fuel/air mixtures begin with different particle distributions and morphologies, as shown in Figures 4.3.1.1 - 4.3.1.3. Figure 4.3.5.1 reiterates the initial Lean and Rich flame particles are different by indicating a different amount of LDSA per particle for each condition at the injection point.

The Lean fuel/air mixture shows a statistically significant difference between the injection point and locations downstream for each leak size. There is not a significant difference between 0.9 and 3.4 m downstream of the leak. As described earlier, the SMPS results indicate the aerosol particles were indeed growing as they traveled downstream from the leak and no significant growth occurs after 0.9 m downstream of the leak.

The Rich fuel/air mixture shows a statistically significant difference between the injection point and locations downstream with the 27 mm leak only. The 10 mm leak

specifies a decrease in LDSA per particle between the injection point and 0.9 m downstream. Then the value increases steadily between 0.9, 1.8, and 3.4 m downstream, until the value at 3.4 m downstream equals the value at the injection point. This trend opposes the data for other conditions and contradicts the theory of particle growth by coagulation. Therefore, the change in jet properties must have influenced this 10 mm leak, Rich fuel/air mixture.

The SMPS results indicate the formation of a bi-modal distribution downstream of the 10 mm leak, Rich fuel/air mixture. The first mode of this distribution contributed significantly to the number concentration and very little to the LDSA concentration, due to the abundance and small size of the first mode particles, respectively. The NSAM/SMPS ratio showed this aerosol was changing, but the SMPS results were required to determine the cause of this change. Overall this NSAM/SMPS ratio is a good indication of particle change and reinforces the SMPS findings very well.

Section 5

TiO_2 and SiO_2 Transport and Particle Change through a Simulated Workplace Environment

Section 5.1: Introduction

The TiO_2 and SiO_2 experiments were conducted to determine the fate of airborne nanoparticles at various locations downstream of a simulated leak in a nanoparticle production process (same purpose as the soot experiments). As with soot, exposure to these nanoparticles may cause adverse health effects as reviewed in Section 2. Generating TiO_2 and SiO_2 nanoparticles involved the use of a precursor material injected into the burner along with methane, oxygen, and air. Upon combustion, this gas mixture created high concentrations of TiO_2 or SiO_2 nanoparticles. Titanium (IV) Isopropoxide (TTIP) and Hexamethyl-disiloxane (HMDSO) were used as the precursors for the TiO_2 and SiO_2 nanoparticles, respectively.

Typically, $TiCl_4$ and $SiCl_4$ are used as precursors for creating TiO_2 and SiO_2 nanoparticles in an industrial combustion process, respectively. This is known as the

"chloride" process and about half of the world's TiO_2 nanoparticles are produced using this method (Grass et al., 2006). However this method is known for producing harmful by-products such as chlorine gas (Cl_2) and hydrochloric acid (HCl) (Briesen et al., 1998). These by-products may damage equipment, poison laboratory personnel, and require careful ventilation practices. TTIP and HMDSO typically produce only CO_2 and H_2O upon combustion, and are therefore less hazardous and more desirable precursors for particle generation in the current study.

Particle generation occurs during combustion of these precursors within the burner. Vaporized precursor is transported into the flame by a carrier gas (Strobel et al., 2006). Once in the flame, the precursor decomposes and oxidizes, forming metal-oxide monomers (Akurati et al., 2006; Grass et al., 2006; Strobel et al., 2006). These monomers coagulate and sinter towards the top of the flame, forming spherical primary particles (Akurati et al., 2006; Grass et al., 2006). This high concentration of primary particles may immediately undergo further coagulation and a small amount of sintering to form hard chain-type agglomerates (Grass et al., 2006). Coagulation may continue in a lower temperature region of the flame forming soft (loose) agglomerates, which are not sintered (Grass et al., 2006). TiO_2 can form into anatase and/or rutile phase particles as the monomers nucleate and sinter (Akurati et al., 2006). The methods used to produce these particles and monitor particle fate are outlined in Section 5.2.

Section 5.2: Methods

In the current study, TiO_2 and SiO_2 nanoparticles were created using a diffusion burner and injected into a modified ASHRAE 52.2-2007 Classified wind tunnel (Figure

3.3.9). The diffusion burner is described in the Section 1.3. Methane (Airgas North Central, >93%) was used as the fuel and oxygen (Minneapolis Oxygen Co, >99.5%) was the oxidizer. Clean, dry lab air was also used in the burner for dilution purposes, although the oxygen component may have caused additional oxidation. Nitrogen (Airgas North Central, >99.999%) was used as the carrier gas for each precursor material. The precursors were Titanium (IV) Isopropoxide (TTIP, Aldrich, 97%) and Hexamethyl-disiloxane (HMDSO, Aldrich, >98%) for TiO_2 and SiO_2, respectively. The carrier gas (N_2) was bubbled through the precursor material creating very small carrier gas bubbles, saturated with precursor vapor. These very small gas bubbles were created by delivering the carrier gas through a fine mesh (Air Stone, Topfin, Pheonix AZ) inside the precursor bottle.

When producing SiO_2, this bottle and the delivery system were constructed as specified by Scheckman et al. (2009). The precursor bottle was kept in a constant temperature water bath of 3°C to ensure repeatable particle production. The tubing between the precursor bottle and the burner was wrapped with heat tape, held at approximately 35°C to prevent precursor condensation within this line. The precursor vaporization system is shown in Figure 5.2.1.

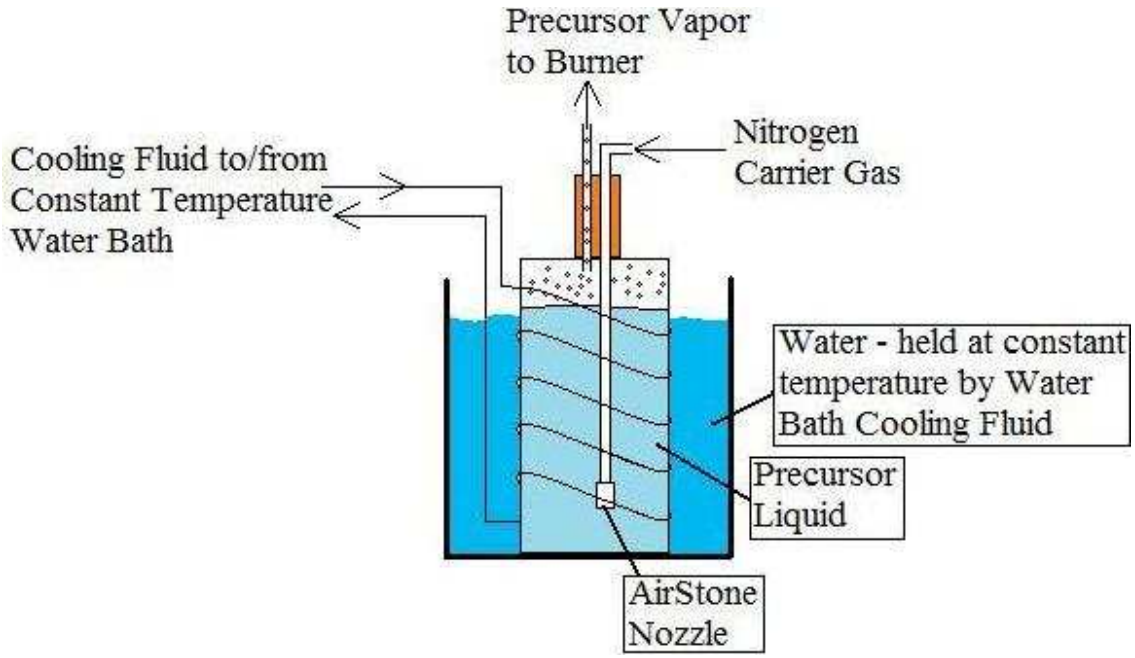

Figure 5.2.1: Precursor vaporization schematic. Heat tape wrapped around Precursor Vapor line.

When producing TiO_2, this bottle and the delivery system were constructed using the same specifications as the SiO_2 experiments. The bottle was kept in a constant temperature water bath of 30°C. The tubing between the precursor bottle and the burner was wrapped with heat tape and held at approximately 35°C to prevent precursor condensation within this line. Other researchers have used higher temperatures (175°C - Akurati et al., 2006; 150°C - Kammler et al., 2003; 125°C - Yeh et al., 2004); however these researchers took an extra step to ensure the safety of their experimental setup by conducting experiments within a fume hood. This precaution was not available with the present experimental setup. Therefore the temperatures of the water bath and heat tape were kept below the flash point of TTIP (46°C - MSDS) to prevent the formation of an ignitable vapor prior to the burner.

The burner gas flow rates were controlled with Rotameters (Cole Palmer), specifically designed for each type of gas. The flame was contained within the burner housing described in the Section 1.3, which was connected to the injection probe (also described in the Section 1.3). This injection probe served as the leak in the wind tunnel. The reconfigured ASHRAE 52.2-2007 Classified wind tunnel (described in the Section 3.3) served as the simulated workplace environment as shown in Figure 3.3.9. The injection probe was aligned at the centerline of the wind tunnel. After injection into the wind tunnel, the particles were measured at several locations as they traveled downstream from the leak.

A Scanning Mobility Particle Sizer (SMPS Model 3034, TSI, Shoreview, MN) and a Nanoparticle Surface Area Monitor (NSAM Model Aerotrak 9000, TSI, Shoreview, MN) were used to measure particle distribution by number concentration and lung deposited surface area (LDSA) concentration, respectively. A Nanometer Aerosol Sizer (NAS Model 3089, TSI Shoreview, MN) was used to capture particles onto Lacey grids for imaging using a Transmission Electron Microscope (TEM, FEI Tecnai T12). The SMPS and NSAM were operated simultaneously. The NAS was operated (at 1 lpm) simultaneously with the NSAM for few select trials due to the time-intensive analysis procedure for TEM. Several primary particles were sized for each condition sampled. An average size was determined for each condition and a 95% confidence interval was calculated using the student's t-distribution. Sample calculations are located in Appendix K. EDS/TEM (Energy-dispersive X-ray spectroscopy with the Transmission Electron Microscope, Tecnai T12) analysis was conducted to determine the chemical composition of the TiO_2 and SiO_2 particles collected on the TEM grids.

A sample at the outlet of the injection probe (injected particle concentration) could not be taken without diluting the sample flow by 100:1 with clean, dry lab air. This dilution lowered the particle concentration to within the measureable size range of the SMPS. When measuring SiO_2, the 100:1 dilution ratio was insufficient, so the sampling probe was moved to sample outside the centerline of the injected aerosol plume. This provided approximately 400:1 dilution, but the exact ratio cannot be determined.

Diluting the flow also minimized additional particle dynamics (coagulation, diffusion losses, growth by condensation) from occurring within the sampling line, providing a true sample from within the wind tunnel. Without this freezing affect, the particles would likely change within the sampling lines and not represent the true particle distribution from within the wind tunnel. The dilution set is described in Section 3.5.

This 100:1 dilution was not required for measurement locations downstream of the injection point since the wind tunnel air flow provided sufficient dilution. A 10:1 dilution ratio was required for only the highest particle concentrations downstream of the injection point, which occurred at sampling position (0,23) in Figure 4.2.2. The dilution air was supplied at the sampling point to prevent additional particle dynamics from occurring within the sampling line (just as the dilution air was supplied to provide the 100:1 dilution ratio at the injection point).

Section 5.3: Results and Discussion

Section 5.3.1: Initial TiO_2 and SiO_2 Aerosol Properties

The SiO_2 and TiO_2 particles produced in the current study are different. They have different chemical properties, are used in different applications, and have different

size distributions (in current study). The injected particle size distributions for SiO_2 and TiO_2 are shown in Figure 5.3.1.1. The initial particle morphology for TiO_2 and SiO_2 are shown in TEM images in Figures 5.3.1.2 and 5.3.1.3, respectively. The SiO_2 primary particles obtained several different diameters (Figure 5.3.1.3), whereas the TiO_2 primary particle size was much more consistent (Figure 5.3.1.2).

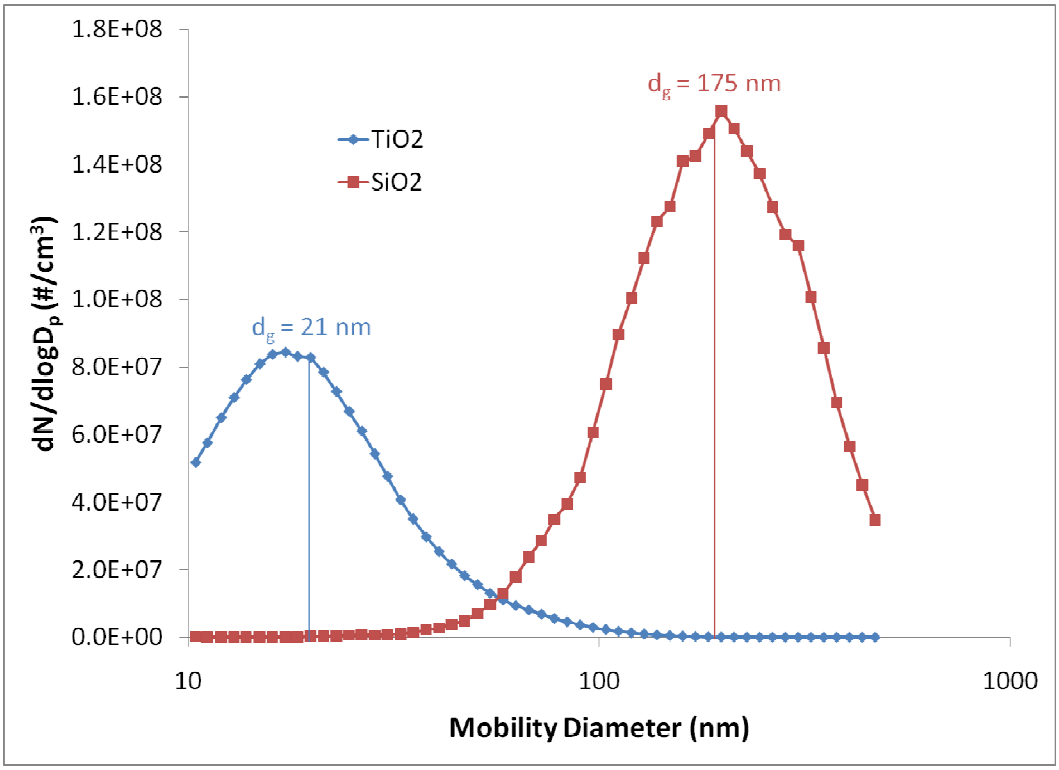

Figure 5.3.1.1: Injected aerosol size distributions for TiO_2 and SiO_2.

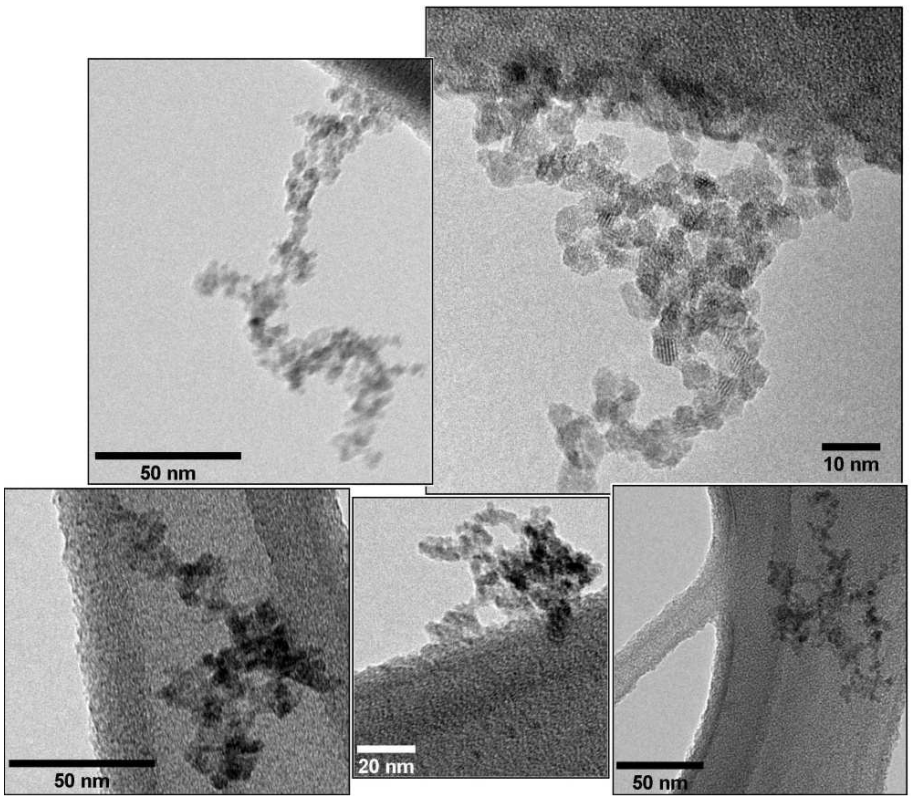

Figure 5.3.1.2: TEM images of initial TiO_2 particle morphology.

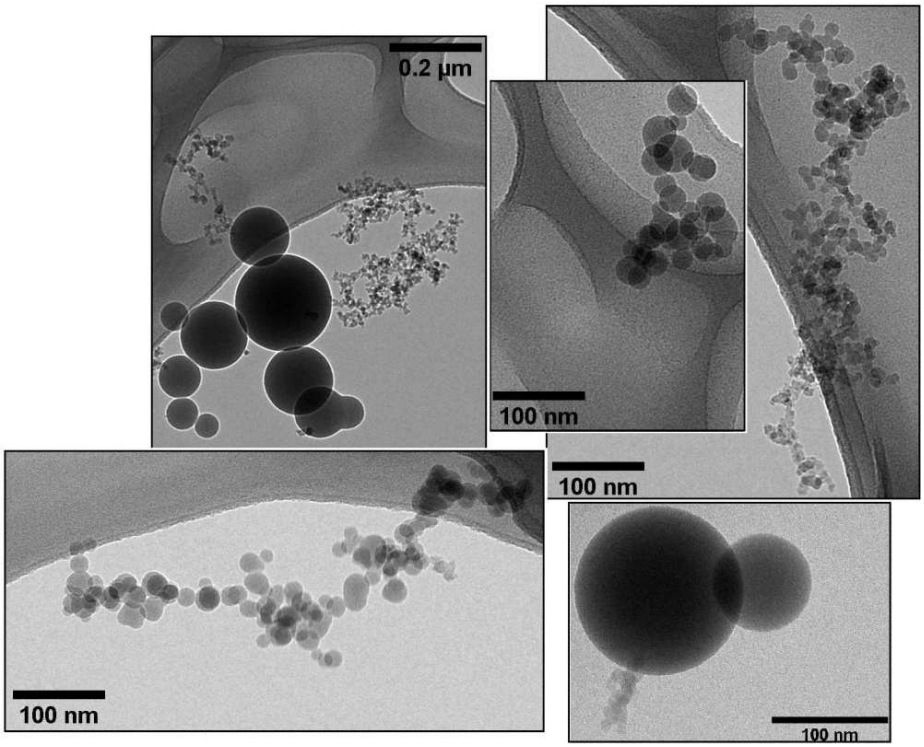

Figure 5.3.1.3: TEM images of initial SiO_2 particle morphology.

The TiO_2 and SiO_2 primary particle sizes were measured from TEM images using computer software, as described in the Section 4.3.1. The initial TiO_2 primary particle diameters were measured from TEM images gathered in 3 different imaging sessions. The first two imaging sessions produced images with insufficient resolution to reasonably determine any primary particle sizes within the agglomerates. The third session produced higher resolution images (such as the image with 10 nm scale bar shown in Figure 5.3.1.2), and the primary particle size was determined to be $d_{pp} = 4.5 \pm 0.4$ nm. Small, sub-primary particles are apparent in this distribution as well, however the diameters of these particles are too small ($d_{sp} < 3$ nm) to be measured confidently.

The SiO_2 primary particle sizes were determined separately for smaller and larger particles. These different size classes of particles can be easily identified from the TEM images (Figure 5.3.1.3). The larger particles are much darker (and much larger) while the smaller particles are lighter colored. There actually appear to be three different primary particle modes within this distribution. These are characterized as small, mid-sized, and larger particles. The larger and mid-sized particles are mostly spherical, with smooth rounded edges. The small particles have rough edges and more of a flake-like appearance. The primary particle size of the mid-sized and larger particles was determined. The primary particle size of the small particles was not determined, because the edge of the small particles is difficult to reasonably identify within an agglomerate. Although through qualitative observation, the small and mid-sized particles have approximately the same primary particle size. The primary particle sizes of the larger and mid-sized particles are $d_{pp} = 117 \pm 17$ nm and $d_{pp} = 24 \pm 1.2$ nm, respectively. The smaller, flake-like particles are apparent in Figure H.3, and are discussed in Appendix H.

The chemical composition of the TiO_2 and SiO_2 particles was verified using EDS/TEM analysis. Figure G.1 in Appendix G and Figure H.7 in Appendix H show the EDS measured compositions of TiO_2 and SiO_2, respectively. Figure H.7 includes results for the larger, mid-sized, and small SiO_2 primary particle sizes. Each figure contains some Carbon and Copper, because Lacey grids are composed of a Carbon sheet laid over a Copper substrate. Carbon, Copper, Oxygen, and a small amount of Silicon were all detected when examining background portions of the Lacey grids (sections with no particles). These elements are commonly found in TEM Lacey grids and are considered background elements. When TTIP was the precursor vapor, the particles were composed of Titanium and Oxygen, accounting for background elements. When HMDSO was the precursor vapor, the particles were composed of Silicon and Oxygen, accounting for background elements. The background Silicon concentrations are very small compared to the Silicon concentrations of a SiO_2 particle. Therefore the EDS analysis verifies TiO_2 and SiO_2 particles were created with the burner and injected into the wind tunnel.

The SiO_2 particles were not consistently produced. Therefore the data and analysis downstream of the injection point is omitted from the body of this thesis. The SiO_2 data is instead presented and analyzed in Appendix H. The inconsistent particle production is also analyzed in Appendix H.

Section 5.3.2: TiO_2 Aerosol Properties Downstream of Leak

The particle size distribution was measured at each measurement location (Injected, 0.9, 1.8, and 3.4 m) downstream of the leak using TiO_2. The time between the injection point and each measurement location is approximately 3.6, 7.2, and 13.6

seconds (for 0.9, 1.8, and 3.4 m, respectively) assuming a constant background face velocity of 0.25 m/s. The normalized distribution for each measurement location is plotted for each leak size in Figures 5.3.2.1 - 5.3.2.2. The raw data for each figure is located in Appendix G as Tables G.1 and G.2. Figure 5.3.2.1 shows the particle size distribution change between the injection point and 0.9 m downstream when using TiO_2 and the 27 mm leak. This particle size distribution remains consistent as the particles travel downstream of the leak (no change in particle size distribution after 0.9 m downstream). Figure 5.3.2.2 shows a change in particle size distribution between the injection point and 0.9 m downstream when using TiO_2 and the 10 mm leak. This change in particle size distribution continues between measurement locations downstream of the injection point.

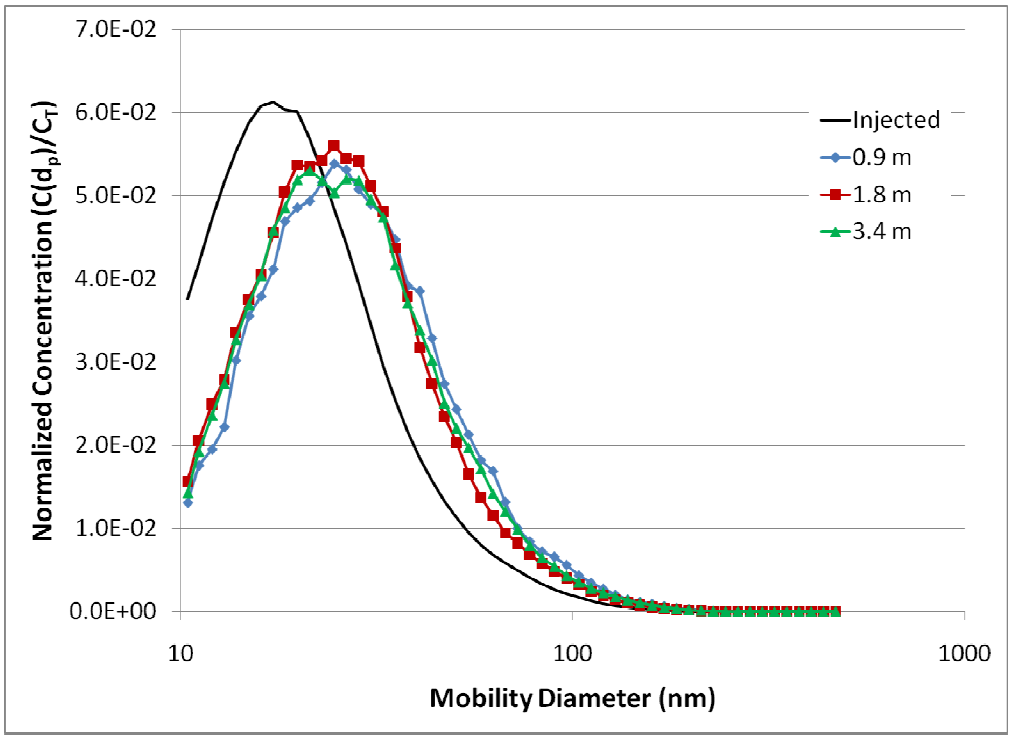

Figure 5.3.2.1: Normalized particle size distributions at each measurement location using TiO_2 and 27 mm leak.

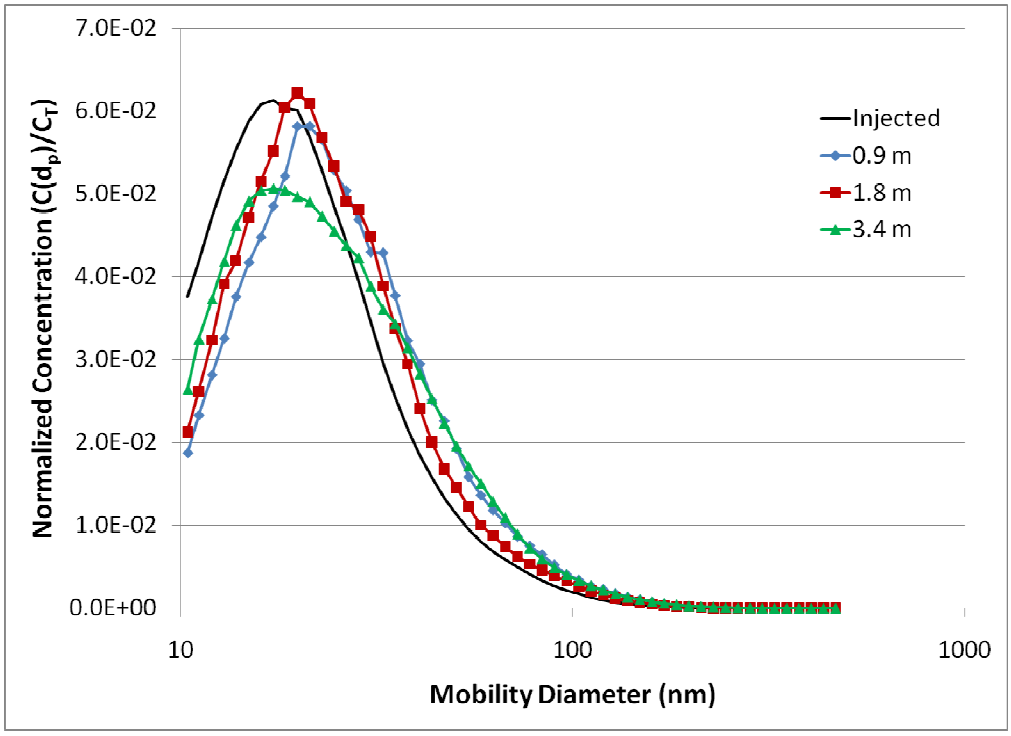

Figure 5.3.2.2: Normalized particle size distributions at each measurement location using TiO_2 and 10 mm leak.

In Figure 5.3.2.2, the shape of the 3.4 m particle size distribution curve is different from the Injected, 0.9 m, and 1.8 m curves. This discrepancy was most likely caused by an inconsistent precursor vapor delivery system. Each condition was randomly tested at each measurement location. The results at each measurement location (Location 2, 3, or 4) for each leak size (27 or 10 mm) are shown in Appendix G. These figures show the average particle size distribution for each sampling location depicted in Figure 4.2.2.

The TiO_2 nanoparticles used in the current study were created by injecting TTIP precursor vapor into the burner flame, described in the Section 5.2. The nozzle delivering Nitrogen gas into the precursor bottle was an AirStone (TopFin, Pheonix AZ), consisting of several small pores for the Nitrogen to pass through. This creates very small bubbles of Nitrogen gas, evenly distributed throughout the liquid precursor. These small bubbles

become saturated with precursor vapor, and carry this vapor into the flame; however the small pores become clogged if precautions are not observed. If the pores clog, the pressure drop across the Nitrogen nozzle increases, causing a change in the amount of precursor vapor injected during different TiO_2 trials. This inconsistent vapor injection would result in an inconsistent production of TiO_2 particles by the burner. This would make it impossible to determine if the aerosol was changing throughout the wind tunnel or at the production site. Therefore, precautions were taken to prevent these pores from becoming clogged.

After each day an experiment was conducted, the precursor bottle was removed from the burner setup for proper overnight storage. Removing the nozzle from the precursor bottle caused the nozzle to be exposed to lab air, and the moisture in the air. TTIP reacts quickly with moisture to form a precipitate. The nozzle clogs when the TTIP solids precipitate inside the pores of the nozzle. The pores remain unclogged if the nozzle is rinsed with Isopropyl Alcohol before this moisture can cause significant precipitation. This rinsing was carried out at the end of each experiment day, prior to overnight storage, except once. The pores were rinsed with the wrong bottle of Isopropyl Alcohol (which was 10% Isopropyl Alcohol and 90% water) prior to the last day of experimentation. This mix-up was the cause of the discrepancy in the TiO_2 particle size distributions downstream of the injection point. The nozzle was replaced and the trials were repeated at a later date. The 27 mm leak showed consistency with the new nozzle, but the 10 mm leak did not. The test using the 10 mm leak was repeated again and each trial was averaged to form the Location 4 normalized distribution plotted in Figure 5.3.2.2.

The Nitrogen used as the carrier gas was >99.999% pure. Even with proper rinsing it is difficult to prevent moisture from reaching the nozzle, resulting in the formation of solids, and clogging of the AirStone pores. Most likely there was some precipitate within the pores of the AirStone after the initial particle distribution was established at the injection point. This moderate amount of precipitation created a unique nozzle, which created a unique particle size distribution. In order to repeat the results of the current study, the initial particle distribution must be established using a unique and consistent nozzle. The characteristics of this unique nozzle must be maintained throughout the entire experiment. In the current study, the uniqueness of the nozzle was not maintained, and installing a new nozzle did not fix the problem.

Once the new nozzle was installed, the initial particle concentration should have been re-established. Since it was not, the inconsistent data at 3.4 m downstream should be omitted since it caused a change in particle production within the burner. Excluding the data gathered when the N_2 nozzle was clogged allows an accurate figure to be produced. Figure 5.3.2.3 shows normalized particle size distributions with only data obtained using the original N_2 injection nozzle. This figure shows a much more consistent particle size distribution at locations downstream of the injection point.

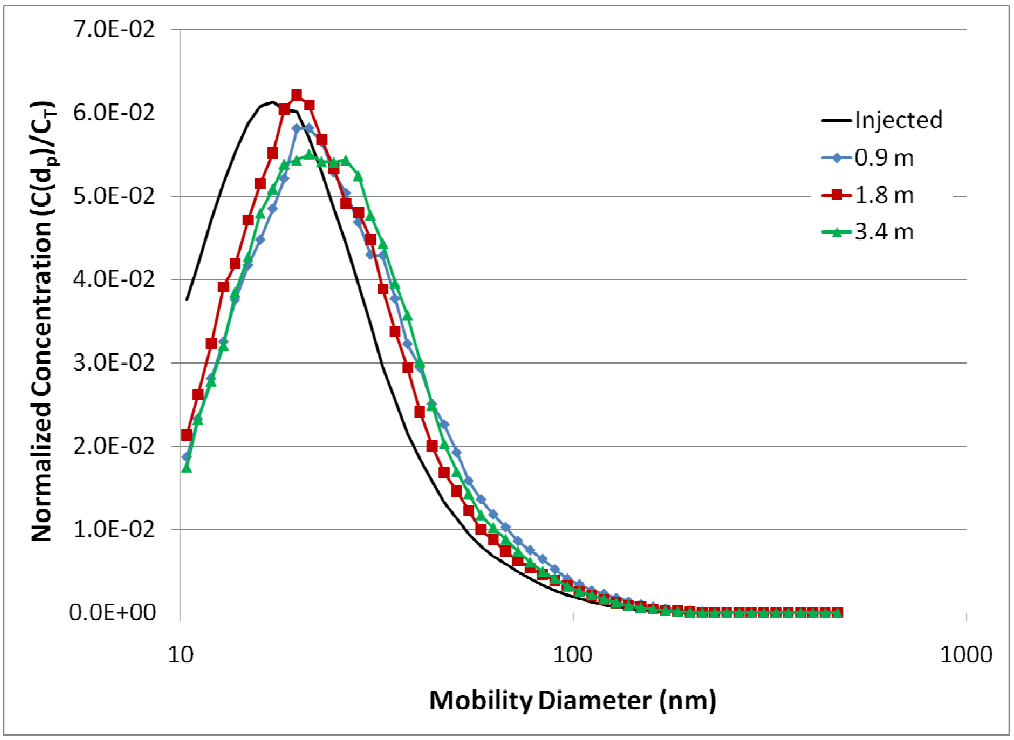

Figure 5.3.2.3: Normalized particle size distributions for each measurement location using data only from the original N_2 injection nozzle with TiO_2 and 10 mm leak.

Figure 5.3.2.4 shows TEM images for TiO_2 particles collected 3.4 m downstream from the injection point. By observation, the morphology at the injection point (Figure 5.3.1.2) is similar to 3.4 m downstream. The samples were gathered on different days; after sampling with the clogged nozzle produced an inconsistent SMPS-measured particle distribution (2/22). Small primary particle diameters and highly compact agglomerates make the measurement difficult. However 100 primary particles were randomly selected and measured for the 27 mm leak and 146 were randomly sampled for the 10 mm leak to obtain a high degree of confidence. The primary particle diameters are $d_{pp} = 6.5 \pm 0.5$ nm and $d_{pp} = 7.0 \pm 0.3$ nm for the 27 and 10 mm leak sizes, respectively. There is no statistically significant difference between the primary particle diameters when using the

27 and 10 mm leak size. Therefore the primary particle size increases between the injection point and 3.4 m downstream of the leak.

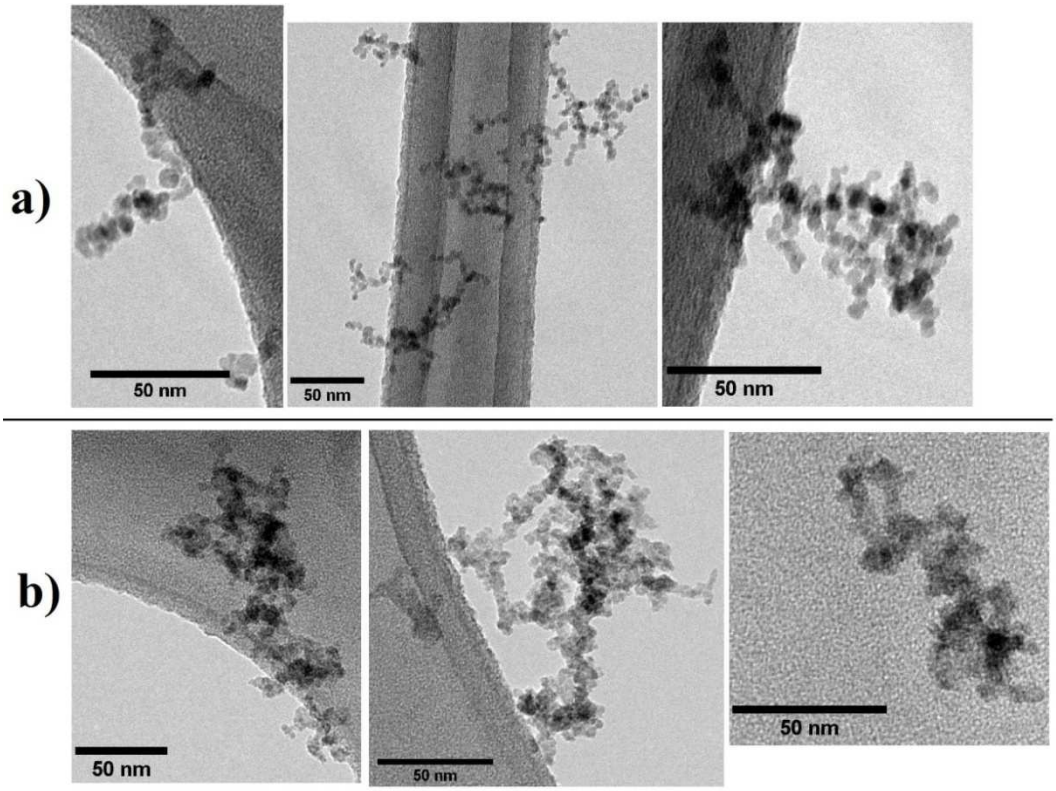

Figure 5.3.2.4: TiO_2 TEM images from 3.4 m downstream using 27 mm leak. Samples gathered on a) 2/22 and b) 2/25.

This increase in primary particle size is most likely not an artifact of the N_2 nozzle. The 10 mm leak primary particle size was repeatable even when the SMPS measurements were inconsistent. The 27 mm leak produced consistent primary particle sizes and SMPS measured distributions with both a clogged and unclogged N_2 nozzle.

Several studies within the literature have examined particle formation within the flame and in the high temperature region above the flame, but flame synthesis experiments are always conducted within a fume hood. These published experiments typically use fast cooling and dilution to prevent particle change during sampling, while

examining: burner configurations (Akurati et al., 2006), precursors (Arabi-Katbi et al., 2002), flame temperature/condition (Grass et al., 2006; Nakaso et al., 2003; Yeh et al., 2004), flame cooling rate (Grass et al., 2006), and electric field effect (Kammler et al., 2003). Tsantilis and Pratsinis (2004) noted the primary growth mechanism for TiO_2 particles created with TTIP is coagulation after 0.1 s within the flame (Tsantilis and Pratsinis, 2004). Grass et al. (2006) noted primary particle change stops after 0.07 s with TTIP produced TiO_2. However initial particle growth is often obscured by coagulation (Tsantilis et al., 2002), and when the flame is cooled fast, primary particle growth virtually stops (Kammler et al., 2003).

The cooling and dilution effects following particle injection may have affected primary particle size. Arabi-Katbi et al. (2002) showed primary particle size increases with decreasing temperature above the burner. Nakaso et al. (2003) studied the effects of flame temperature on primary particle size when using TTIP as the chemical precursor. The particle formation was discovered to occur in 2 phases. The first phase is the condensation of product monomers. Monomers are produced by thermal decomposition of TTIP. These monomers nucleate and sinter into spherical primary particles within the high temperature region of the flame (Nakaso et al., 2003). The second phase occurs after the TTIP has finished reacting and consists of coagulation and/or sintering of the newly formed primary particles.

In the current study, sintering between primary particles is not observed for TiO_2. This indicates a low reaction temperature and/or low particle residence time within the flame (Nakaso et al., 2003). A low reaction temperature would indicate a slow reaction of monomers and the formation of large primary particles (Nakaso et al., 2003), which does

not occur in the current study. Therefore the particles must have experienced a low residence time within the high temperature region of the flame. The total time between the flame and the injection point is 20 seconds. This is plenty of time for the primary particles to form loose, chain-type agglomerates within the burner housing and injection probe through coagulation. These agglomerates continued to grow after being injected into the wind tunnel, although coagulation is likely to be finished well before the injection point.

Cooling of the aerosol within the burner housing and injection probe appears to have occurred relatively slowly. Cooling within the wind tunnel occurred quickly, accompanied by dilution. This fast cooling may have caused reactions between the injected particles, exhaust gases, and background flow; contributing to the change in primary particle diameter (TEM analysis) and mobility diameter (SMPS data).

Temperature change can affect particle density as well as the internal structure of the primary particles, both of which may cause a change in particle size, without changing particle mass. Fast cooling of the injected aerosol and exhaust gas may also create a supersaturated vapor, allowing for nucleation. Exhaust gas nucleation onto the surface of primary particles would cause an increase in particle size and mass. Coagulation would also cause an increase in particle size and mass, although this phenomenon is likely to be finished by the injection point. Since mass measurements were not a part of this study, it is not possible to tell if the cooling effects, nucleation, or coagulation caused the change in primary particle size and/or geometric mean particle size. Analytical models may be applied to this data to determine the cause of this change. Theories and analytical models are examined in Section 6.

Section 5.3.3: TiO_2 Particle Statistics

The TiO_2 geometric mean particle sizes are shown in Table 5.3.3.1 for each leak size and each measurement location. Since several trials were conducted, a statistical analysis may be used to determine if the geometric mean particle sizes are truly different at locations downstream of the leak. These geometric mean particle sizes were analyzed using a t-test of unequal variance with degrees of freedom calculated using Welch's method for each nanoparticle material and each leak size. The specific details of this statistical analysis can be found in Appendix K.

Table 5.3.3.1: TiO_2 geometric mean particle size for each leak size at each measurement Location.

	27 mm	10 mm
0 m downstream	21	
0.9 m downstream	28	25
1.8 m downstream	26	24
3.4 m downstream	27	24

A statistically significant difference exits between the injection point and 0.9 m downstream at a confidence level of 95% for each leak size. A statistically significant difference was also determined between the injection point and 1.8 m downstream at a confidence level of 95% for each leak size. However there is not a statistically significant difference between the injection point and 3.4 m downstream due to the inconsistencies in the precursor delivery system during this round of experiments.

Table 5.3.3.2 shows the total particle concentration of TiO_2 for each measurement location and each leak size. Turbulent mixing is most likely the cause of the differences in total particle concentrations as outlined in the analysis of soot particle dispersion in Section 4.3.2. The differences may have also been caused by day-to-day variations in

burner output, which is especially likely when working with highly reactive precursor material, although the TiO_2 particle distribution was very consistent at the injection point.

Table 5.3.3.2: TiO_2 total particle concentrations for each leak size at each measurement Location.

	27 mm	10 mm
0 m downstream	4.3E+07	
0.9 m downstream	4.2E+05	4.9E+05
1.8 m downstream	7.4E+05	5.5E+05
3.4 m downstream	6.8E+05	8.8E+05

Section 5.3.4: NSAM/SMPS Ratio for TiO_2

The NSAM was operated simultaneously with the SMPS, measuring the Alveolar Lung Deposited Surface Area (LDSA) concentration (amount of particulate surface area deposited in the Alveolar region of the lung for an average worker) of the sampled aerosol. The NSAM results may be used to determine a ratio of LDSA per particle. This ratio will show if the particles are growing by adding surface area to a particle (agglomeration or nucleation). For each trial, the NSAM measured lung deposited surface area was plotted against the corresponding SMPS measurement of total particle concentration. These plots typically revealed a linear relationship between the two measurements. The ratio was determined by fitting a regression curve to these plots. Figure 5.3.4.1 shows this LDSA per particle value for each condition at each measurement location. A 95% confidence interval was also calculated for each regression fit parameter, which is plotted as error bars (along with instrumentation bias from the feasibility study) in Figure 5.3.4.1. The NSAM/SMPS regression fit plots for each location and condition are located in Appendix G.

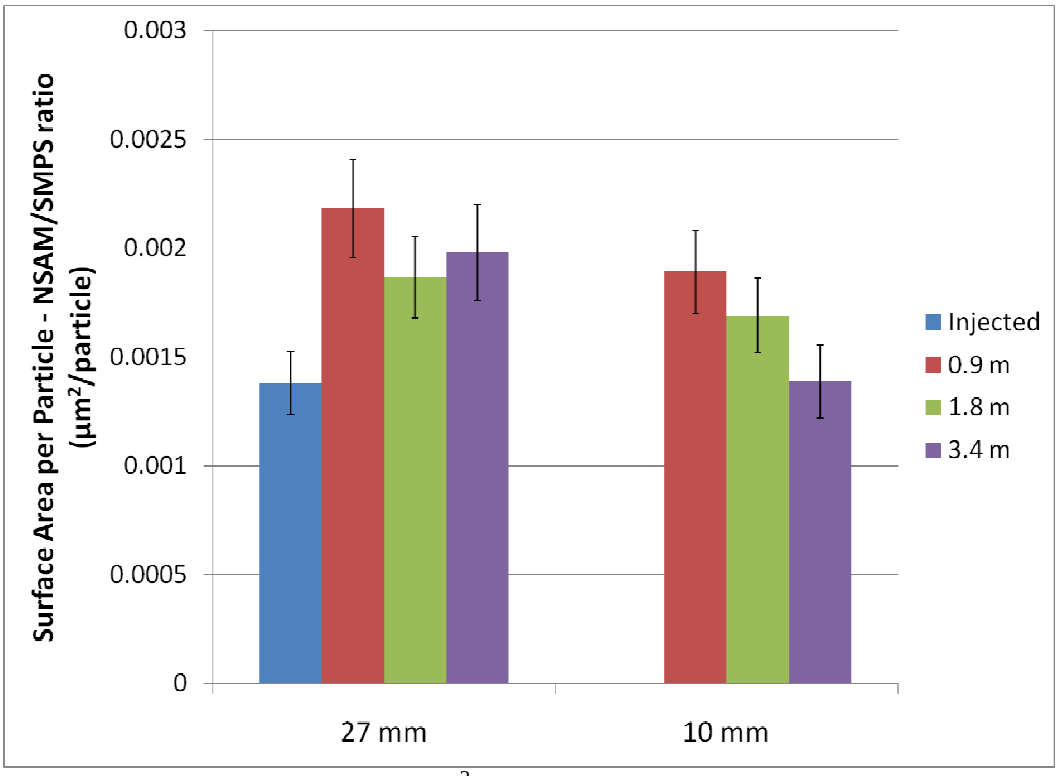

Figure 5.3.4.1: NSAM/SMPS ratio (μm^2/particle) for TiO_2 at each measurement location. Error bars obtained through regression analysis with 95% confidence interval.

The amount of LDSA per particle (NSAM/SMPS ratio) was determined for each leak size (27 mm and 10 mm) and each measurement location downstream of the leak (Injected, 0.9, 1.8, and 3.4 m) for TiO_2. The TiO_2 particles grew between the particle injection site and 0.9 m downstream for each leak size. The TiO_2 particles do not significantly change (in LDSA per particle) between 0.9 m and 3.4 m downstream for the 27 mm leak size. The 10 mm leak size shows a decrease between 0.9 m and 3.4 m downstream. The LDSA per particle is not significantly different between the injection point and 3.4 m downstream for the 10 mm leak, however these results are affected by the lack of trials for TiO_2 at 3.4 m downstream with the 10 mm leak.

Overall there is an increase in LDSA per particle between the injection point and 0.9 m downstream. There is no change after 0.9 m downstream for TiO_2 (when using data

sets of high confidence) This result reinforces the SMPS results, which indicate an increase in the geometric mean particle size of TiO_2 at measurement locations downstream of the injection point. The cause of this growth for the Soot (Lean fuel/air mixture) and TiO_2 particles is examined in Section 6.

Section 6
Analytical Analysis of Combustion Particle Change during Transport

Section 6.1: Introduction

There are still many unknowns with regards to particles produced through flame and combustion processes. When comparing particles produced through combustion: fuel type, fuel/oxidant ratio, combustion process, and burner configuration (premixed or non-premixed) can affect the resulting particle size, shape, concentration, and chemistry (D'Anna, 2009). These variations are subtle, but state of the art equipment can be used to detect minor differences (D'Anna, 2009). This section explores particle change of Soot (Lean fuel/air mixture) and TiO_2, noticed in the current study, through literature review and analytical modeling. These particles can be affected by exhaust gases and dilution air, as presented in the literature. Analytical models for particle formation and growth are also discussed.

The basic formation of soot particles begins with the pyrolysis of fuel. During combustion, the fuel is first decomposed into reactive small molecules and radicals, which happens almost instantly at high temperatures of combustion. The presence of oxygen is necessary for combustion, but not for pyrolysis. When oxygen is present (oxidative pyrolysis), the oxygen mixes with free hydrogen molecules forming water and releasing heat (Siegmann et al., 2002). This process typically occurs within a millisecond. The free reactive molecules and radicals avoid combustion and chemically condense to form small nuclei particles. Small aromatic rings are formed as more free reactive molecules and radicals condense on the surface, causing the particles to grow. These particles can continue to grow and/or experience desorption as Polycyclic Aromatic Hydrocarbons (PAHs) detach from the surface of the soot particle. This process can occur at any point as the soot particle grows. However, large PAHs with around 1000 amu molecular mass (approximately 80 carbon atoms) could also be soot particle precursors (Bockhorn, 1994).

The nanoparticles (1 - 5 nm in diameter) formed within the flame by coagulation of chemical precursors, have previously been defined as “sub-primary” particles. Some of these sub-primary particles coagulate to form soot primary particles, and some do not, resulting in a bi-modal distribution (D’Anna, 2009; Sgro et al., 2007). However the sub-primary particles experience a decreased coagulation rate at flame temperatures due to thermal rebound (D’Anna, 2009), while primary particles typically coagulate to form chain-type agglomerates. Primary particle formation and coagulation occur in different temperature regions of the flame, dependent upon fuel type, fuel/oxidant ratio, combustion process, and burner configuration. Primary particles and agglomerates are

also affected by the cooling and dilution effects of background air (D'Anna, 2009; Ning and Sioutas, 2010).

A complex mixture of exhaust gases and particulate matter is also emitted from combustion sources (Ning and Sioutas, 2010). Particulate matter (sub-primary particles, primary particles, and agglomerates) within the exhaust can change as exhaust gases nucleate on the particle surface and new particle formation can occur through homogeneous nucleation of exhaust gases in background air (Seinfeld and Pandis, 1998). Therefore, these sub-primary particles can form within the flame and serve as the building blocks of soot primary particles (di Stasio, 2001), or they can form within combustion exhaust gases during dilution and cooling within the wind tunnel (Ning and Sioutas, 2010; Kulmala et al., 2000).

Rapid cooling and dilution effects of background air cause a supersaturated vapor of low volatility gaseous compounds to form from the exhaust gas (Ning and Sioutas, 2010; Seinfeld and Pandis, 1998). A supersaturated vapor occurs when the partial pressure of a vapor becomes greater than the saturation vapor pressure (Hinds, 1999). The degree of supersaturation required for particle formation through homogeneous or heterogeneous nucleation is dependent upon the specific vapor substance as well as temperature (Hinds, 1999). Supersaturation conditions are difficult to identify for combustion exhaust because combustion exhaust gases are of complex chemistry (Ning and Sioutas, 2010).

A higher vapor pressure is required for smaller particles to form (Kelvin effect) compared to larger particles (Ning and Sioutas, 2010). If a high vapor pressure is not maintained, small particulate organic aerosols can evaporate (Shrivastava et al., 2006). If

a high vapor pressure is maintained, then smaller nanoparticles actually have a longer lifetime than particles larger than 6 -7 nm formed in the combustion process (Sgro et al., 2007). If aerosol concentrations are low, new particle formation is more likely (Kulmala et al., 2000). With high aerosol concentrations, condensation onto pre-existing particles is more likely than new particle formation (Kerminen et al., 2001). Once again, the sub-primary particles present in the exhaust of a combustion process can form within the flame or in the cooling, dilution air after being released. These particles may then survive or disintegrate in the atmosphere depending on the chemical composition of the supersaturated vapor.

In the current study, there were several different conditions used for creating combustion particles in a non-premixed, diffusion burner. A lean mixture of methane and air was used, and sub-primary particles were imaged through TEM analysis along with chain-type agglomerates of spherical primary particles. This type of distribution seems typical of combustion aerosols from burners (Maricq, 2006), diesel engines (DeFilippo and Maricq, 2008), and wood burning (Gwaze et al., 2006). The sub-primary particles were not reported in the wood burning study (Gwaze et al., 2006). In aircraft engine exhaust, a trimodal distribution exists, consisting of accumulation mode particles, carbon soot, and a completely volatile mode of small particles (Onasch et al., 2009).

A rich mixture of methane and air was also used in the current study. Sub-primary particles were imaged along with single primary particles and agglomerates (with a high degree of necking). These agglomerates are atypical for soot and the exhaust of this rich mixture most likely contained a large quantity of semi-volatile components from unburned fuel (Tobias et al., 2001). Semi-volatile vapors may interfere with the

formation of non-volatile particles during dilution and cooling of combustion exhaust gases (Maricq, 2007b; Meyer and Ristovski, 2007; Ning and Sioutas, 2010).

Metal-oxide particles were also created in the current study using a methane and oxygen flame with a chemical precursor. The SiO_2 studies did not produce good data due to inconsistencies in the flame-produced aerosol distribution. The TiO_2 studies produced acceptable data and sub-primary particles were imaged under TEM analysis along with chain-type agglomerates of primary TiO_2 particles. However the sub-primary particles were too small ($d_{sp} < 3$ nm) to be accurately sized using the techniques of the current study. Higher resolution TEM images may have allowed for accurate sizing of the TiO_2 sub-primary particles.

The smallest mode of particles formed during the combustion process is sub-primary particles (defined in the current study). However this particle formation can also occur within the sampling device. Sampling devices can affect the reaction dynamics of combustion aerosols (Ossler et al., 2009). Particle dynamics within the sampling lines and particle measurement instrumentation can also cause a change in aerosol properties (D'Anna, 2009; Ossler et al., 2009). Cooling and diluting the aerosol for measurement purposes can cause a change in particle size, shape, and concentration (Ning and Sioutas, 2010). Cooling can also change the molecular structure and density of the primary soot particles within agglomerates (Fugaciu et al., 1999; Hermann et al., 2001; Ossler et al., 2009).

Section 6.2: Theories of Sub-Primary Particle Formation

Burner configuration and sampling techniques affect produced aerosols. The sub-primary particles are especially sensitive due to their small size, unknown chemistry, speed of formation, and potential to disintegrate, evaporate, or coagulate out of the aerosol plume. Sub-primary particles can be created within the burner, within the wind tunnel, or within the sampling system. The literature review presented earlier in this section outlines the potential for each of these processes. Therefore specific aspects of the current study must be examined to determine the most likely scenario.

The sub-primary particles may have been produced within the burner. The literature identifies sub-primary particles as the building blocks of primary particles, yet some avoid coagulation and remain a part of the distribution downstream of the initial particle formation process (D'Anna, 2009; di Stasio, 2001). These particles have a low coagulation rate at flame temperatures (D'Anna, 2009), and the burner housing and injection probe are heated to flame temperatures during particle production. If the sub-primary particles were produced within the burner, then they should be observed in TEM images at locations downstream of the injection point. These particles should have remained entrained in the background air flow due to turbulent mixing within the wind tunnel. Since these particles were not noticed in TEM images downstream of the leak, it is possible these particles did not form within the burner. However, they may have also disintegrated while traveling through the wind tunnel.

The sub-primary particles may have formed within the sampling nozzle at the injection point. The cooling and dilution effects, combined with the pressure drop across the sampling nozzle (~0.9 in H_2O), may have lead to the formation of a supersaturated

vapor, causing new particle formation. New particle formation may occur through either homogeneous nucleation of combustion gases, or heterogeneous nucleation of combustion gases onto smaller particles produced within the burner. Particles as small as 1 nm have been measured within burner combustion processes (D'Anna, 2009; di Stasio, 2001), and could serve as seed nuclei for heterogeneous nucleation (Hinds, 1999). It is difficult to directly test this theory without knowing the concentration and composition of the exhaust gases.

If the sub-primary particles were formed due to the instantaneous cooling and dilution within the sampling probe, then the more gradual cooling and dilution effect of the wind tunnel may cause heterogeneous nucleation onto the surfaces of the agglomerates within the plume. Heterogeneous nucleation would cause the particles within the aerosol plume to grow. Primary particles would also appear to grow. In the current study, the particles measured downstream of the injection point have grown. The primary particles have also grown (within the agglomerates); however this could be caused by a change in particle density and structure due to cooling effects. Higher resolution TEM images do not allow for viewing a change in particle structure to verify this theory, since the soot particles are composed of amorphous carbon.

Section 6.3: Maricq (2007a) Coagulation Model

The coagulation theory can be tested by applying a coagulation model to the various distributions measured at the injection point. Maricq (2007a) outlined a coagulation model for burner produced agglomerates which applies to the current study. The objective of this model is to obtain a fractal dimension to be applied to Equation

6.3.1 (Maricq, 2007a). Equation 6.3.1 represents a relationship between the number of primary particles per agglomerate (N_{pp}) based on the radius of gyration (R_g), primary particle size (d_{pp}), fractal dimension (D_f), and a scaling factor (K, typically equal to 1). The primary particle size has been measured in TEM images, and the mobility diameter (d_m) is assumed to be equal to $2R_g$. Therefore the only unknown in Equation 6.3.1 is the fractal dimension.

Equation 6.3.1: $$N_{pp} = K\left(\frac{2R_g}{d_{pp}}\right)^{D_f} \approx K\left(\frac{d_m}{d_{pp}}\right)^{D_f}$$

The coagulation model is outlined in Appendix I, however due to the lack of empirical data it is difficult to obtain a confident fractal dimension. The best fractal dimensions for the Lean and Rich soot distributions, as well as the TiO_2 distribution are listed in Table 6.3.1. Only 27 mm leak data was used because there was no statistically significant difference noticed between the 27 and 10 mm leak sizes for Lean soot and TiO_2. The Rich soot particle distribution was different between the 27 and 10 mm leak sizes, but this was due to the formation of a bi-modal distribution, which is examined in Section 4.3.3. Table 6.3.1 also shows the primary particle size, mobility diameter, and number of primary particles per agglomerate (N_{pp} was calculated with the fractal dimension from the coagulation model).

Table 6.3.1: Fractal dimensions determined through Maricq (2007a) coagulation model.

	Lean/27		Rich/27		TiO2/27	
	0 m	3.4 m	0 m	3.4 m	0 m	3.4 m
σ_g	1.91	1.85	1.8	1.75	1.65	1.66
d_g (nm)	113	132	59	75	21	27
d_{pp} (nm)	30	34	56.5	47	4.5	6.5
Df	2.4	2.4	2.6	2.6	2.4	2.4
K	1	1	1	1	1	1
N_{pp} (#/agg)	24.1	25.9	1.1	3.4	40.3	30.5

Due to the lack of empirical data, it is difficult to obtain the correct fractal dimension. Since the fractal dimension is the only unknown in Equation 6.3.1, the number of primary particles per agglomerate can be plotted against all possible fractal dimensions ($1.0 \leq D_f \leq 3.0$). The fractal dimension should not change as the aerosol experiences coagulation (Maricq, 2007a). So if coagulation is causing the particles to grow, then the agglomerated particles at 3.4 m downstream of the leak should have more primary particles per agglomerate than the agglomerated particles at the injection point. Figure 6.3.1 is a plot of number of primary particles per agglomerate against all possible fractal dimensions for Soot (Lean fuel/air mixture) and TiO_2.

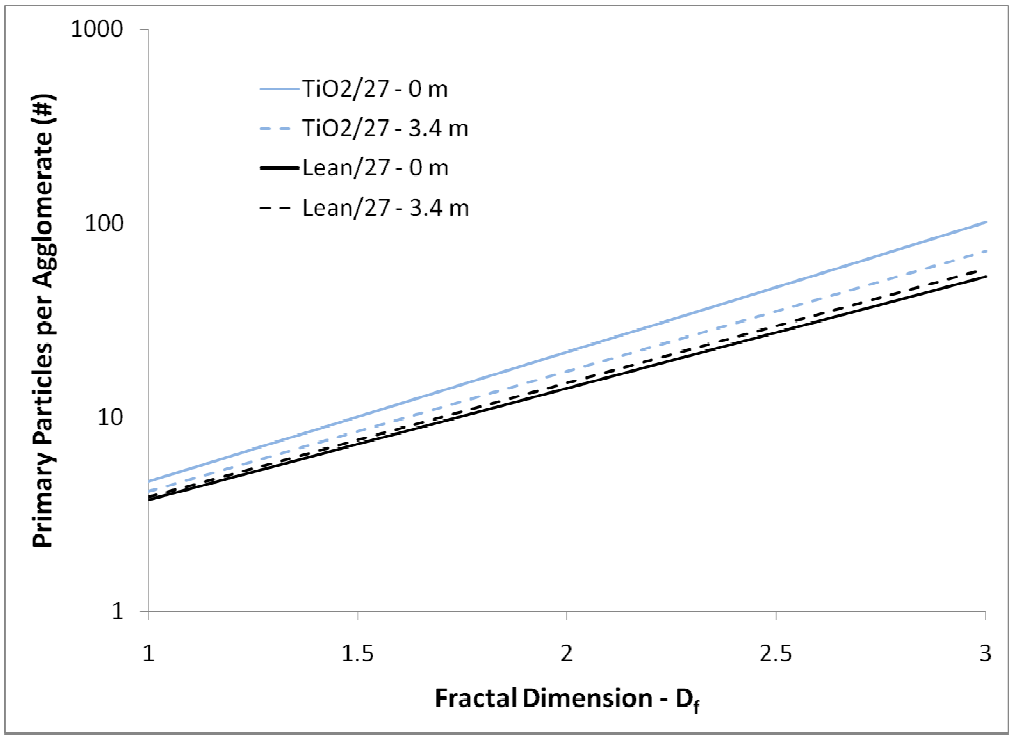

Figure 6.3.1: Number of primary particles per agglomerate over range of fractal dimensions.

Figure 6.3.1 shows the number of primary particles per agglomerate increases for the Lean soot data and decreases for the TiO_2 data (between the injection point and 3.4 m downstream). Applying error bars to this figure will show if these changes are statistically significant. Figures 6.3.2 and 6.3.3 show the Soot (Lean fuel/air mixture) and TiO_2 data with error bars, respectively. There is not a statistically significant change for either data set.

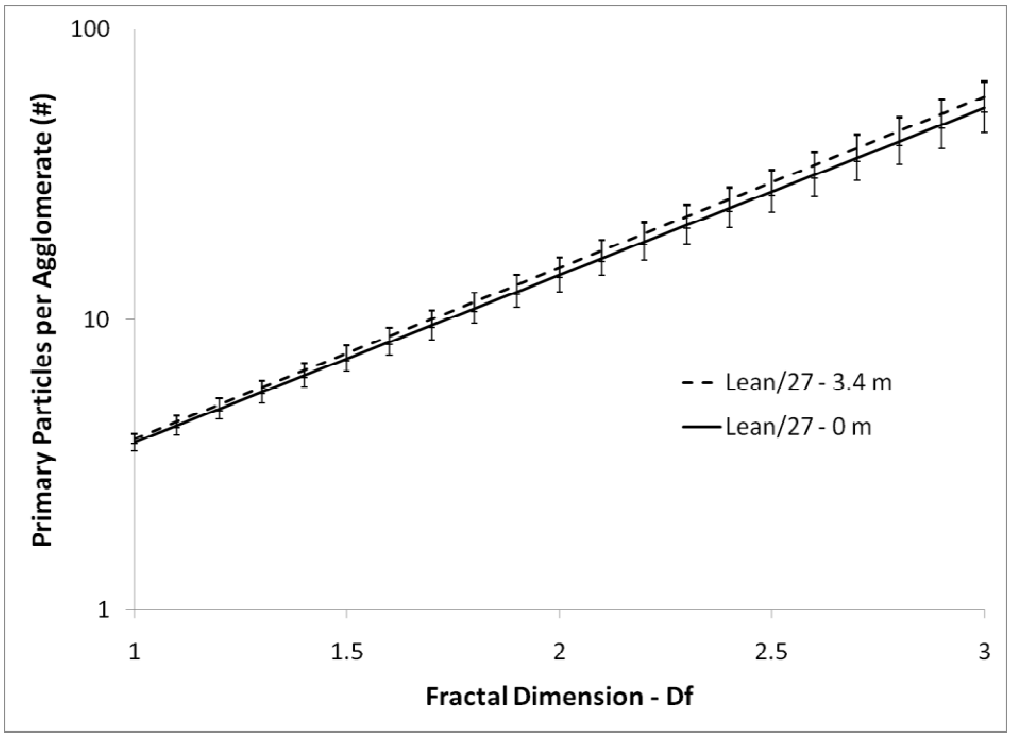

Figure 6.3.2: Soot (Lean fuel/air mix and 27 mm leak) data with error bars for number of primary particles per agglomerate over range of fractal dimensions.

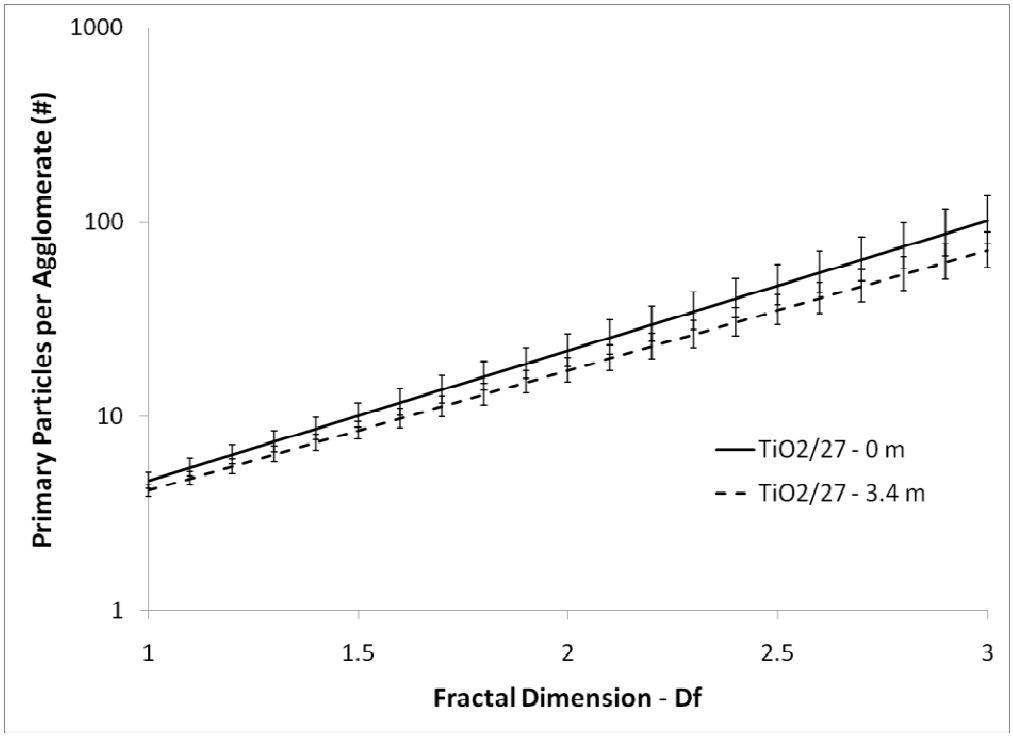

Figure 6.3.3: TiO_2 (27 mm leak) data with error bars for number of primary particles per agglomerate over range of fractal dimensions.

Simple coagulation theories assume liquid particles; colliding particles coalesce to form a larger spherical particle of equal volume, and therefore cannot be used in the current study. The Maricq (2007a) model did not work for the current study due to the sensitivity of the fit parameter (D_f), lack of empirical data (to ensure a proper fit parameter), and high dilution ratio within the wind tunnel. Also, the change in primary particle size is too low for a statistically significant change in number of primary particles per agglomerate using the Maricq (2007a) model. A different approach to this agglomerate analysis is presented below using the Lall and Friedlander (2006) correction theory for agglomerates.

Section 6.4: Lall and Friedlander (2006) Correction Theory

Lall and Friedlander (2006) developed a relationship for agglomerates, which relates mobility diameter to the number of primary particles per agglomerate. This relationship derived by Lall and Friedlander (2006) is depicted as Equation 6.4.1. The slip correction factor (C_c) is outlined in Section 3.5. The SMPS (TSI, model 3034) software adjusts the raw measurement data for several factors, including slip correction, so this term (originally included in the Lall and Friedlander, 2006 model) is excluded from Equation 6.4.1. The air mean free path (λ = 66 nm) and dimensionless drag force on an agglomerate (c* = 9.17) are constant. A sample calculation is located in Appendix K.

Equation 6.4.1:

$$N_{pp} = \frac{3\pi\lambda d_m}{c^*\left(\frac{d_{pp}}{2}\right)^2}$$

The mobility diameter (d_m) and primary particle diameter (d_{pp}) both change as the particles travel downstream from the simulated leak. Therefore it is unclear whether the change in mobility diameter is due to coagulation or simply a by-product of the change in primary particle size. When the Soot (Lean fuel/air mixture) and TiO_2 particle size distributions are plotted against mobility diameter, there is a shift towards higher mobility diameters, indicating particle growth. If the number of primary particles per agglomerate increases, then coagulation is the cause of the particle growth. If this increase is not apparent, then the change in primary particle size must be causing the change in mobility diameter. Figure 6.4.1 shows this comparison for the lean soot particle distribution using the 27 mm leak size after applying the Lall and Friedlander (2006) model.

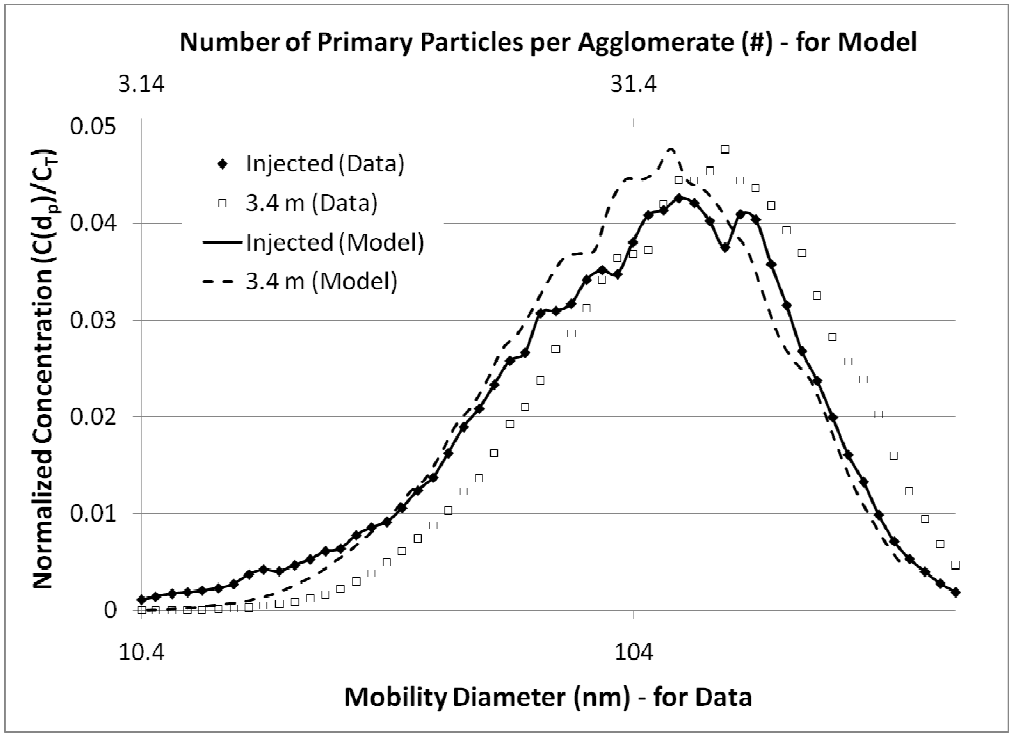

Figure 6.4.1: Normalized concentration plotted against number of primary particles per agglomerate and mobility diameter for the lean soot distribution, using 27 mm leak size.

Figure 6.4.1 shows the number of primary particles per agglomerate does not increase between the injection point and 3.4 m downstream. The particle size distribution does not shift when plotted against number of primary particles per agglomerate calculated with the Lall and Friedlander (2006) model. Therefore the increase in particle size (mobility diameter) cannot be caused by coagulation. Figure 6.4.2 shows the number of primary particles per agglomerate for the TiO_2 particle distribution with the 27 mm leak size. In this case, the particle size distribution at 3.4 m downstream decreases to lower than the particle size distribution at the injection point after applying the Lall and Friedlander (2006) model. So the model does not match up as well in this situation, yet also shows coagulation cannot cause the shift towards larger particles. The rich soot distribution and SiO_2 data cannot be used with the Lall and Friedlander (2006) model. The rich soot particles are not loose agglomerates and the SiO_2 particle generation process was not consistent throughout the duration of the experiments (discussed in Appendix H).

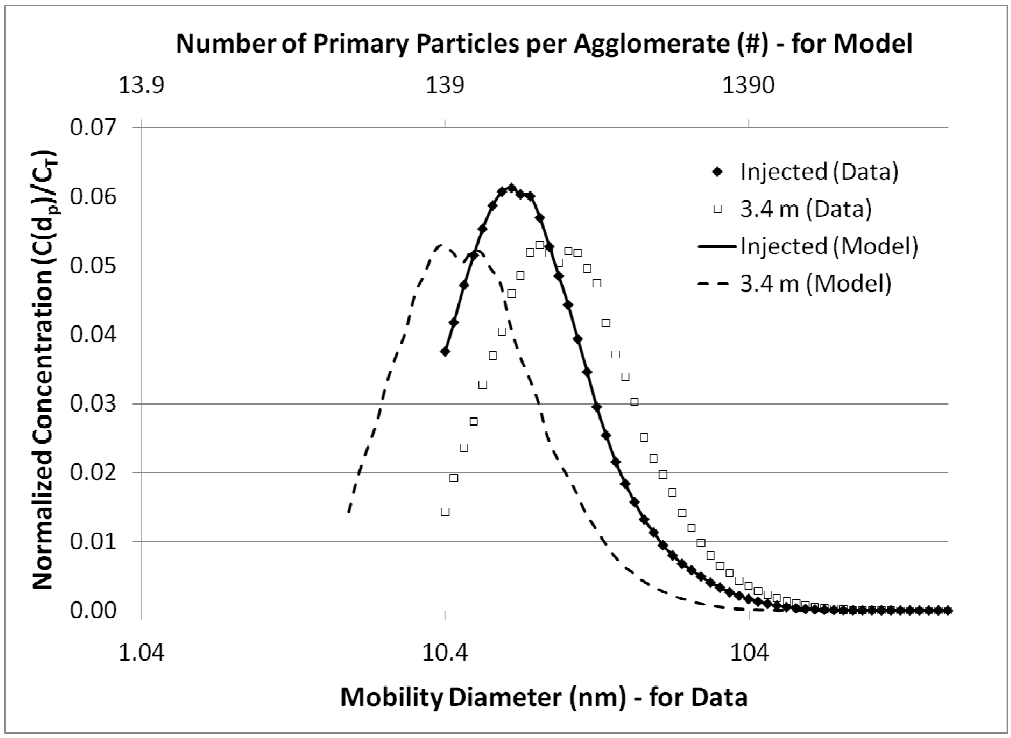

Figure 6.4.2: Normalized concentration plotted against number of primary particles per agglomerate and mobility diameter for the TiO_2 distribution, using 27 mm leak size.

Section 6.5: Conservation of Mass Analysis

The theory of combustion gas nucleation can be tested with a simple Conservation of Mass analysis. The number of primary particles per agglomerate does not change between the injection site and 3.4 m downstream, yet there is an increase in mobility diameter. If the sub-primary particles formed within the sampling probe at the injection point by instantaneous homogeneous nucleation, then the mass of that condensed matter should be conserved between the injection point and 3.4 m downstream as the gases condense onto agglomerates within the wind tunnel. Therefore, the mass of particles at the injection point (sub-primary and agglomerates) must be equal to the mass of particles at 3.4 m downstream (assuming no change in particle density and no particle deposition onto the walls of the wind tunnel). The lean fuel air mixture and 27 mm leak size results

will be used to test this particle formation theory because the size of sub-primary particles, primary particles, and agglomerates (mobility diameter) have been measured at both the injection point and 3.4 m downstream.

The first step is determining the initial concentration of sub-primary particles. According to the NAS manual, particles less than 20 nm are sampled with approximately 100% efficiency. Therefore the sub-primary particles deposited on the TEM grids represent the distribution of sub-primary particles. The number of sub-primary particles per unit area on the grid should represent the cross-sectional surface area concentration (C_{sa}). The total cross-sectional area of the NAS sampler was measured at the TEM grid location (A_s). The sample flow rate (Q_s) and time (T_s) are both known, as these parameters were set during sampling. Therefore the concentration of sub-primary particles (C_{sp}) can be determined using these terms in Equation 6.5.1. After finding C_{sp}, the primary particle diameter can be used to get the total volumetric concentration (V_T), outlined in Equations 6.5.2 and 6.5.4, assuming the sub-primary particles are mono-dispersed (n = 1). The sample calculations can be found in Appendix K.

Equation 6.5.1: $$C_{sp}\left(\frac{\#}{cm^3}\right) = \frac{(C_{sa})(A_s)}{(Q_s)(T_s)}$$

Equation 6.5.2: $$V_i\left(\frac{\mu m^3}{cm^3}\right) = \frac{\pi}{6} C_i d_i^3$$

Equation 6.5.3: $$V_i\left(\frac{\mu m^3}{cm^3}\right) = \frac{\pi}{6} K C_m \left(\frac{d_m}{d_{pp}}\right)^{D_f} d_{pp}^3$$

Equation 6.5.4: $$V_T\left(\frac{\mu m^3}{cm^3}\right) = \sum_{i=1}^{n} V_i$$

To determine the volume of an agglomerate, a combination of Equations 6.3.1 and 6.5.2 must be used. This is Equation 6.5.3, which will be used to determine the agglomerate volume for each mobility diameter measured by the SMPS. The total volume is obtained by applying Equation 6.5.4. The sample calculations can be found in Appendix K. Equation 6.5.3 and 6.5.4 were applied at the injection point and 3.4 m downstream. The total volume concentrations are shown in Table 6.5.1.

Table 6.5.1: Total volume concentration ($\mu m^3/cm^3$) of sub-primary particles and agglomerates at the injection point and 3.4 m downstream for the Lean soot and 27 mm leak distribution.

Injected			**3.4 m**
Sub-Primary	Agglomerates	Total	Agglomerates
3.1E+04	2.8E+04	**6.0E+04**	**2.5E+05**

It is unlikely the sub-primary particle mass is greater than the agglomerate mass at the injection point. The problem arises during counting of the sub-primary particles. Some of the sub-primary particles are too small to be measured accurately, but they are not too small to be counted. Therefore the volume of these sub-primary particles is exaggerated in this analysis. The volume at 3.4 m downstream is also exaggerated due to the dilution ratio.

The dilution ratio within the wind tunnel is 1.8:1000 (injected mass to background air mass). However, the majority of the thermal aerosol plume travels to the upper portion of the wind tunnel. This aerosol is then unaffected by the majority of the background air

mass. Due to the uneven mixing within the wind tunnel it is not possible to determine the actual dilution ratio. A best estimate from the mapping experiments would decrease the dilution ratio by 75 - 87.5%, which would result in an increase in agglomerate volume concentration at 3.4 m downstream by the same amount.

This analysis technique is not valid for the current study, since the sub-primary particle volume at the injection point and the agglomerate volume at 3.4 m downstream are incorrect and cannot be accurately corrected. The future work section outlines a method of producing and injecting a combustion aerosol to account for thermal buoyancy and unknown dilution through the use of a different experimental setup.

Coagulation is likely not the cause of the particle growth noticed in the current study for Soot (Lean fuel/air mixture) and TiO_2. The particles likely grow due to the increase in primary particle size, which may have been caused by an internal restructuring of the particles, or through nucleation of the combustion vapors. Internal restructuring may have caused a decrease in density which would cause a volume increase, but this is just a theory. A nucleation model would help determine if nucleation of combustion vapors caused the particle growth.

A nucleation model is not possible to create without knowing the mass concentration of the injected burner exhaust gases. A supersaturated vapor may form due to the dilution of the combustion gases in the wind tunnel and cause nucleation, which would lead to particle growth. However, nucleated vapors may evaporate under the low pressure and high energy electron beam of the TEM microscope. More research must be conducted to determine how these exhaust gases interact with combustion particles during dilution.

Section 7
Conclusions

The current study began with a feasibility study in order to compare an established aerosol measurement instrument (SMPS) to a new measurement instrument (NSAM). When operating the NSAM and SMPS simultaneously, the aerosol distribution must fall within the size range of 20 to 400 nm for an accurate measurement. The devices correlate very well when using a liquid aerosol (in the proper size range), since liquid aerosols form spherical particles. The devices do not correlate as well when using a salt aerosol (KCl solution) due to the shape factor of the aerosol particles (cubic shape, not spherical). Therefore the shape of the aerosol particles affects the response of the NSAM. These results ultimately led to a new way of measuring aerosol size change, utilized in the current study.

The shape of the particles is not considered when determining the ratio of NSAM measured Alveolar Lung Deposited Surface Area (LDSA) concentration to SMPS measured total number concentration. The NSAM/SMPS ratio provides a measure of LDSA per particle, which provided a good indication of particle change for most of the

examined aerosols in the current study. If this ratio increases, then particle growth is likely occurring since the particles have gained surface area. The Soot (Lean fuel/air mixture) aerosol experienced particle growth with both leak sizes (27 mm and 10 mm). The Soot (Rich fuel/air mixture) aerosol experienced particle growth with only one leak size (27 mm). The Soot (Rich fuel/air mixture) aerosol formed a bi-modal distribution when using the 10 mm leak size, which lead to a discrepancy in the ratio. When a new mode is formed or an established mode disappears within a distribution, this method will not provide a good indication of particle change as an aerosol ages. The TiO_2 aerosol experienced particle growth with one leak size (27 mm); however the 10 mm leak size did not show a statistically significant growth throughout the duration of the wind tunnel using this NSAM/SMPS ratio. The SiO_2 aerosol was not consistently produced within the burner and the data cannot be used to draw significant conclusions.

The SMPS data is useful beyond the NSAM/SMPS ratio. The SMPS data was used to create normalized particle size distributions and geometric mean particle diameters for each condition and location examined. Comparisons were made between geometric mean particle diameters at the injection point and locations downstream (for each condition).

- The Soot (Lean fuel/air mixture) aerosol experienced an increase in geometric mean particle diameter between the injection point and 0.9 m downstream for each leak size (no change after 0.9 m).
- The Soot (Rich fuel/air mixture) aerosol experienced an increase in geometric mean particle diameter between the injection point and 0.9 m downstream (no

change after 0.9 m) for the 27 mm leak size only. This was due to the formation of the bi-modal distribution when using the 10 mm leak size (Rich soot aerosol).

- The TiO_2 aerosol experienced an increase in geometric mean particle diameter between the injection site and 0.9 m (and 1.8 m) downstream for each leak size. The change between the injection site and 3.4 m downstream was not statistically significant for TiO_2 due to issues with the precursor delivery system (clogged N_2 nozzle).
- There was no change in geometric mean particle diameter between the downstream locations (0.9 m, 1.8 m, and 3.4 m) for aerosols tested in the current study.

The geometric mean diameter analysis incorporated statistics to show a change in the aerosol distribution. The plots of normalized particle size distributions illustrated this change for each condition. The Soot (Lean and Rich fuel/air mixtures) and TiO_2 normalized particle size distributions shifted to the right (increased in mobility diameter) downstream of the injection point. The Soot (Rich fuel/air mixture) distribution formed a small mode (d_g < 20 nm) of particles downstream of the injection point when using the 10 mm leak size.

These small mode particles were most likely semi-volatile, but this cannot be verified without further experimentation. These particles likely formed just downstream of the injection probe, due to the turbulence induced by the 10 mm leak size and the amount of excess unburned fuel (with the Rich fuel/air mixture). The Richardson number (Ri) changes from 197 to 0.42 when changing leak sizes (from 27 mm to 10 mm) at exhaust temperatures (calculations performed using air) with the Rich fuel/air mixture.

This indicates a change in flow regime from laminar to turbulent. Ultrafine particle formation has been attributed to flow regime transition in polluted air (Wehner et al., 2010), by local supersaturation of precursor gases, which leads to nucleation.

The TEM images were initially gathered to provide a qualitative analysis of particle morphology (single primary particles, sintered aggregates, or loose, chain-type agglomerates). Fortunately, these images were clear enough to determine primary particle size within agglomerates imaged at the injection point and 3.4 m downstream for the Soot (Lean fuel/air mixture) and TiO_2 distributions when using the 27 mm leak. Primary particle sizes were determined at the injection point when using the 27 mm leak only, since the particles could not be measured at the injection point when using the 10 mm leak. The primary particle size increased between the injection point and 3.4 m downstream for the Soot (Lean fuel/air mixture) and TiO_2 distributions.

The normalized particle size distributions for Soot (Lean fuel/air mixture) and TiO_2 were re-plotted against the number of primary particles per agglomerate (instead of mobility diameter). This is simply a change in x-axis by scaling mobility diameter to number of primary particles per agglomerate using the Lall and Friedlander (2006) model. This method can be used when primary particle size and mobility diameter are known. After changing the x-axis, the distributions at the injection point and 3.4 m downstream no longer depicted a shift for the Soot (Lean fuel/air mixture) aerosol. Therefore there is no change in the number of primary particles per agglomerate, which indicates coagulation is not the cause of the particle growth. The TiO_2 distribution was also plotted in this manner, and no longer shows an increase in particle size distribution;

however the small primary particle sizes may have affected the accuracy of the model in the case of TiO_2.

There are several factors presented in the literature, which could have caused primary particle growth between the injection point and 3.4 m downstream. Cooling and dilution effects of the wind tunnel background air may have induced molecular re-structuring within the primary particles, causing a density change. Cooling and dilution of the combustion vapors may have formed a supersaturated vapor causing nucleation. The sub-primary particles may have coagulated onto the surfaces of the primary particles causing growth. An attempt to address these theories was made in the Section 6, however none of these theories can be tested with the data gathered in the current study. Future experiments are needed to determine the specific cause of the primary particle growth, which are outlined in Section 8.

In the event of a leak in a nanoparticle production process, the workers in the area of the leak would be exposed to high concentrations of dangerous nanoparticles. If soot is being produced, then a bi-modal distribution will be released into the workplace. The first mode may consist of small semi-volatile particles (< 20 nm) if using a Rich fuel/air mixture (depending on the cooling rate of the leaked combustion vapors). The particles grow after being leaked; however coagulation is likely to have completed within the particle reactor and will likely not continue following the leak. Most of the toxicology studies have focused on the toxicity of a specific aerosol particle type, chemistry, size, and/or concentration. Future toxicology studies should account for the change in particle size when examining the adverse health effects of a specific aerosol chemistry, size, and concentration.

Section 7.1: Potential Adverse Health Effects of Leaked Aerosol

Chronic exposure to particulate matter causes workplace related diseases (Borm, 2002; Castranova, 2000). Incidences of lung inflammation, coughing, and wheezing have been shown in epidemiological studies investigating ultrafine particles and respiratory illness (Handy and Shaw, 2007). Such epidemiological studies have also shown carcinogenic effects (Handy and Shaw, 2007), although the toxic effects of nanoparticle exposure are currently not well understood (Donaldson et al., 2004). There has not been a dose-response relationship established for soot exposure as occupational monitoring in nanoparticle production facilities is still in its infancy (Morawska et al., 2009). Several long-term diesel exhaust exposure studies have shown accumulation of soot particles in the lungs of exposed rats (Gradon et al., 1996). This accumulation without removal could lead to carcinogenic health effects (Gradon et al., 1996). All locations downstream from the injection point show a decrease in total particle concentration of at least 2 orders of magnitude for each fuel/air mixture and leak size tested. Although this concentration is low enough to prohibit coagulation, it may still be high enough to cause adverse health effects for anyone exposed, especially over a long period of exposure.

If the workplace is to be monitored for the situation examined in the current study, the locations of monitors and measurement metrics must be considered. As stated previously, this is a very hot aerosol leaking into a cool background air flow. An accidentally released plume of particles will eventually disperse, but first buoyancy forces cause the particles to rise above the leak site. This could push the particles above the breathing zone of any potentially exposed workers, depending on the layout of the production facility. If the facility has walk-ways or ventilation ductwork above the leak,

then workers could still be exposed. If drawn into ductwork, the leaked particles could be dispersed throughout the building.

It would be nice if every square inch of the production plant could be accurately monitored in real-time, but this suggestion would never be adopted. Current work place practices of periodic monitoring may not be able to detect a high concentration leak prior to hazardous worker exposure (and potentially irreversible health damage). A real-time monitor should be in place to measure the particle concentration within the breathing zone of at-risk workers. The specific location of the particle monitor will be different for each site, depending on the layout of the production facility. If an air supply ventilation source (ductwork) exists above potential leak sites, then this should be tapped for periodic monitoring. Number and surface area measurement devices have each proven to be effective for monitoring nanoparticle concentrations in real-time. Either of the devices utilized in the current study would be appropriate for real-time nanoparticle concentration monitoring in a nanoparticle production facility. A CPC is recommended over a SMPS for number concentration measurements.

The most effective means of worker protection is not always Personal Protective Equipment (PPE). PPE, such as goggles, respirators, and protective clothing, can be used incorrectly without proper training. Individual employees can also find it difficult to wear PPE as facial features (i.e. facial hair, glasses) differ from person to person. Engineering controls, such as air-tight enclosures and local exhaust may be effective for a leak. Local exhaust is typically utilized during specific activities, and would not be ideal for an undetected leak. The burner may be able to be contained within an air-tight enclosure,

and a clever design may mitigate the potential for worker exposure. These designs would need to be created specifically for each facility.

The easiest and most reliable method of cleaning a contaminated workplace is general ventilation with filtration. Recirculating the air within the workplace through low efficiency filters would remove airborne pollutants with HEPA efficiency (Pui et al., 2008). Injecting a concentration of large particles to remove small particles by scavenging may also be effective. Particle scrubbing was briefly investigated during the current study; however more work is required to determine the efficacy of this technique.

Section 8
Future Work

The main objective of the current study was accomplished despite the following setbacks. The injection probe, the sampling section, and the wind tunnel were built, rebuilt, and reconfigured, respectively, for the current study. This new equipment and changes to existing equipment still provided a non-ideal experimental setup, due to the thermal buoyancy of the injected aerosol. The injection probe could have been made shorter to allow more space within the wind tunnel for the aerosol plume to rise before wall affects became apparent. The sampling section was not designed to measure the entire cross-section of the wind tunnel. Instead it was limited at the upper and lower portion due to the dilution air supply (providing dilution at the sampling location). The wind tunnel was originally designed to induce turbulent mixing, while low turbulence conditions were desired for the current study. Reconfiguring the wind tunnel and introducing flow straighteners helped correct the mixing issues, however designing a new experimental setup is recommended for future studies.

The wind tunnel is horizontal, meaning horizontal air flow. The burner aerosol is hot and buoyant, which causes vertical air flow. Therefore the wind tunnel should be vertical, not horizontal when examining buoyant aerosols. The wind tunnel also does not need to be so large. The aerosol change may occur instantly, but it definitely occurs within 0.9 m from the leak. In order to repeat this experiment with limited affect of the wind tunnel, a vertical stack should contain the burner aerosol and provide background air flow. The background air should be supplied using compressed air (if possible) instead of a fan to limit the turbulence within the stack/column. The injection probe would not be needed if the burner were placed directly inside of the vertical stack. The sampling probe can be placed on the vertical stack itself; able to be moved vertically (up/down) and horizontally (in/out) through the column. This design can be very similar to the current study. The vertical stack should have a circular cross section for symmetrical particle dispersion measurement capacity.

The measurements in future studies should occur at the injection site and downstream of the injection site, simultaneously. Any day-to-day variations in burner production can be accounted for with this type of measurement scheme. Therefore any change in particle size distribution, primary particle size, sub-primary particles, and chemistry would be undeniable (relative to the current study).

A Nano-DMA may be able to measure the sub-primary particles noticed in TEM images at the injection site. However, a systematic approach should be used for gathering TEM images. Each TEM grid should be imaged prior to sampling to account for any background discrepancies. At least 2 grids should be sampled at each location to ensure repeatability of primary particle size. The Lacey substrate is not desirable for sampling

soot since both are amorphous carbon. Chemical composition of the burner exhaust vapors should be measured at the injection point as well. Determining this complex chemistry may aid in developing a nucleation model for examined combustion fuels.

The Soot (Rich fuel/air mixture), 10 mm leak size experiments formed a bi-modal distribution at locations downstream of the injection point. The first mode of this distribution could not be imaged with the TEM, indicating it is most likely composed of semi-volatile particles. A thermal denuder or catalytic stripper could be used to remove this semi-volatile fraction. Sampling with and without such a device would show if the first mode were removed, and therefore, truly semi-volatile. These experiments could be conducted with the current wind tunnel setup.

Particle scrubbing was tested in the current study. The wind tunnel was extended so a background aerosol of Oleic acid could be injected upstream of the burner particle injection point. The schematic is shown as Figure 8.1. The Soot (Rich fuel/air mixture) distribution with the 10 mm leak size was used in these particle scrubbing experiments, because of the bi-modal distribution. The background particles did reduce the number of smaller, first mode particles, but the second mode particles were not affected. The results are shown in Figure 8.2. When using Soot and Oleic acid, particles less than 35 nm are reduced by approximately 38%, compared to Soot (Rich fuel/air mixture) alone.

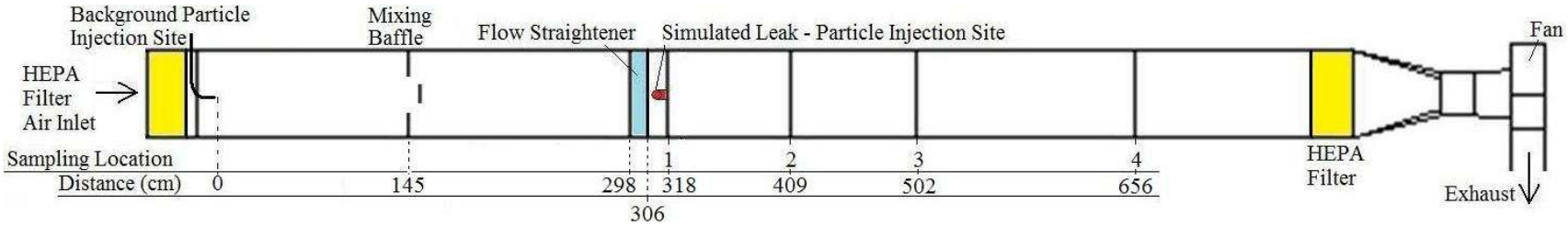

Figure 8.1: Wind tunnel reconfigured for particle scrubbing experiments.

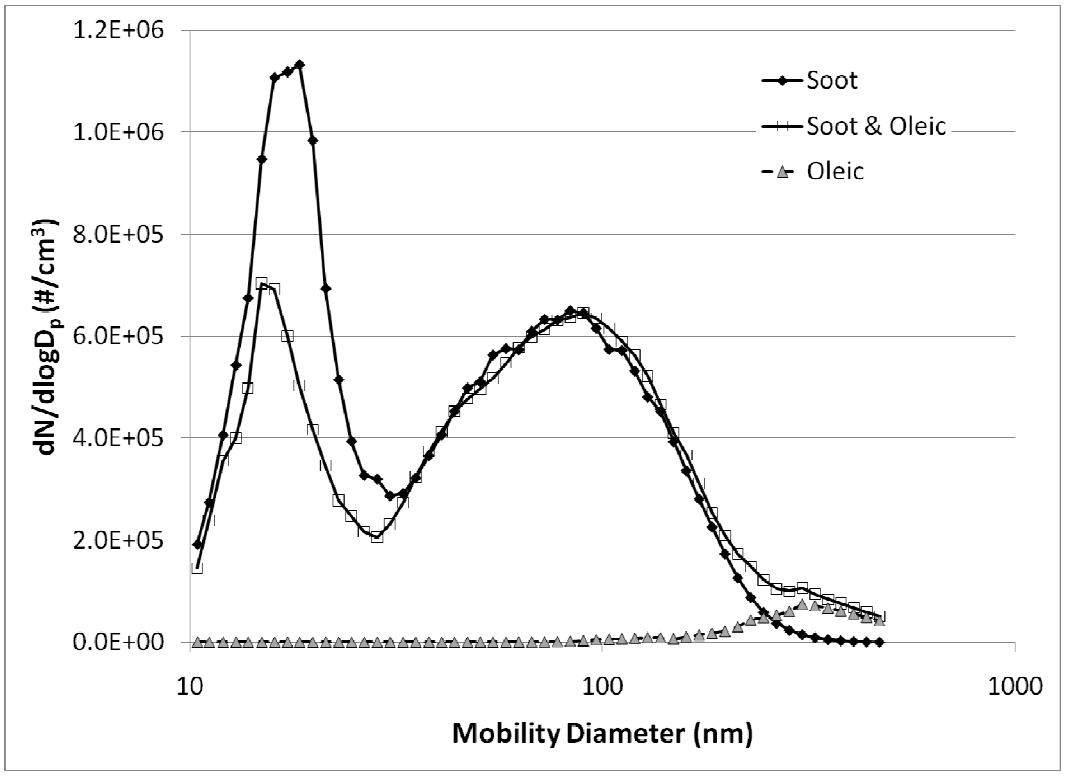

Figure 8.2: Results of particle scrubbing experiments using Oleic acid background particles and Rich soot fuel/air mix with 10 mm leak size.

Perhaps larger background particles would have affected the second soot mode particles; however larger particles would have been above the size range of the SMPS. An additional measurement instrument would be needed for larger particles (d_g > 500 nm). An Aerodynamic Particle Sizer (APS) is not recommended because particle distributions are measured for aerodynamic particle size, which does not have a direct correlation to mobility diameter for agglomerates.

There were some problems when using the organic precursors for creating metal-oxide nanoparticles with the diffusion burner. The TiO_2 particles were created with TTIP, which eventually clogged the carrier gas injection nozzle and affected the data at 3.4 m downstream. This could have been prevented by rinsing the carrier gas injection nozzle

properly. It also could have potentially been prevented by leaving the nozzle inside the precursor bottle; however University of Minnesota safety regulations require hazardous substances to be stored properly when not in use. If future studies are conducted within a fume hood, then the carrier gas nozzle can remain submerged within the precursor bottle without violating University of Minnesota safety regulations (assuming the bottle is kept within the fume hood).

The SiO_2 precursor (HMDSO) did not cause a problem. The particles produced with HMDSO however, did cause a problem within the burner. The formation of the material cap caused a change in particle properties over the duration of the burner operation. When using HMDSO in future studies, the burner should be monitored during particle production to identify this cap formation as it occurs. If detected early, this cap formation can potentially be avoided. Injecting some diluting Nitrogen gas into the burner causes the flame to lift off the surface of the burner, preventing SiO_2 particles from depositing on the burner gas outlet. Premixing the precursor and fuel prior to feeding into the burner may prevent this cap formation as well. These techniques were learned through personal communications with other researchers using HMDSO in a diffusion burner setup to create SiO_2 nanoparticles.

Bibliography

A. Afshari, U. Matson, and L. E. Ekberg, Characterization of indoor sources of fine and ultrafine particles: a study conducted in a fullscale chamber, *Indoor Air*, **15**, 141-150 (2005).

R. J. Aitken, K. S. Creely, and C. L. Tran, Nanoparticles: An occupational hygiene review, Suffolk, UK: Health and Safety Executive (2004).

K. K. Akurati, A. Vital, U. E. Klotz, B. Bommer, T. Graule, and M. Winterer, Synthesis of non-aggregated titania nanoparticles in atmospheric pressure diffusion flames, *Powder Technology*, **165**, 73-82 (2006).

K. K. Akurati, A. Vital, R. Hany, B. Bommer, T. Graule, and M. Winterer, One-step flame synthesis of SnO_2/TiO_2 composite nanoparticles for photocatalytic applications, *International Journal of Photoenergy*, **7**, 153-161 (2005).

AMS Glossary of Meteorology website, (http://amsglossary.allenpress.com/glossary).

O. I. Arabi-Katbi, S. E. Pratsinis, and P. W. Morrison Jr, In situ infrared measurements on TiO_2 flames: gas and particle concentrations, *AIChE Journal*, **48**(1), 59-68 (2002).

O. I. Arabi-Katbi, S. E. Pratsinis, P. W. Morrison, and P. M. Megadiris, Monitoring the flame synthesis of TiO_2 particles by in-situ FTIR spectroscopy and thermophoretic sampling, *Combustion and Flame*, **124**, 560-572 (2001).

C. Asbach, H. Fissan, B. Stahlmecke, T. A. J. Kuhlbusch, and D.Y.H. Pui, Conceptual limitations and extensions of lung-deposited Nanoparticle Surface Area Monitor (NSAM), *J Nanopart Res*, DOI 10.1007/s11051-008-9479-8.

M. D. Avakian, B. Dellinger, H. Fiedler, B. Gullet, C. Koshland, S. Marklund, G. Oberdorster, S. Safe, A. Sarofim, K. R. Smith, D. Schwatrz, and W. A. Suk, The Origin, Fate, and Health Effects of Combustion By-Products: A Research Framework, *Environmental Health Perspectives*, **110**(11), 1155-1162 (2002).

R. Baan, K. Straif, Y. Grosse, B. Secretan, F. E. Ghissassi, and V. Cogliano, Carcinogenicity of carbon black, titanium dioxide, and talc, *Lancet Oncol*, **7**, 295-296 (2006).

J. M. Balbus, A. D. Maynard, V. L. Colvin, V. Castranova, G. P. Daston, R. A. Denison, K. L. Dreher, P. L. Goering, A. M. Goldberg, K. M. Kulinowski, N. A. Monteiro-Riviere, G. Oberdorster, G. S. Omenn, K. E. Pinkerton, K. S. Ramos, K. M. Rest, J. B. Sass, E. K. Silbergeld, and B. A. Wong, Meeting report: hazard assessment for nanoparticles – report from an interdisciplinary workshop, *Environmental Health Perspectives*, **115**(11), 1654-1659 (2007).

M. Balthasar and M. Frenklach, Detailed kinetic modeling of soot aggregate formation in laminar premixed flames, *Combustion and Flame*, **140**, 130-145 (2005).

M. Balthasar, F. Mauss, A. Knobel, and M. Kraft, Detailed modeling of soot formation in a partially stirred plug flow reactor, *Combustion and Flame*, **128**, 395-409 (2002).

P. A. Baron, A. D. Maynard, and M. Foley, Evaluation of aerosol release during the handling of unrefined single walled carbon nanotube material, *NIOSH DART-02-191 Rev 1.1*, 1-21 (2003).

S. Becker, J. M. Soukup, C. Sioutas, and F. R. Cassee, Response of human alveolar macrophages to ultrafine, fine, and coarse urban air pollution particles, *Experimental Lung Research*, **29**, 29-44 (2003).

R. Behra and H. Krug, Nanoparticles at large, *Nature Nanotechnology*, **3**, 253-254 (2008).

D. Bemer, M. T. Lecler, R. Regnier, G. Hecht, and J. M. Gerber, Measuring the emission rate of an aerosol source placed in a ventilated room using a tracer gas: influence of particle wall deposition, *Ann. Occup. Hyg*, **46**(3), 347-354 (2002).

M. Berges, C. Mohlmann, B. Swennen, Y. V. Rompaey, and P. Berghmans, Workplace exposure characterization at TiO_2 nanoparticle production, in: Proceedings of the 3rd International Symposium on Nanotechnology, Occupational and Environmental Health, Taipei, Taiwan (2007).

H. Bockhorn (Ed.), Soot Formation in Combustion: Mechanisms and Models, Springer, Berlin, 1994.

P. Boffetta, A. Soutar, J. W. Cherrie, F. Granath, A. Andersen, A. Anttila, M. Blettner, V. Gaboriaeu, S. J. Klug, S. Langard, D. Luce, F. Merletti, B. Miller, D. Mirabelli, E. Pukkala, H. O. Adami, and E. Weiderpass, Mortality among workers employed in the titanium dioxide production industry in Europe, *Cancer Causes Control*, **15**, 697-706 (2004).

P. J. A. Borm, Particle toxicology: from coal mining to nanotechnology, *Inhalation Toxicology*, **14**, 311-324 (2002).

H. Briesen, A. Fuhrmann, and S. E. Pratsinis, The effect of precursor in flame synthesis of SiO_2, *Chem Eng Sci*, **53**(24), 4105-4112 (1998).

D. H. Brouwer, J. H. J. Gijsbers, and M. W. M. Lurvink, Personal exposure to ultrafine particles in the workplace: Exploring sampling techniques and strategies, *Ann Occup Hyg*, **48**(5), 439-453 (2004).

D. M. Brown, V. Stone, P. Findlay, W. MacNee, and K. Donaldson, Increased inflammation and intracellular calcium caused by ultrafine carbon black is independent of transition metals or other soluble components, *Occup Environ Med*, **57**, 685-691 (2000).

V. Castranova, From coal mine dust to quartz: mechanisms of pulmonary pathogenicity, *Inhalation Toxicology*, **12**, 7-14 (2000).

D. C. Chalupa, P. E. Morrow, G. Oberdorster, M. J. Utell, and M. W. Frampton, Ultrafine particle deposition in subjects with asthma, *Environ Health Perspect*, **112**(8), 879-882 (2004).

T. M. Chen, J. Gokhale, S. Shofer, and W. G. Kuschner, Outdoor Air Pollution: Particulate Matter Health Effects, *Am J Med Sci*, **333**(4), 235-243 (2007).

H. Y. Chuang and D. H. Chen, Catalyst-free low temperature synthesis of discrete anatase titanium dioxide nanocrystals with highly thermal stability and UVC-cut capability, *J Nanopart Res*, **10**, 233-241 (2008).

V. L. Colvin, The potential environmental impact of engineered nanomaterials, *Nature Biotechnology*, **21**(10), 1166-11 (2003).

C. C. Daigle, D. C. Chalupa, F. R. Gibb, P. E. Morrow, G. Oberdorster, M. J. Utell, and M. W. Frampton, Ultrafine Particle Deposition in Humans During Rest and Exercise, *Inhal Toxicol*, **15**, 539-552 (2003).

A. D'Anna, Combustion-formed nanoparticles, *Proceedings of the Combustion Institute*, **32**, 593-613 (2009).

A. D'Anna and J. H. Kent, A model of particulate and species formation applied to laminar, nonpremixed flames for three aliphatic-hydrocarbon fuels, *Combust Flame*, **152**, 573-587 (2008).

A. DeFilippo and M. M. Maricq, Diesel nucleation mode particles: semivolatile or solid? *Environ Sci Technol*, **42**, 7957-7962 (2008).

S. di Stasio, Electron microscopy evidence of aggregation under three different size scales for soot nanoparticles in flame, *Carbon*, **39**(1), 109-118 (2001).

R. A. Dobbins, R. A. Fletcher, and H.-C. Chang, The evolution of soot precursor particles in a diffusion flame, *Combust Flame*, **115**, 285-298 (1998).

R. A. Dobbins and C. M. Megaridis, Morphology of flame-generated soot as determined by thermophoretic sampling, *Langmuir*, **3,** 254-259 (1987).

K. Donaldson, V. Stone, C. L. tran, W. Kreyling, and P. J. A. Borm, Nanotoxicology, *Occup Environ Med*, **61**, 727-728 (2004).

J.-B. Donnet, R. C. Bansal, M.-J. Wang, Carbon Black, Marcel Dekker, New York, 1993.

M. J. Dunn, J.-L. Jimenez, D. Baumgardner, T. Castro, P. H. McMurry, and N. J. Smith, Measurements of Mexico City nanoparticles size distributions: Observations of new particle formation and growth, *Geophys Res Lett*, **31**, L10102 (2004), doi: 10.1029/2004GL019483.

ET website, Engineering Toolbox - http://www.engineeringtoolbox.com.

E. Fabian, R. Landsiedel, L. Ma-Hock, K. Wiench, W. Wohlleben, and B. van Ravenzwaay, Tissue distribution and toxicity of intravenously administered titanium dioxide nanoparticles in rats, *Arch Toxicol*, **82**, 151-157 (2008).

C. W. Fan and J. J. Zhang, Characterization of emissions from portable household combustion devices: particle size distributions, emission rates and factors, and potential sources, *Atmos Environ*, **35**, 1281-1290 (2001).

H. Fissan, S. Neumann, A. Trampe, D. Y. H. Pui, and W. G. Shin, Rationale and principle of an instrument measuring lung deposited nanoparticle surface area, *Journal of Nanoparticle Research*, **9**, 53-59 (2007).

M. W. Frampton, Systemic and cardiovascular effects of airway injury and inflammation: ultrafine particle exposure in humans, *Environ. Health Perspect*, **109**(sup 4), 529-532 (2001).

M. Frenklach, Reaction mechanism of soot formation in flames, *Phys Chem Chem Phys*, **4**, 2028-2037 (2002).

J. P. Fryzek, B. Chadda, D. Marano, K. White, S. Schweitzer, J. K. McLaughlin, and W. J. Blot, A cohort mortality study among titanium dioxide manufacturing workers in the United States, *J Occup Environ Med*, **45**, 400-409 (2003).

F. Fugaciu, H. Hermann, and G. Seifert, Concentric-shell fullerenes and diamond particles: A molecular-dynamics study, *Physical Review B*, **60**(15), 10711-10714 (1999).

E. Gehin, O. Ramalho, and S. Kirchner, Size distribution and emission rate measurement of fine and ultrafine particle from indoor human activities, *Atmospheric Environment*, **42**, 8341-8352 (2008).

L. Gradon, S. E. Pratsinis, A. Podgorski, S. J. Scott, and S. Panda, Modeling retention of inhaled particles in rat lungs including toxic and overloading effects, *J Aerosol Sci*, **27**(3), 487-503 (1996).

R. N. Grass, S. Tsantilis, and S. E. Pratsinis, Design of high-temperature, gas-phase synthesis of hard or soft TiO_2 agglomerates, *AIChE Journal*, **52**(4), 1318-1325 (2006).

V. H. Grassian, P. T. O'Shaughnessy, A. Adamcakova-Dodd, J. M. Pettibone, and P. S. Thorne, Inhalation exposure study of titanium dioxide nanoparticles with a primary particle size of 2 to 5 nm, *Environ Health Perspect*, **115**, 397-402 (2007).

P. Gwaze, O. Schmid, H. J. Annegarn, M. O. Andreae, J. Huth, G. Helas, Comparison of three methods of fractal analysis applied to soot aggregates from wood combustion, *J Aerosol Sci*, **37**, 820-838 (2006).

M. R. Gwinn and V. Vallyathan, Nanoparticles: Health Effects – Pros and Cons, *Environ. Health Perspect*, **114**(12), 1818-1825 (2006).

J. H. Han, E. J. Lee, J. H. Lee, K. P. So, Y. H. Lee, G. N. Bae, S. B. Lee, J. H. Ji, M. H. Cho, and I. J. Yu, Monitoring multiwalled carbon nanotube exposure in carbon nanotube research facility, *Inhal Toxicol*, **20**, 741-749 (2008).

R. D. Handy and B. J. Shaw, Toxic effects of nanoparticles and nanomaterials: implications for public health, risk assessment and the public perception of nanotechnology, *Health Risk Soc*, **9**, 125-144 (2007).

R. Hauser, E. A. Eisen, L. Pothier, and D. C. Christiani, A prospective study of lung function among boilermaker construction worker exposed to combustion particles. *Am. J. Ind. Med.*, **39**, 454-462 (2001).

M. C. Heine and S. E. Pratsinis, Agglomerate TiO_2 Aerosol Dynamics at High Concentrations, *Part Part Syst Charact*, **24**, 56-65 (2007).

H. Hermann, F. Fugacui, and G. Seifert, Towards controlled production of specific carbon nanostructures - A theoretical study on structural transformations of graphitic and diamond particles, *Applied Physics Letters*, **79**(1), 63-65 (2001).

W. C. Hinds, Aerosol Technology: Properties, Behavior, and Measurement of Airborne Particles, 2nd Ed, John Wiley & Sons, Inc, (1999).

A. L. Holder, D. Lucas, R. Goth-Goldstein, and C. P. Koshland, Cellular response to diesel exhaust particles strongly depends on the exposure method, *Toxicological Sciences*, **103**(1), 108-115 (2008).

M. N. Holman, M. Novotny, M. Kemsley, et al, The nanotech report, 5th ed. New York: Lux Research, 1-298 (2007).

ICRP Publication 66: Human respiratory tract model for radiological protection, *Annals of the ICRP*, **24**/1-3 (1994).

H. K. Kammler, R. Jossen, P. W. Morrison Jr, S. E. Pratsinis, and G. Beaucage, The effect of external electric fields during flame synthesis of titania, *Powder Technol*, **135-136**, 310-320 (2003).

H. K. Kammler, R. Mueller, O. Senn, and S. E. Pratsinis, Synthesis of Silica-Carbon particles in a turbulent H_2-air flame aerosol reactor, *AIChE J*, **47**(7), 1533-1543 (2001).

H. K. Kammler and S. E. Pratsinis, *Chem Eng Process*, **39**, 219-227 (2000).

C. R. Kaplan and K. Kailsanath, Flow-field effects on soot formation in normal and inverse methane-air diffusion flames, *Combust Flame*, **124**, 275-294 (2001).

V. M. Kerminen, L. Pirjola, and M. Kulmala, How significantly does coagulation scavenging limit atmospheric particle production? *J Geophys Res Atmo*, **106**, 24119-24125 (2001).

C. H. Kim, F. Xu, and G. M. Faeth, Soot surface growth and oxidation at pressures up to 8.0 atm in laminar nonpremixed and partially premixed flames, *Combustion and Flame*, **152**, 2301-316 (2008).

C. S. Kim and P. A. Jaques, Total lung deposition of ultrafine particles in elderly subjects during controlled breathing, *Inhal Toxicol*, **17**, 387-399 (2005).

C. S. Kim and P. A. Jaques, Analysis of total respiratory deposition of inhaled ultrafine particles in adult subjects at various breathing patterns, *Aerosol Sci Technol*, **38**, 525-540 (2004).

S.C. Kim, J. Wang, M.S. Emery, W.G. Shin, G. W. Mulholland, and D.Y.H. Pui, Structural property effect of nanoparticle agglomerates on particle penetration through fibrous filter, *Aerosol Sci Technol*, **43**, 344-355 (2009).

W. Kim, C. M. Sorensen, D. Fry, and A. Chakrabarti, Soot aggregates, superaggregates, and gel-like networks in laminar diffusion flames, *J Aerosol Sci*, **37**, 386-401 (2006).

D. B. Kittelson, W. F. Watts, and J. P. Johnson, On-road and laboratory evaluation of combustion aerosols-Part I: Summary of diesel engine results, *J Aerosol Sci*, **37**, 913-930 (2006).

A. M. Knaapen, P. J. A. Borm, C. Albrecht, and R. P. F. Schins, Inhaled Particles and Lung Cancer. Part A: Mechanisms, *Int J Cancer*, **109**, 799-809 (2004).

E. Koike and T. Kobayashi, Organic extract of diesel exhaust particles stimulates expression of Ia and costimulatory molecules associated with antigen presentation in rat peripheral blood monocytes but not in alveolar macrophages, *Toxicol Appl Pharmacol*, **209**, 277-285 (2005).

U. O. Koylu, Y. Xing, and D. E. Rosner, Fractal Morphology analysis of combustion-generated aggregates using angular light scattering and electron microscope images, *Langmuir*, **11**, 4848-4854 (1995).

E. D. Kuempel, C. L. Tran, V. Castranova, and A. J. Bailer, Lung dosimetry and risk assessment of nanoparticles: evaluating and extending current models in rats and humans, *Inhal Toxicol*, **18**, 717-724 (2006).

T. A. J. Kuhlbusch, S. Neumann, and H. Fissan, Number size distribution, mass concentration, and particle composition of PM1, PM2.5, and PM10 in bag filling areas of carbon black production, *J Occup Environ Hyg*, **50**, 437-439 (2004).

M. Kulmala, U. Pirjola, and J. M. Makela, Stable sulphate clusters as a source of new atmospheric particles, *Nature*, **404**, 66-69 (2000).

A. A. Lall and S. K. Friedlander, On-line measurement of ultrafine aggregate surface area and volume distributions by electrical mobility analysis, I: Theoretical analysis, *J Aerosol Sci*, **37**, 260-271 (2006).

S. C. Lee, S. Lam, and H. K. Fai, Characterization of VOCs, ozone, and PM10 emissions from office equipment in an environmental chamber, *Building Environment*, **36**, 837-842 (2001).

C-.M. Liao, Y-.H. Chiang, and C.-P. Chio, Assessing the airborne titanium dioxide nanoparticle-related exposure hazard at workplace, *Journal of Hazardous Materials*, **162**, 57-65 (2009).

G. Liden and M. Harper, Analytical performance criteria: The need for an international convention for inhalable dust in calm air. *J Occup Environ Hyg*, **3**, D94-D101 (2006).

L. K. Limbach, Y. Li, R. N. Grass, T. J. Brunner, M. A. Huntermann, M. Muller, D. Gunter, and W. J. Stark, Oxide nanoparticle uptake in human lung fibroblasts: effects of particles size, agglomeration, and diffusion at low concentrations, *Environ Sci technol*, **39**, 9370-9376 (2005).

L. Ma-Hock, A. O. Gamer, R. Landsiedel, E. Leibold, T. Frechen, B. Sens, M. Linsenbuehler, and B. van Ravenzwaay, Generation and characterization of test atmospheres with nanomaterials, *Inhal Toxicol*, **19**, 833-848 (2007).

M. M. Maricq, Coagulation dynamics of fractal-like soot aggregates, *J Aerosol Sci*, **38**, 141-156 (2007a).

M. M. Maricq, Chemical characterization of particulate emissions from diesel engines: a review, *J Aerosol Sci*, **38**, 1079-1118 (2007b).

M. M. Maricq, A comparison of soot size and charge distributions from ethane, ethylene, acetylene, and benzene/ethylene premixed flames, *Combustion and Flame*, **144**, 730-743 (2006).

A. D. Maynard, P. A. Baron, M. Foley, A. A. Shvedova, E. R. Kisin, and V. Castranova, Exposure to carbon nanotube material: Aerosol release during the handling of unrefined single-walled carbon nanotube material, *Journal of Toxicology and Environmental Health, Part A*, **67**, 87-107 (2004).

A. D. Maynard, Experimental determination of ultrafine TiO_2 deagglomeration in a surrogate pulmonary surfactant: preliminary results, *Ann Occup Hyg*, **46**(Suppl. 1), 197-202 (2002).

J. R. McCormick, B. Zhao, S. A. Rykov, H. Wang, and J. G. Chen, Thermal stability of flame-synthesized anatase TiO_2 nanoparticles, *J Phys Chem B*, **108**, 17398-17402 (2004).

N. K. Meyer and Z. D. Ristovski, Ternary nucleation as a mechanism for the production of diesel nanoparticles: experimental analysis of the volatile and hygroscopic properties of diesel exhaust using the volatilization and humidification tandem differential mobility analyzer, *Environ Sci Technol*, **41**, 7309-7314 (2007).

J. B. A. Mitchell, S. di Stasio, J. L. LeGarrec, A. I. Florescu-Mitchell, T. Narayanan, and M. Sztucki, Small angle x-ray scattering study of flame soot nanoparticle aggregation and restructuring, *J Appl Phys*, **105**, 124904 (2009).

P. Mitchell and M. Frenklach, Monte Carlo simulation of soot particle aggregation with simultaneous surface growth: Why primary particles appear spherical, *Proc Combust Inst*, **27**, 1507-1514 (1998).

D. Mitrakos, J. Jokiniemi, U. Beckman, and C. Housiadas, Aerosol flow in a tube furnace reactor of gas-phase synthesized silver nanoparticles, *J Nanopart Res*, **10**, 153-161 (2008).

M. J. Moran and H. N. Shapiro, Fundamentals of Engineering Thermodynamics, 5th Ed, John Wiley & Sons, Inc, (2004).

L. Morawska, H. Wang, Z. Ristovski, E. R. Jayaratne, G. Johnson, H. C. Cheung, X. Ling, and C. He, JEM Spotlight: Environmental monitoring of airborne nanoparticles, *J Environ Monit*, **11**, 1758-1773 (2009).

R. Mueller, H. K. Kammler, S. E. Pratsinis, A. Vital, G. Beaucage, and P. Burtscher, Non-agglomerated dry silica nanoparticles, *Powder Technol*, **140**, 40-48 (2004).

S. Nagamine, A. Sugioka, H. Iwamoto, and Y. Konishi, Formation of TiO_2 hollow nanoparticles by spraying water droplets into an organic solution of titanium

tetraisopropoxide (TTIP) – Effects of TTIP concentration and TTIP-Protecting additives, *Powder Technol*, doi: 10.1016/j.powtec.2007.11.027.

K. Nakaso, K. Okuyama, M. Shimada, and S. E. Pratsinis, Effect of reaction temperature on CVD-made TiO_2 primary particle diameter, *Chem Eng Sci*, **58**, 3327-3335 (2003).

A. Nemmar, H. Vanbilloen, M. F. Hoet, P. H. M. Verbruggen, and B. Nemery, Passage of intratracheally instilled ultrafine particles from the lung into the systemic circulation in hamster, *Am J Respir Crit Care Med*, **164**, 1665-1668 (2001).

Z. Ning and C. Sioutas, Atmospheric processes influencing aerosols generated by combustion and the inference of their impact on public exposure: A review, *Aerosol and Air Quality Research*, **10**, 43-58 (2010).

L. Ntziachristos, A. Polidori, H. Phuleria, M. D. Geller, and C. Sioutas, Application of a diffusion charger for the measurement of particle surface concentration in different environments, *Aerosol Sci Technol*, **41**, 571-580 (2007).

G. Oberdorster, E. Oberdorster, and J. Oberdorster, Nanotoxicology: an emerging discipline evolving from studies of ultrafine particles, *Environ Health Perspect*, **113**(7), 823-839 (2005).

G. Oberdorster, Z. Sharp, V. Atudorei, A. Elder, R. Gelein, W. Kreyling, and C. Cox, Translocation of inhaled ultrafine particles to the brain, *Inhal Toxicol*, **16**, 437-445 (2004).

G. Oberdorster, Toxicokinetics and effects of fibrous and nonfibrous particles, *Inhal Toxicol*, **14**, 29-56 (2002).

G. Oberdorster, Pulmonary effects of inhaled ultrafine particles, *Int Arch Occup Environ Health*, **74**, 1-8 (2001).

G. Oberdorster, Significance of particle parameters in the evaluation of exposure-dose-response relationships of inhaled particles, *Inhal Toxicol*, **8**, S73-S89 (1996).

G. Oberdorster, Lung particle overload: implications for occupational exposures to particles, *Regulatory Toxicology and Pharmacology*, **27**, 123-135 (1995).

T. B. Onasch, J. T. Jayne, S. Herndon, D. R. Worsnop, R. C. Miake-Lye, I. P. Mortimer, and B. E. Anderson, Chemical properties of aircraft engine particulate exhaust emissions, *Journal of Propulsion and Power*, **25**(5), 1121-1137 (2009).

F. Ossler, S. E. Canton, and J. Larsson, X-ray scattering studies of the generation of carbon nanoparticles in flames and their transition from gas phase to condensed phase, *Carbon*, **47**, 3498-3507 (2009).

H. B. Palmer and C. F. Cullis, *Chemistry and Physics of Carbon, Vol. 1*, (P. L. Walker, Jr. and P. A. Thrower, Eds.) Marcel Dekker, 265-325 (1965).

P. Pandey, B. P. Pundir, and P. K. Panigrahi, Hydrogen addition to acetylene-air laminar diffusion flames: studies on soot formation under different flow arrangements, *Combustion and Flame*, **148**, 249-262 (2007).

D. Park, M. An, and J. Hwang, Development and performance test of a unipolar diffusion charger for real-time measurements of submicron aerosol particles having a log-normal size distribution, *J Aerosol Sci*, **38**, 420-430 (2007).

I. P. Parkin and R. G. Palgrave, Self-cleaning coatings, *J Mater Chem*, **15**, 1689-1695 (2005).

P. Penttinen, K. L. Timonen, P. Tiittanen, A. Mirme, J. Ruuskanen, and J. Pekkanen, Ultrafine particles in urban air and respiratory health among adult asthmatics, *Eur Respire J*, 428-435 (2001).

A. Peters, H. E. Wichmann, T. Tuch, J. Heinrich, and J. Heyder, Respiratory effects are associated with the number of ultrafine particles, *Am J Respir Crit Care Med*, **155**, 1376-1383 (1997).

S. E. Pratsinis W. Zhu, and S. Vemury, The role of gas mixing in flame synthesis of titania powders, *Powder Technol*, **86**, 87-93 (1996).

D. Y. H. Pui, C. Qi, N. Stanley, G. Oberdorster, and A. Maynard, Recirculating air filtration significantly reduces exposure to airborne nanoparticles, *Environ Health Perspect*, **117**(7), 863-866 (2008).

C. Qi, N. Stanley, D. Y. H. Pui, and T. H. Kuehn, Laboratory and on-road evaluations of cabin air filters using number and surface area concentration monitors, *Environ Sci Technol*, **42**, 4128-1432 (2008a).

C. Qi, N.J. Stanley, and D.Y.H. Pui, "Evaluation and Comparison of Filtration Efficiency using Number and Surface Area Concentration Monitors," Proceedings: AFS 2008 Annual Conference, Valley Forge, Pennsylvania, May 19-22, 2008b.

L. C. Renwick, D. Brown, A. Coulter, and K. Donaldson, Increased inflammation and altered macrophage chemotactic responses caused by two ultrafine particle types, *Occup Environ Med*, **61**, 442-447 (2004).

J. Ristimaki, K. Vaaraslahti, M. Lappi, and J. Keskinen, Hydrocarbon condensation in heavy-duty diesel exhaust, *Environ Sci Technol*, **41**, 6397-6402 (2007).

T. Ronkko, A. Virtanen, J. Kannosto, J. Keskinen, M. Lappi, and L. Pirjola, Nucleation mode particles with a nonvolatile core in the exhaust of a heavy duty diesel vehicle, *Environ Sci Technol*, **41**, 6384-6389 (2007).

C. M. Sayes, R. Wahi, P. A. Kurian, Y. Liu, J. L. West, K. D. Ausman, D. B. Warheit, and V. L. Colvin, Correlating nanoscale titania structure with toxicity: a cytotoxicity and inflammatory response study with human dermal fibroblasts and human lung epithelial cells, *Toxicol Sci*, **92**, 174-185 (2006).

J. H. Scheckman, P. H. McMurry, and S. E. Pratsinis, Rapid characterization of agglomerate aerosols by in situ mass-mobility measurements, *Langmuir*, **25**(14), 8248-8254 (2009).

T. Schneider and K. A. Jensen, Combined single-drop and rotating drum dustiness test of fine to nanosized powders using a small drum, *Ann Occup Hyg*, **52**(1), 23-34 (2008).

P. A. Schulte, M. K. Schabauer-Berigan, C. Mayweather, C. L. Geraci, R. Zumwalde, and J. L. McKernan, Issues in the development of epidemiologic studies of workers exposed to engineered nanoparticles, *Journal of Occupational and Environmental Medicine*, **51**(3), 323-335 (2009).

A. Seaton, W. MacNee, K. Donaldson, and D. Godden, Particulate are pollution and acute health effects, *Lancet*, 176-178 (1995).

J. Seinfeld and S. Pandis, Atmospheric Chemistry and Physics, Wiley, New York (1998).

M. Seipenbusch, A. Binder, and G. Kasper, Temporal evolution of nanoparticle aerosols in workplace exposure, *Ann Occup Hyg*, **52**(8), 707-716 (2008).

B. Shannak, L. Friedel, M. Alhusein, and A. Azzi, Experimental investigation of contraction in single- and two-phase flow through sharp-edged short orifice, *Forschung IM Ingenieuwesen-Engineering Research*, **64**(11), 291-295 (1999).

M. K. Shrivastava, E. M. Lipsky, C. O. Stanier, and A. L. Robinson, Modeling semivolatile organic aerosol mass emissions from combustion systems, *Environ Sci Technol*, **40**, 2671-2677 (2006).

K. Siegmann, K. Sattler, and H. C. Siegmann, Clustering at high temperatures: carbon formation in combustion, *J Electron Spectroscopy and Related Phenomena*, **126**, 191-202 (2002).

L. A. Sgro, A. De Filippo, G. Lanzuolo, A. D'Alessio, Characterization of nanoparticles of organic carbon (NOC) produced in rich premixed flames by differential mobility analysis, *Proceedings of the Combustion Institute*, **31**, 631-638 (2007).

W. G. Shin, D. Y. H. Pui, H. Fissan, S. Neumann, and A. Trampe, Calibration and numerical simulation of Nanoparticle Surface Area Monitor (TSI Model 3550 NSAM), *J Nanoparticle Res*, **9**, 61-69 (2007).

N. J. Stanley, C. Qi, and D.Y.H. Pui, A new method of filter efficiency evaluation using the nanoparticle surface area monitor (NSAM) for a nanoparticle health relevant filter efficiency measure, *FILTRATION*, **10**(1), 40-46 (2010).

T. Stoeger, C. Reinhard, S. Takenaka, A. Schroeppel, E. Karg, and B. Ritter, Instillation of six different ultrafine carbon particles indicates a surface area threshold dose for acute lung inflammation in mice, *Environ Health Perspect*, **114**(3), 328-333 (2006).

R. Strobel, A. Baiker, and S. E. Pratsinis, Aerosol flame synthesis of catalysts, *Advanced Powder Technol*, **17**(5), 457-480 (2006).

W. C. Su and Y. S. Cheng, Deposition of fiber in human airway replica, *J Aerosol Sci*, **37**, 1429-1441 (2006).

H. Tobias, D. Beving, P. Ziemann, H. Sakurai, M. Zuk, P. McMurry, D. Zarling, R. Waytulonis, and D. Kittelson, Chemical analysis of diesel engine nanoparticles using a Nano-DMA/Thermal desorption particle beam mass spectrometer, *Environ Sci Technol*, **35**, 2233-2243 (2001).

C. L. Tran, D. Buchanan, C. T. Cullen, A. Searl, A. D. Jones, and K. Donaldson, Inhalation of poorly soluble particles II: Influence of particle surface area on inflammation and clearance, *Inhal Toxicol*, **12**, 1113-1126 (2000).

S. Tsantilis, H. K. Kammler, and S. E. Pratsinis, Population balance modeling of flame synthesis of titania nanoparticles, *Chem Eng Sci*, **57**, 2139-2156 (2002).

S. Tsantilis and S. E. Pratsinis, Narrowing the size distribution of aerosol-made titania by surface growth and coagulation, *J Aerosol Sci*, **35**, 405-420 (2004).

Ullmann, Ullmann's Encyclopedia of Industrial Chemistry, *WILEY-VCH* (2005).

M. J. Utell and M. W. Frampton, Acute health effects of ambient air pollution: the ultrafine particle hypothesis, *J Aerosol Med*, **13**, 355-359 (2000).

S. Vemury and S. E. Pratsinis, Charging and coagulation during flame synthesis of silica, *J Aerosol Sci*, **27**(6), 951-966 (1996).

W.- N. Wang, I. W. Lenggoro, Y. Terashi, T. O. Kim, and K. Okuyama, One-step synthesis of titanium oxide nanoparticles by spray pyrolysis of organic precursors, *Materials Sci Eng B*, **123**, 194-202 (2005).

D. B. Warheit, T. R. Webb, C. M. Sayes, V. L. Colvin, and K. L. Reed, Pulmonary instillation studies with nanoscale TiO_2 rods and dots in rats: toxicity is not dependent upon particle size and surface area, *Toxicol Sci*, **9**, 227-236 (2006).

S. J. Wasson, Z. Guo, J. A. McBrian, and L. O. Beach, Lead in candle emissions, *The Science of the Total Environment*, **296**, 159-174 (2002).

B. Wehner, H. Siebert, A. Ansmann, F. Ditas, P. Seifert, F. Stratmann, A. Wiedensohler, A. Apituley, R. A. Shaw, H. E. Manninen, and M. Kulmala, Observations of turbulence-induced new particle formation in the residual layer, *Atmospheric Chemistry and Physics*, **10**, 4319-4330 (2010).

J. J. Whicker, P. T. Wasiolek, and R. A. Tavani, Influence of room geometry and ventilation rate on airflow and aerosol dispersion: implications for worker protection, *Health Physics*, **82**(1), 52-63 (2002).

H. E. Wichmann and A. Peters, Epidemiological evidence of the effects of ultrafine particulate exposure, *Philos Trans R Soc Lond A*, **358**, 2751-2769 (2000a).

H. E. Wichmann, C. Spix, T. Tuch, G. Wolke, A. Peters, J. Heinrich et al, Daily mortality and fine and ultrafine particles in Erfurt, Germany. Part I. Role of particle number and particle mass, *Res rep Health Eff Inst*, **98**, 5-86 (2000b).

P. Wiebert, A. Sanchez-Crespo, R. Falk, K. Philipson, A. Lundin, S. Larsson, W. Moller, W. G. Kreyling, and M. Svartengren, No significant translocation of inhaled 35-nm carbon particles to the circulation in humans, *Inhal Toxicol*, **18**, 741-747 (2006).

M. R. Wilson, J. H. Lightbody, K. Donaldson, J. Sales, and V. Stone, Interactions between ultrafine particles and transition metals in vivo and in vitro, *Toxicol Appl Pharmacol*, **184**, 172-179 (2002).

R. Wottrich, S. Diabate, and H. F. Krug, Biological effects of ultrafine particles in human macrophages and epithelial cells in mono- and co-culture, *Int J Hyg Environ Health*, **207** 353-361 (2004).

Z. Wu, M. Hu, S. Liu, B. Wehner, S. Bauer, A. Weidensohler, T. Petaja, M. Dal Maso, and M. Kulmala, New particle formation in the mega-city: Beijing, China, *J Geophs Res*, 112, D09209 (2007), doi: 10.1029/2006JD007406.

Y. Xiong and S. E. Pratsinis, Gas phase production of particles in reactive turbulent flows, *J Aerosol Sci*, **27**(5), 637-655 (1991).

F. Xu, K.-C. Lin, and G. M. Faeth, Soot formation in laminar premixed Methane/Oxygen flames at atmospheric pressure, *Combust Flame*, **115**, 195-209 (1998).

C. L. Yeh, S. H. Yeh, and H. K. Ma, Flame synthesis of titania particles from titanium tetraisopropoxide in premixed flames, *Powder Technol*, **145**, 1-9 (2004).

K. Yin Win and S.-S. Feng, Effects of particle size and surface coating oncellular uptake of polymeric nanoparticles for oral delivery of anticancer drugs, *Biomaterials*, **26**, 2713-2722 (2005).

W. Zhu and S. E. Pratsinis, Synthesis of SiO_2 and SnO_2 particles in diffusion flame reactors, *AIChE J Ceramics Processing*, **43**(11A), 2657-2664 (1997).

Appendix A: Additional Instrumentation Figures

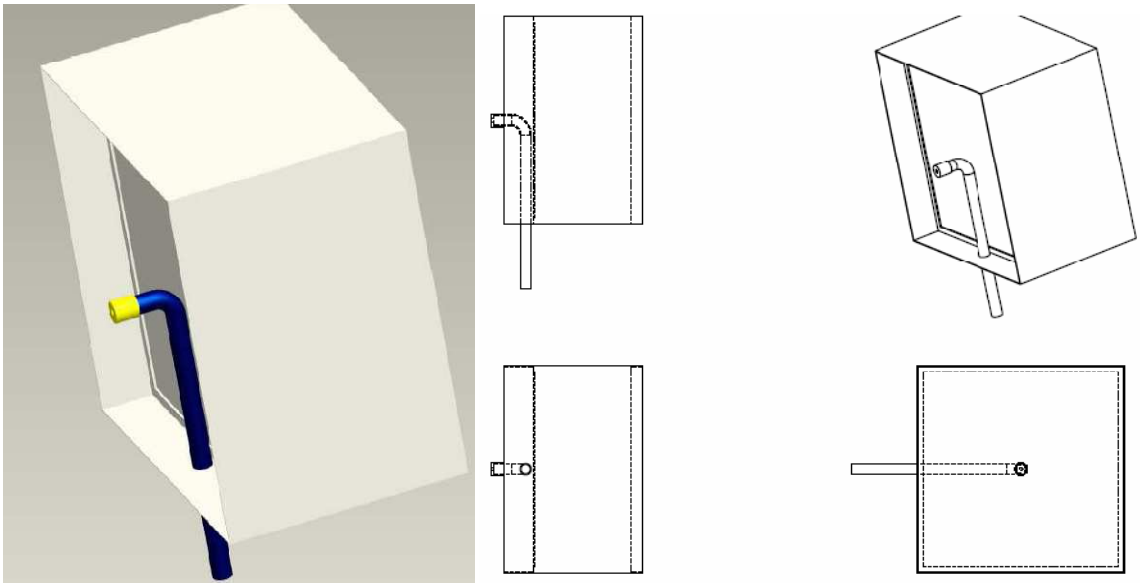

Figure A.1: First version of injection section with the injection probe and orifice insert.

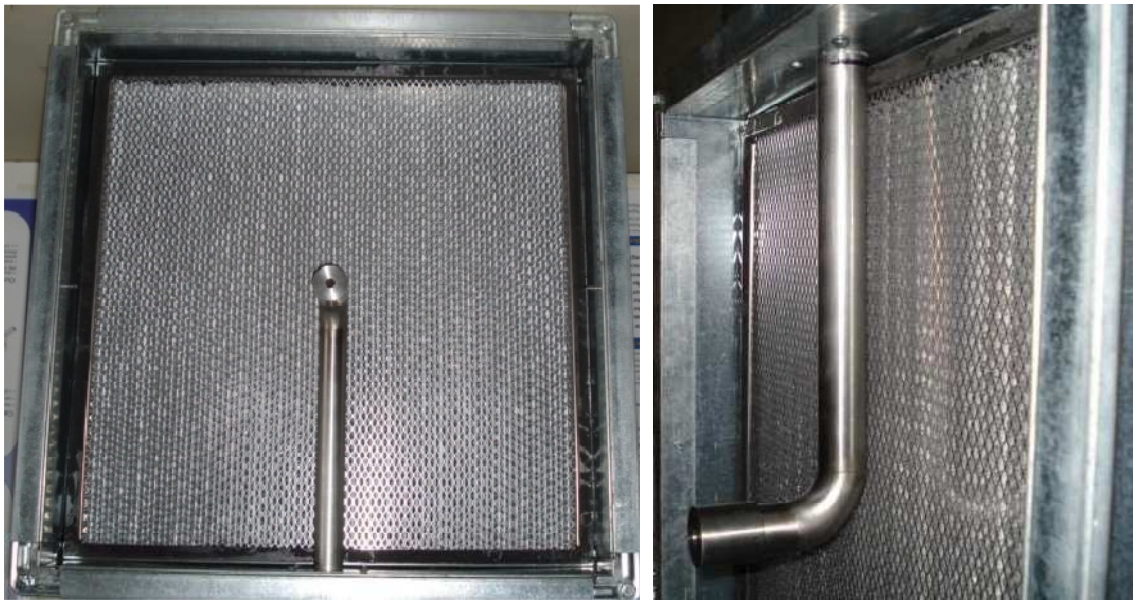

Figure A.2: Picture of first version of injection section with the injection probe and orifice insert.

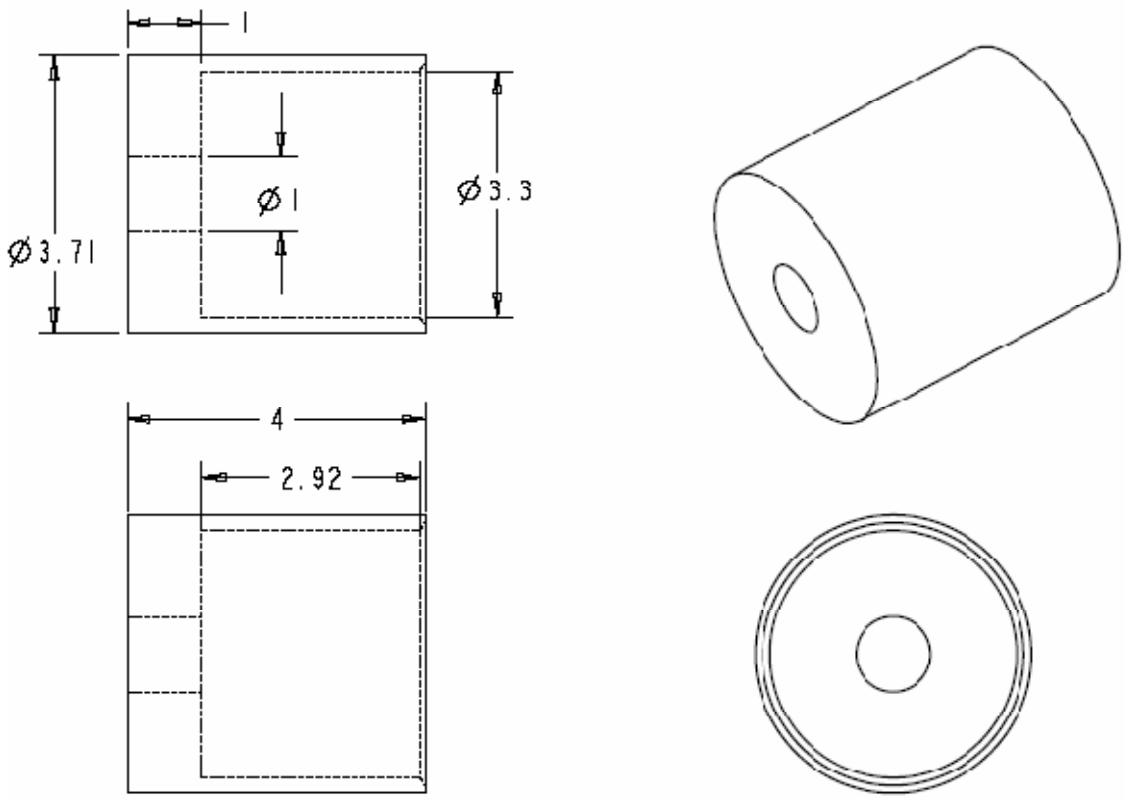

Figure A.3: Orifice for injection probe, all dimensions in cm.

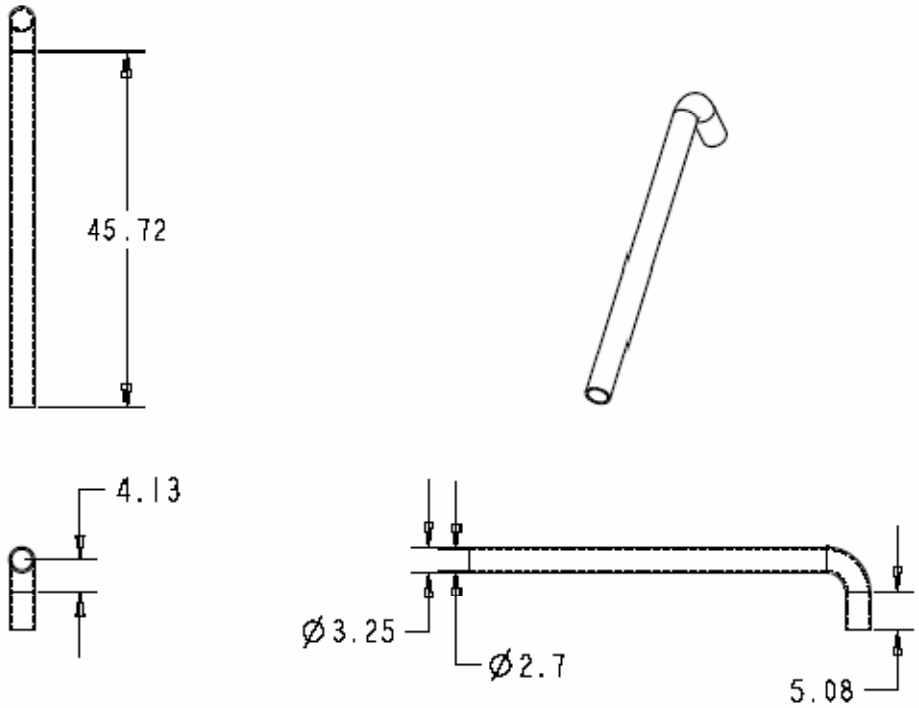

Figure A.4: Injection Probe (w/o/orifice) for injection, all dimensions in cm. ID: 2.7 cm, OD: 3.25 cm.

Appendix B: Ambient Aerosol Filter Efficiency Summary (Stanley et al., 2010)

The filter efficiencies from the NSAM and UCPC devices while measuring atmospheric aerosol are shown in Figure B.1. The filter efficiencies are similar for each CPC trial as well as each different NSAM lung region response. However the number based efficiencies from the CPC are approximately 11% higher than the LDSA based efficiencies. This is most likely due to the differences between the aerosol distributions with the geometric mean particle size of the number distribution corresponding to a higher filtration efficiency (on the filter efficiency curves shown in Figures 3.1.4 and 3.1.5) than the geometric mean particle size of the surface area distribution. As also shown in Figure B.1, the filter efficiency based on LDSA from the NSAM is closer to the minimum efficiency of the filter than the number based efficiency. Similar observations were made in our campaigned study (Qi et al., 2008a), in which the filter efficiency experiment was carried out using an on-road automobile cabin air filter test and a wind tunnel filter test. NSAMs and CPCs were used to determine the LDSA based and number based filter efficiencies.

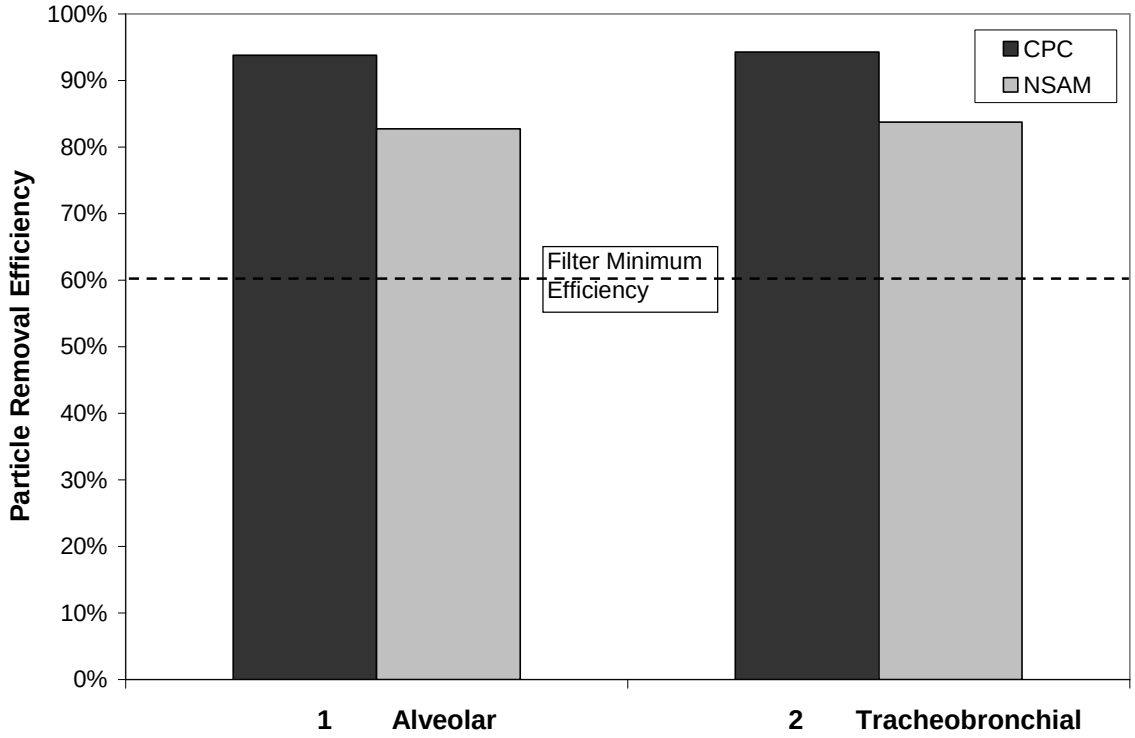

Figure B.1: CPC and NSAM based filter efficiencies for atmospheric aerosol.

For nanoparticles, which mainly distribute less than 300 nm, the LDSA concentration measured with the NSAM is very consistent with the calculated concentration from the lung deposition curves and the particle size distribution measured by a SMPS. The LDSA based filter efficiency obtained from NSAM and SMPS data agree very well with each other (with a difference of only 0.3 – 1.8%) for the test filter. Since most filters have a MPPS at around 100-300 nm, the geometric mean size of nanoparticles based on surface area is closer to the MPPS than that based on number. Hence, the LDSA based filter efficiency is closer to the minimum efficiency of the filter than the number based efficiency. Similar observations were also obtained in on-site and on-road filter tests with atmospheric aerosols. Due to the high surface area to mass ratio of nanoparticles and the concerns raised by toxicologists regarding surface area toxicity,

this LDSA filter efficiency measurement represents not only a more health relevant filter evaluation but also a better characterization of the filter when concerned with an aerosol mainly composed of nanoparticles.

Appendix C: Additional Particle Dispersion Distributions

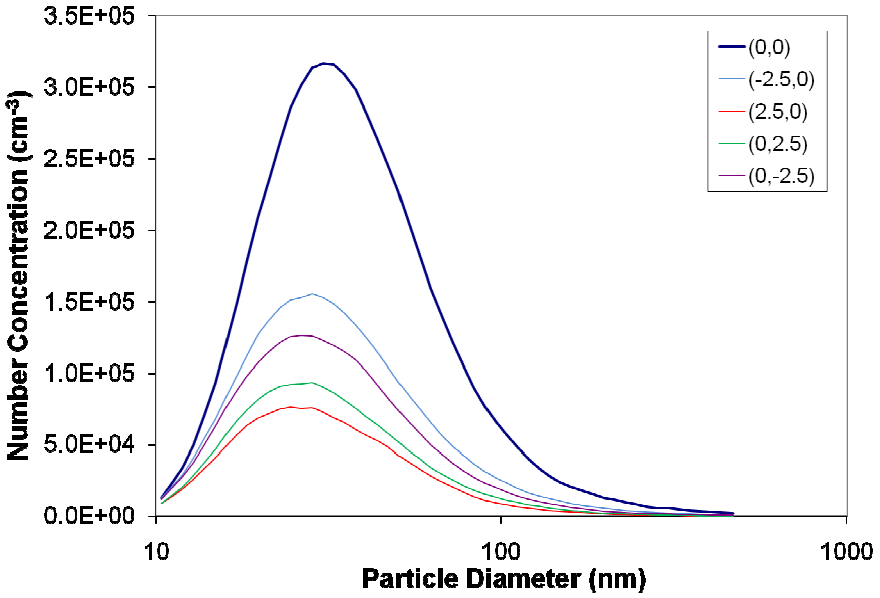

Figure C.1: Dispersion study particle concentration at Location 1a, 200 cfm.

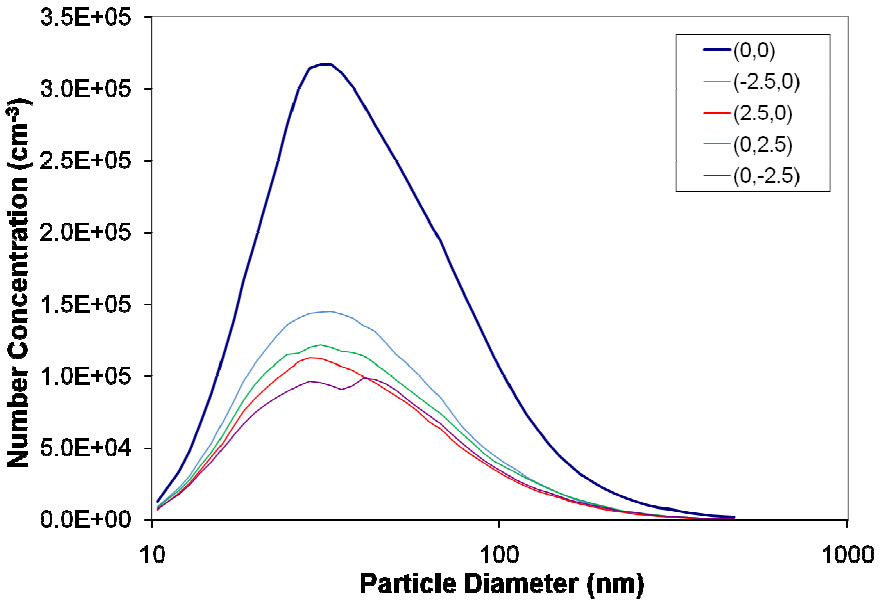

Figure C.2: Dispersion study particle concentration at Location 1a, 500 cfm.

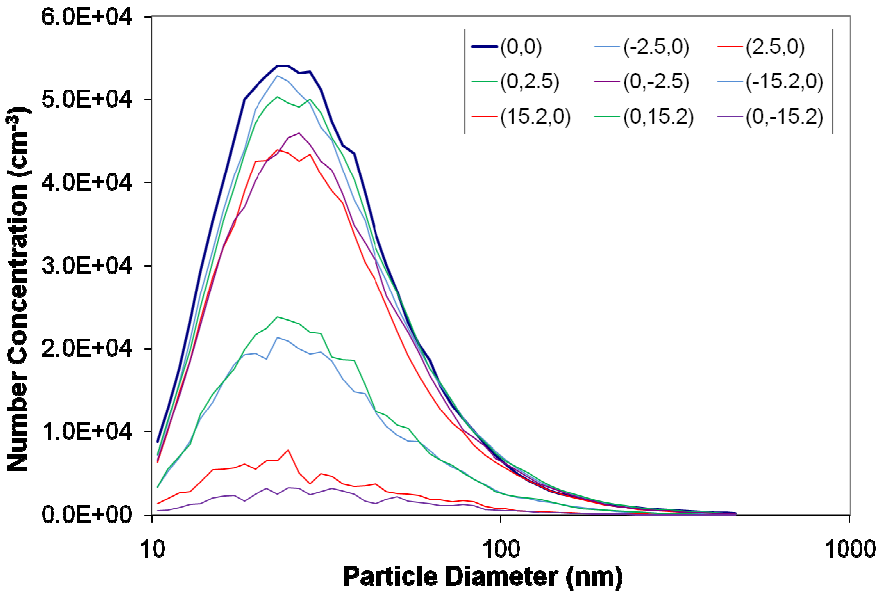

Figure C.3: Dispersion study particle concentration at Location 2, 200 cfm.

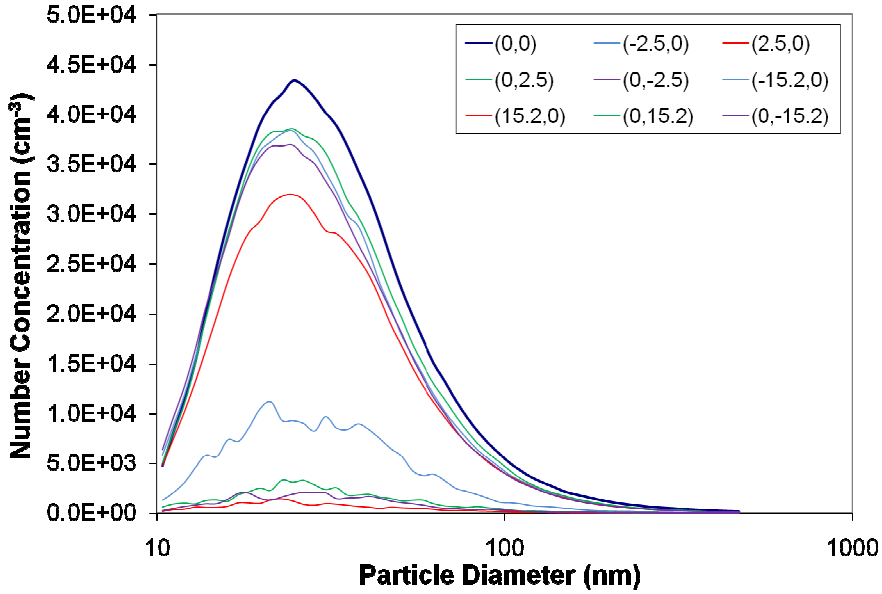

Figure C.4: Dispersion study particle concentration at Location 2, 500 cfm.

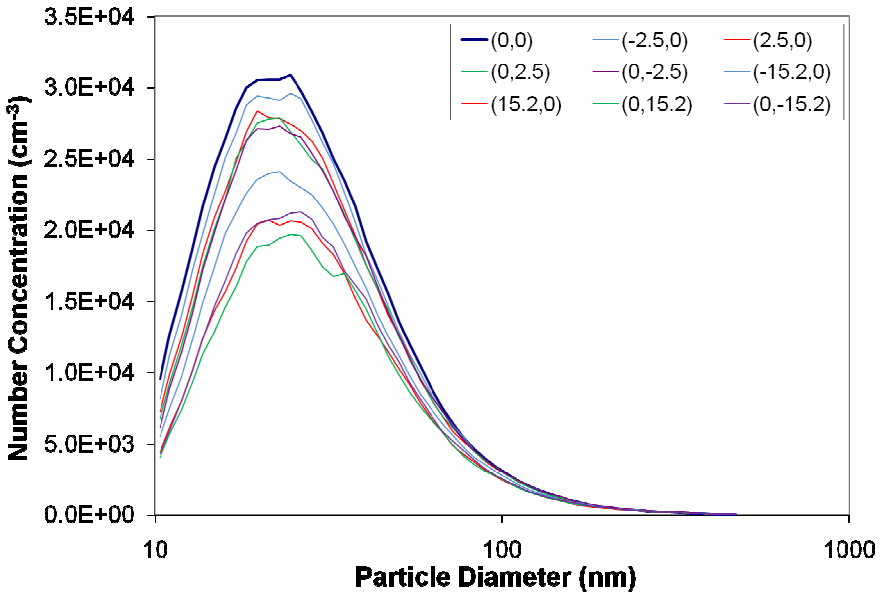

Figure C.5: Dispersion study particle concentration at Location 3, 200 cfm.

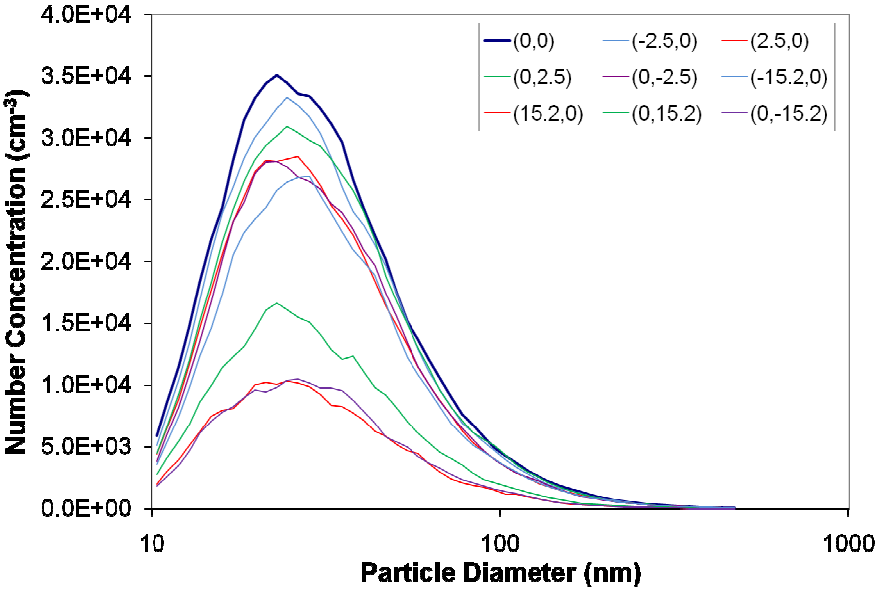

Figure C.6: Dispersion study particle concentration at Location 3, 500 cfm.

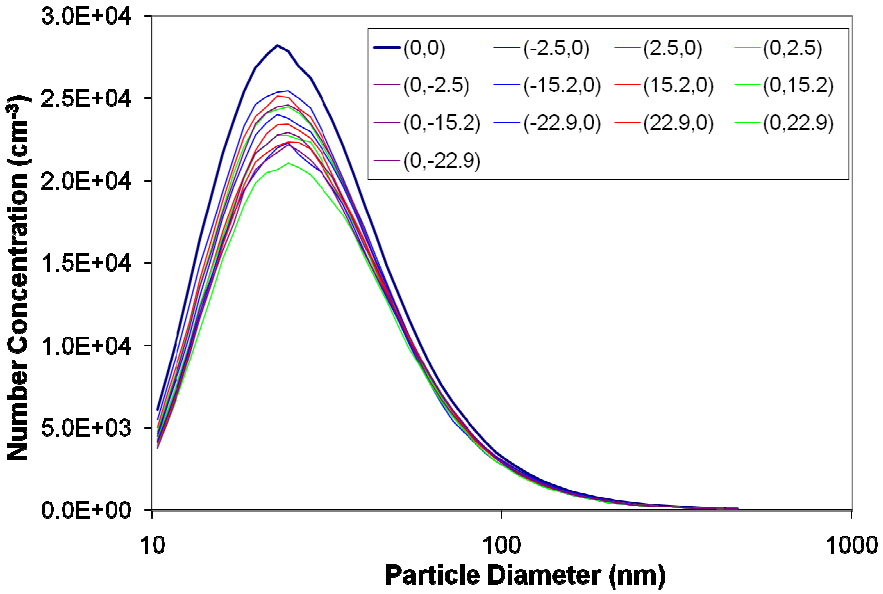

Figure C.7: Dispersion study particle concentration at Location 4, 200 cfm.

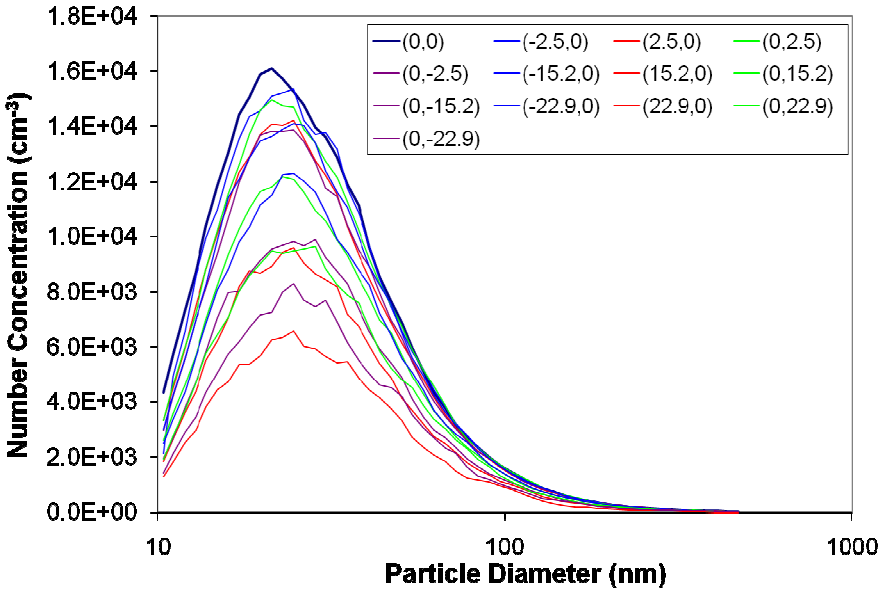

Figure C.8: Dispersion study particle concentration at Location 4, 500 cfm.

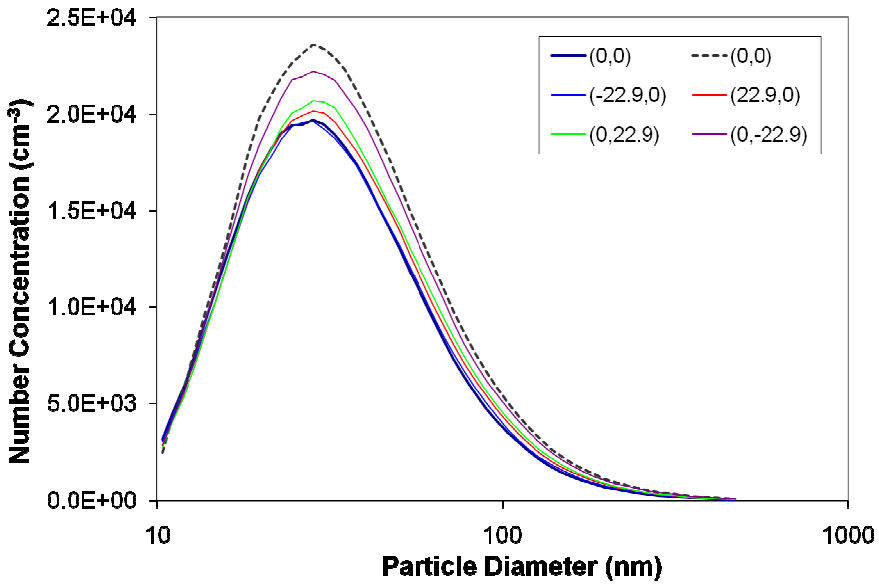

Figure C.9: Dispersion study particle concentration at Location 6, 200 cfm.

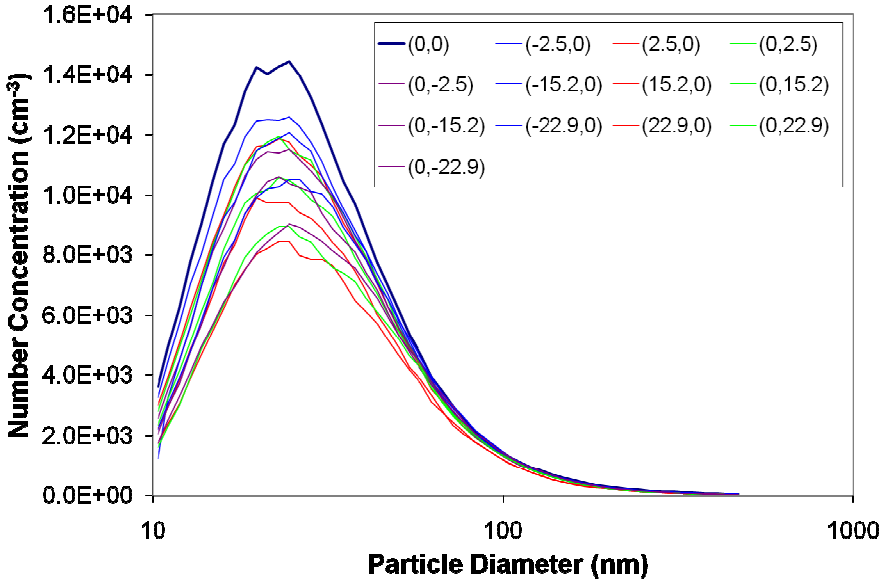

Figure C.10: Dispersion study particle concentration at Location 6, 500 cfm.

Appendix D: Additional Wind Tunnel Velocity Profile Figures

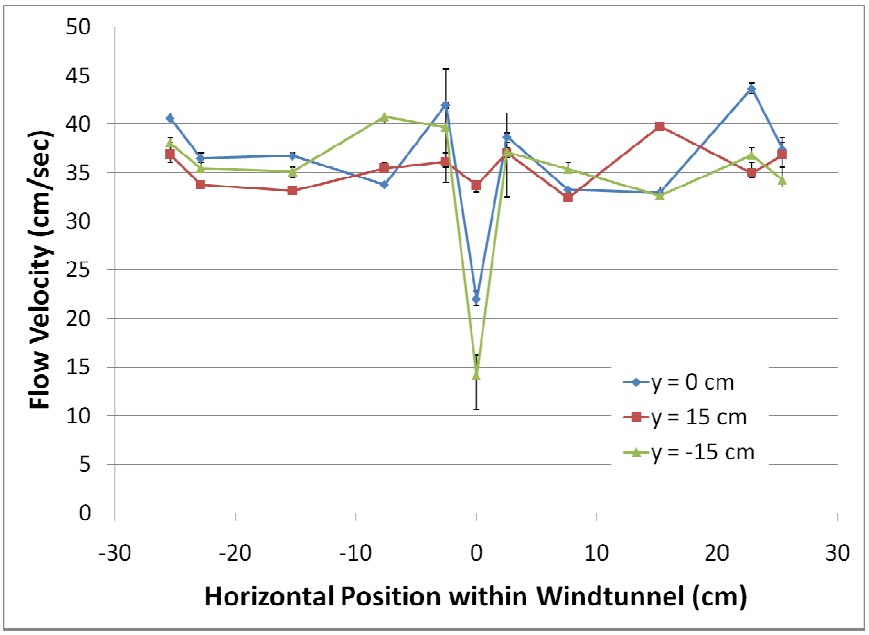

Figure D.1: Velocity profile at injection point (Location 1) with straight duct.

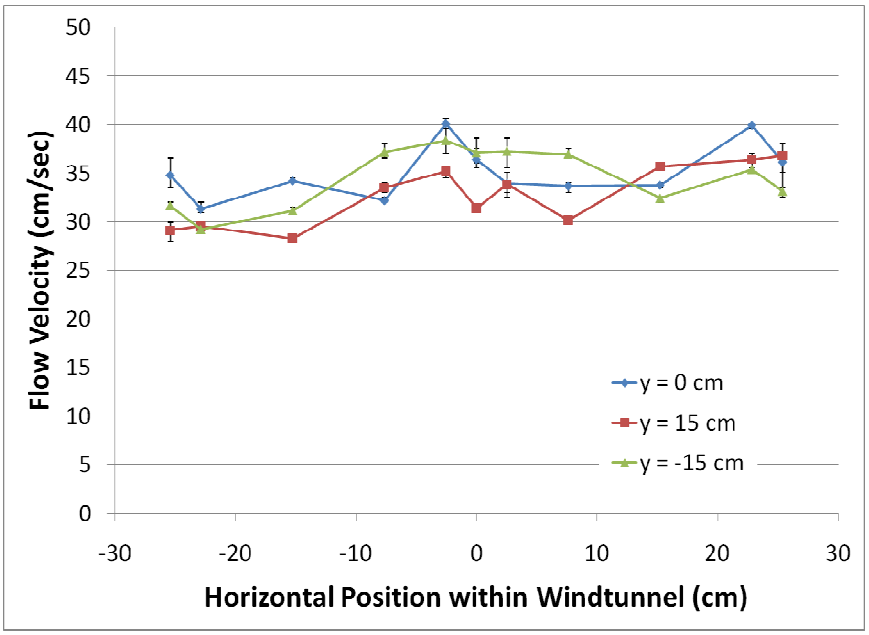

Figure D.2: Velocity profile at 0.15 m downstream (Location 1a) with straight duct.

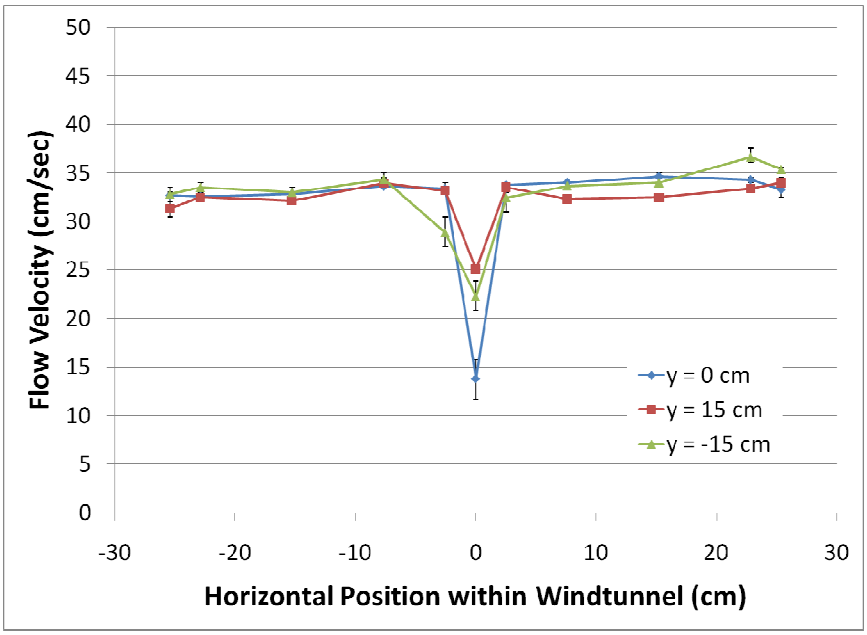

Figure D.3: Velocity profile at injection point (Location 1) with flow straightener.

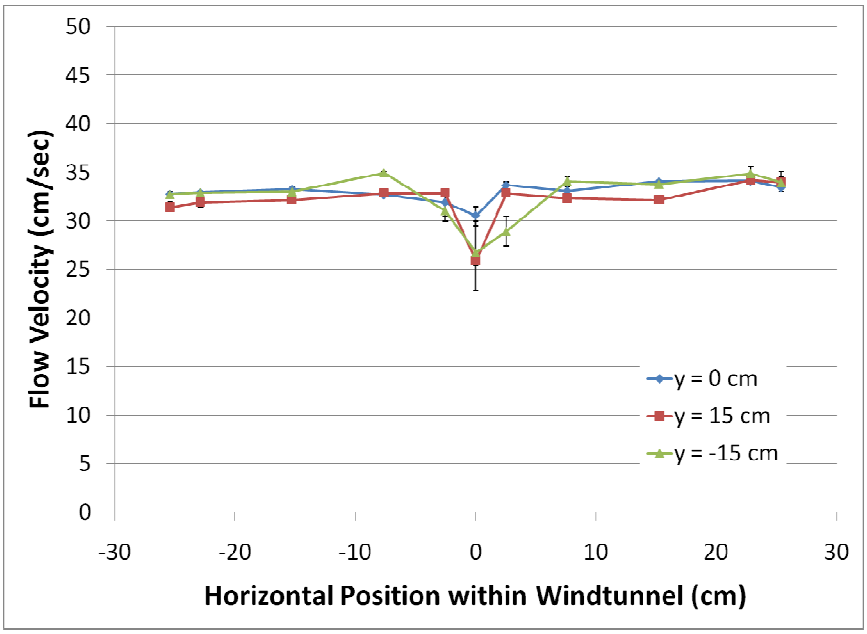

Figure D.4: Velocity profile at 0.15 m downstream (Location 1a) with flow straightener.

The initial velocity profile simulation was conducted by personnel at IUTA for the geometry of the wind tunnel (Figure D.5). There is much more turbulence in the measured velocity profile than the simulated velocity profile, but the results are

quantitatively similar. Both shows an effect of the injection probe, which is magnified for a side-by-side comparison in Figure D.6. The experiment and simulation used the same duct dimensions and fan speed; however the simulation assumed laminar flow and used a much finer grid for data acquisition.

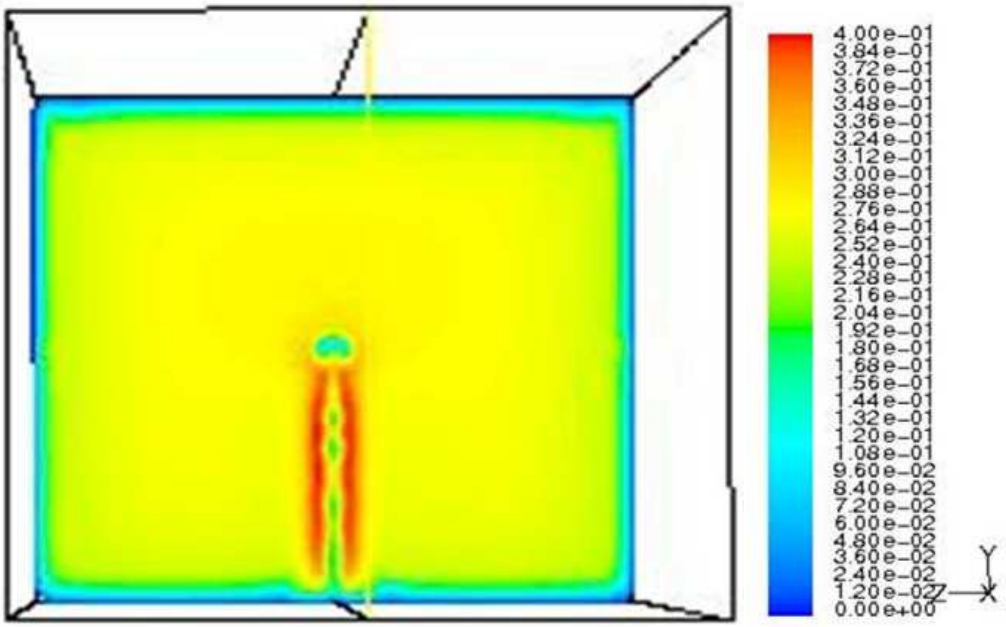

Figure D.5: Numerically simulated velocity profile at 20 cm downstream.

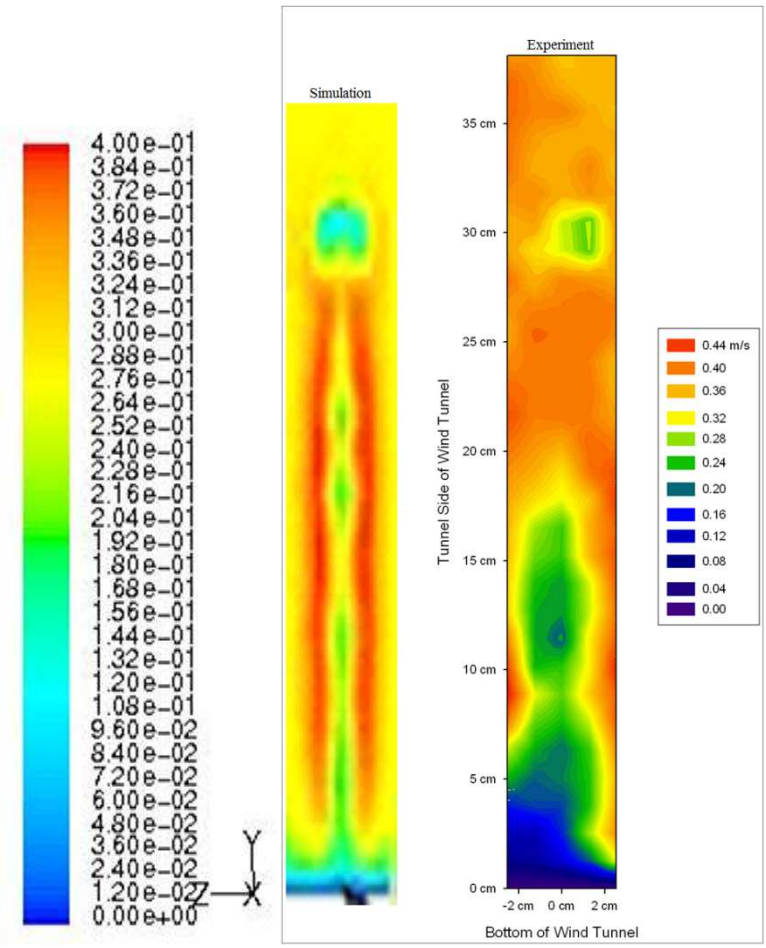

Figure D.6: Experimental and simulated velocity profile of injection probe area at 20 cm downstream.

A uniform flow velocity is mostly desired to obtain comparable experimental and simulation results. It may be more feasible to adjust the simulation parameters to match experimental parameters. Flow straighteners were inserted into the wind tunnel following these simulations.

New simulations were carried out (Dr. Christof Asbach at IUTA), which incorporate a turbulence model (do not assume laminar flow as in the initial simulations). These results are depicted as Figures D.7 and D.8. The effect of the injection probe is not

observed very far downstream and the flow profile is uniform. Therefore, the experimental results of the current study may be repeatable through numerical modeling.

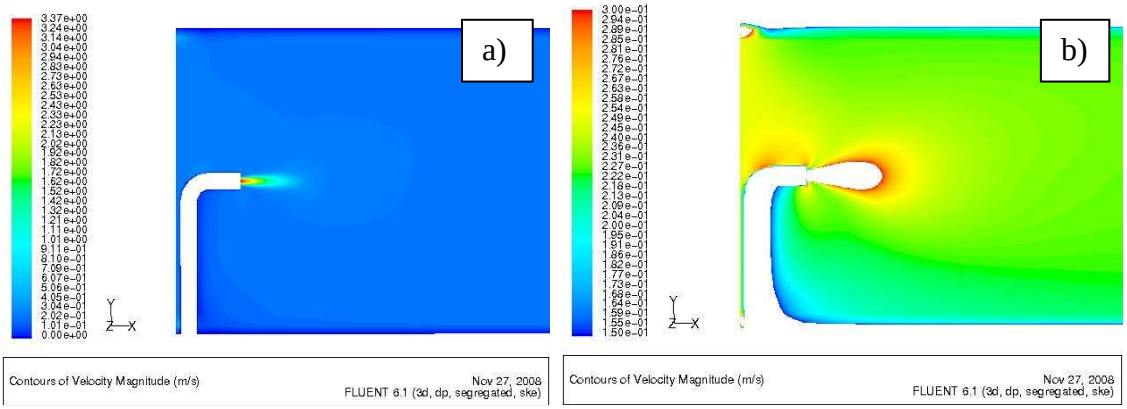

Figure D.7: Wind tunnel simulation results with different velocity range of a) 0-3.37 m/s and b) 0.15-0.3 m/s. Courtesy Dr. Christof Asbach, IUTA.

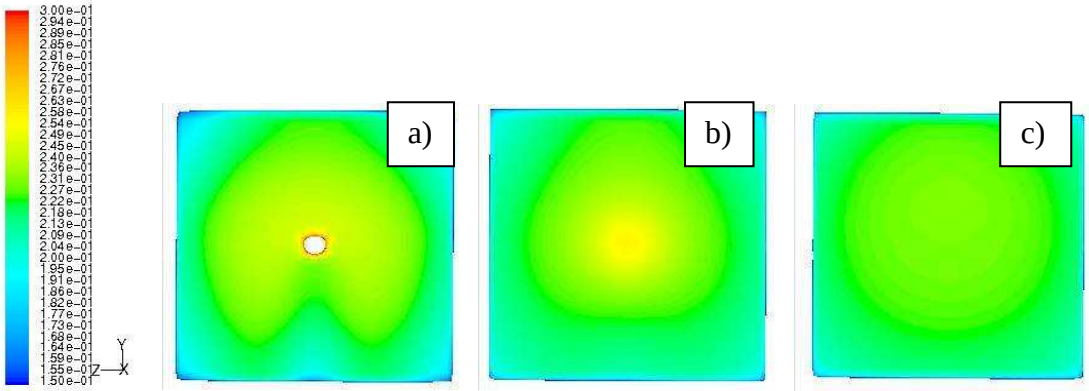

Figure D.8: Wind tunnel simulation results with velocity range of 0.15-0.3 m/s at distances downstream from injection probe of: a) 5 cm, b) 20 cm, and c) 50 cm. Courtesy Dr. Christof Asbach, IUTA.

Appendix E: Additional Orifice Calibration Figures

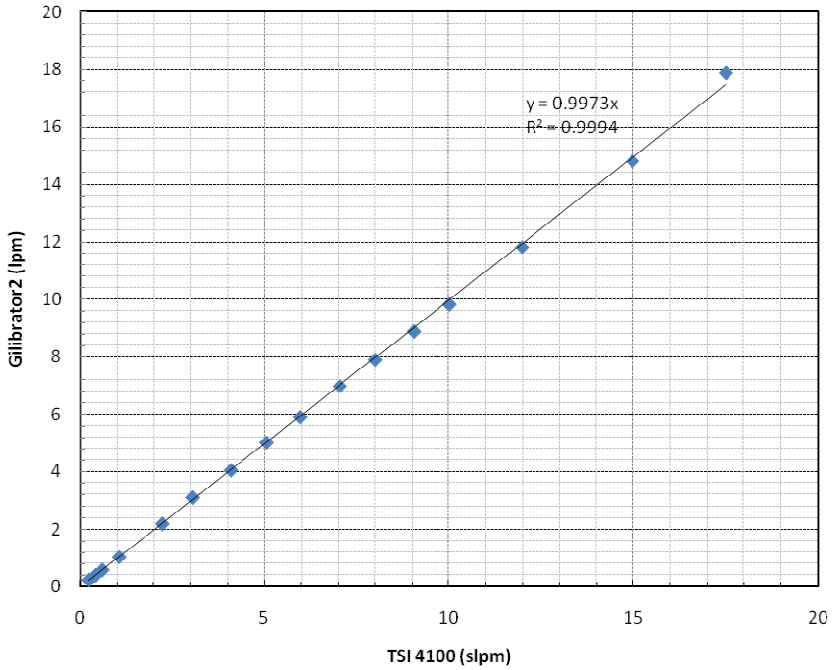

Figure E.1: Calibration curve for flow meter #3.

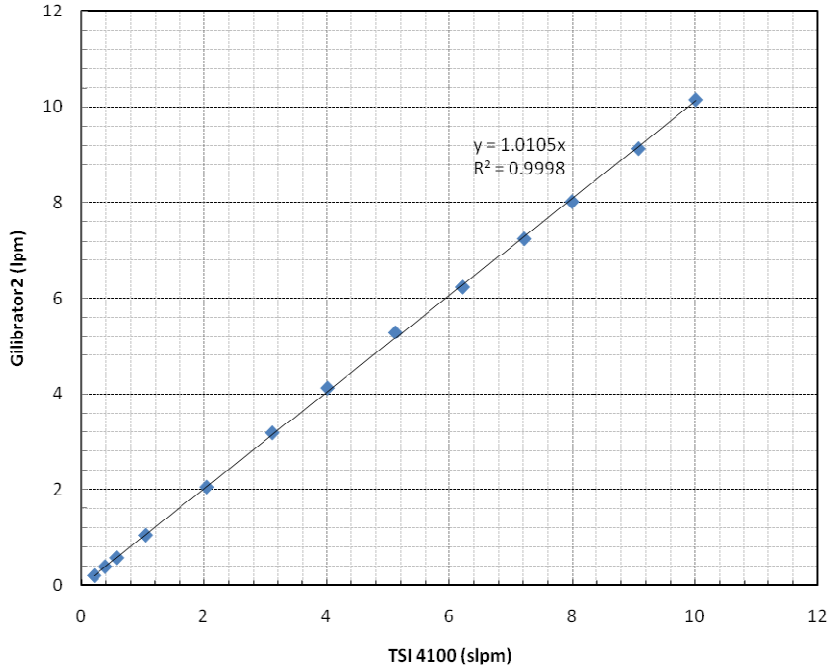

Figure E.2: Calibration curve for flow meter #4.

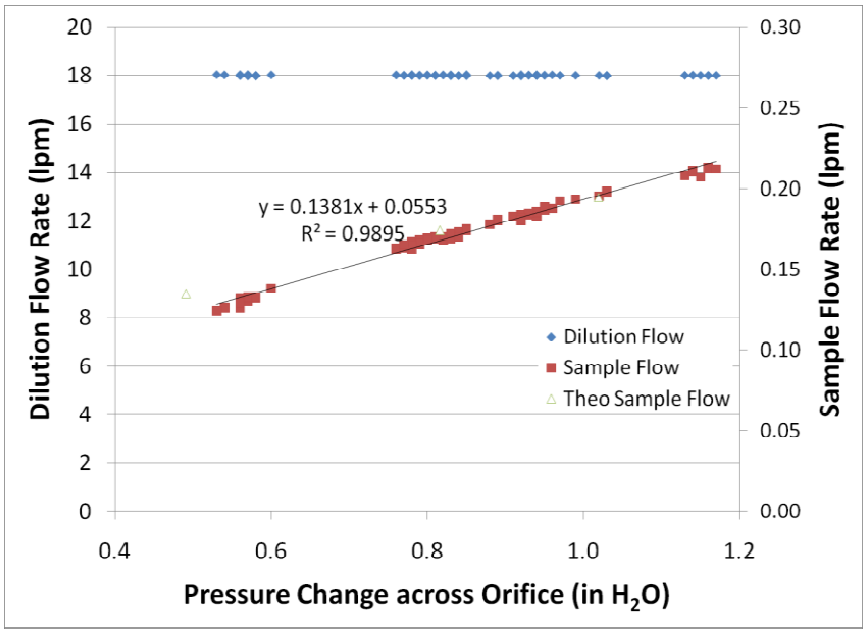

Figure E.3: Calibration curve for no leak trial #1.

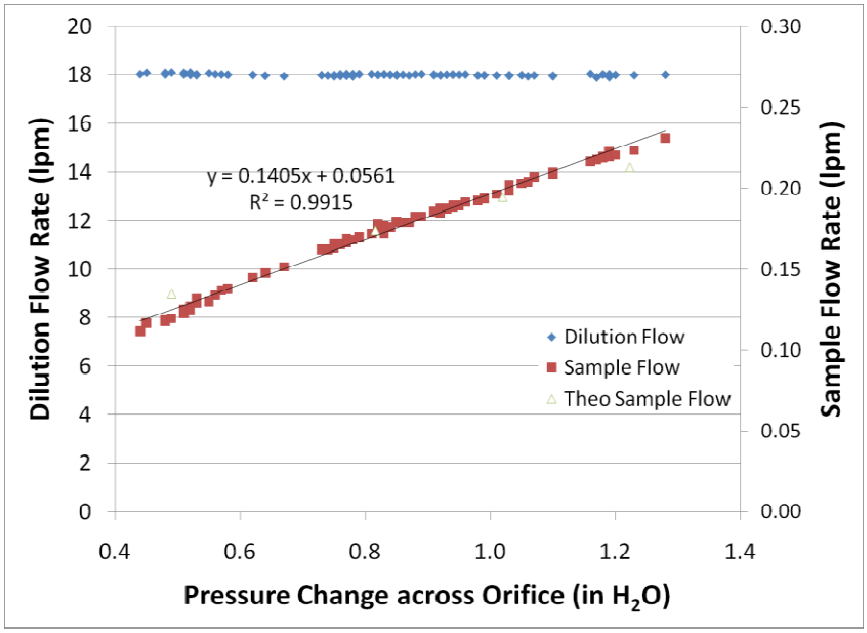

Figure E.4: Calibration curve for no leak trial #2.

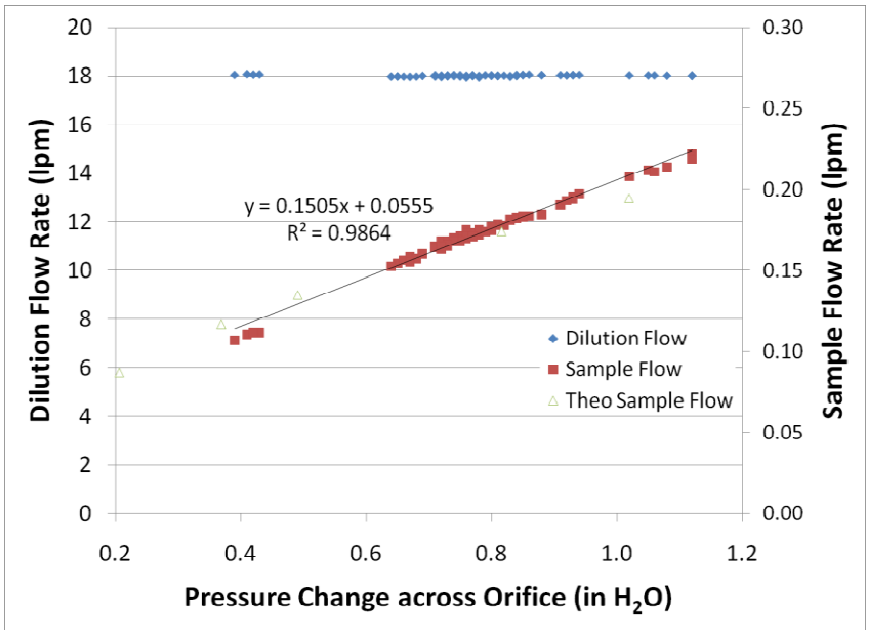

Figure E.5: Calibration curve for no leak trial #3.

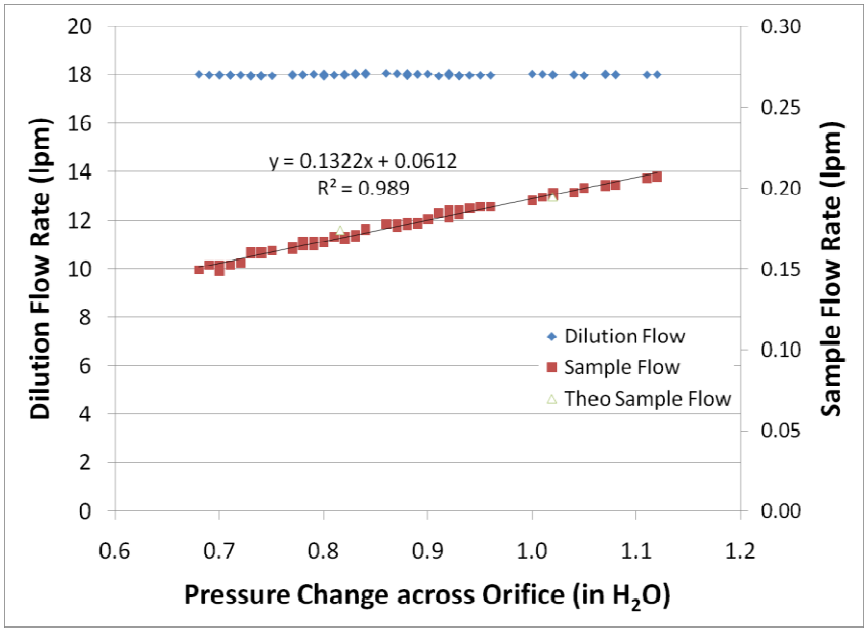

Figure E.6: Calibration curve for no leak trial #4.

Appendix F: Soot Mapping Experiments, Distributions, and NSAM/SMPS Ratio Figures

The total aerosol concentration was measured at 16 different locations within the wind tunnel cross section at 0.9 m, 1.8 m, and 3.4 m downstream of the injection site for two test conditions: Lean fuel/air mixture, 27 mm leak (Lean/27) and Rich fuel/air mixture, 10 mm leak (Rich/10). These experiments were conducted to determine the distribution of the burner aerosol throughout the wind tunnel. The total concentration is plotted at 7.6 cm (3 inch) horizontal and vertical intervals. The values in between each measurement are interpolated.

The injection probe was placed at the centerline of the wind tunnel, making the wind tunnel symmetric about the y-axis. In the preliminary dispersion experiments (Section 3.2), particle dispersion throughout the wind tunnel was approximately symmetrical about the centerline. However, the preliminary dispersion experiments were conducted with a non-thermal aerosol. The burner produced aerosols were much hotter, and therefore more buoyant, than the KCl aerosols produced during the preliminary dispersion tests. Therefore the highest concentrations are expected to lie somewhere within the centerline of the wind tunnel, above the injection point (due to the buoyancy of the aerosol plume). The positive-(x,y) section of Figure 4.2.2 was mapped out for the specified test conditions (Lean/27 and Rich/10).

Figures F.1 - F.6 show the particle dispersion throughout the wind tunnel. This dispersion does not progress as it did during the preliminary dispersion study. At 0.9 m, the aerosol has moved to the top and across the top of the wind tunnel. This pattern is apparent for both conditions tested (Lean/27 and Rich/10). After 0.9 m, the conditions

behaved differently. The Lean/27 condition became vertically stratified throughout the cross-section (highest concentrations at top of wind tunnel) at 1.8 m and 3.4 m, with consistent horizontal concentrations.

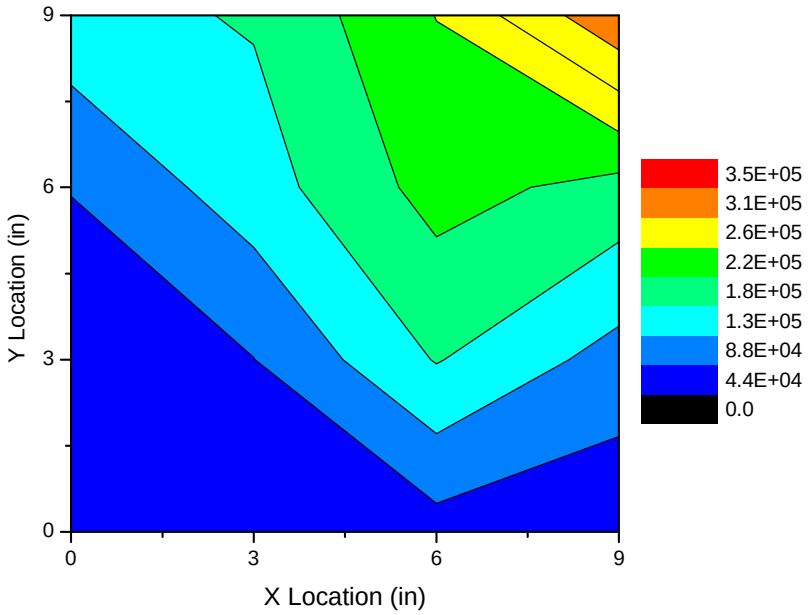

Figure F.1: Total concentration mapped at 0.9 m downstream using lean fuel/air mix, 27 mm leak.

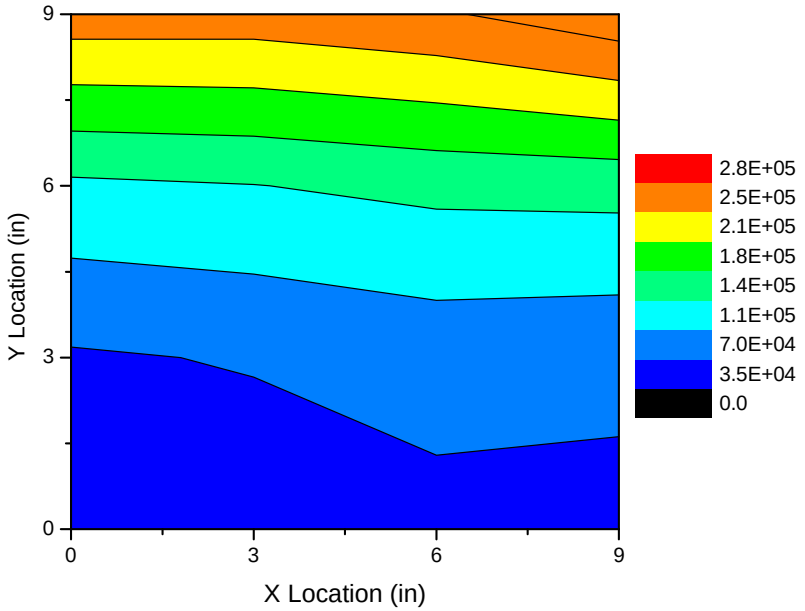

Figure F.2: Total concentration mapped at 1.8 m downstream using lean fuel/air mix, 27 mm leak.

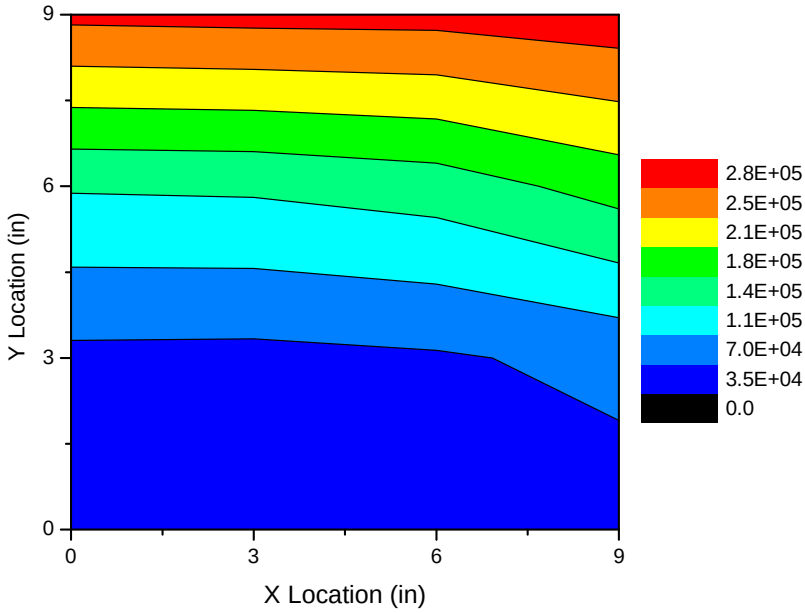

Figure F.3: Total concentration mapped at 3.4 m downstream using lean fuel/air mix, 27 mm leak.

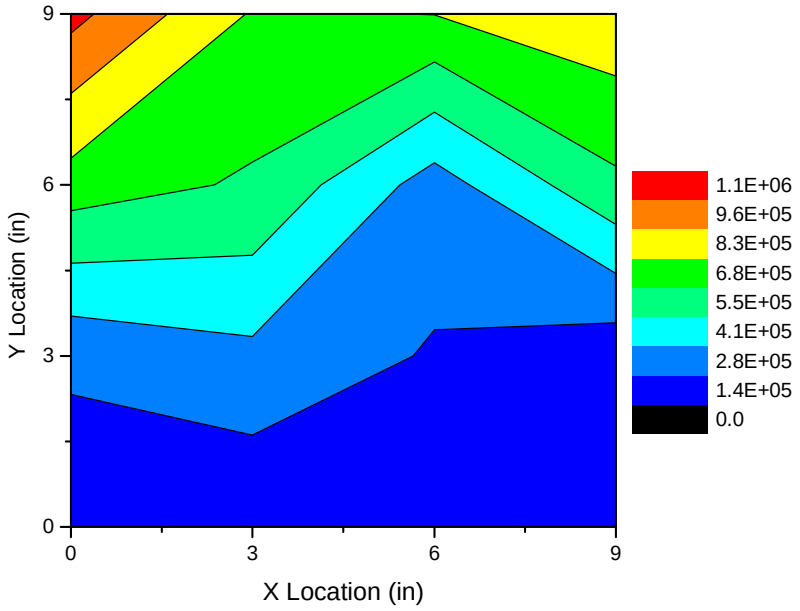

Figure F.4: Total concentration mapped at 0.9 m downstream using rich fuel/air mix, 10 mm leak.

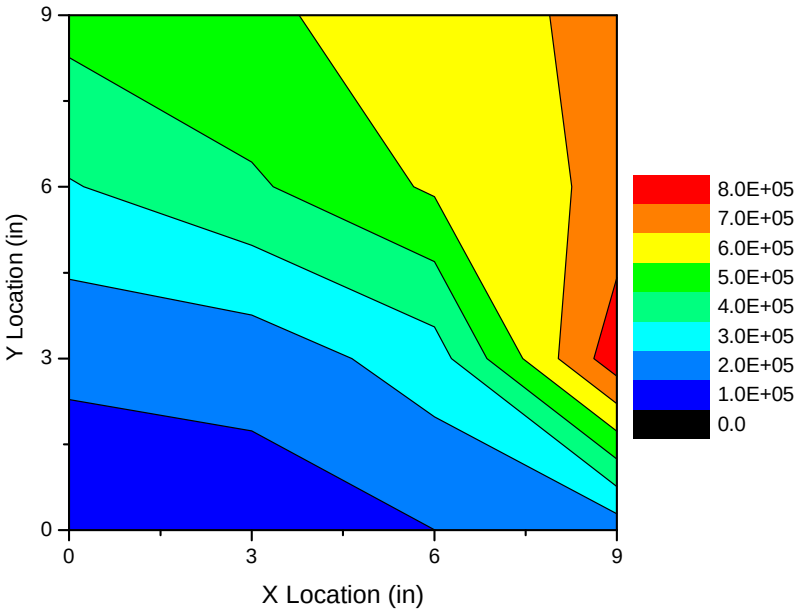

Figure F.5: Total concentration mapped at 1.8 m downstream using rich fuel/air mix, 10 mm leak.

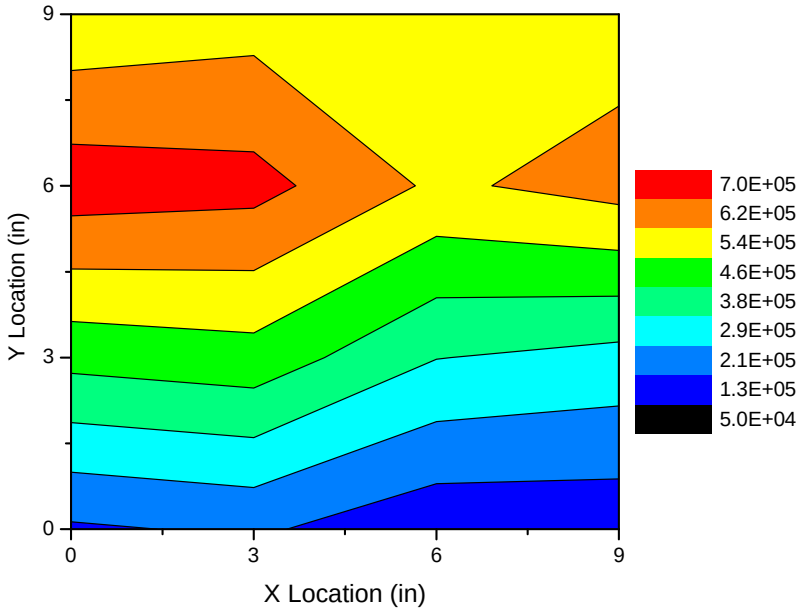

Figure F.6: Total concentration mapped at 3.4 m downstream using rich fuel/air mix, 10 mm leak.

The Rich/10 condition has moved across the top and down the side of the wind tunnel at 1.8 m downstream. The movement to the top of the wind tunnel was caused by the buoyancy forces of the hot aerosol in the much cooler background air flow. Once the aerosol reached the top of the wind tunnel, it was impeded by the tunnel wall, and forced to move across the top of the wind tunnel. Once it reached the corner, it was pushed down the side by the oncoming aerosol. The highest concentration was not located at the top of the wind tunnel at this point. At 3.4 m downstream, the aerosol became more stratified, similar to the results of Lean/27, which was likely a result of particle dispersion via turbulent mixing and Brownian motion.

As these burner aerosols traveled through the wind tunnel, they cooled down and dispersed via Brownian motion and turbulent mixing processes. Between 1.8 m and 3.4 m

downstream there is more intense mixing as the velocity profiles become less uniform (Figures 3.3.11 and 3.3.12). This dispersion is apparent for each fuel/air mixture and each leak size. The buoyancy of the plume caused the highest particle concentration to not always be located at the same position within the wind tunnel cross-section. Even though this highest particle concentration position was not always at (0,23), the measurement at position (0,23) is a good representation of the highest particle concentration. The (0,23) measurement position always had the same geometric mean particle size, the same geometric standard deviation, and in most cases, a similar concentration (never off by more than a factor of 3) as the highest particle concentration measurement.

Table F.1: Raw data for Lean fuel/air mixture particle size distributions, using 27 mm leak. Injected data was measured at centerline of wind tunnel. Downstream Location data was measured at point of highest concentration (0,23).

		Downstream Locations		
d_m (nm)	Injected	0.9 m	1.8 m	3.4 m
10.4	1127564	373	847	330
11.1	1444230	223	473	274
12	1766756	142	305	285
12.9	1921178	154	330	401
13.8	2110014	238	510	605
14.9	2374158	321	809	1033
16	2802890	534	1307	1896
17.2	3861460	922	1961	3054
18.4	4376464	1524	2945	4824
19.8	4203360	2006	4691	6273
21.3	4845620	2767	6815	8107
22.9	5484740	4032	10585	11678
24.6	6356160	5633	14327	15497
26.4	6636700	7428	19191	21279
28.4	8071740	9245	24962	28570
30.5	8927600	12609	31411	36264
32.8	9501940	16029	37699	47090
35.2	11000220	20856	45794	57677
37.9	12909200	26617	52092	70636
40.7	14295000	29235	64147	83577
43.7	16929400	32744	80555	97701
47	19755200	41777	95737	116458
50.5	21728600	48525	117691	129496
54.2	24297200	54085	132369	153753
58.3	26899600	60952	150378	182136
62.6	27764400	73437	179914	199708
67.3	32005200	80279	206325	225357
72.3	32258400	85006	220603	256024

		Downstream Locations		
d_m (nm)	Injected	0.9 m	1.8 m	3.4 m
77.7	33038800	90321	251956	271197
83.5	35625600	96473	281452	295983
89.8	36691200	117586	276891	323576
96.5	36235800	135464	280668	345318
103.7	39667200	146563	309566	349541
111.4	42590600	156899	335216	352984
119.7	43123000	157285	353007	397800
128.6	44424600	176146	371552	421817
138.2	43904600	194410	390312	421510
148.6	41957600	180736	400341	430525
159.6	39123600	173649	408128	451820
171.5	42688600	171490	422710	421393
184.3	42119200	166268	419816	413647
198.1	37306600	159007	401815	396825
212.9	32877800	145985	371607	372350
228.8	27940600	136625	333151	350333
245.8	24730800	122581	302785	308251
264.2	20781600	114787	262684	267795
283.9	16755200	105059	219576	243793
305.1	13843600	94966	206599	226409
327.8	10270500	77480	176588	191816
352.3	7411120	65489	144746	151523
378.6	5524600	51279	112847	117006
406.8	4141180	39017	87078	89761
437.1	2866680	29354	63278	64607
469.8	1921500	20987	47653	44510
d_g (nm)	113	137	136	132
σ_g	1.92	1.84	1.84	1.85
N_{total} (cm^{-3})	3.3E+07	116987	273025	296315

Table F.2: Raw data for Lean fuel/air mixture particle size distributions, using 10 mm leak. Injected data was measured at centerline of wind tunnel. Downstream Location data was measured at point of highest concentration (0,23).

		Downstream Locations		
d_m (nm)	Injected	0.9 m	1.8 m	3.4 m
10.4	1127564	602	485	327
11.1	1444230	350	293	286
12	1766756	294	272	323
12.9	1921178	362	354	468
13.8	2110014	658	536	763
14.9	2374158	1066	784	1313
16	2802890	1793	1291	2015
17.2	3861460	2389	1838	3247
18.4	4376464	3650	2516	5058
19.8	4203360	5433	3938	7362
21.3	4845620	7419	5618	9920
22.9	5484740	9631	6873	13687
24.6	6356160	13509	9215	18402
26.4	6636700	16567	11706	24104
28.4	8071740	21551	14267	30213
30.5	8927600	25474	18341	38217
32.8	9501940	30932	21727	47065
35.2	11000220	39599	28572	57370
37.9	12909200	47891	36299	67191
40.7	14295000	54388	42274	78388
43.7	16929400	62697	47691	86357
47	19755200	72154	57721	101702
50.5	21728600	78108	64928	121049
54.2	24297200	92738	73573	138079
58.3	26899600	105063	85673	151652
62.6	27764400	120898	99271	175022
67.3	32005200	130656	109913	194516
72.3	32258400	140897	118869	210161

		Downstream Locations		
d_m (nm)	Injected	0.9 m	1.8 m	3.4 m
77.7	33038800	151628	125383	228891
83.5	35625600	164250	133107	252898
89.8	36691200	185193	148867	275553
96.5	36235800	191291	168458	292354
103.7	39667200	204553	172161	302400
111.4	42590600	215148	183421	316200
119.7	43123000	230221	188529	337118
128.6	44424600	242554	183330	348200
138.2	43904600	249543	176018	361746
148.6	41957600	260290	173860	370659
159.6	39123600	259018	191651	373116
171.5	42688600	244300	191767	364766
184.3	42119200	231304	186712	343186
198.1	37306600	232197	181830	324729
212.9	32877800	219326	180817	308035
228.8	27940600	197777	177395	287720
245.8	24730800	174605	154639	260159
264.2	20781600	156689	129725	228056
283.9	16755200	131641	110484	200465
305.1	13843600	117450	96865	177012
327.8	10270500	99992	79407	143525
352.3	7411120	83242	65890	115833
378.6	5524600	63632	51520	90784
406.8	4141180	45696	39089	69698
437.1	2866680	34431	29713	51832
469.8	1921500	25723	22412	36985
d_g (nm)	113	129	130	129
σ_g	1.92	1.87	1.87	1.87
N_{total} (cm^{-3})	3.3E+07	171827	137747	251443

Table F.3: Raw data for Rich fuel/air mixture particle size distributions, using 27 mm leak. Injected data was measured at centerline of wind tunnel. Downstream Location data was measured at point of highest concentration (0,23).

		Downstream Locations		
d_m (nm)	Injected	0.9 m	1.8 m	3.4 m
10.4	12385538	4163	12260	5182
11.1	9361920	4997	9737	8149
12	3347900	5390	7617	14129
12.9	4538860	5689	8702	17427
13.8	10113000	10903	13699	22620
14.9	8426060	18501	21664	19747
16	11022240	26311	23320	23228
17.2	17382400	19966	30339	31972
18.4	21617000	22394	39957	43291
19.8	23371000	32650	52099	53111
21.3	30093000	43307	66517	71105
22.9	36273200	54554	91409	96626
24.6	44232200	72360	122368	119676
26.4	49132000	101098	167092	161054
28.4	64854000	120869	211366	195360
30.5	72080200	138680	259845	230704
32.8	75501600	170311	292411	314931
35.2	82352600	219971	346008	378855
37.9	89474000	232919	409103	415844
40.7	97633200	274418	470538	475730
43.7	103377800	317205	537654	521031
47	109755600	354738	574418	565551
50.5	105546400	412269	627212	590557
54.2	115233400	428667	696182	658493
58.3	116419600	441703	725250	715629
62.6	116130400	468276	754621	726888
67.3	114980000	480301	858326	819718
72.3	112406200	471436	898943	797660

		Downstream Locations		
d_m (nm)	Injected	0.9 m	1.8 m	3.4 m
77.7	103932800	499261	882139	768697
83.5	94115600	482925	933689	768706
89.8	96249600	463945	939174	779458
96.5	87615600	481951	911750	744903
103.7	77405000	482672	906110	739388
111.4	70786000	473645	899613	726011
119.7	62060200	445549	886681	668976
128.6	53060600	417528	850526	622567
138.2	44767200	393838	790754	575714
148.6	39103800	347006	674327	520931
159.6	31374400	289937	585963	421466
171.5	24443000	244004	496815	309740
184.3	17414200	189315	389617	245487
198.1	11970720	148098	292639	186648
212.9	8472660	110933	208117	138094
228.8	6082640	75849	140662	90000
245.8	3813500	49843	92164	57013
264.2	2291920	30229	57880	36269
283.9	1445962	18171	37689	20249
305.1	855440	10959	23913	12120
327.8	496962	6645	14386	7341
352.3	272640	3920	8506	4272
378.6	146552	2192	4996	2300
406.8	77777	1178	2776	1165
437.1	38851	665	1697	643
469.8	23810	407	928	371
d_g (nm)	59	77	80	75
σ_g	1.80	1.77	1.76	1.75
N_{total} (cm^{-3})	7.8E+07	332022	605068	516962

Table F.4: Raw data for Rich fuel/air mixture particle size distributions, using 10 mm leak. Injected data was measured at centerline of wind tunnel. Downstream Location data was measured at point of highest concentration (0,23).

		Downstream Locations		
d_m (nm)	Injected	0.9 m	1.8 m	3.4 m
10.4	12385538	477383	292725	246903
11.1	9361920	624240	314999	312926
12	3347900	784384	361824	364794
12.9	4538860	685285	681386	496043
13.8	10113000	623136	714895	703705
14.9	8426060	1718693	591848	736264
16	11022240	2353525	709048	747508
17.2	17382400	1253371	692311	869029
18.4	21617000	1226225	715139	837843
19.8	23371000	736365	637456	620896
21.3	30093000	498023	399329	478134
22.9	36273200	431537	323294	423868
24.6	44232200	191024	307235	353015
26.4	49132000	103569	228577	282439
28.4	64854000	128603	184020	246467
30.5	72080200	149915	183976	242362
32.8	75501600	128507	189376	264578
35.2	82352600	142044	222040	302992
37.9	89474000	184650	276739	357342
40.7	97633200	205930	309263	407074
43.7	103377800	214033	322262	438467
47	109755600	241044	361782	461543
50.5	105546400	287194	406988	500979
54.2	115233400	281149	418360	547637
58.3	116419600	290945	430386	568758
62.6	116130400	292875	439315	584803
67.3	114980000	242693	425892	600326
72.3	112406200	269494	435722	590202

		Downstream Locations		
d_m (nm)	Injected	0.9 m	1.8 m	3.4 m
77.7	103932800	279531	463712	593304
83.5	94115600	261244	474934	594734
89.8	96249600	240761	449254	597723
96.5	87615600	269623	455786	605339
103.7	77405000	259937	450512	586417
111.4	70786000	236105	411370	552876
119.7	62060200	237195	387520	525599
128.6	53060600	217695	359742	493342
138.2	44767200	197460	324066	444474
148.6	39103800	160269	283638	394938
159.6	31374400	141492	252729	343433
171.5	24443000	108951	206117	284846
184.3	17414200	93668	162159	225123
198.1	11970720	71374	126124	170872
212.9	8472660	60452	93464	124587
228.8	6082640	38106	65785	87256
245.8	3813500	25971	43697	59570
264.2	2291920	16738	28533	38733
283.9	1445962	10003	17712	24844
305.1	855440	7000	11132	15958
327.8	496962	4217	7194	9994
352.3	272640	2564	4355	5970
378.6	146552	1497	2573	3470
406.8	77777	782	1523	1942
437.1	38851	378	824	1104
469.8	23810	263	485	623
d_g (nm)	59	29	43	45
σ_g	1.80	2.29	2.37	2.35
N_{total} (cm^{-3})	7.8E+07	553410	520660	636687

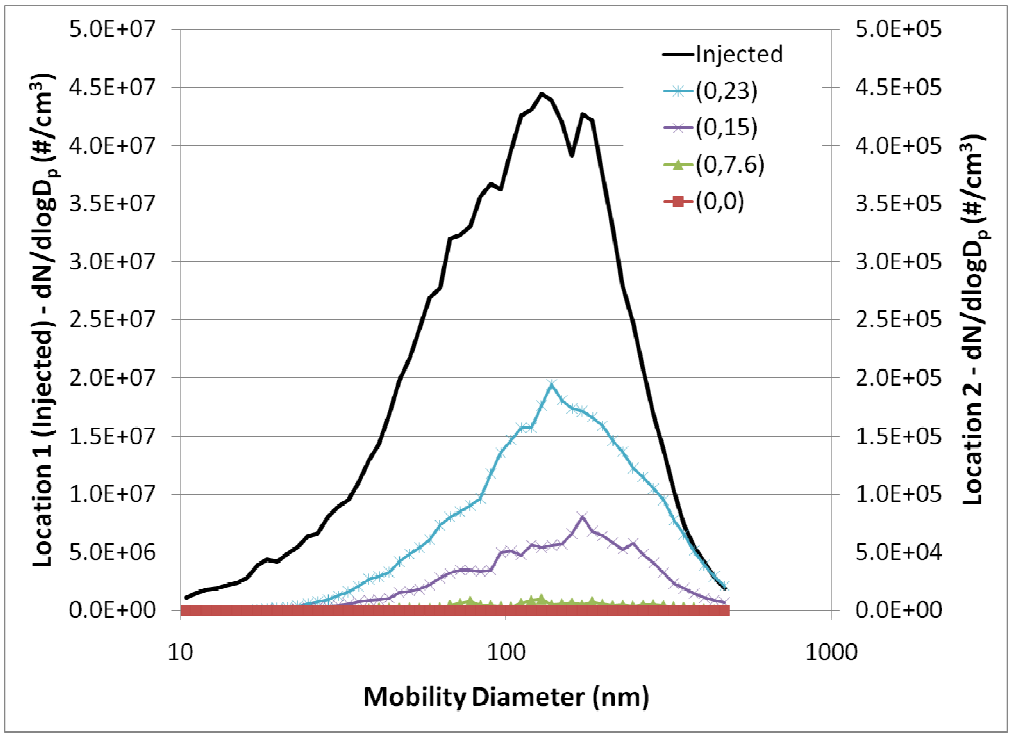

Figure F.7: 0.9 m downstream of leak (Location 2) using lean fuel/air mix and 27 mm leak.

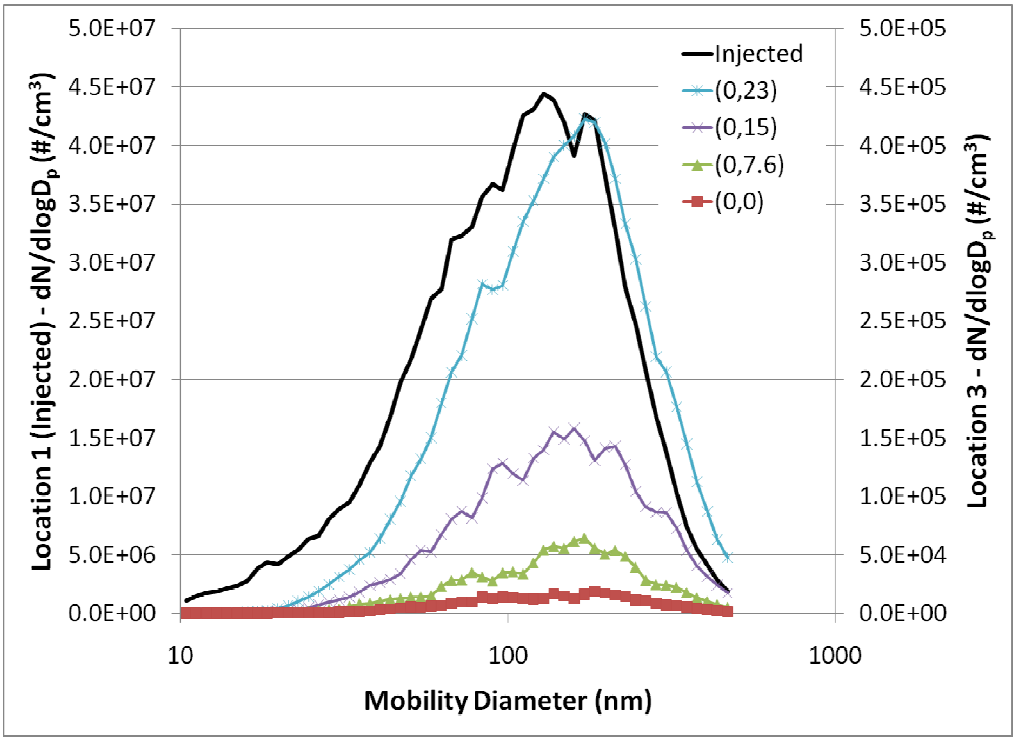

Figure F.8: 1.8 m downstream of leak (Location 3) using lean fuel/air mix and 27 mm leak.

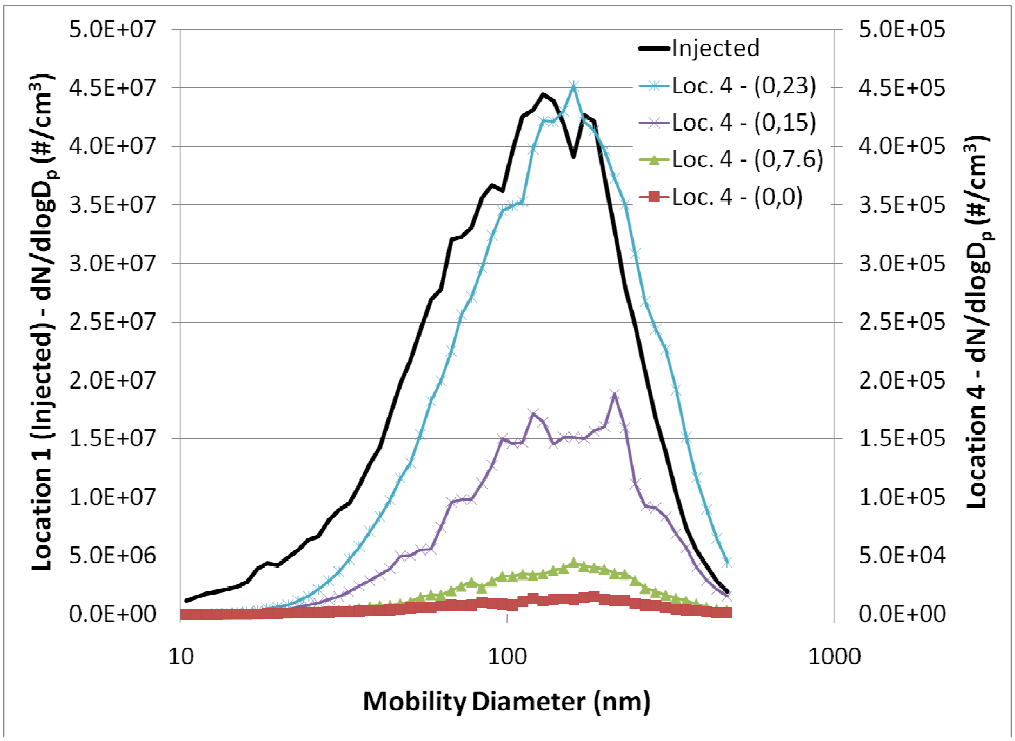

Figure F.9: 3.4 m downstream of leak (Location 4) using lean fuel/air mix and 27 mm leak.

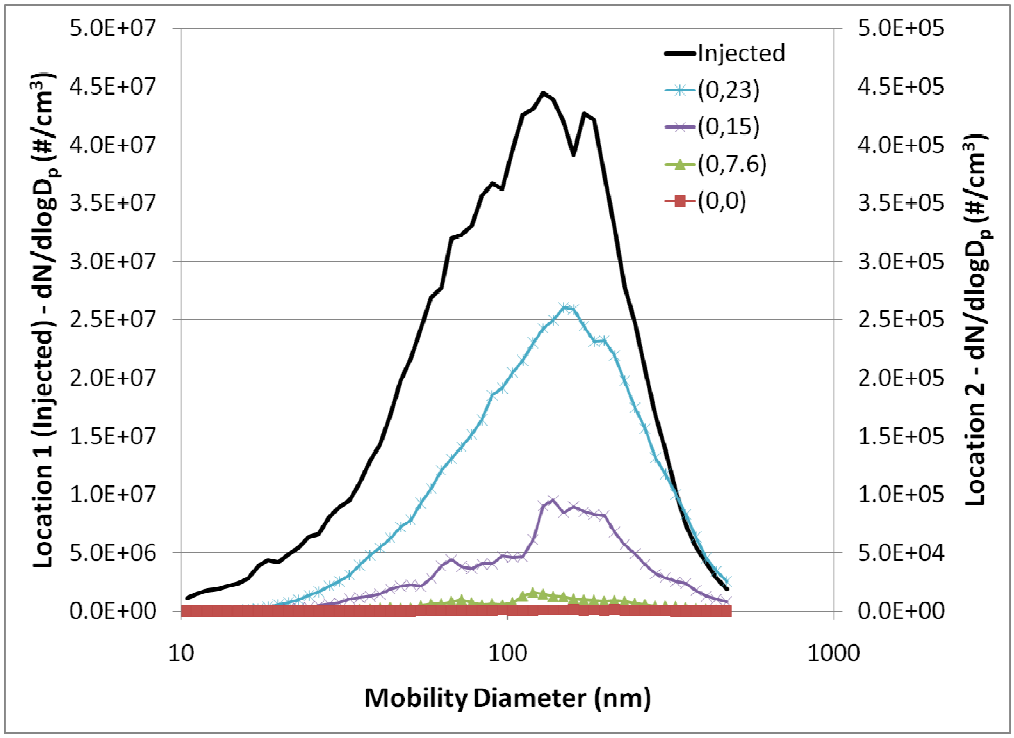

Figure F.10: 0.9 m downstream of leak (Location 2) using lean fuel/air mix and 10 mm leak.

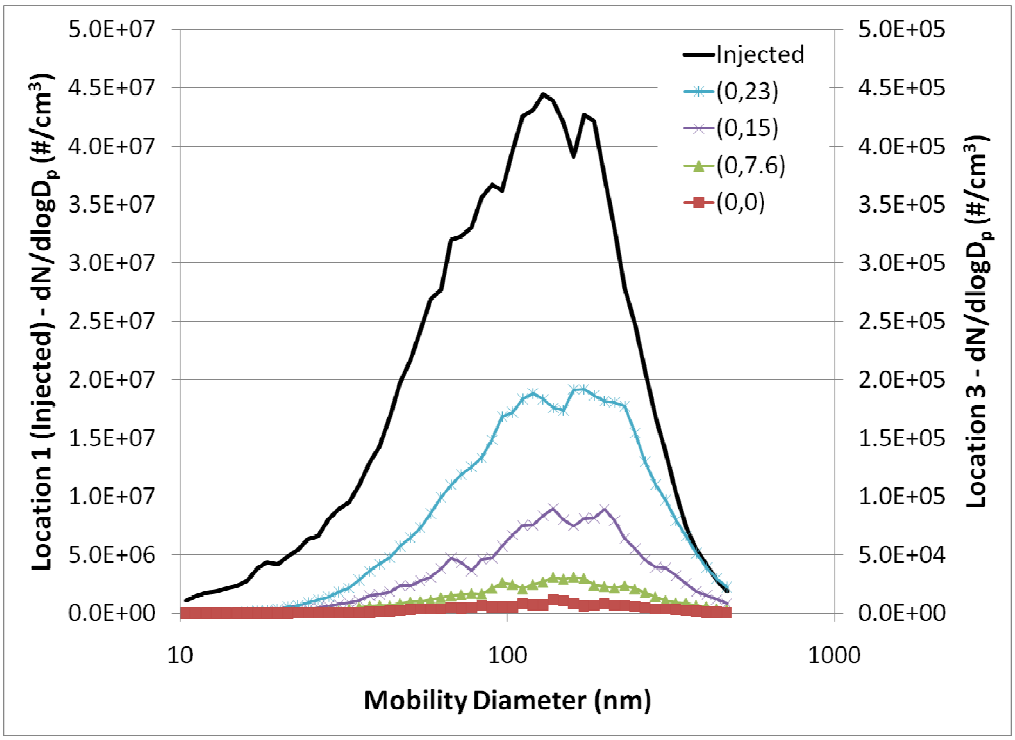

Figure F.11: 1.8 m downstream of leak (Location 3) using lean fuel/air mix and 10 mm leak.

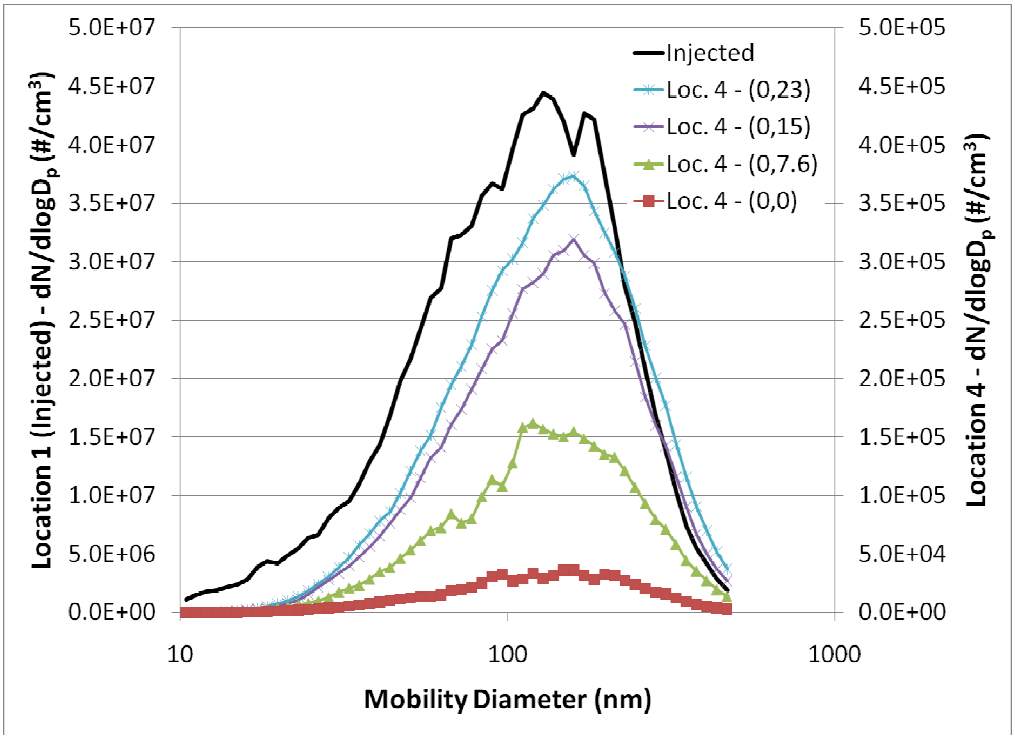

Figure F.12: 3.4 m downstream of leak (Location 4) using lean fuel/air mix and 10 mm leak.

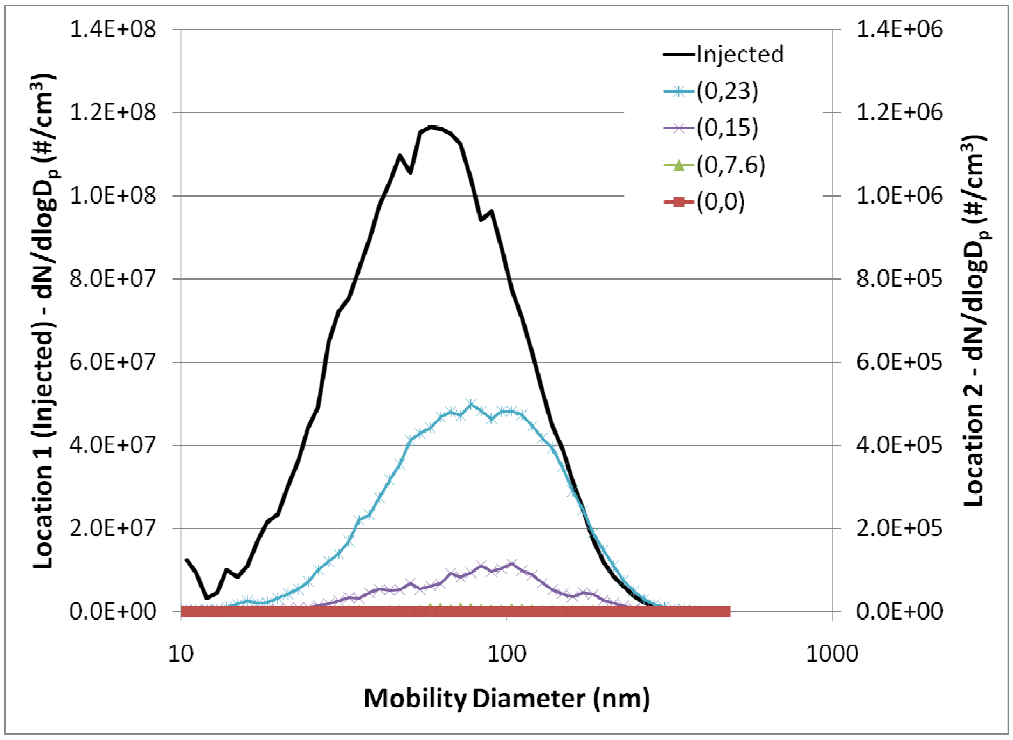

Figure F.13: 0.9 m downstream of leak (Location 2) using rich fuel/air mix and 27 mm leak.

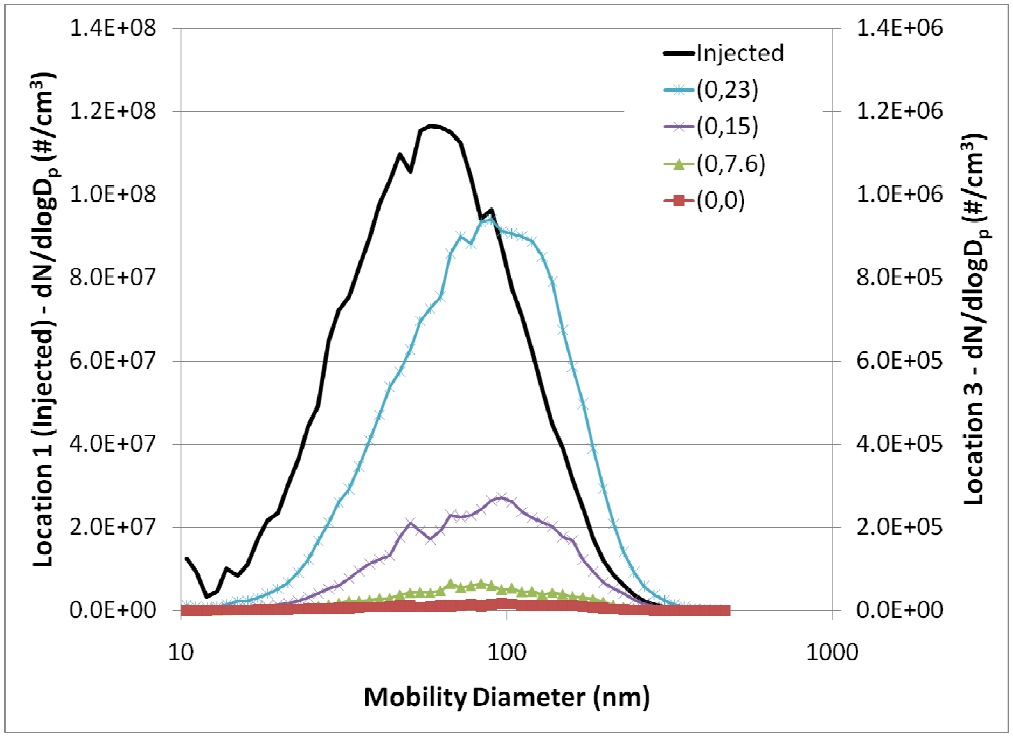

Figure F.14: 1.8 m downstream of leak (Location 3) using rich fuel/air mix and 27 mm leak.

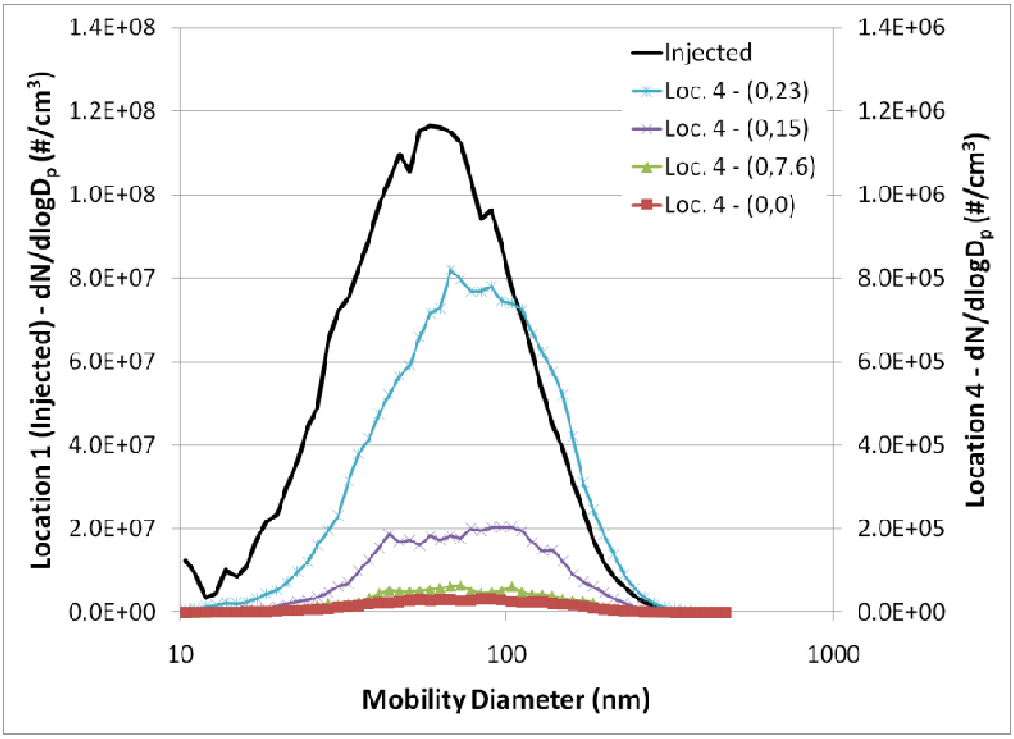

Figure F.15: 3.4 m downstream of leak (Location 4) using rich fuel/air mix and 27 mm leak.

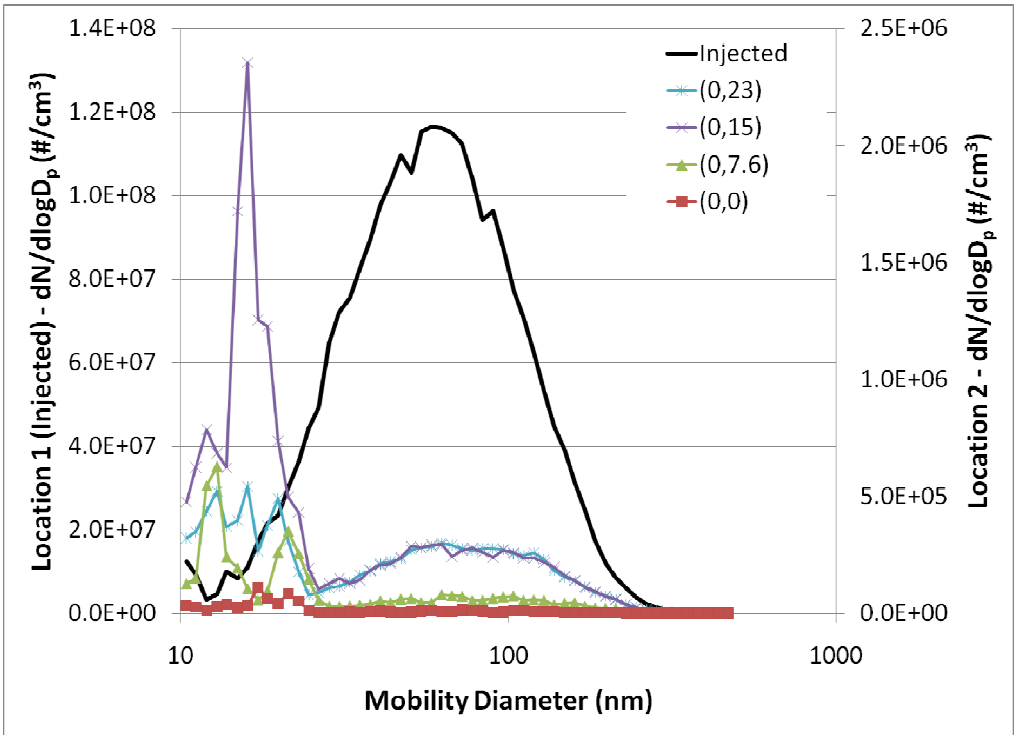

Figure F.16: 0.9 m downstream of leak (Location 2) using rich fuel/air mix and 10 mm leak.

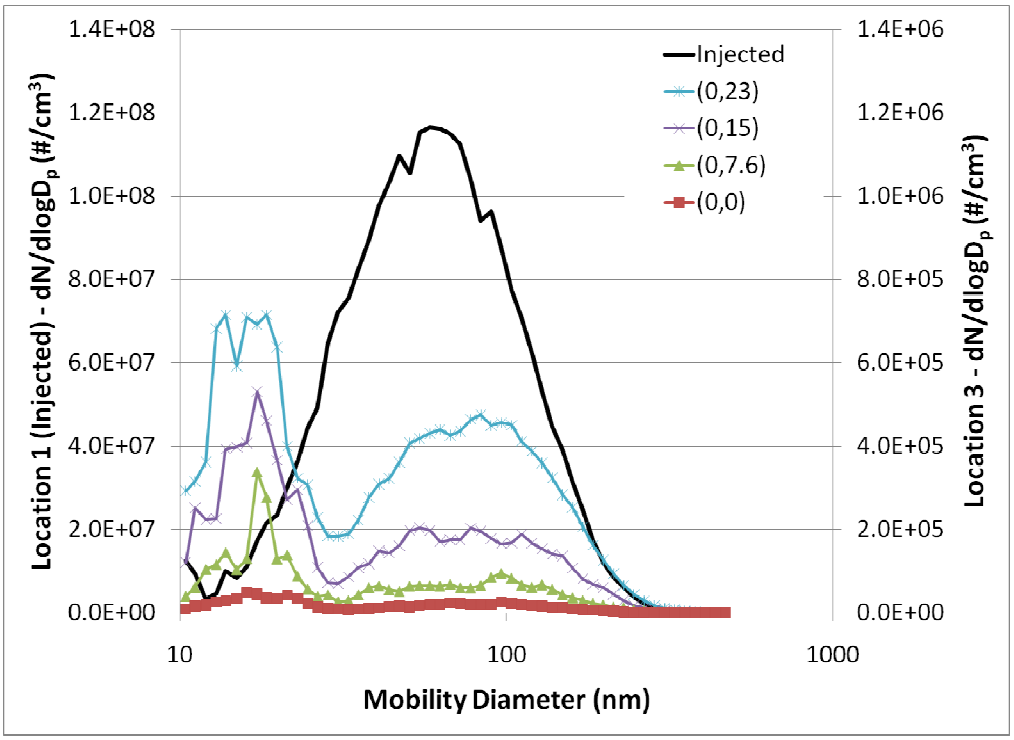

Figure F.17: 1.8 m downstream of leak (Location 3) using rich fuel/air mix and 10 mm leak.

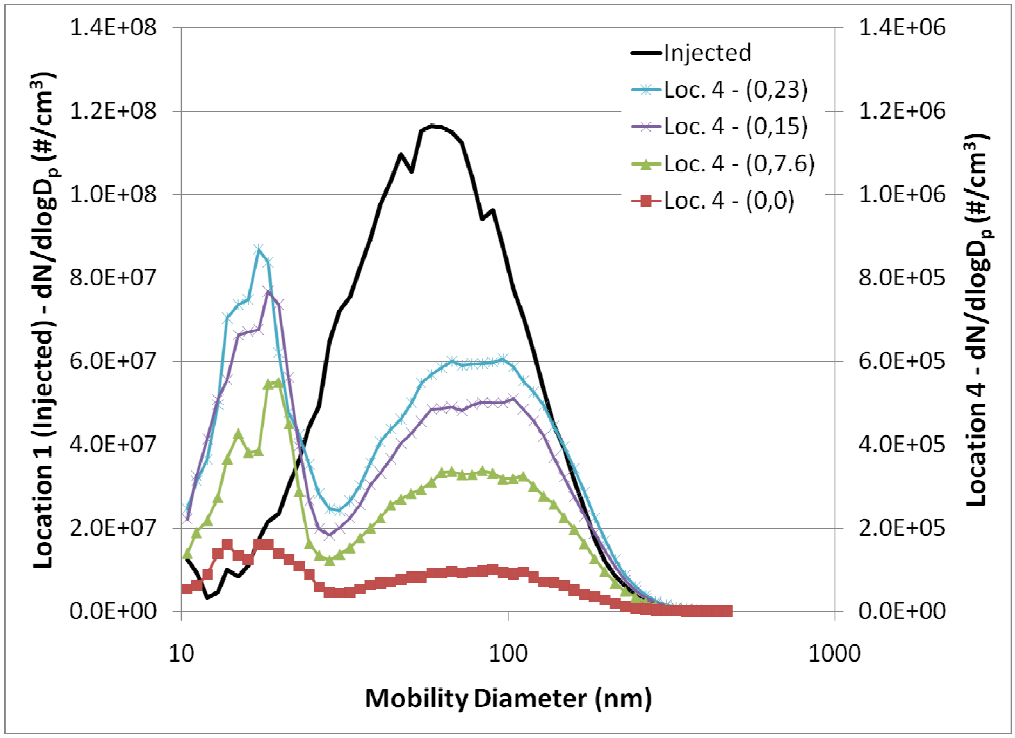

Figure F.18: 3.4 m downstream of leak (Location 4) using rich fuel/air mix and 10 mm leak.

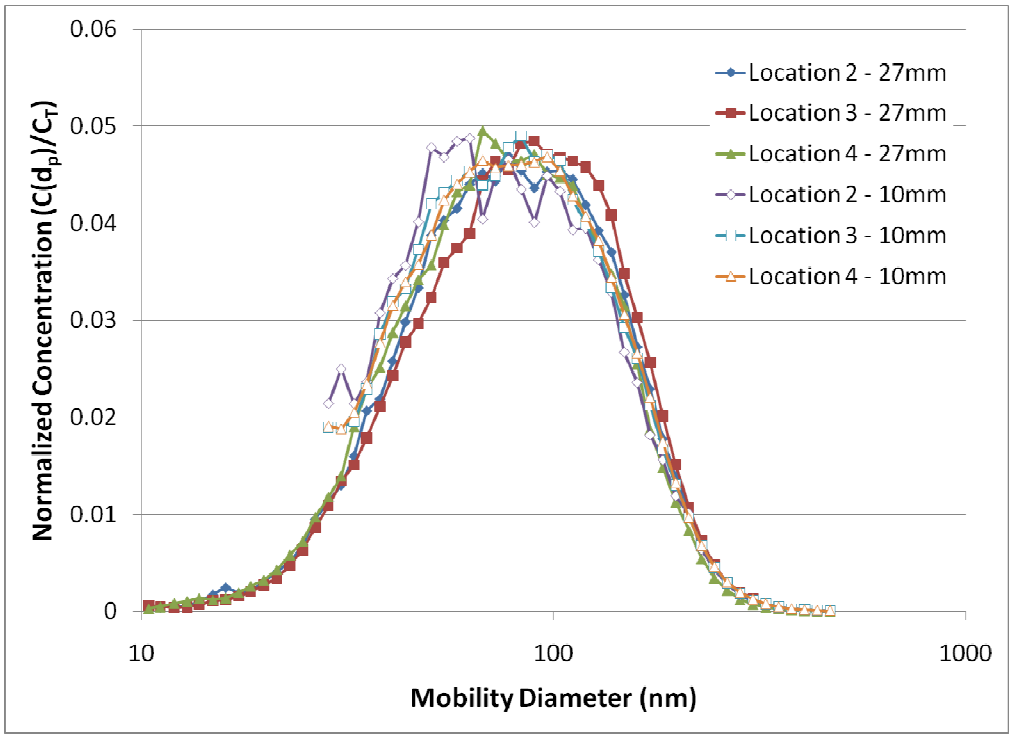

Figure F.19: Rich fuel/air mix with 27 mm leak normalized distributions and 10 mm leak larger particle mode normalized distributions for 0.9 m, 1.8 m, and 3.4 m downstream (Locations 2, 3, and 4).

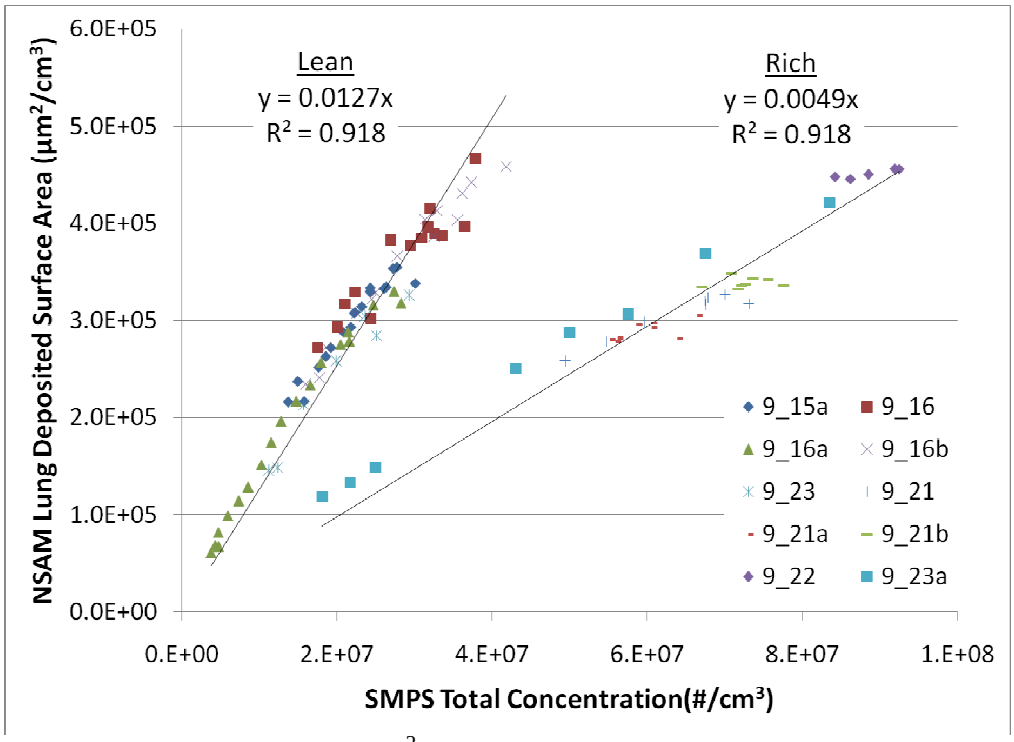

Figure F.20: NSAM/SMPS ratio (μm^2/particle) at the injection point.

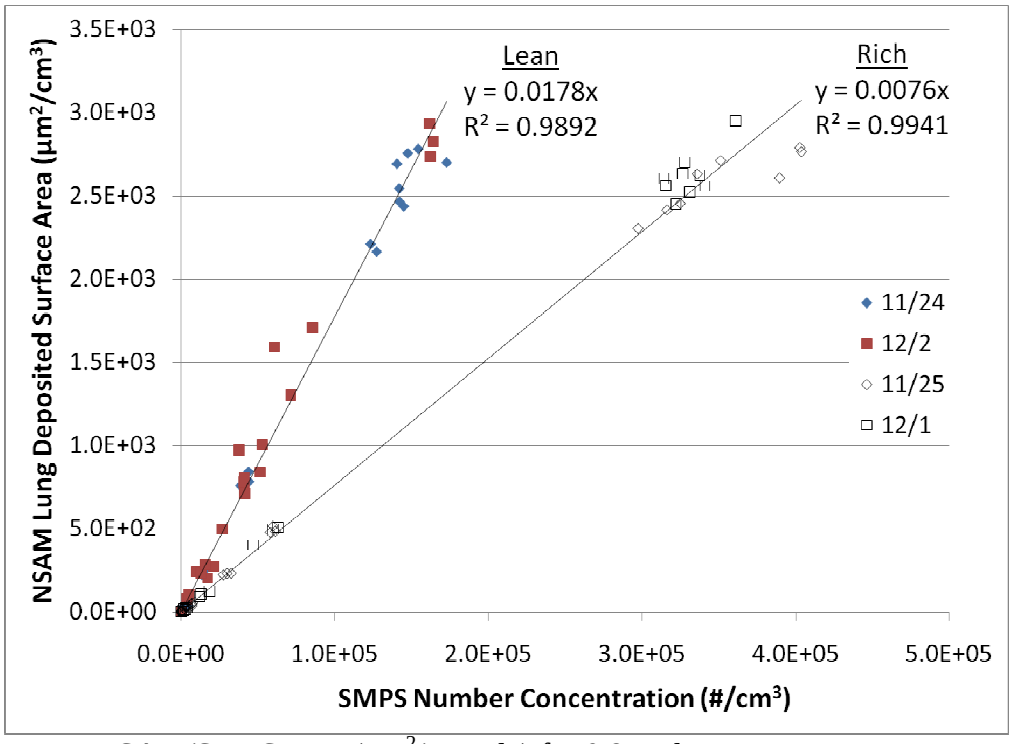

Figure F.21: NSAM/SMPS ratio (µm^2/particle) for 0.9 m downstream, using 27 mm leak.

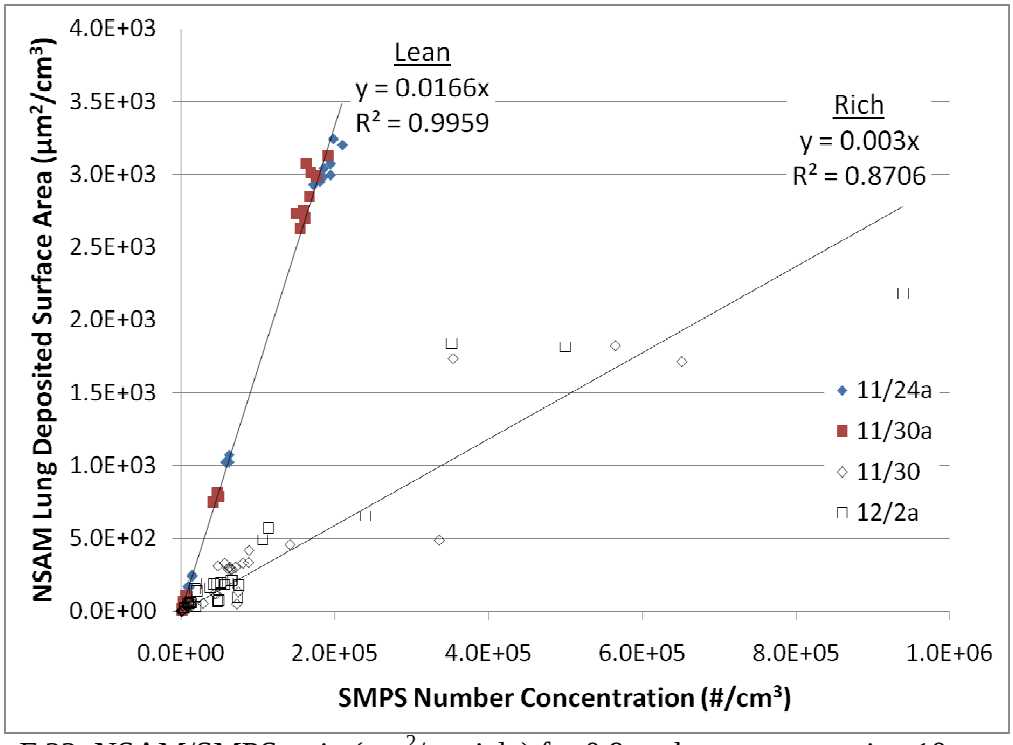

Figure F.22: NSAM/SMPS ratio (µm^2/particle) for 0.9 m downstream, using 10 mm leak.

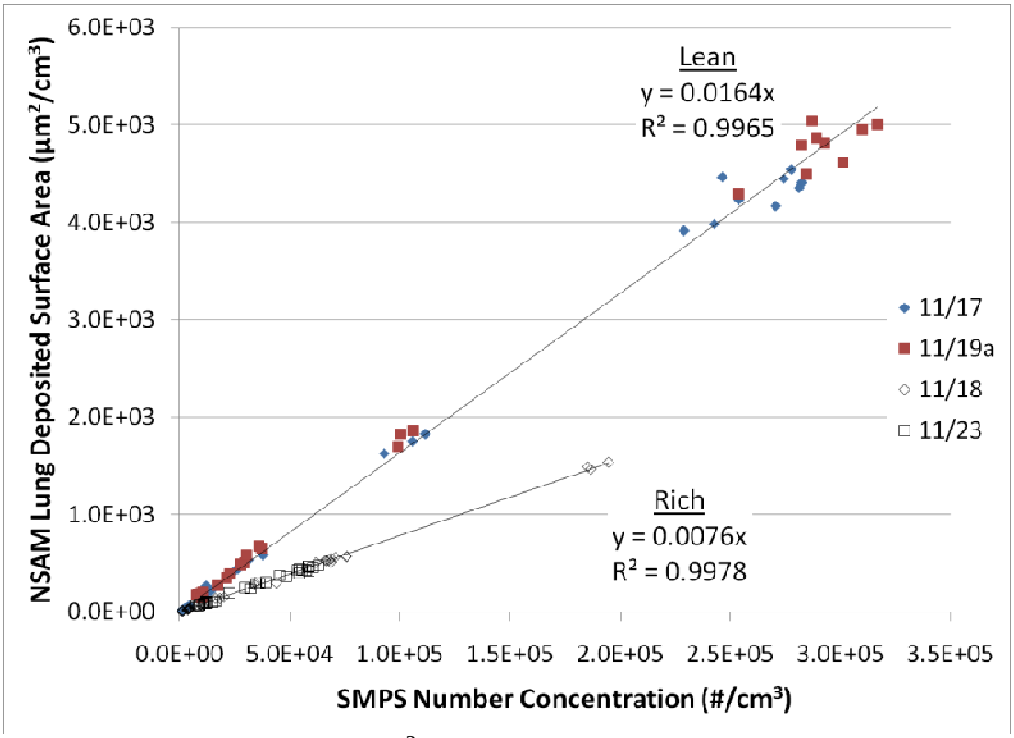

Figure F.23: NSAM/SMPS ratio (µm^2/particle) for 1.8 m downstream, using 27 mm leak.

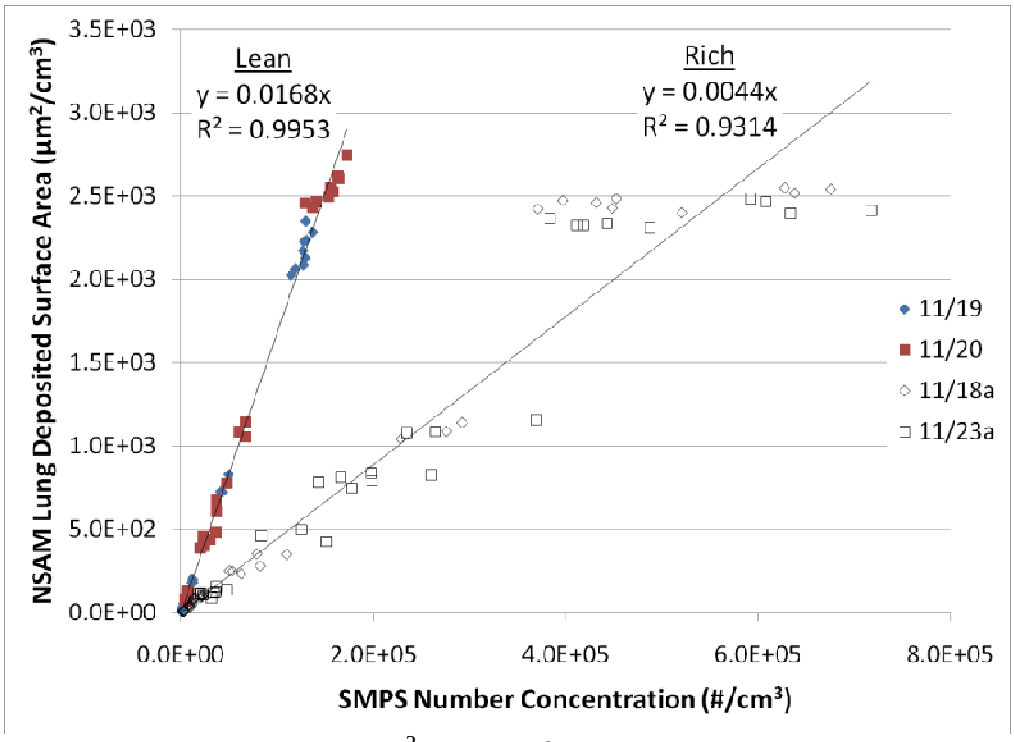

Figure F.24: NSAM/SMPS ratio (µm^2/particle) for 1.8 m downstream, using 10 mm leak.

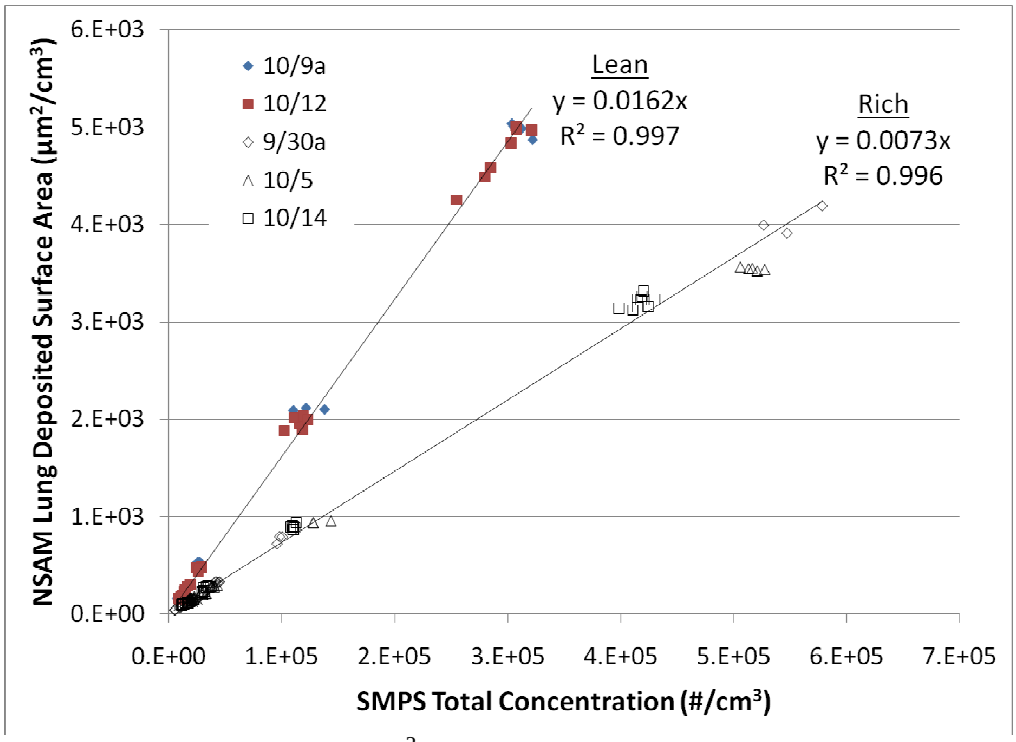

Figure F.25: NSAM/SMPS ratio (µm^2/particle) for 3.4 m downstream, using 27 mm leak.

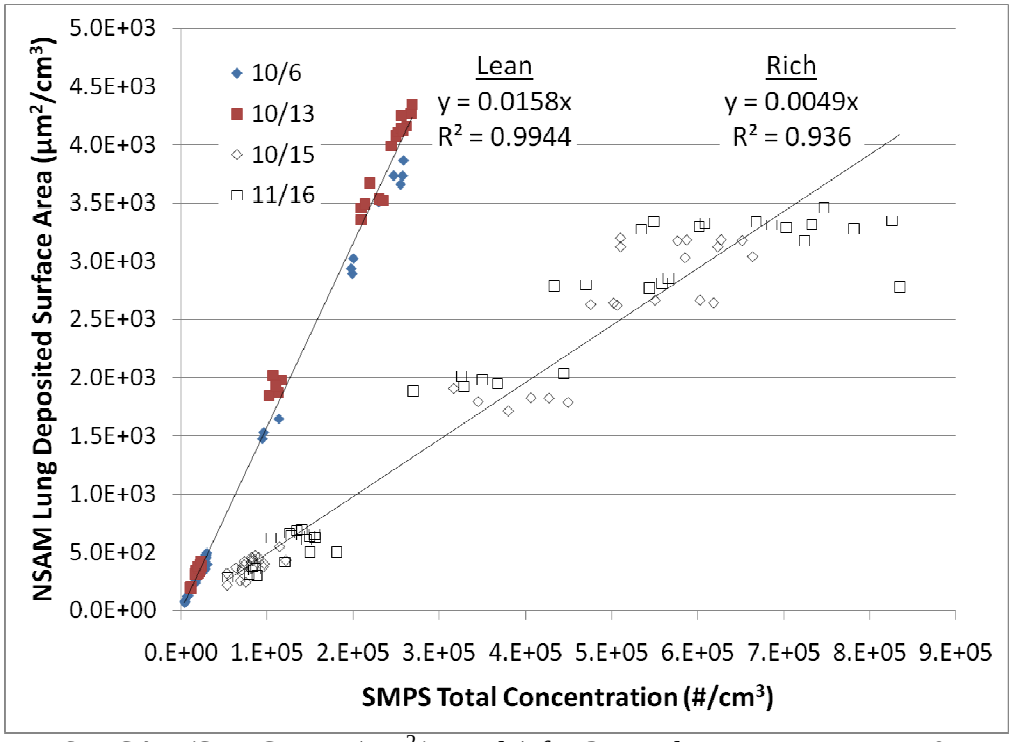

Figure F.26: NSAM/SMPS ratio (µm^2/particle) for 3.4 m downstream, using 10 mm leak.

Appendix G: TiO_2 EDS/TEM, Distributions, Fume Hood Plots, and NSAM/SMPS Ratio Figures

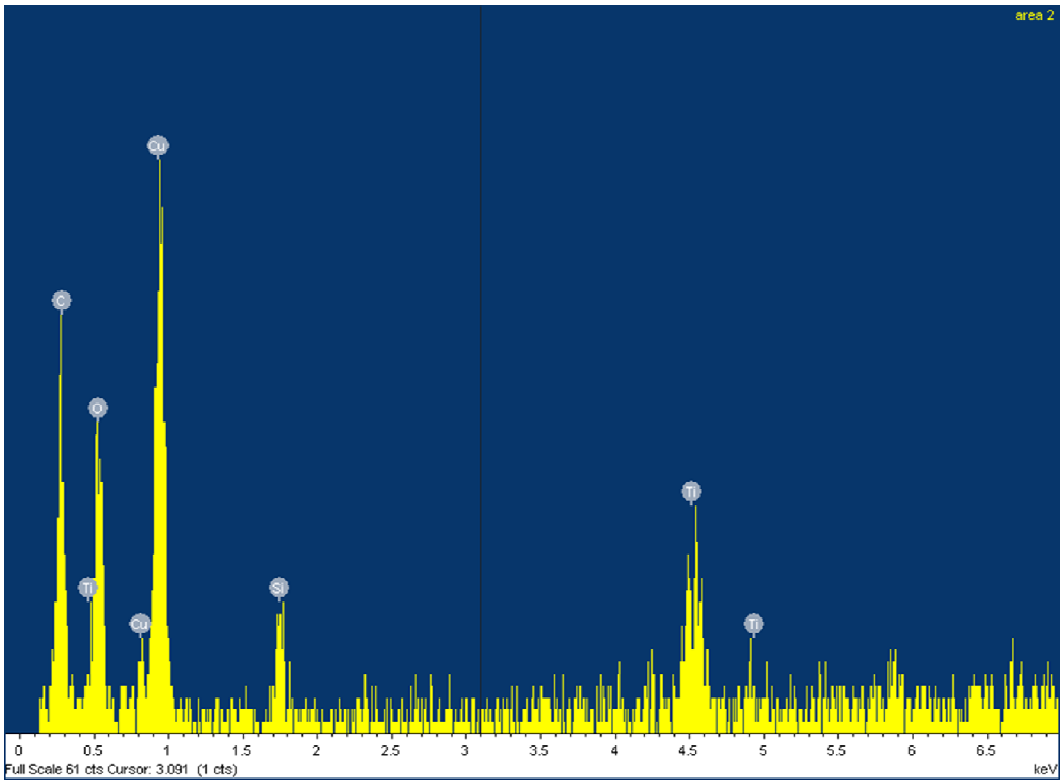

Figure G.1: TiO_2 particle composition by EDS analysis.

Table G.1: Raw data for TiO_2 particle size distributions, using 27 mm leak. Injected data was measured at centerline of wind tunnel. Downstream Location data was measured at point of highest concentration (0,23).

		Downstream Locations		
d_m (nm)	Injected	0.9 m	1.8 m	3.4 m
10.4	51745503	175269	368797	310683
11.1	57536102	235167	485393	418126
12	64990797	261258	590129	512983
12.9	70952853	297358	659668	596375
13.8	76217558	404533	795108	710937
14.9	80866127	476156	887631	802945
16	83674496	508103	958259	878537
17.2	84364374	551841	1077683	997753
18.4	83097202	628938	1193443	1055683
19.8	82764051	650993	1270808	1129055
21.3	78449113	661674	1265221	1152632
22.9	72699509	691400	1282683	1127039
24.6	66820466	721713	1324635	1095911
26.4	61065136	712240	1288549	1132103
28.4	54250083	680732	1281838	1127853
30.5	47656077	656584	1210986	1077620
32.8	40692549	639834	1137601	1031470
35.2	35028122	599621	1033956	906526
37.9	29687800	525347	897171	806527
40.7	25371011	516520	751316	736276
43.7	21706661	440672	649039	658298
47	18201435	366911	554539	545575
50.5	15610122	325958	482094	479533
54.2	13046027	285355	391870	428548
58.3	11024784	243858	323168	373240
62.6	9362043	226444	272950	308170
67.3	8080571	176354	224438	261524
72.3	6810334	134299	195007	214904

		Downstream Locations		
d_m (nm)	Injected	0.9 m	1.8 m	3.4 m
77.7	5592331	112915	163285	173213
83.5	4603820	96962	136846	141018
89.8	3665954	88259	113844	118722
96.5	2960569	75116	95114	93881
103.7	2327508	58206	75313	76825
111.4	1792246	46376	57090	61636
119.7	1354324	36358	44972	48983
128.6	1002016	27063	33572	38744
138.2	720084	19329	25573	30008
148.6	496793	15446	18457	22481
159.6	334421	12257	13066	16373
171.5	219066	8941	8711	11325
184.3	140032	5727	5656	7518
198.1	84825	3760	3526	4792
212.9	50858	2282	2077	3115
228.8	31080	1318	1123	1928
245.8	19470	753	581	1113
264.2	12855	405	279	620
283.9	10000	195	128	313
305.1	8356	96	61	162
327.8	5975	43	27	83
352.3	4260	20	15	44
378.6	3344	11	8	22
406.8	2385	5	6	14
437.1	1790	5	6	9
469.8	1414	5	7	8
d_g (nm)	21	28	26	27
σ_g	1.62	1.71	1.67	1.66
N_{total} (cm^{-3})	4.3E+07	418968	739167	679042

Table G.2: Raw data for TiO_2 particle size distributions (Figure 5.3.2.3), using 10 mm leak. Injected data was measured at centerline of wind tunnel. Downstream Location data was measured at point of highest concentration (0,23).

		Downstream Locations		
d_m (nm)	Injected	0.9 m	1.8 m	3.4 m
10.4	51745503	290585	373466	375973
11.1	57536102	361460	458901	499122
12	64990797	437085	566769	598633
12.9	70952853	505448	685883	689974
13.8	76217558	583238	734593	827701
14.9	80866127	647755	825700	918313
16	83674496	695378	902359	1031078
17.2	84364374	753218	967377	1094208
18.4	83097202	809420	1059464	1158350
19.8	82764051	902746	1088891	1168328
21.3	78449113	903306	1067352	1183808
22.9	72699509	877679	995078	1164600
24.6	66820466	820381	934215	1163098
26.4	61065136	782246	860656	1168623
28.4	54250083	727783	842181	1127879
30.5	47656077	667384	786079	1026208
32.8	40692549	665863	681670	953682
35.2	35028122	585579	591191	851817
37.9	29687800	501205	516386	768388
40.7	25371011	457427	421977	649381
43.7	21706661	389583	350671	535659
47	18201435	350854	294631	436552
50.5	15610122	298819	255708	364133
54.2	13046027	245937	214953	307587
58.3	11024784	211376	174870	252455
62.6	9362043	183242	153803	220060
67.3	8080571	159555	129421	190052
72.3	6810334	133812	108733	159043

		Downstream Locations		
d_m (nm)	Injected	0.9 m	1.8 m	3.4 m
77.7	5592331	116823	93370	130469
83.5	4603820	100485	80817	107074
89.8	3665954	81105	69019	88817
96.5	2960569	63443	57442	68335
103.7	2327508	52892	45730	55454
111.4	1792246	41605	36390	45656
119.7	1354324	35064	27974	35653
128.6	1002016	27540	21239	26498
138.2	720084	20884	15819	19640
148.6	496793	15815	12073	14021
159.6	334421	11561	8391	9458
171.5	219066	8053	5457	6026
184.3	140032	5388	3627	3671
198.1	84825	3585	2339	2181
212.9	50858	2156	1420	1238
228.8	31080	1261	773	662
245.8	19470	665	402	324
264.2	12855	346	199	148
283.9	10000	168	97	69
305.1	8356	79	45	34
327.8	5975	38	23	18
352.3	4260	17	9	14
378.6	3344	10	7	6
406.8	2385	7	5	6
437.1	1790	5	5	5
469.8	1414	5	5	4
d_g (nm)	21	25	24	25
σ_g	1.62	1.70	1.65	1.66
N_{total} (cm^{-3})	4.3E+07	485543	547677	671881

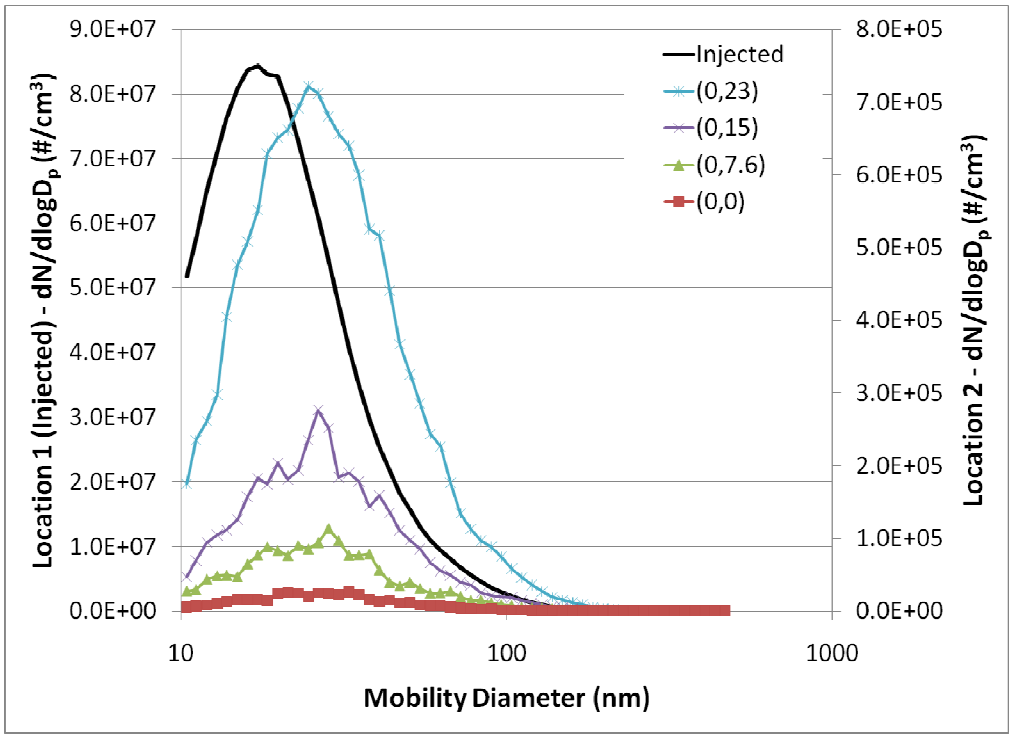

Figure G.2: 0.9 m downstream of leak (Location 2) with 27 mm leak, using TiO_2.

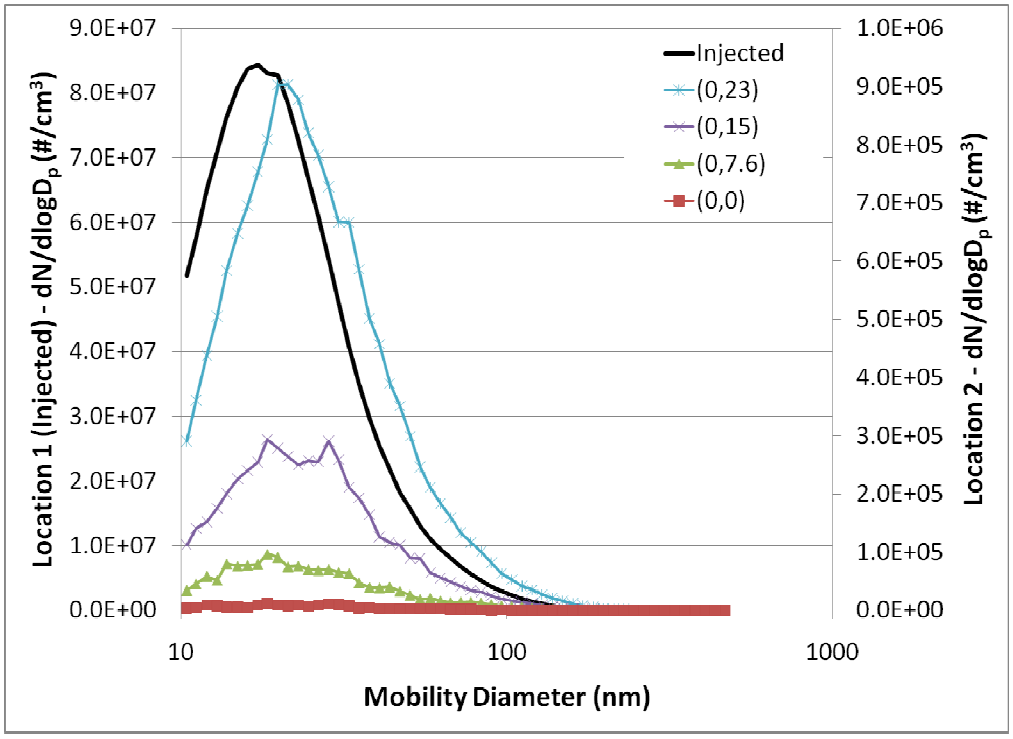

Figure G.3: 0.9 m downstream of leak (Location 2) with 10 mm leak, using TiO_2.

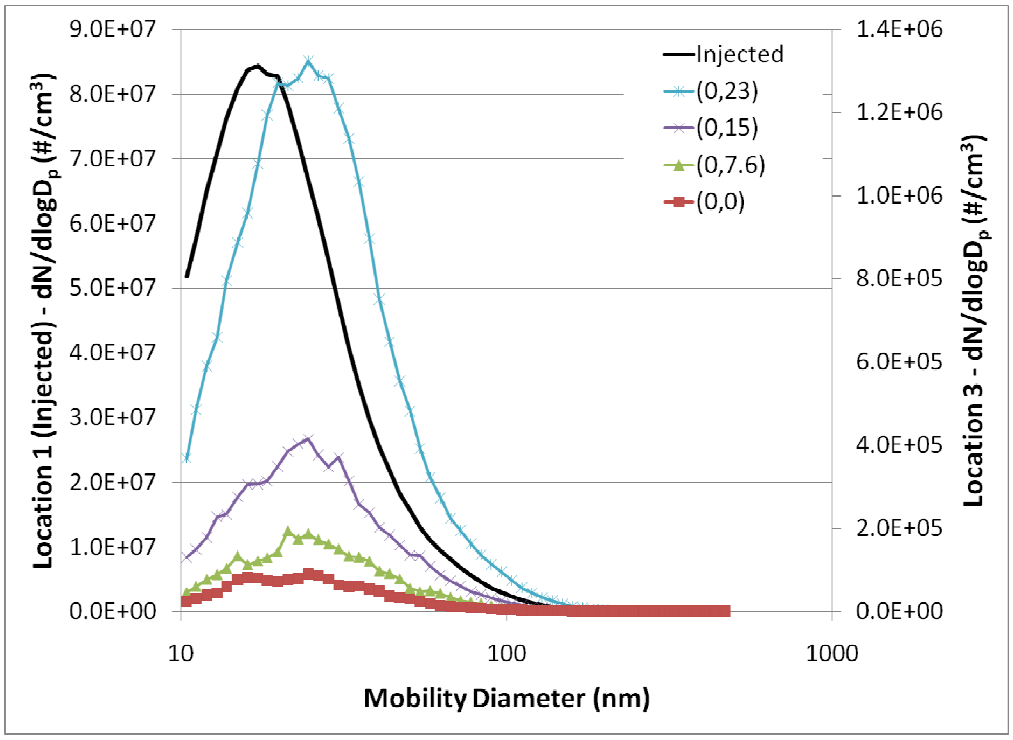

Figure G.4: 1.8 m downstream of leak (Location 3) with 27 mm leak, using TiO_2.

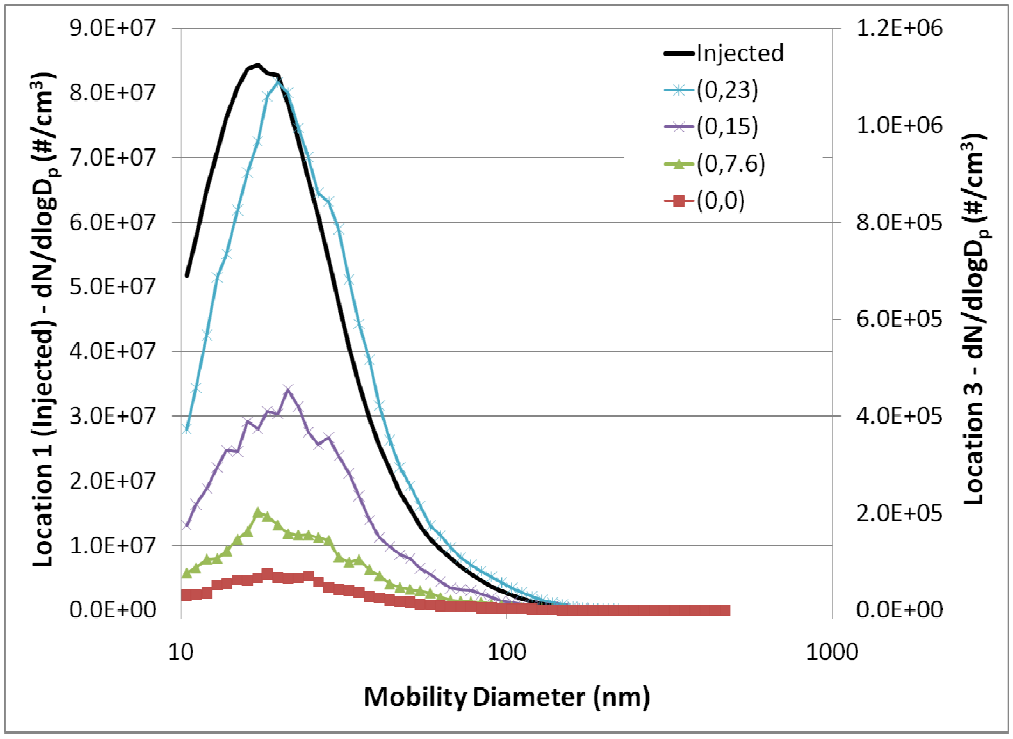

Figure G.5: 1.8 m downstream of leak (Location 3) with 10 mm leak, using TiO_2.

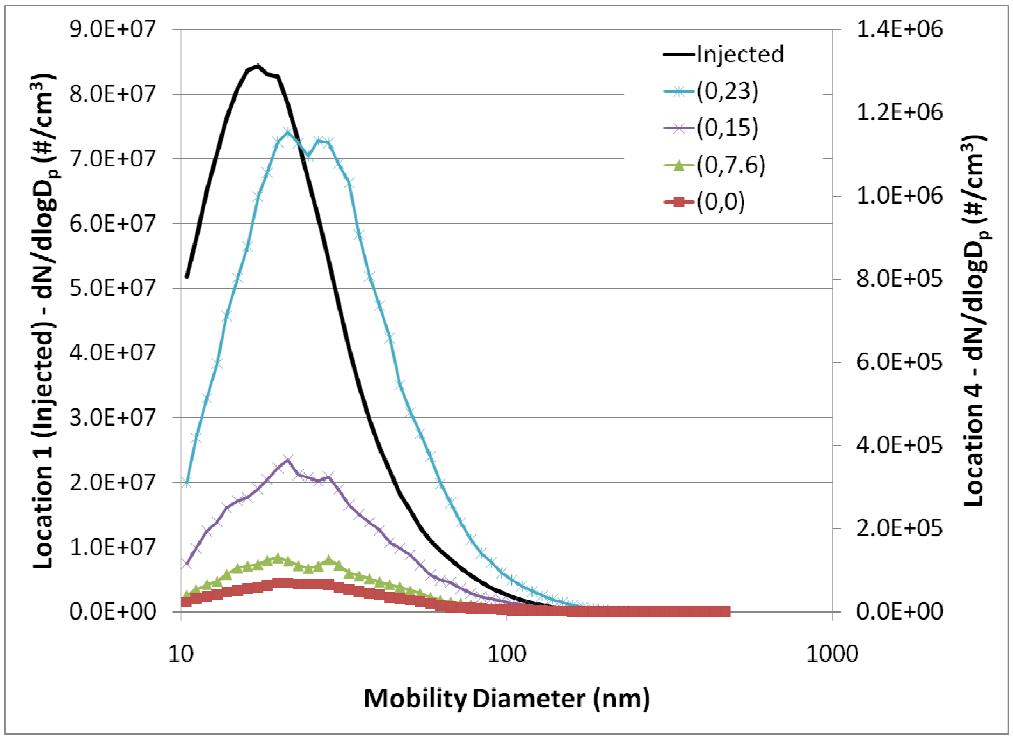

Figure G.6: 3.4 m downstream of leak (Location 4) with 27 mm leak, using TiO_2.

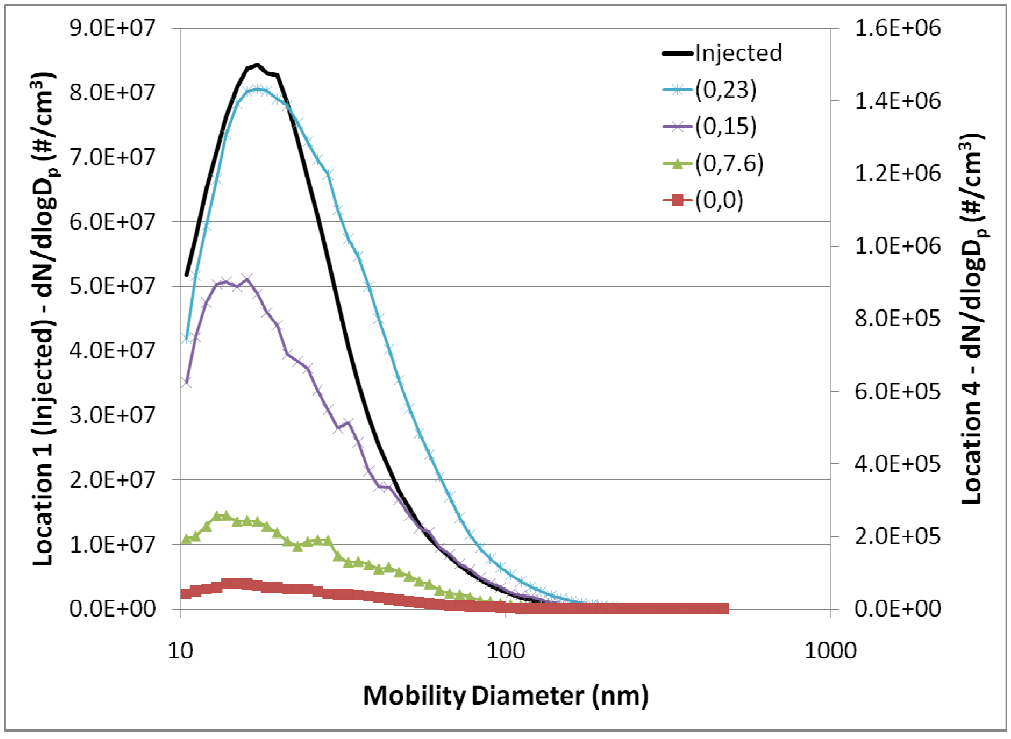

Figure G.7: 3.4 m downstream of leak (Location 4) with 10 mm leak, using TiO_2.

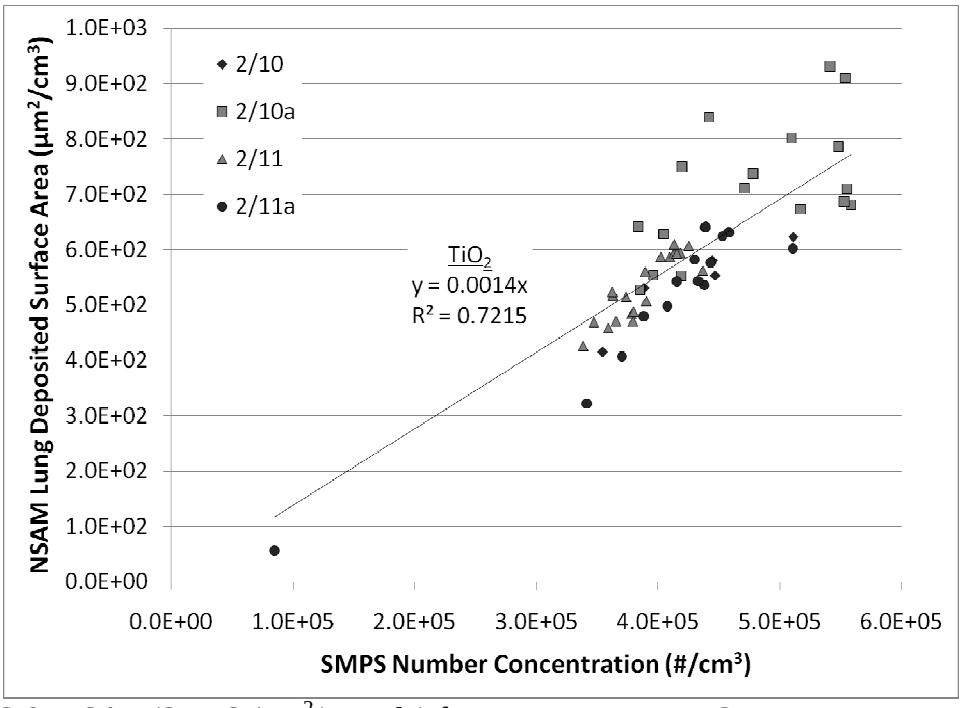

Figure G.8: NSAM/SMPS (μm^2/particle) for injection point, TiO_2.

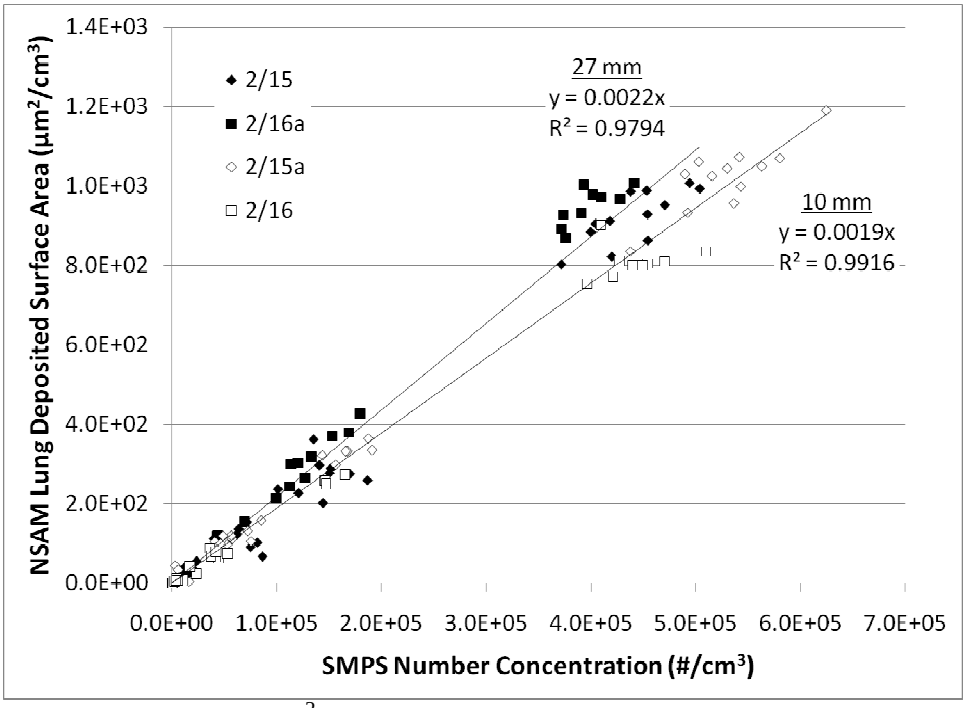

Figure G.9: NSAM/SMPS (μm^2/particle) at 0.9 m downstream, TiO_2.

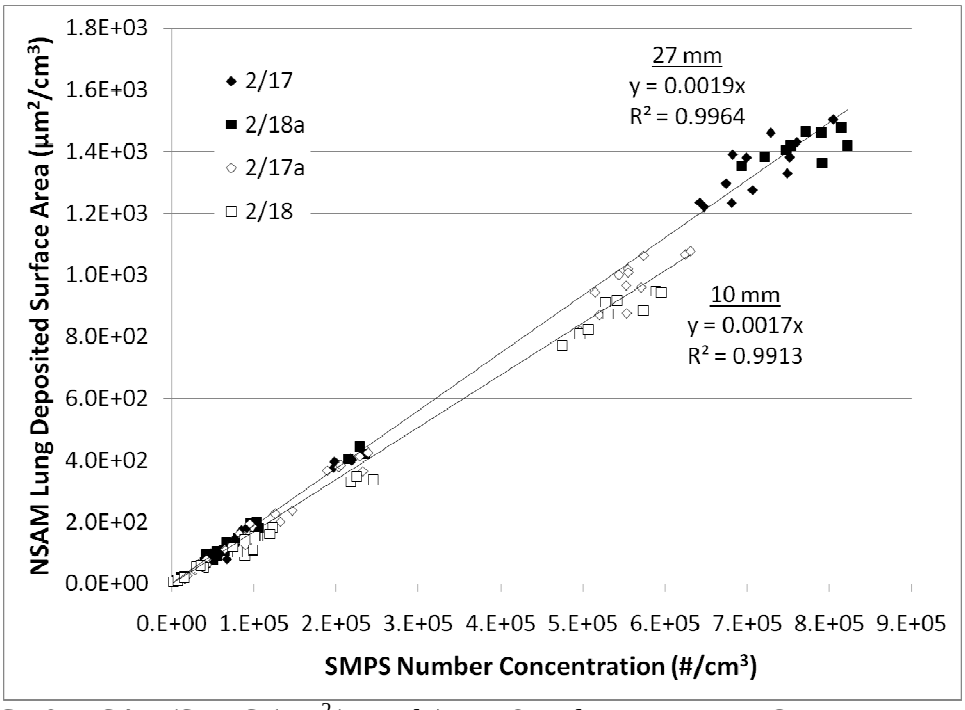

Figure G.10: NSAM/SMPS (µm^2/particle) at 1.8 m downstream, TiO_2.

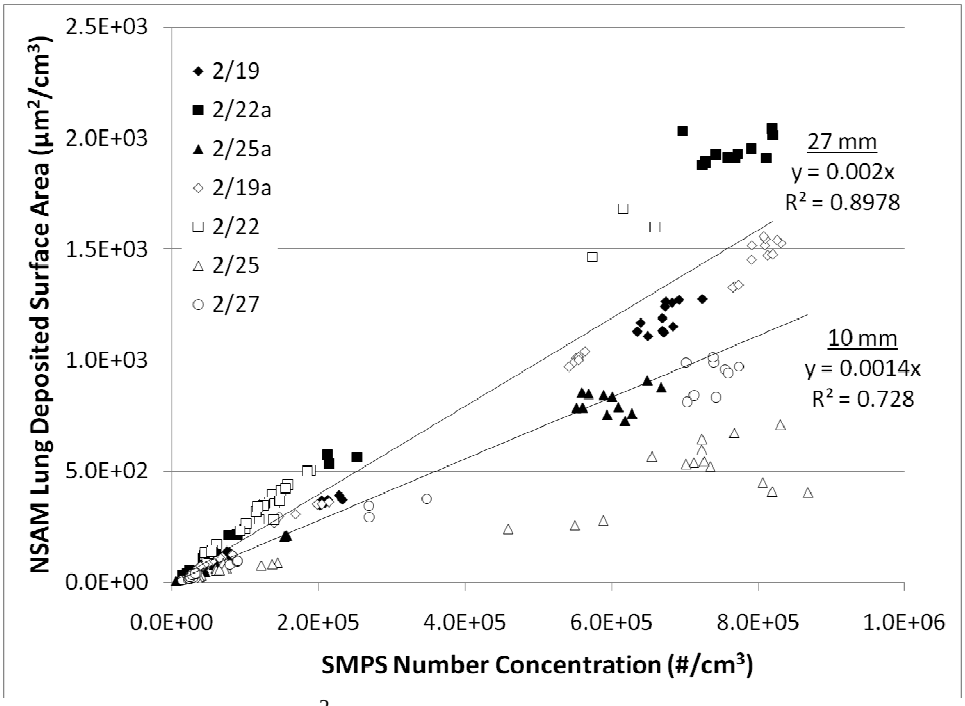

Figure G.11: NSAM/SMPS (µm^2/particle) at 3.4 m downstream, TiO_2.

Appendix H: SiO_2 Transport and Particle Change through a Simulated Workplace Environment including SiO_2 EDS/TEM, Distributions, Fume Hood Plots, and NSAM/SMPS Ratio Figures

The SiO_2 geometric mean particle sizes are shown in Table H.1 for each leak size and each measurement location. Since several trials were conducted, a statistical analysis may be used to determine if the geometric mean particle sizes are truly different at locations downstream of the leak. These geometric mean particle sizes were analyzed using a t-test of unequal variance with degrees of freedom calculated using Welch's method for each nanoparticle material and each leak size. The specific details of this statistical analysis can be found in Appendix K.

The SiO_2 geometric mean particle sizes for each leak size at each measurement location downstream are shown in Table H.1. A statistical analysis was performed to see if the geometric mean particle sizes are significantly different. The details of the statistical analysis were described above. Statistically, there is no difference between the different measurement locations when using the 27 mm leak. When using the 10 mm leak, there is a statistically significant difference between the injection point and 0.9 m downstream and there is not a statistically significant difference between 0.9, 1.8, and 3.4 m downstream. Therefore, according to the SMPS, the SiO_2 particles decrease in geometric mean particle size downstream of the leak.

Table H.1: SiO_2 geometric mean particle size for each leak size at each measurement Location.

	27 mm	10 mm
0 m downstream	175	
0.9 m downstream	151	139
1.8 m downstream	156	142
3.4 m downstream	164	132

Table H.2 shows the total particle concentration of SiO_2 for each measurement location and each leak size. Turbulent mixing is most likely the cause of the differences in total particle concentrations as outlined in the analysis of soot particle dispersion in Section 4.3.2. However the differences may have also been caused by day-to-day variations in burner output, which is especially likely when working with highly reactive precursor material.

Table H.2: SiO_2 total particle concentrations for each leak size at each measurement Location.

	27 mm	10 mm
0 m downstream	8.5E+07	
0.9 m downstream	2.9E+05	3.4E+05
1.8 m downstream	3.8E+05	3.3E+05
3.4 m downstream	5.6E+05	5.9E+05

SiO_2 Aerosol Properties Downstream of Leak

The normalized particle size distributions for SiO_2 using the 27 mm and 10 mm leak size are shown in Figures H.1 and H.2, respectively. The raw data for each figure is located in Tables H.3 and H.4. For each figure, the particle size distributions are consistent at locations downstream of the leak. When using the 27 mm leak (Figure H.1), there is a shift in the particle distribution towards smaller particle sizes. This shift

towards smaller sized particles is more noticeable when using the 10 mm leak size (Figure H.2). The high concentrations of particles should lead to coagulation, causing particle growth and a shift towards larger particles. During the current study, particle growth was noticed when examining soot and TiO_2. For SiO_2, a decrease in particle size is apparent instead. Each condition was randomly tested at each measurement location. The results at each measurement location (Location 2, 3, or 4) for each leak size (27 or 10 mm) are shown as Figures H.8 - H.13. These figures show the average particle size distribution for each sampling location depicted in Figure 4.2.2.

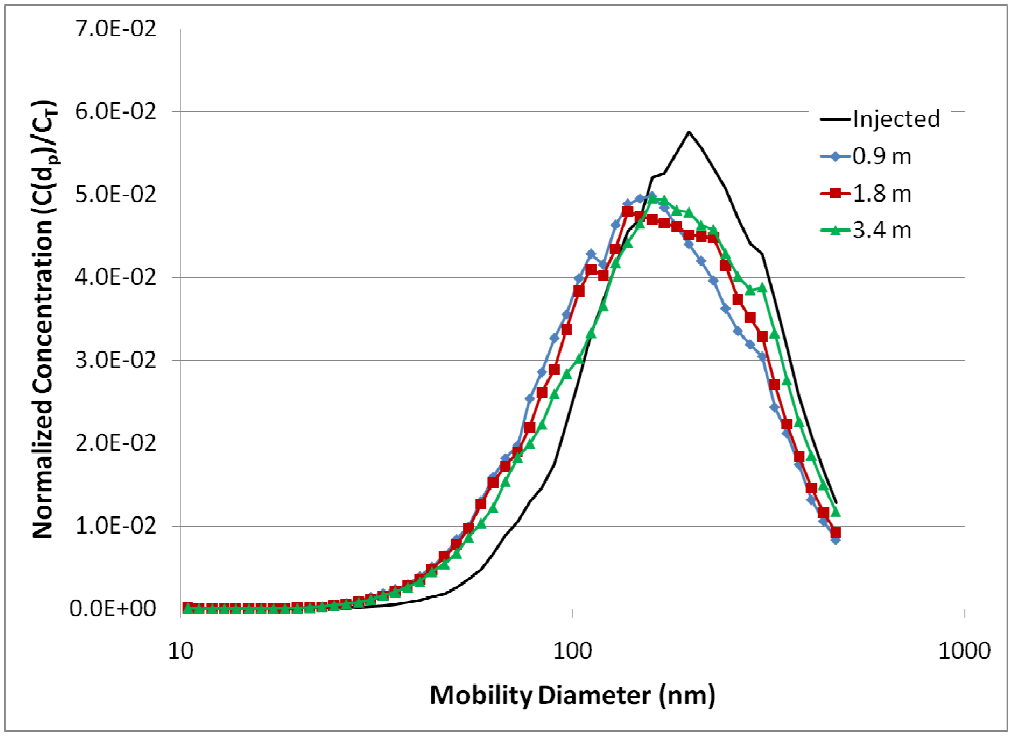

Figure H.1: Normalized particle size distributions at each measurement location using SiO_2 and 27 mm leak.

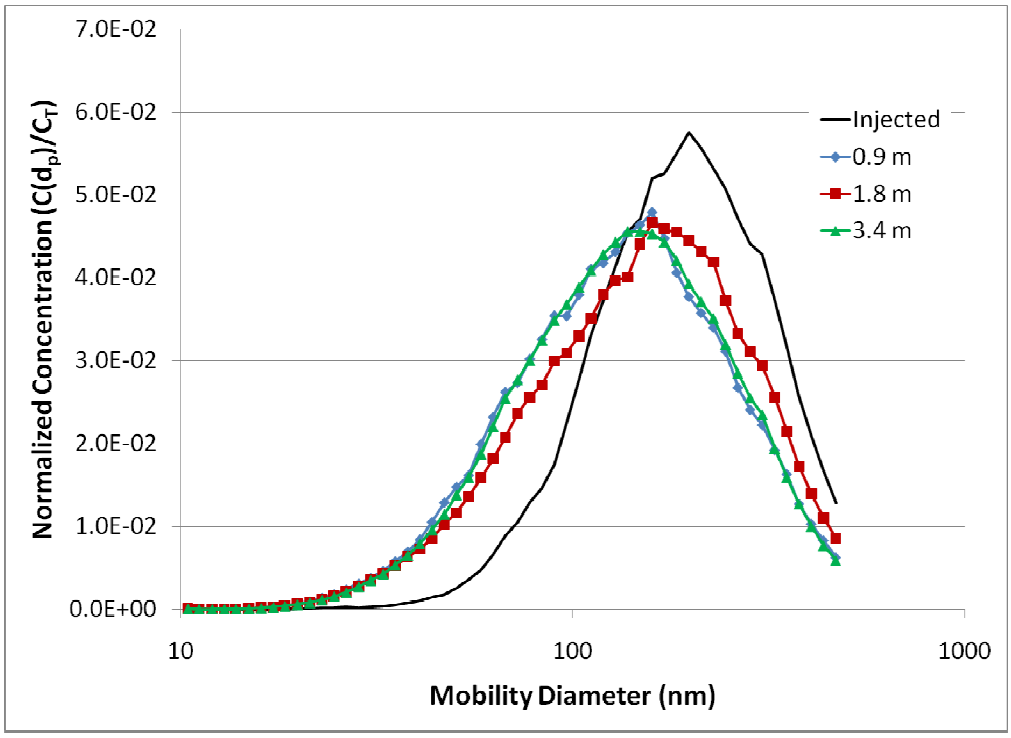

Figure H.2: Normalized particle size distributions at each measurement location using SiO_2 and 10 mm leak.

TEM images of SiO_2 particles at the injection point are shown in Figure 5.3.1.3, where larger, mid-sized, and smaller SiO_2 particles are apparent. Figure H.3 shows TEM images of SiO_2 particles at 3.4 m downstream of the leak. These SiO_2 particles at 3.4 m downstream consist of more of the larger particles than at the particle injection point. Therefore, the change in particle size distribution most likely occurred over time within the burner and not throughout distance in the wind tunnel. The burner gas flow rates were not changed; however changing the burner physical characteristics could also cause a change in primary particle size within the burner. The burner characteristics were not manually changed throughout the course of these experiments, however there was a change imparted by the formation of a SiO_2 "cap" on the top of the burner.

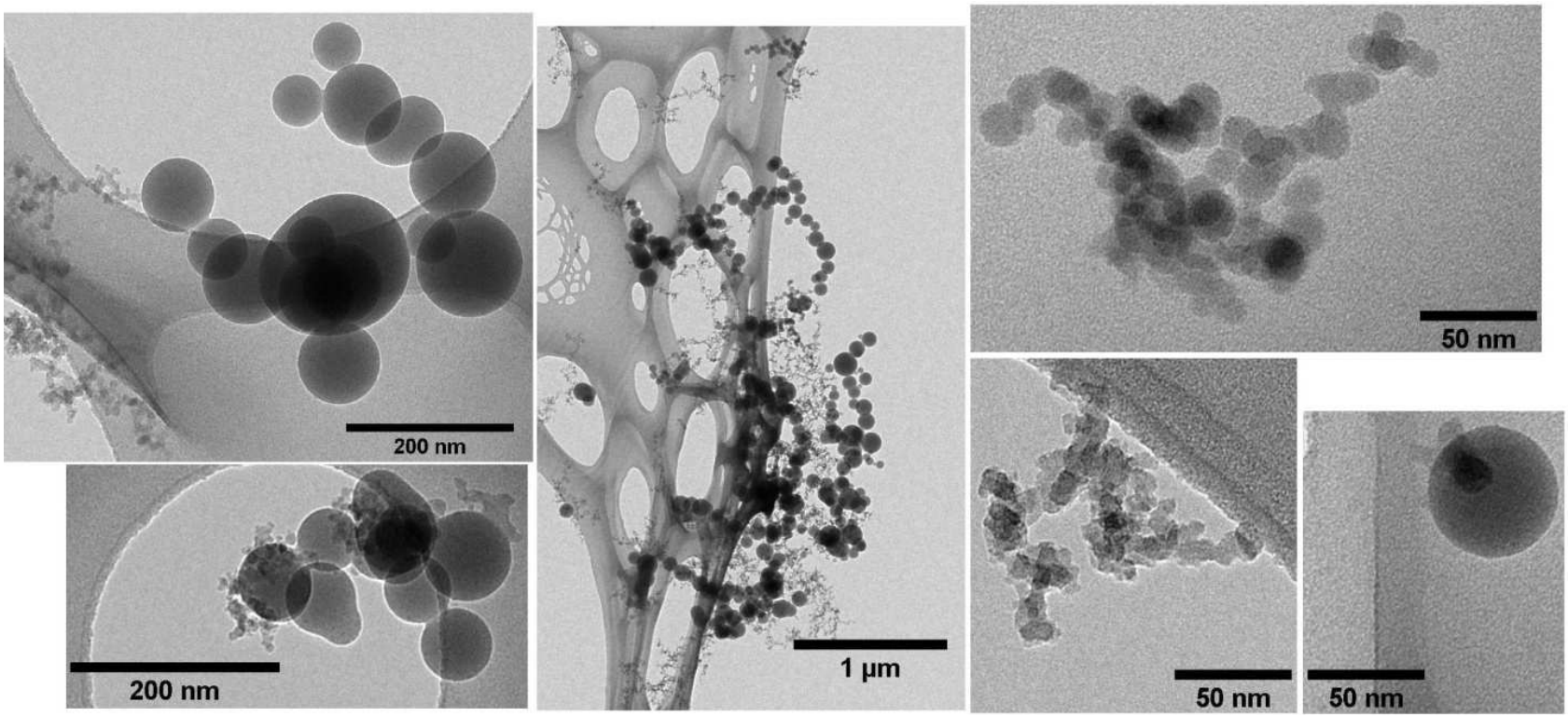

Figure H.3: SiO_2 TEM images at 3.4 m downstream of leak.

A picture of the burner after a SiO_2 cap has formed is shown in Figure H.14. As the burner produced particles, a large amount of SiO_2 settled on the edge of one of the gas carrier tubes in the middle of the burner (over the gas outlet). This build up of SiO_2 continued until a mushroom-shaped cap was formed, covering the methane and HMDSO burner gas outlet tubes. As the cap built over the duration of the experiment, the burner characteristics changed, and a different particle distribution may have been produced. This build up occurred over the course of each SiO_2 experimental trial. Testing the burner in a fume hood will verify the injected wind tunnel SiO_2 particles were influenced by the SiO_2 cap, formed within the burner over time.

When injecting SiO_2 into the wind tunnel, the initial characterization trials conducted at the injection point, could not last longer than 25 minutes. The sampling nozzle became clogged after just 6 minutes of sampling at the injection point with SiO_2. This clogging occurred due to the high concentration of large SiO_2 nanoparticle agglomerates produced by the burner. The sampling orifice could be pulsed clean; however this pulse cleaning became less effective as the sampling progressed (resulting in 25 minute trials). These initial trials were conducted until steady state was reached and maintained for soot and TiO_2 without significant clogging of the sampling nozzle.

Figure H.4 shows the normalized particle size distributions of SiO_2 as the burner was operated within a fume hood. Measurements were taken using the sampling orifice so dilution air could be introduced at the point of sampling. The fume hood was used so the sampling probe could be cleaned with an alcohol wipe between each measurement, preventing the clogging which occurred within the wind tunnel. These results verify the theory of a time-dependent burner output. Therefore the size distributions and aerosol

characteristics of SiO_2 within the wind tunnel were not consistently produced throughout the duration of the experiments. The SiO_2 size distribution decreases with time (Figure H.4), which is why the particles seem to decrease downstream of the injection point during the wind tunnel experiments. Figure H.5 shows the geometric mean particle size decreasing with time during the fume hood experiments. The NSAM results from the fume hood are inconsistent and inconclusive (Figure H.15).

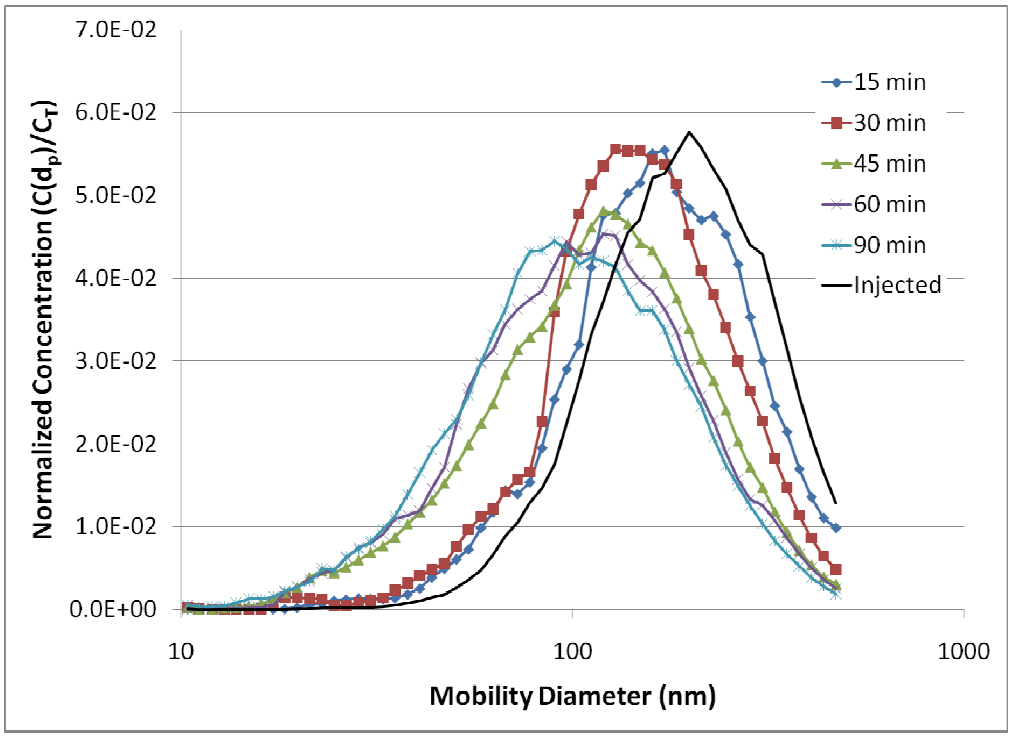

Figure H.4: Normalized particle distributions of SiO_2 throughout fume hood experiments (each averaged over 15 minutes).

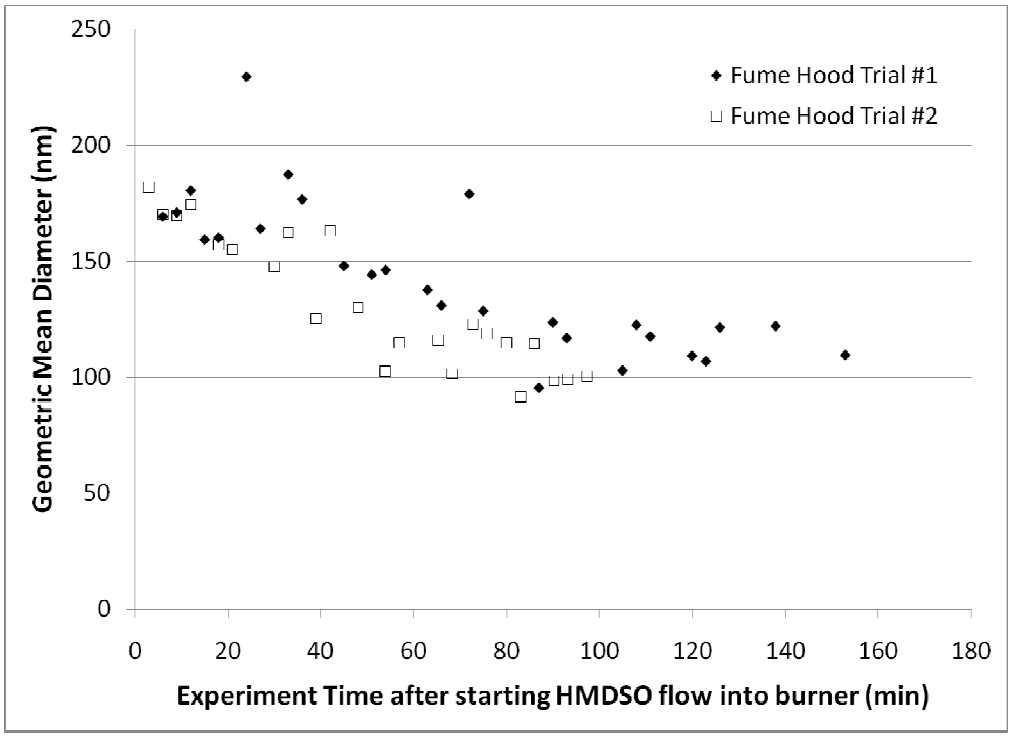

Figure H.5: Geometric mean particle size of SiO_2 throughout fume hood experiments.

Each trial within the wind tunnel was 1.7 - 2.5 hours in duration. After operating for 2.5 hours within the fume hood, the SiO_2 geometric mean particle size decreased from approximately 170 nm to 110 nm. This decrease would account for the apparent decrease in particle size experienced during the SiO_2 wind tunnel experiments. Figures H.16 - H.18 show the geometric mean particle size throughout the duration of each wind tunnel trial. A decrease in the geometric mean particle size occurred for each of these wind tunnel trials; however the change was not consistent. Therefore the data obtained during the fume hood trials cannot be used to correct the wind tunnel data.

Each trial within the wind tunnel began by starting the burner and waiting for the output to reach steady state. With soot this took approximately 45 minutes; 25 minutes for TiO_2. 25 minutes was also used as the time-to-steady-state for SiO_2, however the burner appears to approach steady state after approximately 90 minutes with SiO_2 (fume

hood studies). During wind tunnel sampling at the injection point, the geometric mean diameter did not change over the 25 minute sampling time for SiO_2, and the SiO_2 production was assumed to be at steady state. This assumption was wrong. Therefore the SiO_2 data is simply not consistent and significant conclusions cannot be drawn for SiO_2 in the current study.

Flame technology has been studied extensively as it is a well-established method for the continuous production of large quantities of nanoparticles (Strobel et al., 2006). Burner produced nanoparticles (such as SiO_2) are made on an industrial scale. Industrial production rates are on the order of 25 tons/hr, signifying the scalability of this technology (Strobel et al., 2006). However scaling up the production of an inconsistent particle distribution is not desirable. Any change in fuel or oxidant conditions will affect flame temperature, velocity, and particle concentration, resulting in a change in product particle size and morphology (Zhu and Pratsinis, 1997). Scheckman et al. (2009) produced consistent distributions of SiO_2 by pre-mixing the methane and N_2/HMDSO prior to feeding these gases into the burner. For future studies, reconfiguring the current study burner setup is recommended for the production of consistent SiO_2 size distributions.

NSAM/SMPS Ratio for SiO_2

The NSAM was operated simultaneously with the SMPS, measuring the Alveolar Lung Deposited Surface Area (LDSA) concentration (amount of particulate surface area deposited in the Alveolar region of the lung for an average worker) of the sampled aerosol. The NSAM results may be used to determine a ratio of LDSA per particle. This

ratio will show if the particles are growing by adding surface area to a particle (agglomeration or nucleation). For each trial, the NSAM measured LDSA was plotted against the corresponding SMPS measurement of total particle concentration. These plots typically revealed a linear relationship between the two measurements. The ratio was determined by fitting a regression curve to these plots. Figure H.6 shows this LDSA per particle value for each condition at each measurement location. A 95% confidence interval was also calculated for each regression fit and is plotted as error bars (along with instrumentation bias from the feasibility study) in Figure H.6. The NSAM/SMPS regression fit plots for each location and condition are located as Figures H.19 - H.22.

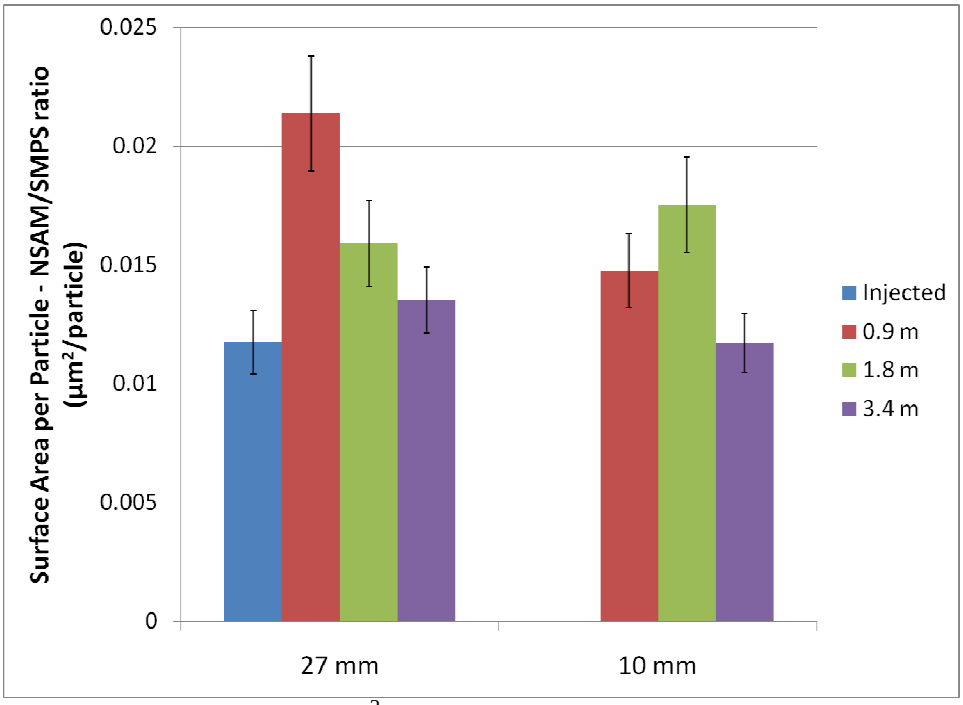

Figure H.6: NSAM/SMPS ratio (μm^2/particle) for SiO_2 at each measurement location. Error bars obtained through regression analysis with 95% confidence interval.

These NSAM/SMPS results seem to show the aerosol initially increasing in size, before decreasing as the particles travel away from the injection point. At 3.4 m

downstream the aerosol has the same NSAM/SMPS ratio as it has at the injection point for both leak sizes. However at most locations the change is not statistically significant. Overall, these NSAM/SMPS comparison results are inconclusive due to the inconsistent burner production, similar to the SMPS wind tunnel results for SiO_2.

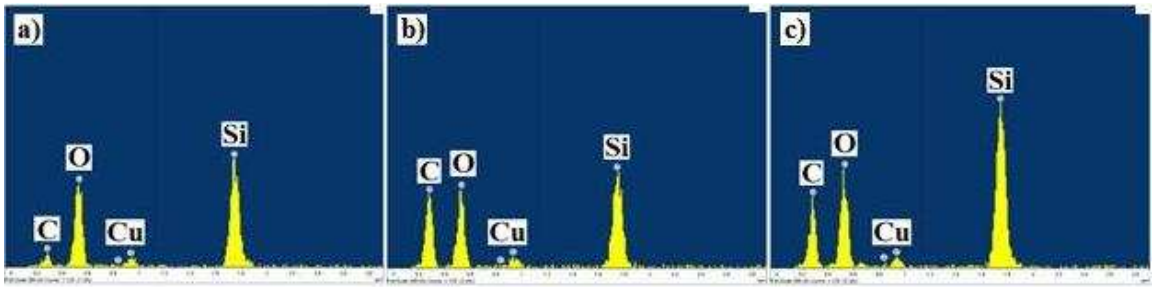

Figure H.7: SiO_2 particle composition by EDS analysis for a) larger, b) mid-sized, and c) smaller primary particles.

Table H.3: Raw data for SiO_2 particle size distributions, using 27 mm leak. Injected data was measured at centerline of wind tunnel. Downstream Location data was measured at point of highest concentration (0,23).

		Downstream Locations		
d_m (nm)	Injected	0.9 m	1.8 m	3.4 m
10.4	164162	688	1067	2003
11.1	82993	370	591	1128
12	35150	252	313	628
12.9	33943	160	179	398
13.8	26573	139	134	329
14.9	42936	162	221	289
16	58007	288	317	439
17.2	79926	527	498	685
18.4	115505	686	791	1258
19.8	297716	1265	1313	2033
21.3	263747	1717	2006	2806
22.9	521710	2677	3039	4600
24.6	624146	3883	4560	7301
26.4	767290	6112	6794	10381
28.4	617815	8991	9986	14636
30.5	760330	13140	13902	20109
32.8	991160	17208	19523	29373
35.2	1485630	22127	25986	36910
37.9	2132920	27208	34595	46734
40.7	2766080	36028	43601	58730
43.7	3893960	47173	58207	79813
47	4815760	58936	77658	97506
50.5	7037840	77229	95388	120226
54.2	9646900	91320	118644	154149
58.3	12881600	119773	155530	185138
62.6	17980400	146344	187887	217990
67.3	23842600	167097	211095	274367
72.3	28561600	181476	232754	325988

		Downstream Locations		
d_m (nm)	Injected	0.9 m	1.8 m	3.4 m
77.7	34846500	233470	269428	356306
83.5	39473800	263071	320854	396999
89.8	47235300	300772	354796	463164
96.5	60606000	327182	414078	506840
103.7	74985000	367096	470978	538869
111.4	89750000	394439	503708	594930
119.7	100409000	382392	494167	652715
128.6	112254000	426481	533912	745215
138.2	123121000	449890	588906	788382
148.6	127440000	455767	581993	829670
159.6	140935000	458235	576922	883360
171.5	142315000	445832	572226	880577
184.3	149021000	424810	566879	858675
198.1	155835000	405210	554649	854480
212.9	150784000	386593	551945	825713
228.8	143922000	364554	550250	817122
245.8	137235000	333791	509378	764729
264.2	127312000	308683	458172	715285
283.9	119186000	293767	431729	687187
305.1	115887000	280336	403735	692305
327.8	100684000	223987	332132	594532
352.3	85647000	195281	274235	492736
378.6	69626000	160463	225766	403293
406.8	56540500	121236	179368	330851
437.1	45122900	97452	142529	267295
469.8	34716300	76625	113165	209372
d_g (nm)	175	151	156	164
σ_g	1.67	1.73	1.73	1.75
N_{total} (cm^{-3})	8.5E+07	287825	383827	557705

Table H.4: Raw data for SiO_2 particle size distributions, using 10 mm leak. Injected data was measured at centerline of wind tunnel. Downstream Location data was measured at point of highest concentration (0,23).

		Downstream Locations		
d_m (nm)	Injected	0.9 m	1.8 m	3.4 m
10.4	164162	1077	892	1373
11.1	82993	636	616	861
12	35150	540	473	784
12.9	33943	626	499	798
13.8	26573	1061	746	1105
14.9	42936	1513	1096	1832
16	58007	2186	1796	3105
17.2	79926	3676	2827	4989
18.4	115505	5799	4638	7694
19.8	297716	8966	6505	11408
21.3	263747	11977	9336	15847
22.9	521710	17351	13063	21527
24.6	624146	22516	17402	29920
26.4	767290	29645	23155	39027
28.4	617815	38868	30099	52121
30.5	760330	46601	38158	66193
32.8	991160	57806	45919	81424
35.2	1485630	72162	56334	101813
37.9	2132920	86596	68231	124530
40.7	2766080	104387	77808	150645
43.7	3893960	130761	91958	182437
47	4815760	159931	109935	218614
50.5	7037840	183332	125180	263591
54.2	9646900	200451	145222	303342
58.3	12881600	247284	170079	356942
62.6	17980400	287690	194799	419822
67.3	23842600	325380	222087	484013
72.3	28561600	339055	253343	526615

		Downstream Locations		
d_m (nm)	Injected	0.9 m	1.8 m	3.4 m
77.7	34846500	374650	274193	571529
83.5	39473800	403923	290003	618051
89.8	47235300	439178	321140	663047
96.5	60606000	438580	331316	700090
103.7	74985000	470317	353433	739647
111.4	89750000	509148	376254	778059
119.7	100409000	517781	407309	814271
128.6	112254000	534819	425238	843122
138.2	123121000	562891	429233	867729
148.6	127440000	574962	472174	866938
159.6	140935000	593861	499987	861799
171.5	142315000	554917	491797	842823
184.3	149021000	503358	487218	800263
198.1	155835000	467523	476934	746540
212.9	150784000	443200	462139	705650
228.8	143922000	421328	449050	667815
245.8	137235000	385989	399200	607923
264.2	127312000	331710	356415	542074
283.9	119186000	298626	332905	485314
305.1	115887000	275709	314890	446859
327.8	100684000	238315	274259	369555
352.3	85647000	202437	229489	303278
378.6	69626000	157881	185105	241993
406.8	56540500	127834	149387	190537
437.1	45122900	103137	118204	146548
469.8	34716300	77791	92059	112567
d_g (nm)	175	131	142	132
σ_g	1.67	1.83	1.85	1.82
N_{total} (cm^{-3})	8.5E+07	387429	334735	593950

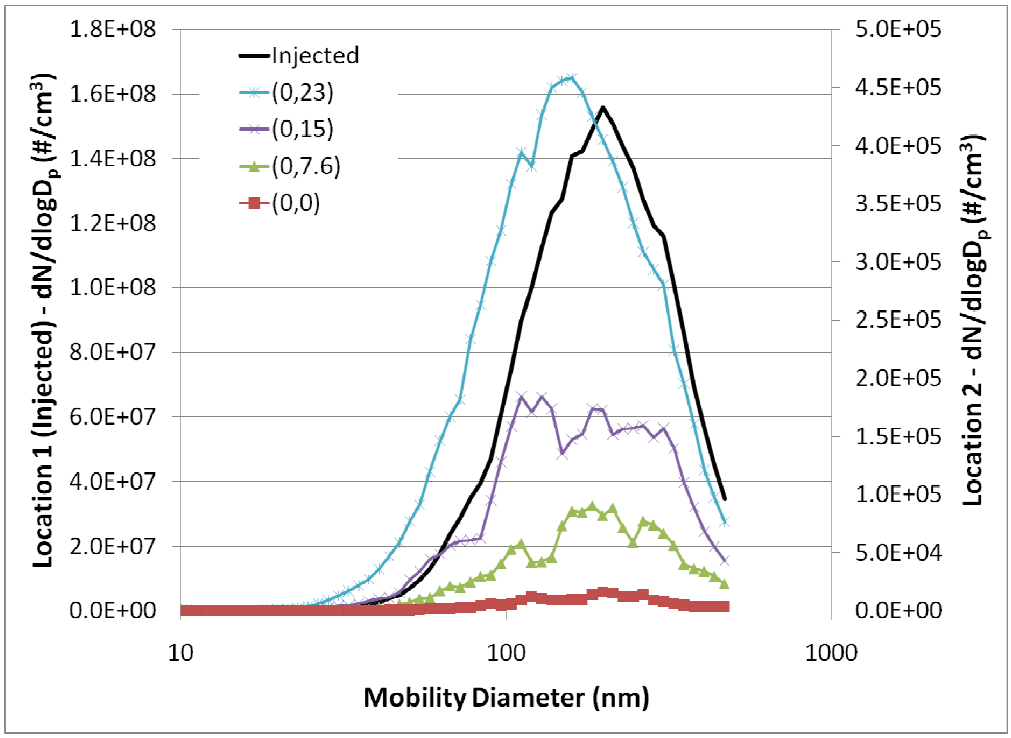

Figure H.8: 0.9 m downstream of leak (Location 2) with 27 mm leak, using SiO_2.

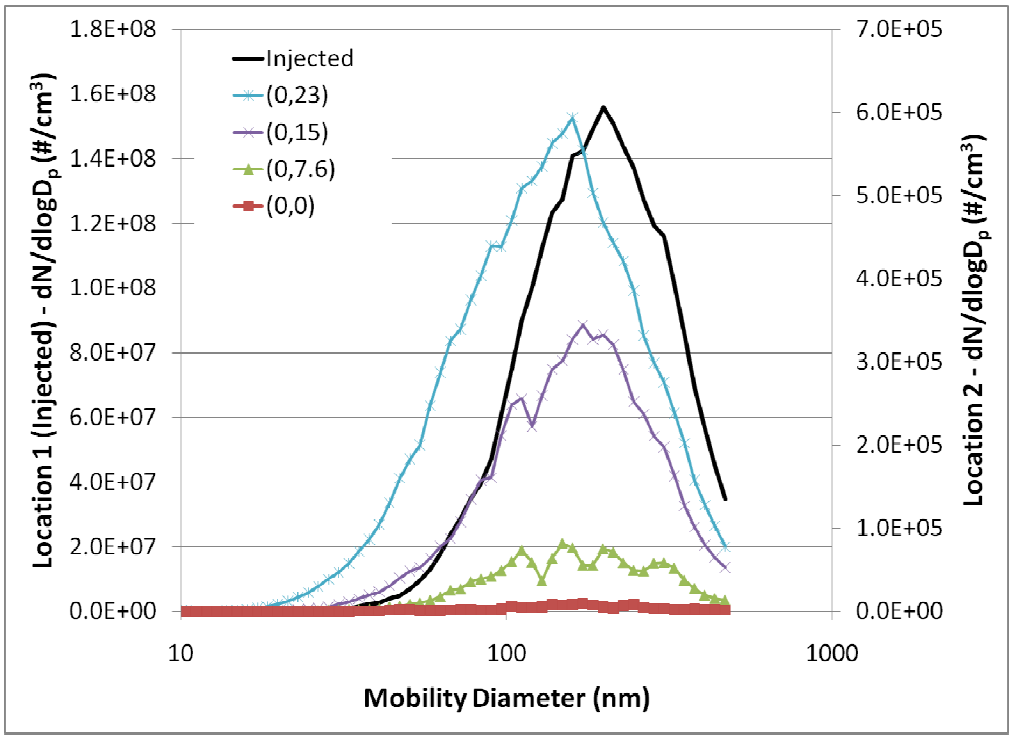

Figure H.9: 0.9 m downstream of leak (Location 2) with 10 mm leak, using SiO_2.

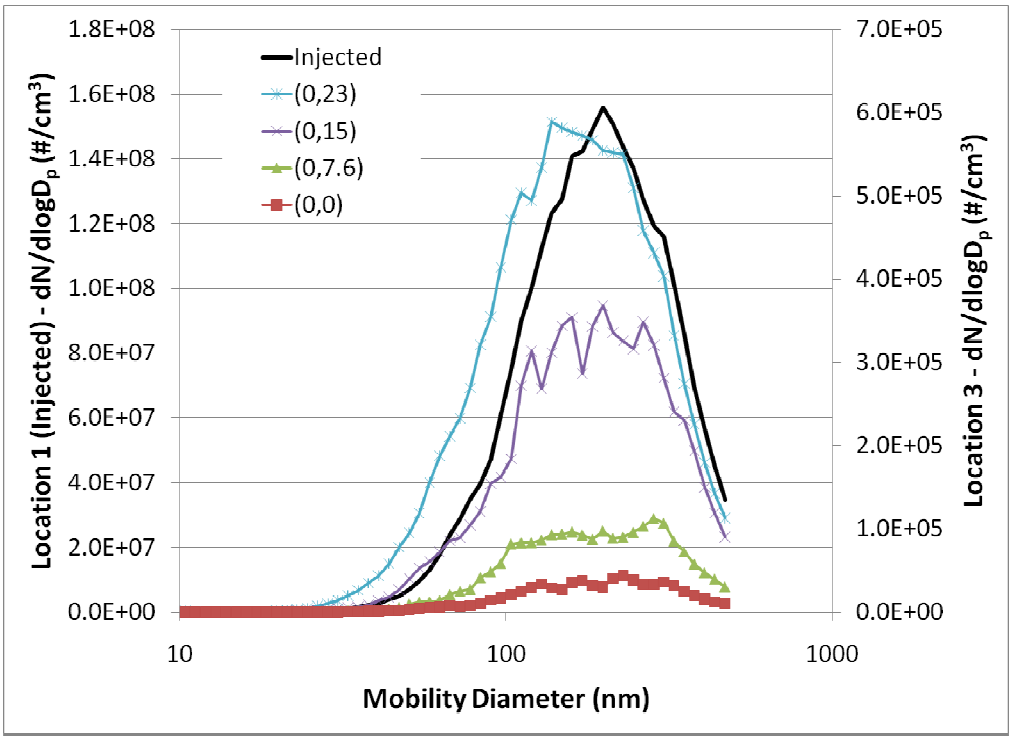

Figure H.10: 1.8 m downstream of leak (Location 3) with 27 mm leak, using SiO_2.

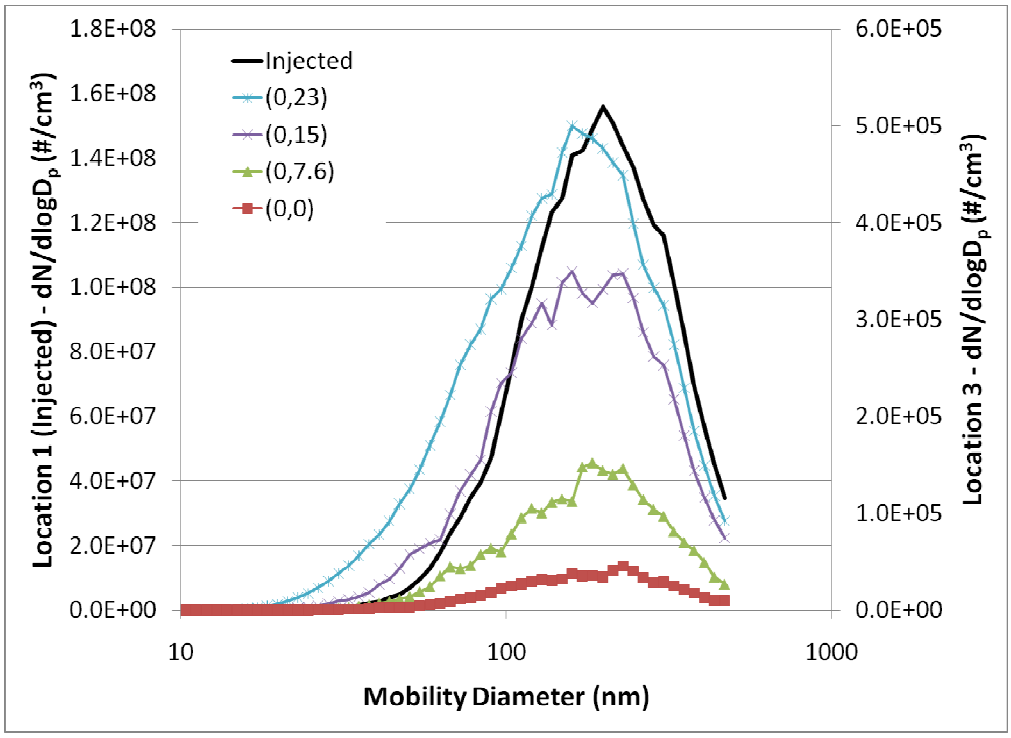

Figure H.11: 1.8 m downstream of leak (Location 3) with 10 mm leak, using SiO_2.

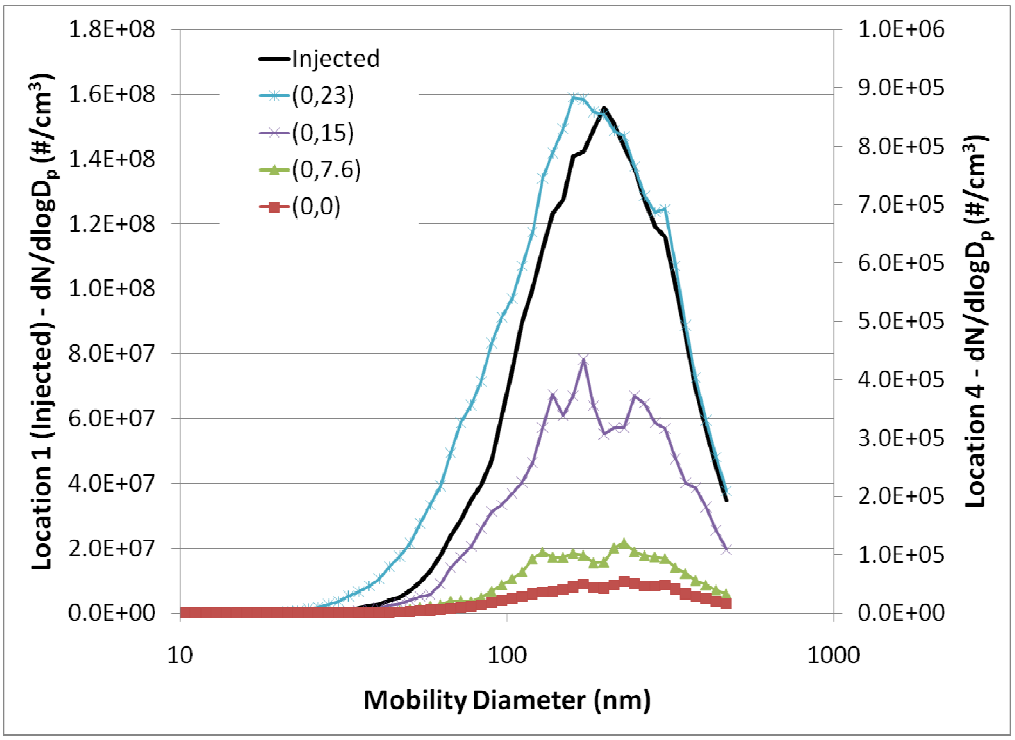

Figure H.12: 3.4 m downstream of leak (Location 4) with 27 mm leak, using SiO_2.

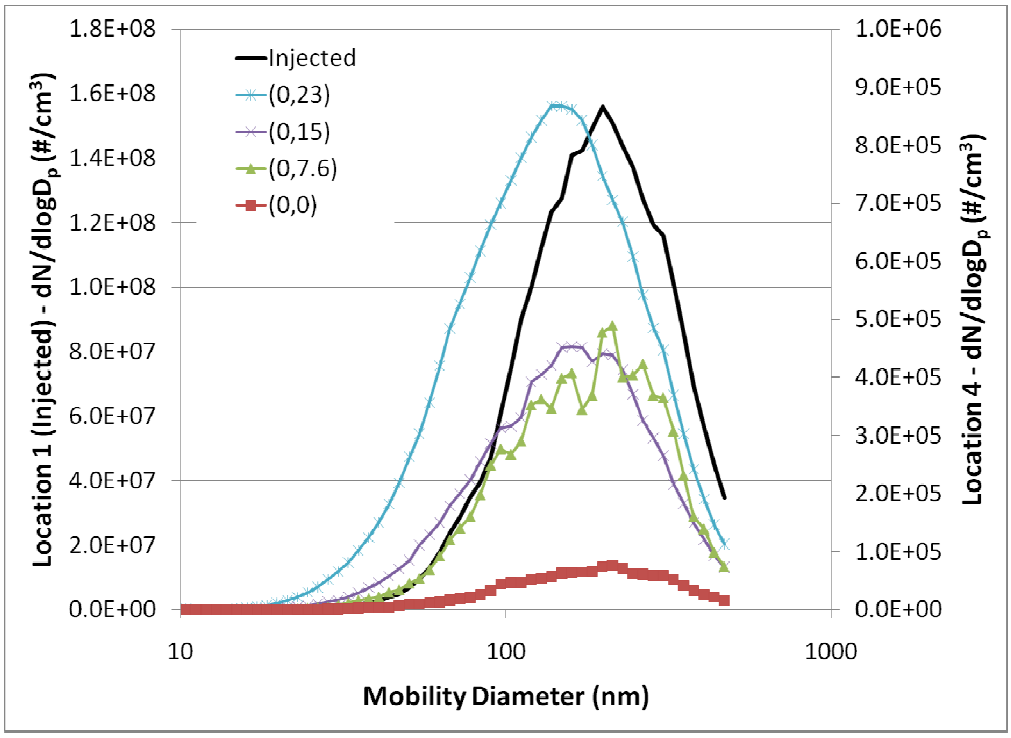

Figure H.13: 3.4 m downstream of leak (Location 4) with 10 mm leak, using SiO_2.

Figure H.14: SiO_2 cap formed at burner outlet after experimental trial.

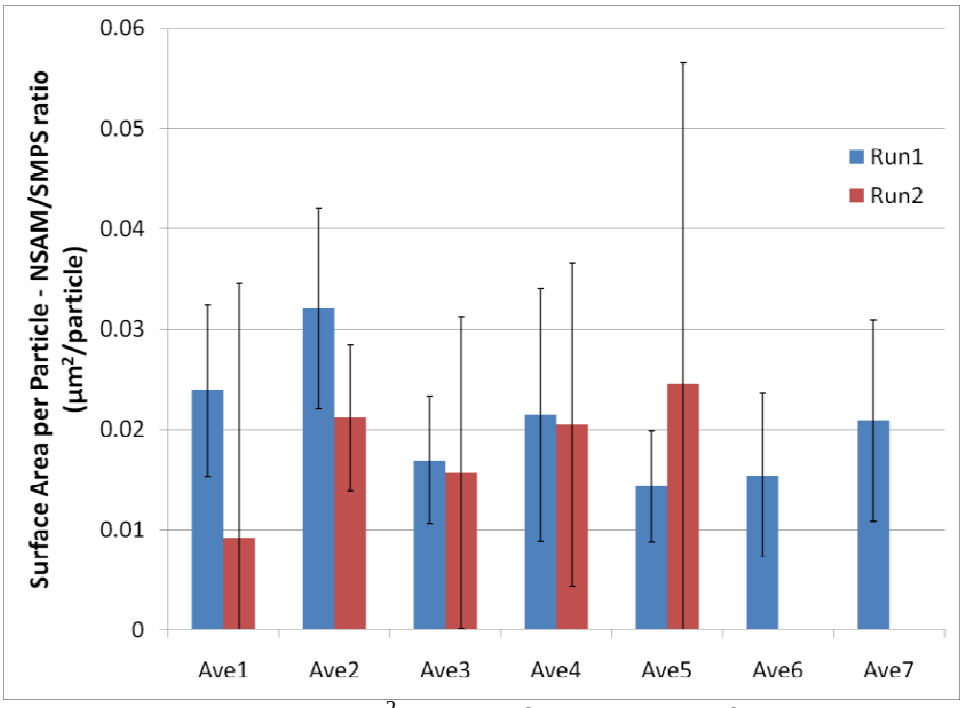

Figure H.15: NSAM/SMPS ratio (µm^2/particle) for SiO_2 during fume hood experiments (each averaged over 15 minutes). Error bars obtained through regression analysis with 95% confidence interval.

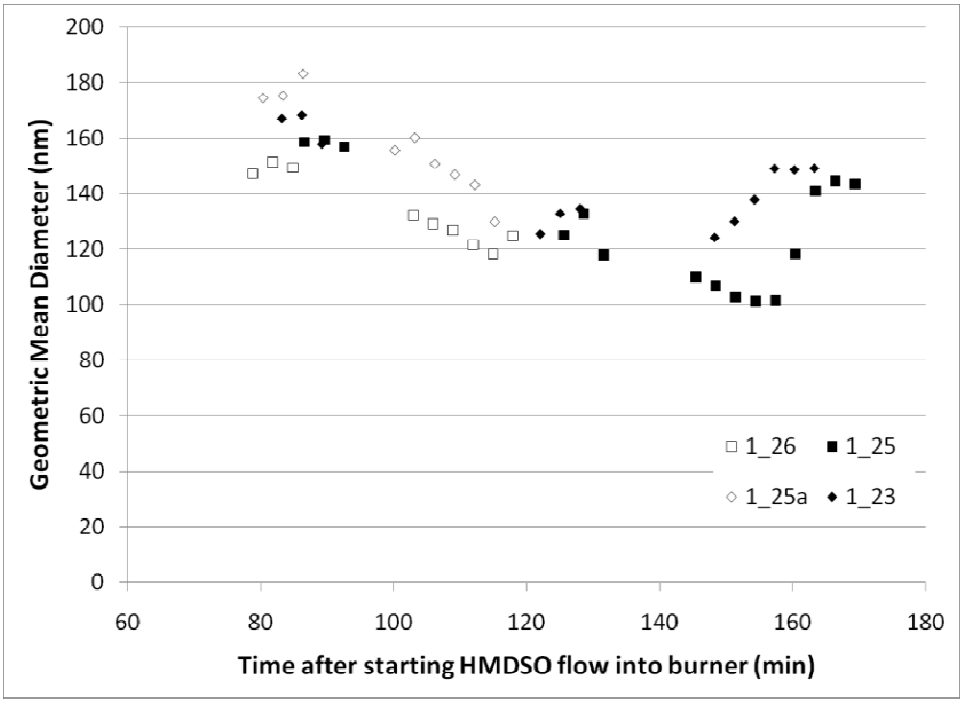

Figure H.16: Geometric mean particle size of SiO_2 throughout wind tunnel experiments at 0.9 m downstream. (Light icons are for 27 mm leak, dark icons are for 10 mm leak.)

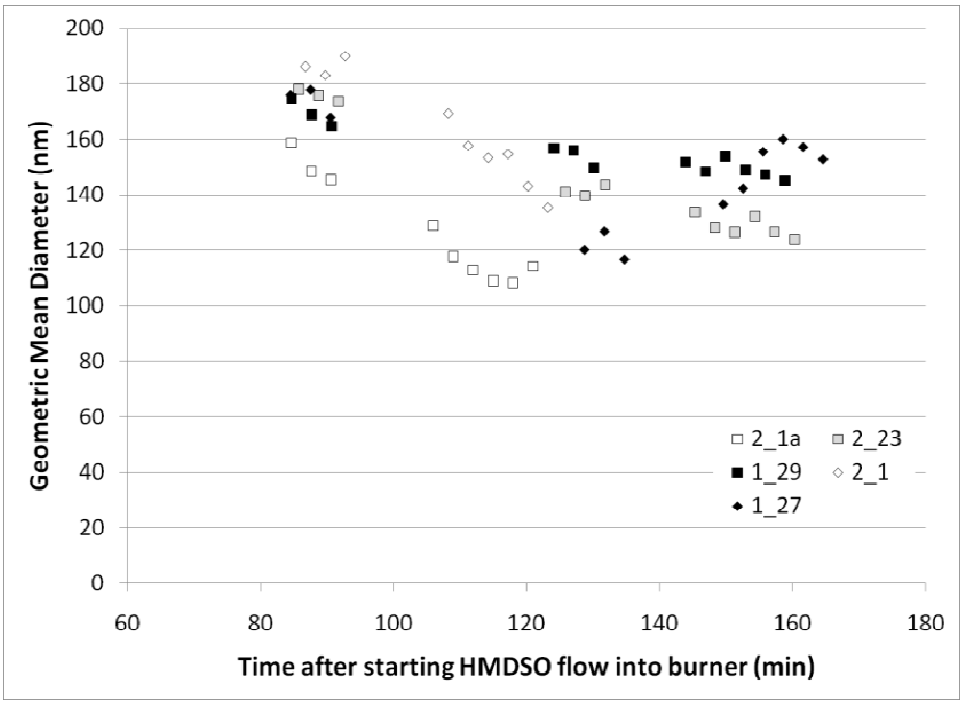

Figure H.17: Geometric mean particle size of SiO_2 throughout wind tunnel experiments at 1.8 m downstream. (Light icons are for 27 mm leak, dark icons are for 10 mm leak.)

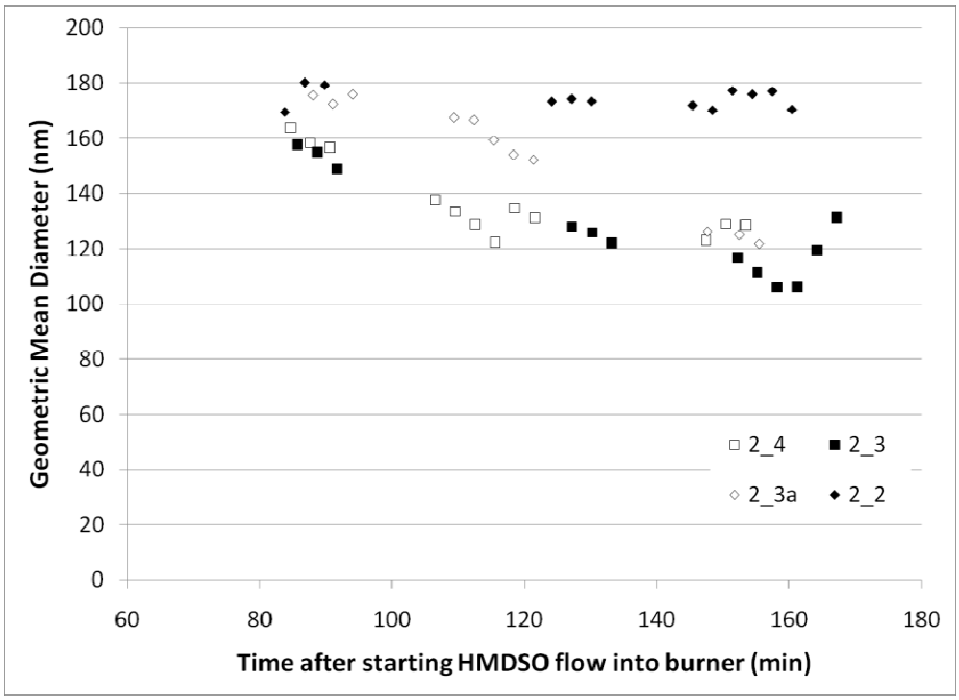

Figure H.18: Geometric mean particle size of SiO_2 throughout wind tunnel experiments at 3.4 m downstream. (Light icons are for 27 mm leak, dark icons are for 10 mm leak.)

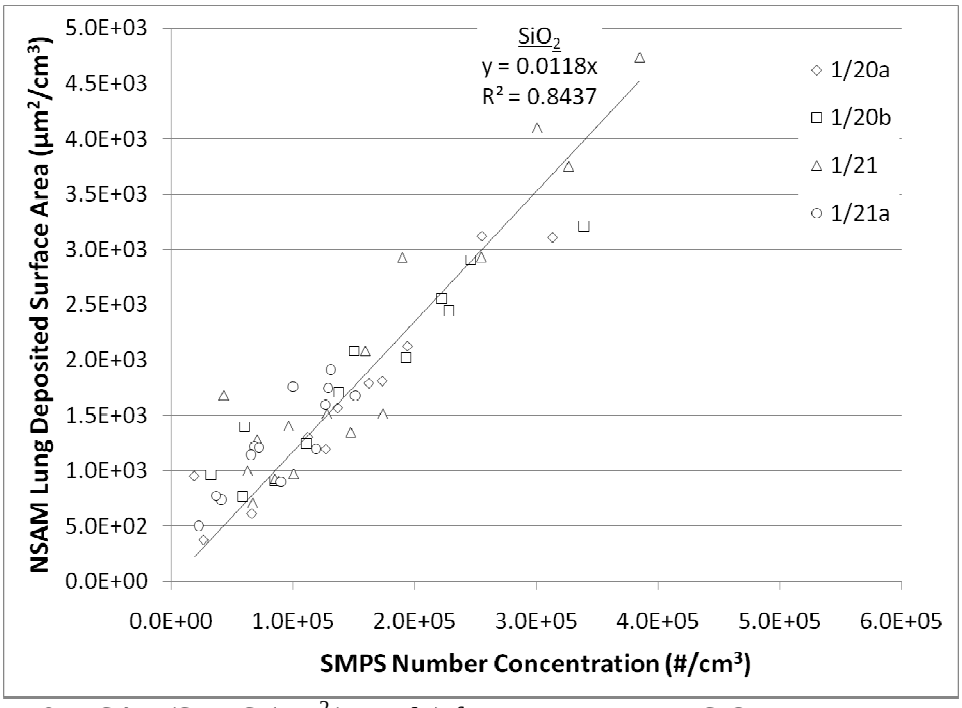

Figure H.19: NSAM/SMPS (μm^2/particle) for injection point, SiO_2.

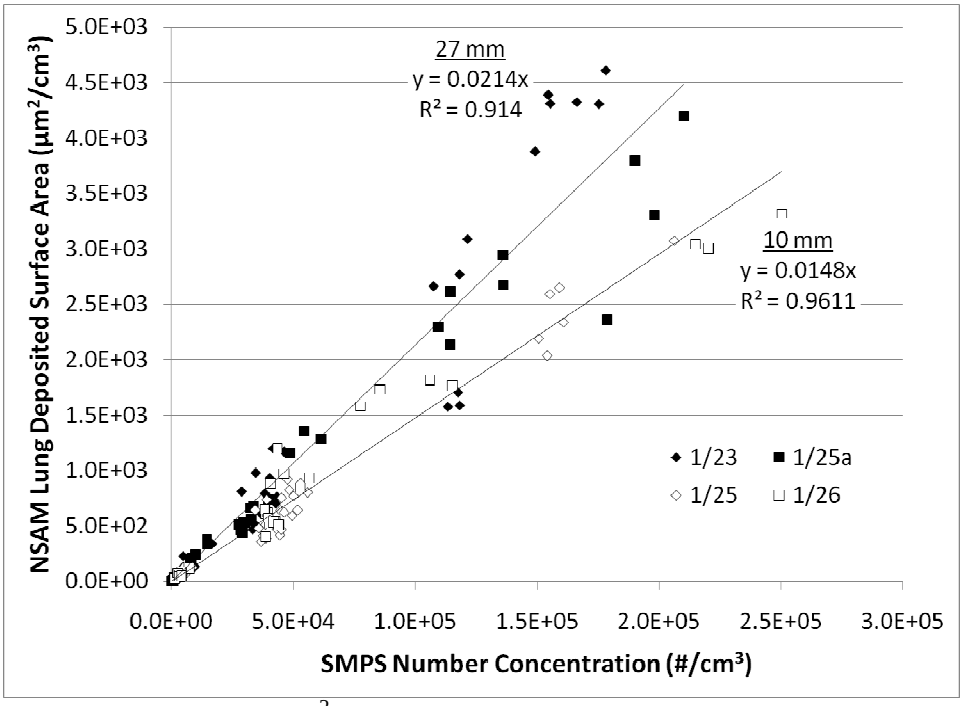

Figure H.20: NSAM/SMPS (μm^2/particle) at 0.9 m downstream, SiO_2.

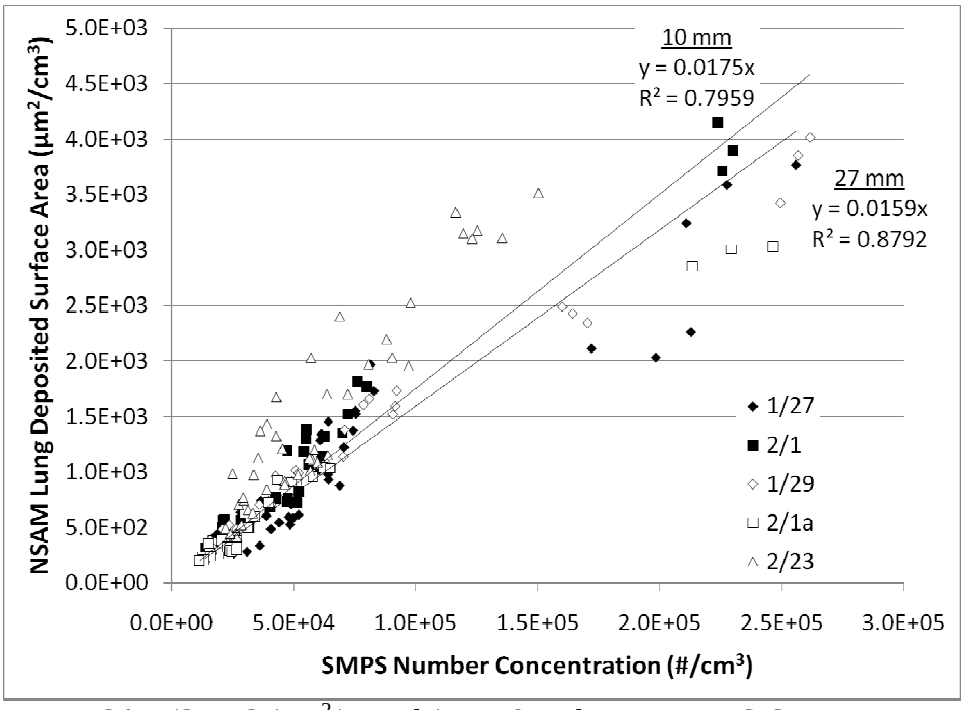

Figure H.21: NSAM/SMPS (µm^2/particle) at 1.8 m downstream, SiO_2.

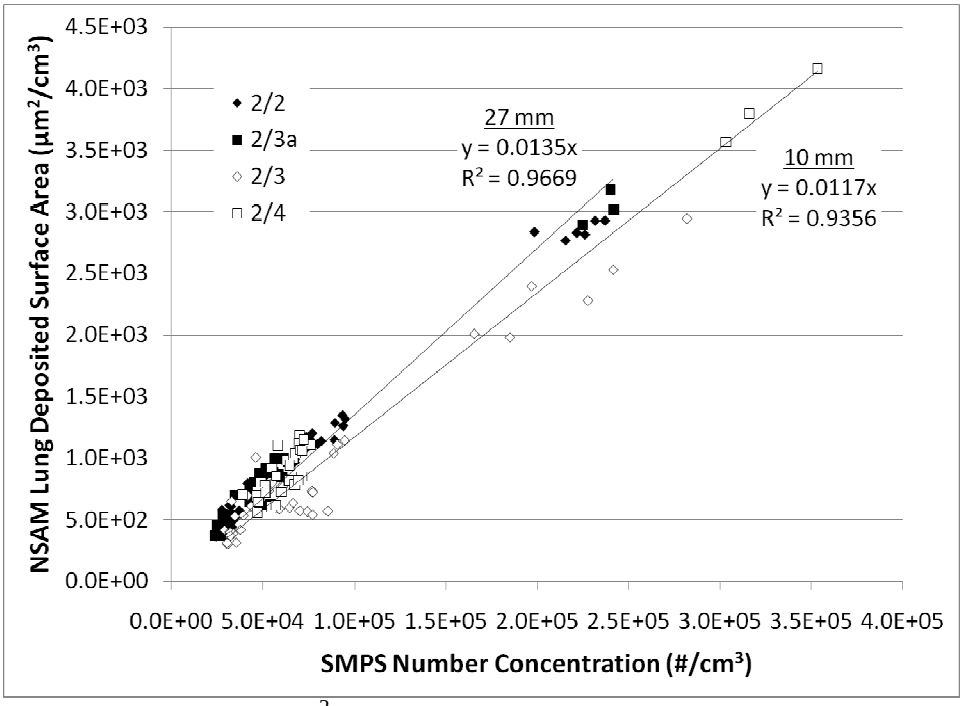

Figure H.22: NSAM/SMPS (µm^2/particle) at 3.4 m downstream, SiO_2.

Appendix I: Maricq (2007a) Coagulation Model with Sample Calculations

The Maricq (2007) coagulation model was built to determine the change in particle size as solid aerosol particles experience coagulation. Basic models assume liquid particles, which coagulate and coalesce to form a single spherical particle. The Maricq (2007) model assumes the particles are agglomerates made up of smaller solid primary particles. These agglomerates form a polydisperse, log-normally distributed aerosol and coagulate over time, which causes the distribution to decrease in concentration and increase in particle size. In the current study, a decrease in concentration is noticed along with an increase in particle size; however Equation 6.3.1 is the main reason for working through this model.

Equation 6.3.1: $$N_{pp} = K\left(\frac{2R_g}{d_{pp}}\right)^{D_f} \approx K\left(\frac{d_m}{d_{pp}}\right)^{D_f}$$

If the number of primary particle per agglomerate increases downstream of the injection site, then coagulation must be occurring. This model provides the fractal dimension, which is the only unknown in Equation 6.3.1 (besides N of course). Since the fractal dimension should not change as coagulation occurs, the number of primary particles per agglomerate can be calculated at the injection site and locations downstream using Equation 6.3.1 and coagulation can be tested analytically. This process is outlined in Section 6.3.

Equation I.1 is the final equation to be solved. An overall kernel must first be determined by summing the Epstein, transition, and free molecule regime kernels together. The model consists of several coagulation kernels, which were programmed

into a spreadsheet. The diameter is scaled with Equation I.2 so size binning can be logarithmic, in order to simplify the model. The equations for terms within various kernels are shown as Equations I.3 - I.6. These kernels are shown below as Equations I.7 - I.9. The Epstein kernel covers both the Epstein and continuum regimes. Sample calculations are shown at the end of this appendix section. Nomenclature is listed at the beginning of this thesis.

The spreadsheet was organized so changing any parameter would change the graphs. Therefore different values of time and D_f could be tested with automatic adjustment of the model curve. The data at the injection site was used as the original particle distribution for each condition; however the diameters of the particles used in the kernels, change with the fractal dimension (Equation I.2). In order to keep the diameters consistent (between model and data), the best fit curve was used instead of the raw data for the injection site data.

Equation I.1: $$\frac{dn_i}{dt} = \frac{1}{2}\sum_{j=0}^{i-1}\beta(j, i-j)n_j n_{i-j} - \sum_{j=0}^{\infty}\beta(i,j)n_i n_j$$

Equation I.2: $d_i = d_{pp}a^{i/D_f}$, where $a = \sqrt{2}$

Equation I.3: $$D_i = \frac{kTC_c(d_i)}{3\pi\eta d_i}$$

Equation I.4: $$\lambda_{p,i} = \frac{2C_c\left(d_{pp}i^{1/D_f}\right)}{3\pi\eta}\left(\frac{kT\rho_{pp}d_{pp}}{3}\right)^{1/2} i^{\left(1/2 - 1/D_f\right)}$$

Equation I.5: $$\gamma = \left(\bar{\lambda}_{p,i}^2 + \bar{\lambda}_{p,j}^2\right)^{1/2}$$

Equation I.6: $$\beta'(i,j)_{Epstein} = 2\pi\left(d_i + d_j + 2\gamma\right)\left(D_i + D_j\right)$$

Equation I.7:

$$\beta(i,j)_{Epstein} = \frac{2kT}{3\eta}\left(i^{1/D_f} + j^{1/D_f}\right)\left(\frac{C_c\left(d_{pp}i^{1/D_f}\right)}{i^{1/D_f}} + \frac{C_c\left(d_{pp}j^{1/D_f}\right)}{j^{1/D_f}}\right)$$

Equation I.8: $\beta(i,j)_{free\ molec} = 2.2\left(\frac{3kTd_{pp}}{\rho_{pp}}\right)^{1/2}\left(i^{1/D_f} + j^{1/D_f}\right)^2\left(\frac{1}{i} + \frac{1}{j}\right)^{1/2}$

Equation I.9: $\beta(i,j)^{-1}_{trans} \cong \beta'(i,j)^{-1}_{Epstein} + \beta(i,j)^{-1}_{free\ molec}$

Maricq (2007) was able to plot this model against his experimental data with very good fit. In the current study, the model does not fit as well. As stated in Section 6.3, the model is not sensitive enough to provide much difference between different fractal dimensions. The high dilution of the wind tunnel and lack of empirical data also hinder the accuracy of this model. If the aerosols had changed continuously throughout the distance of the wind tunnel, then the model may have worked better. The model is fit to the empirical data for the Lean and Rich soot data, as well as the TiO_2 data when using the 27 mm leak size in Figures I.1 - I.3. The data at 3.4 m downstream of the leak is plotted versus the best fit curves.

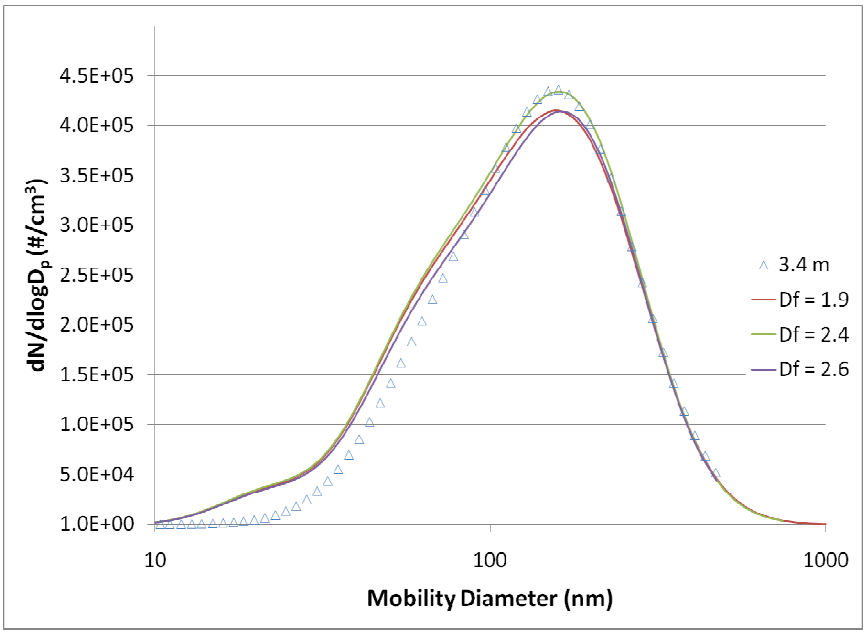

Figure I.1: Lean soot data at 3.4 m downstream plotted with Maricq (2007a) model fit curves.

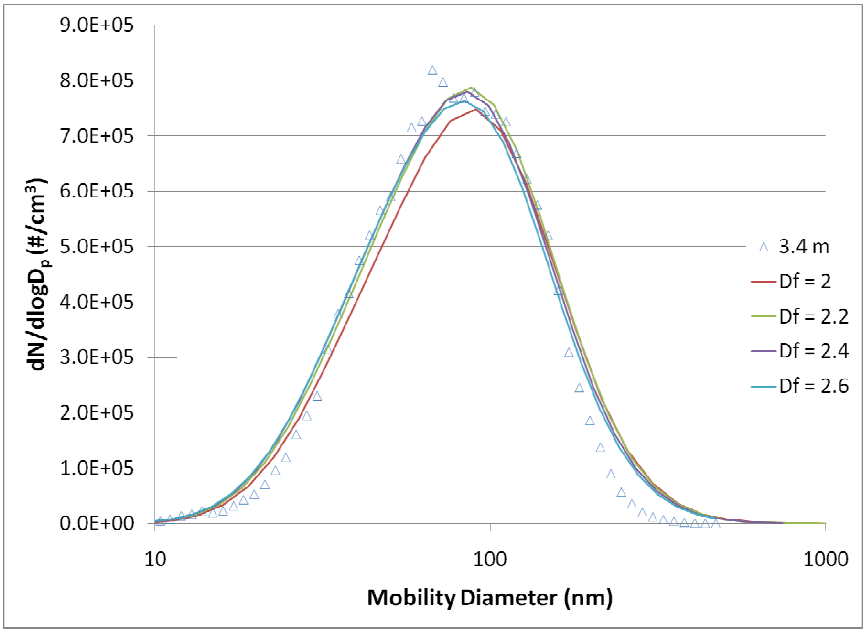

Figure I.2: Rich soot data at 3.4 m downstream plotted with Maricq (2007a) model fit curves.

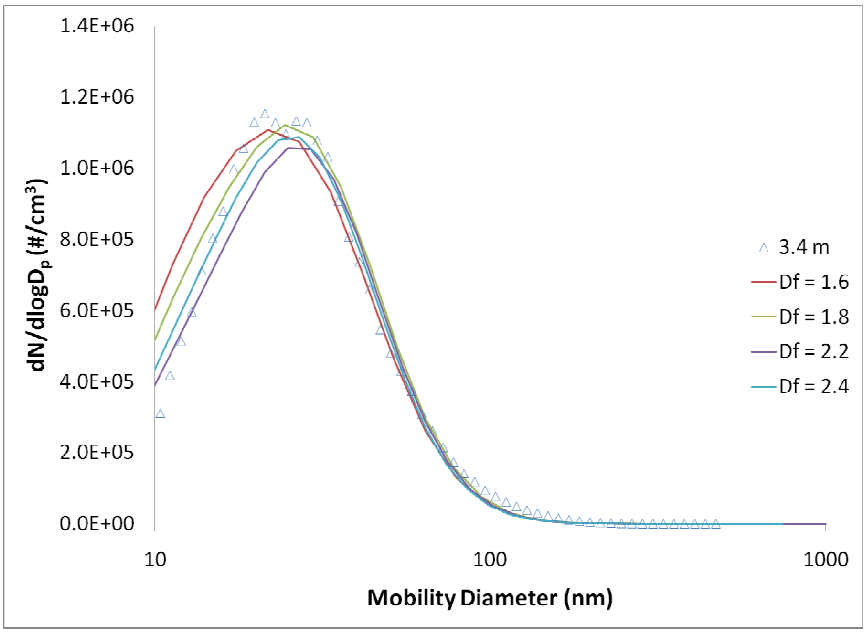

Figure I.3: TiO_2 data at 3.4 m downstream plotted with Maricq (2007a) model fit curves.

A large change in fractal dimension results in a small shift in the shape and size of the particle distribution. A scaling factor (N_T) was used to scale the size of the chart, which introduces more human factors into the model. The time, fractal dimension, primary particle size, and N_T can all be adjusted to get the best fitting model. However there are many combinations of these terms which can be used to get the same result. In order for this model to be applied successfully, the fractal dimension and primary particle size must be consistent for all times distributions are measured as these should not change throughout time. Time change should be known from experiments, or at least an estimate should be available. Particle losses by deposition onto walls of the experimental setup may be unknown, and therefore the N_T adjustment is necessary. In a well controlled study, which is specifically conducted to observe coagulation, this model fits very well (Maricq, 2007a). In the current study, there is simply too much dilution, too little change, and therefore, not enough empirical data to successfully apply this coagulation model.

Sample Calculations

Sample calculations will be conducted using the Lean soot data from the fit curve. All constant terms are defined below.

Nomenclature defined for sample calculations

d_{pp} = 2 nm	D_f = 2.4	ρ_{pp} = 1.7 g/cm^3
i = 5	$C_c(d_i)$ = 58.2	$C_c(d_{pp}i^{1/Df})$ = 57.0
j = 4	$C_c(d_j)$ = 62.5	$C_c(d_{pp}j^{1/Df})$ = 62.5
T = 298 K	t = 6.7 sec	η = 1.81e-5 Pa-sec
λ = 65 nm	k = 1.38e-23 J/K	

Equation I.2: $d_i = d_{pp}a^{i/D_f}$ → (2 nm)(1.41^(3/2.4)) → d_i = 4.1 nm, d_j = 3.6 nm

Equation I.3: $D_i = \frac{kTC_c(d_i)}{3\pi\eta d_i} \rightarrow \frac{(1.38e{-}38 J/K)(298\ K)(72.12)}{3\pi(1.81e{-}5\ Pa{-}\sec)(4.1e{-}9\ m)}$ → D_i = 3.2e-7 m^2/s, D_j = 4.2e-7 m^2/s

Equation I.4: $\lambda_{p,i} = \frac{2C_c\left(d_{pp}i^{1/D_f}\right)}{3\pi\eta}\left(\frac{kT\rho_{pp}d_{pp}}{3}\right)^{1/2} i^{\left(1/2 - 1/D_f\right)}$

→ $\frac{2(57.0)}{3\pi(1.81e{-}5\ Pa{-}\sec)}\left(\frac{(1.38e{-}23 J/K)(298\ K)(1700\ kg/m^3)(2e{-}9m)}{3}\right)^{1/2} 5^{(1/2 - 1/2.4)}$

→ (6.7e+5)(6.8e-14)(1.14) → $\lambda_{p,i}$ = 5.2e-8 m, $\lambda_{p,j}$ = 9.7e-8 m

→ $\lambda_{p,i}$ bar = $\lambda_{p,j}$ bar = 8.3e-8 m (for use in Equation H.5)

Equation I.5: $\gamma = \left(\bar{\lambda}_{p,i}^2 + \bar{\lambda}_{p,j}^2\right)^{1/2}$ → ((8.3e-8 m)^2 + (8.3e-8 m)^2)$^{1/2}$ → γ = 1.2e-7 m

Equation I.6: $\beta'(i,j)_{Epstein} = 2\pi\left(d_i + d_j + 2\gamma\right)\left(D_i + D_j\right)$

→ 2π(4.1e-9 m + 3.6e-9 m +2*1.2e-7 m)(3.2e-7 m^2/s + 4.2e-7 m^2/s)

→ $\beta'(i,j)_{Epstein}$ = 1.3e-12 m^3/s

Equation I.7:

$$\beta(i,j)_{Epstein} = \frac{2kT}{3\eta}\left(i^{1/D_f} + j^{1/D_f}\right)\left(\frac{C_c\left(d_{pp}i^{1/D_f}\right)}{i^{1/D_f}} + \frac{C_c\left(d_{pp}j^{1/D_f}\right)}{j^{1/D_f}}\right)$$

→ $\left(\frac{2(1.38e{-}23 J/K)(298\ K)}{3(1.81e{-}5\ Pa{-}\sec)}\right)\left(5^{1/2.4} + 4^{1/2.4}\right)\left(\frac{57.0}{5^{1/2.4}} + \frac{62.5}{4^{1/2.4}}\right)$

→ $\beta(i,j)_{Epstein}$ = 3.9e-14 m^3/s

Equation I.8: $\beta(i,j)_{free\ molec} = 2.2\left(\frac{3kTd_{pp}}{\rho_{pp}}\right)^{1/2}\left(i^{1/D_f} + j^{1/D_f}\right)^2\left(\frac{1}{i}+\frac{1}{j}\right)^{1/2}$

$\rightarrow 2.2\left(\frac{(1.38e{-}23J/K)(298\ K)(2e{-}9m)}{1700kg/m^3}\right)^{1/2}\left(5^{1/2.4} + 4^{1/2.4}\right)^2\left(\frac{1}{5}+\frac{1}{4}\right)^{1/2}$

→ $\beta(i,j)_{free\ molec}$ = 2.4e-15 m^3/s

Equation I.9: $\beta(i,j)^{-1}_{trans} \cong \beta'(i,j)^{-1}_{Epstein} + \beta(i,j)^{-1}_{free\ molec}$

→ $\beta(i,j)_{trans} \cong \left[\beta'(i,j)^{-1}_{Epstein} + \beta(i,j)^{-1}_{free\ molec}\right]^{-1}$

→ $[(1.3e{-}12)^{-1} + (2.4e{-}15)^{-1}]^{-1}$ → $\beta(i,j)_{trans}$ = 2.4e-15 m^3/s

Equation I.1: $\frac{dn_i}{dt} = \frac{1}{2}\sum_{j=0}^{i-1}\beta(j,i-j)n_j n_{i-j} - \sum_{j=0}^{\infty}\beta(i,j)n_i n_j$

→ $\beta(i,j) = \beta(i,j)_{Epstein} + \beta(i,j)_{trans} + \beta(i,j)_{free\ molec}$ → $\beta(i,j)$ = 4.4e-8 cm^3/s

→ $\beta(j,i-j)$ = 6.6e-8 cm^3/s

→ $\frac{1}{2}\sum_{j=0}^{i-1}\beta(j,i-j)n_j n_{i-j}$ = 1.69e-7 (summed over i = 5)

→ $\sum_{j=0}^{\infty}\beta(i,j)n_i n_j$ = 3.39e-7 (summed over i = 5)

→ dn_i = [(1.69e-7) - (3.39e-7)](dt), where dt = 2.4 s and N_T = 0.72

→ n(t) = $(dn_i + n_o)(N_T)$ → n(t) = -1.01e-2 (cm^{-3}) for i = 5

In this example, the resulting concentration is below 0. This was occasionally noticed for the lowest values of i and j, since these small particles coagulate quickly and have low initial concentrations in the Lean soot distribution. N_T is a fit parameter, outlined by Maricq (2007).

Appendix J: Conservation of Mass Analysis with Sample Calculations

The Conservation of Mass analysis was used to test the theory of combustion gas nucleation onto the agglomerates, causing particle growth. The equations used in the analysis are outlined within this section; however the analysis does not work for this experimental setup. There is too much dilution within the wind tunnel, and the sub-primary particles are too small to be accurately counted in order to accurately determine the concentration of sub-primary particles. Penetration, dilution of sampled flow, and collection efficiency must be accounted for to determine the sub-primary particle concentration (Equation J.1). The agglomerate penetration is greater than 0.99 (for the geometric mean particle size of the Lean soot distribution), so it can be neglected. Penetration is defined in Section 3.5. In this case, P is the overall penetration of sub-primary particles through the sampling lines. All other terms have been defined in Section 6.5 and in the Nomenclature List of this thesis.

Equation 6.5.1: $$C_{sp}\left(\frac{\#}{cm^3}\right) = \frac{(C_{sa})(A_s)}{(Q_s)(T_s)}$$

Equation J.1: $$C_{sp,corr} = C_{sp}/[PD_r(\%\,\eta/100)]$$

Equation 6.5.2: $$V_i\left(\frac{\mu m^3}{cm^3}\right) = \frac{\pi}{6} C_i d_i^3$$

Equation 6.5.3: $$V_i\left(\frac{\mu m^3}{cm^3}\right) = \frac{\pi}{6} K C_i \left(\frac{d_i}{d_{pp}}\right)^{D_f} d_{pp}^3$$

Equation 6.5.4: $$V_T\left(\frac{\mu m^3}{cm^3}\right) = \sum_{i=1}^{n} V_i$$

The volume of agglomerates was determined using the volume of the primary particles and Equation 6.3.1, which gives the number of primary particles per agglomerate for each mobility diameter. The concentration of agglomerates for each mobility diameter was measured by the SMPS. Combining Equation 6.3.1 and the equation of particle volume concentration (Equation 6.5.2) allows for the calculation of volume for a single agglomerate, shown as Equation 6.5.3. Summing for all mobility diameters within SMPS size range gives the total volume concentration for the agglomerates (Equation 6.5.4). This total volume concentration was calculated at the injection site and 3.4 m downstream for the Lean soot distribution. The dilution of the wind tunnel was taken into account for the 3.4 m downstream value in Table 6.5.1.

Sample Calculations

Nomenclature defined for sample calculations

A_s = 55.4 cm^2	C_{sa} = 2.7e11 #/cm^2	%η = 100 %
Q_s = 1 lpm	P = 0.81	D_r = 0.01
t_s = 10 min	d_{sp} = 6.89 nm	d_{pp} = 30.2 nm
C_m = 6.9e5 (cm^{-3})	d_m = 50.5 nm	

Equation 6.5.1: $C_{sp}\left(\frac{\#}{cm^3}\right) = \frac{(C_{sa})(A_s)}{(Q_s)(T_s)} \rightarrow \frac{(2.77e11\ \#/cm^2)(55.4\ cm^2)}{(1000\ cm^3/min)(10\ min)}$
→ C_{sp} = 1.5e9 (#/cm^3)

Equation J.1: $C_{sp,corr} = C_{sp}/[PD_r(\%\eta/100)]$
→ (1.5e9 (#/cm^3))/(0.81*0.01*(100/100))
→ $C_{sp,corr}$ = 1.8e11 (#/cm^3)

Equation 6.5.2: $V_i\left(\frac{\mu m^3}{cm^3}\right) = \frac{\pi}{6} C_i d_i^3 \rightarrow \frac{\pi}{6}(1.8e11\ cm^{-3})\left(\frac{6.89\ nm}{1000}\right)^3$
→ V_{sp} = 3.1e4 (μm^3/cm^3)

Equation 6.5.3: $V_i\left(\frac{\mu m^3}{cm^3}\right) = \frac{\pi}{6} K C_m \left(\frac{d_m}{d_{pp}}\right)^{D_f} d_{pp}^3$

$\rightarrow \frac{\pi}{6}(1.0)(6.9e5\ cm^{-3})\left(\frac{50.5\ nm}{6.89\ nm}\right)^{2.4}\left(\frac{6.89\ nm}{1000}\right)^{3}$

$\rightarrow$ $V_{agg,m} = 34.2\ (\mu m^3/cm^3)$

Equation 6.5.4: $V_T\left(\frac{\mu m^3}{cm^3}\right) = \sum_{i=1}^{n} V_i \rightarrow V_T = 2.8e4\ (\mu m^3/cm^3)$

This value represents the total volume concentration of agglomerates at the injection site.

Appendix K: Sample Calculations and Statistical Analysis

Section 3 sample calculations

For Equations 3.5.1 - 3.5.4 sample calculations, a particle size and concentration will be set, and assumed to be suspended in air at NTP (T = 293 K and P = 101.3 kPa). The relevant values are listed below.

$k = 1.38 \times 10^{-23}$ kg-m^2/K-s^2	$\lambda = 0.066$ μm = 66 nm
$d_p = 100$ nm = 1e-7 m	T = 298 K
$\mu = 1.8134 \times 10^{-5}$ Pa-s	L = 3.1 m
Q = 5e-6 (m^3/s)	$n_{in} = 5e5$ cm^{-3}

Equation 3.5.1: $D = \frac{kTC_c}{3\pi\mu d_p} \rightarrow \frac{(1.38e{-}23\ J/K)(298\ K)(2.93)}{3\pi(1.81e{-}5\ Pa{-}sec)(1e{-}7m)}$

→ D = 7.04e-10 m^2/s

Equation 3.5.2: $C_c = 1 + \frac{\lambda}{d_p}\left[2.34 + 1.05exp^{-0.39\frac{d_p}{\lambda}}\right]$

$\rightarrow 1 + \frac{66\ nm}{100\ nm}\left[2.34 + 1.05exp^{-0.39\frac{100\ nm}{66\ nm}}\right]$

→ $C_c = 2.93$

Equation 3.5.3: $\mu = \frac{DL}{Q} \rightarrow \frac{(7.04e{-}10\ m^2/s)(3.1\ m)}{5e{-}6\ m^3/s} \rightarrow \mu = 4.37e\text{-}4$

Equation 3.5.4a: $P = \frac{n_{out}}{n_{in}} = 1 - 5.50\mu^{2/3} + 3.77\mu$ for $\mu < 0.009$

Equation 3.5.4b: $P = 0.819exp^{-11.5\mu} + 0.0975exp^{-70.1\mu}$ for $\mu \geq 0.009$

$\mu < 0.009$, so Equation 3.5.4a will be used because in this example.

$\rightarrow P = \frac{n_{out}}{n_{in}} = 1 - 5.50\mu^{2/3} + 3.77\mu$

$\rightarrow 1 - 5.50(4.37e-4)^{2/3} + 3.77(4.37e-4)$

→ P = 0.967

→ n_{out} = (0.967)(5e5 cm^{-3})

→ n_{out} = 4.83e5 cm^{-3}

Equation 3.5.5 was used to theoretically determine the correct orifice diameter in order to maintain a constant volumetric flow rate of 0.18 lpm. The orifice size was

limited to the size of the available drill bits. The orifice size was drilled to be approximately 0.52 mm. The orifice was calibrated over a range of flow rates and matched this theory very well.

C = 0.72	A_2 = 2.12e-7 m^2	P_1 = 101325 N/m^2
P_2 = 101109 N/m^2	T_1 = 300 K	M = 28.97 kg/kmole
Z = 1.0	R = 8314 N-m/kmole-K	k = 1.4

Equation 3.5.5: $$mfr = CA_2P_1\sqrt{\left(\frac{2M}{ZRT_1}\right)\left(\frac{k}{k-1}\right)\left[\left(P_2/P_1\right)^{2/k} - \left(P_2/P_1\right)^{(k+1)/k}\right]}$$

$$\rightarrow\left(\frac{2M}{ZRT_1}\right) = \left(\frac{2(28.97\frac{kg}{kmole})}{(1.0)\left(8314\frac{N-m}{kmole-K}\right)(300\ K)}\right) = 2.32e\text{-}5\ kg/(N\text{-}m)$$

$$\rightarrow CA_2P_1 = (0.72)(2.12e\text{-}7\ m^2)(101325\ Pa) = 0.15\ N$$

$$\rightarrow(0.15\ N)\sqrt{\left(2.32e-5\frac{kg}{N-m}\right)\left(\frac{1.4}{0.4}\right)\left[\left(\frac{101109\ Pa}{101325\ Pa}\right)^{2/1.4} - \left(\frac{101109\ Pa}{101325\ Pa}\right)^{(2.4)/1.4}\right]}$$

→<u>mfr = 3.36e-6 kg/s</u>

Through calibration, this mass flow rate can be maintained if the pressure drop across the orifice is set to approximately 0.88 in. H_2O (217 Pa). The dilution set is capable of maintaining and measuring this small pressure drop in real-time, as the sampling instruments are operating.

Section 6 Sample Calculations

Equations 6.3.1 and 6.4.1 each outline different methods of determining the number of primary particles per agglomerate (N_{pp}). The Lean soot distribution data will be used for this example. The terms for each equation are defined below.

d_{pp} = 30 nm	D_f = 2.4	K = 1.0
d_m = 113 nm	c* = 9.17	λ = 0.066 μm = 66 nm

Equation 6.3.1: $N_{pp} = K\left(\frac{2R_g}{d_{pp}}\right)^{D_f} \approx K\left(\frac{d_m}{d_{pp}}\right)^{D_f} \rightarrow (1.0)\left(\frac{113\ nm}{30\ nm}\right)^{2.4}$
→ $N_{pp} = 24.1$

Equation 6.4.1: $N_{pp} = \frac{3\pi\lambda d_m}{c^*\left(\frac{d_{pp}}{2}\right)^2} \rightarrow \frac{3\pi(6.6e{-}8m)(1.13e{-}7\ m)}{(9.17)\left(\frac{3.0e{-}8\ m}{2}\right)^2} \rightarrow N_{pp} = 34.1$

95% Confidence Interval (95% CI) Sample Calculation using Student's t-distribution

A different statistical analysis was used for different data sets. When determining if the primary particle sizes are different, one cannot simply compare the average values for each measurement location. Each average value has a 95% confidence interval (95% CI). These 95% CI's were calculated for each average primary particle size. The Lean soot fuel/air mix will be used as the example. Summations, averages, and standard deviations were calculated using Microsoft Excel. Other terms needed for this example are listed below.

N = 46 samples $t_{\alpha/2,N-1} = 2.01$ $\alpha = 0.05$

Equation K.1: $\bar{x} = \frac{\sum_{i=1}^{N} x_i}{N} \rightarrow \bar{x} = 30.2\ nm$

Equation K.2: $\sigma = \sqrt{\frac{\sum_{i=1}^{N}(x_i - \bar{x})^2}{N}} \rightarrow \sigma = 6.68\ nm$

Equation K.3: $SE = \frac{\sigma}{\sqrt{N}} \rightarrow$ SE = (6.68 nm)/$(46)^{1/2}$ → SE = 0.98 nm

Equation K.4: 95% $CI = \bar{x} \pm t_{\alpha/2,N-1} \times SE \rightarrow$ 30.2 nm ± (2.01)(0.98 nm)
→ 95% CI = 30.2 ± 1.98 nm
→ $d_{pp} = 30.2 \pm 1.98$ nm

Welch's Method Equations and Sample Calculations

Welch's Method was used to determine if there was a difference in geometric mean particle size between the injection site and points downstream. The values

throughout each experiment were very consistent, so the average values were used in this analysis. This examined the confidence in repeatable experimental results. The null hypothesis and alternative hypothesis are listed below as Equation K.5. The P-value can be determined using the t-statistic (t) and degrees of freedom (d.f.). If the P-value is less than 0.5, than the null can be rejected, which would indicate a change in geometric mean particle size.

$\bar{x}_1 = 112\ nm$ $s_1 = 5.06$ nm $N_1 = 5$
$\bar{x}_1 = 137\ nm$ $s_1 = 0.224$ nm $N_1 = 2$

Equation K.5: H_o: $d_g(0\text{ m}) = d_g(0.9\text{ m})$ H_a: $d_g(0\text{ m}) \neq d_g(0.9\text{ m})$
Reject H_o if P-value < 0.05.

Equation K.6: $t = \frac{\bar{x}_1 - \bar{x}_2}{\sqrt{\frac{s_1^2}{N_1} + \frac{s_2^2}{N_2}}} \rightarrow \frac{112-137}{\sqrt{\frac{5.06^2}{5} + \frac{0.224^2}{2}}} \rightarrow$ t = -11.2

Equation K.7: $d.f. = \frac{\left(\frac{s_1^2}{N_1} + \frac{s_2^2}{N_2}\right)^2}{\frac{s_1^4}{N_1^2(N_1-1)} + \frac{s_2^4}{N_2^2(N_2-1)}}$ (Welch-Satterthwaite Equation)

$\rightarrow \frac{\left(\frac{5.06^2}{5} + \frac{0.224^2}{2}\right)^2}{\frac{5.06^4}{5^2(5-1)} + \frac{0.224^4}{2^2(2-1)}} \rightarrow$ d.f. = 4.04 (dimensionless)

P-value(t = -11.2, d.f. = 4.04) = 0.0003, which is less than 0.05, so the null hypothesis is rejected. Therefore, there is a significant difference between the geometric mean diameter at the injection point and 0.9 m downstream when using the Lean soot fuel/air mix with the 27 mm leak size. The P-values for each condition are located in Tables K.1 - K.8.

Table K.1: d_g P-values for Lean soot fuel/air mix, using 27 mm Leak.

d_g (nm)					
Injected	0.9 m	1.8 m	3.4 m		P-value
113	137	134	132	0.9 & 1.8 m	0.546
116	138	138	136	1.8 & 3.4 m	0.542
113				0.9 & 3.4 m	0.298
114					
103					
P-value	0.0003	0.0015	0.0016		

Table K.2: d_g P-values for Lean soot fuel/air mix, using 10 mm Leak.

d_g (nm)					
Injected	0.9 m	1.8 m	3.4 m		P-value
113	127	128	131	0.9 & 1.8 m	0.753
116	131	131	127	1.8 & 3.4 m	0.712
113				0.9 & 3.4 m	0.928
114					
103					
P-value	0.0030	0.0014	0.0069		

Table K.3: d_g P-values for Rich soot fuel/air mix, using 27 mm Leak.

d_g (nm)					
Injected	0.9 m	1.8 m	3.4 m		P-value
57	77	81	75	0.9 & 1.8 m	0.084
57	77	80	78	1.8 & 3.4 m	0.199
56				0.9 & 3.4 m	0.614
63					
61					
P-value	0.0002	0.00004	0.0054		

Table K.4: d_g P-values for Rich soot fuel/air mix, using 10 mm Leak.

d_g (nm)					
Injected	0.9 m	1.8 m	3.4 m		P-value
57	29	41	47	0.9 & 1.8 m	0.071
57	29	44	44	1.8 & 3.4 m	0.365
56				0.9 & 3.4 m	0.063
63					
61					
P-value	0.00002	0.008	0.018		

Table K.5: d_g P-values for TiO_2, using 27 mm Leak.

d_g (nm)					
Injected	0.9 m	1.8 m	3.4 m		P-value
20	27	26	25	0.9 & 1.8 m	0.243
22	29	26	23	1.8 & 3.4 m	0.242
21			32	0.9 & 3.4 m	0.072
21					
P-value	0.029	0.001	0.166		

Table K.6: d_g P-values for TiO_2, using 10 mm Leak.

d_g (nm)					
Injected	0.9 m	1.8 m	3.4 m		P-value
20	26	24	25	0.9 & 1.8 m	0.094
22	25	23	17	1.8 & 3.4 m	0.394
21			21	0.9 & 3.4 m	0.718
21			33		
P-value	0.004	0.005	0.456		

Table K.7: d_g P-values for SiO_2, using 27 mm Leak.

d_g (nm)					
Injected	0.9 m	1.8 m	3.4 m		P-value
177	144	149	174	0.9 & 1.8 m	0.631
177	158	164	154	1.8 & 3.4 m	0.596
170				0.9 & 3.4 m	0.397
177					
P-value	0.159	0.221	0.478		

Table K.8: d_g P-values for SiO_2, using 10 mm Leak.

d_g (nm)					
Injected	0.9 m	1.8 m	3.4 m		P-value
177	128	156	127	0.9 & 1.8 m	0.299
177	133	127	137	1.8 & 3.4 m	0.383
170		144		0.9 & 3.4 m	0.810
177					
P-value	0.0058	0.052	0.048		